International Doctorate on AstroParticle Physics

università degli studi di padova
dipartimento di fisica
scuola di dottorato di ricerca in fisica
ciclo xxxiii

université paris diderot
école doctorale 517:
particules, noyaux et cosmos

Diffuse γ-ray Emission Observed by the Fermi Large Area Telescope

massive stars, cosmic rays and the census of the interstellar medium in the Galaxy

thesis presented by

Luigi TIBALDO

supervisors

Giovanni BUSETTO — Isabelle A. GRENIER

directors of the doctoral schools

Attilio STELLA — Philippe SCHWEMLING

To my mother, Gabriella

ABSTRACT

Galactic diffuse γ-ray emission is produced by interactions of cosmic rays (CRs) with interstellar gas and low-energy radiation fields. This is the brightest component of the high-energy γ-ray sky, surveyed since 2008 with unprecedented sensitivity and angular resolution by the Large Area Telescope (LAT) on board the *Fermi Gamma-ray Space Telescope*. Galactic diffuse emission constitutes not only a bright and structured background which needs to be modeled in order to study individual sources and fainter diffuse components, but it can be used also as a probe of the interstellar environment of the Milky Way.

We present in-depth studies of LAT γ-ray observations of selected regions in the local and outer Galaxy. LAT data are compared with multiwavelength tracers of the interstellar medium (ISM), including radio/mm-wave lines of gas and infrared emission/extinction from dust. The impact of the H I optical depth, often overlooked in the past, is carefully examined and recognized currently as the dominant source of uncertainty in the interpretation of observations.

On one hand, we discuss the constraints provided by the γ-ray data on the census of the interstellar gas. We determine the $X_{\rm CO} = N({\rm H_2})/W_{\rm CO}$ ratio for several clouds, finding no significant gradients in the Galactic disc over a range of ~ 3.5 kpc in Galactocentric radius, and variations of a factor $\lesssim 2$ in nearby local clouds. We also find evidence for an ubiquitous dark phase of interstellar gas which does not shine at radio/mm wavelengths and which provides a mass $\sim 50\%$ of that traced by CO. For the first time we determine its γ-ray spectrum which is found to be well correlated with that of H I, thus further confirming that the emission originates from interstellar gas.

On the other hand, we use the emissivity per hydrogen atom to infer the distribution of CRs in distant locations not accessible by direct measurements. While the local H I emissivity is consistent with the CR spectra measured near the Earth, no significant decrease is found toward the outer Galaxy in spite of the steep decline in number density of putative CR sources. The implications for CR origin and propagation are detailed.

Our models successfully reproduce LAT data over most of the regions considered. A remarkably hard and extended excess of γ-rays is detected in the innermost ~ 100 pc of the massive-star forming region in Cygnus. The γ-ray excess fills a ionized cavity, which apparently extends from the Cyg OB2 stellar cluster toward the γ Cygni supernova remnant, and it hints to the presence of an excess of high-energy particles with respect to the surrounding clouds. We discuss its origin, the relationship with spatially coincident TeV emission detected by Milagro and the possible link with CR acceleration in the region.

SOMMARIO

L'emissione γ Galattica diffusa è prodotta dalle interazioni dei raggi cosmici con il gas e i campi di radiazione di bassa energia nello spazio interstellare. Essa costituisce la componente più brillante del cielo γ ad alte energie, osservato dal 2008 con una sensibilità e una risoluzione angolare senza precedenti dal Large Area Telescope (LAT) a bordo del telescopio spaziale *Fermi*. L'emissione Galattica diffusa costituisce non solo un fondo intenso e strutturato che è necessario modellare per studiare le sorgenti γ individuali e le componenti diffuse più deboli, ma anche un mezzo per sondare l'ambiente interstellare della Via Lattea.

In questa tesi si riportano alcuni studi delle osservazioni γ del LAT per regioni selezionate della Galassia locale ed esterna. I dati del LAT sono confrontati con traccianti multifrequenza del mezzo interstellare, tra cui righe radio e millimetriche del gas e emissione e estinzione dovute alle polveri. L'impatto dello spessore ottico dell'idrogeno atomico, spesso trascurato in passato, è esaminato con cura e identificato allo stato attuale come la principale sorgente di incertezza nell'interpretazione delle osservazioni.

Da un lato si discutono i vincoli dati dall'emissione γ sul censimento del gas interstellare. Il rapporto $X_{\rm CO} = N({\rm H_2})/W_{\rm CO}$ è determinato per varie nubi: non si osserva un gradiente significativo nel disco Galattico su una distanza di 3.5 kpc in raggio Galattocentrico, ma si evidenziano variazioni di un fattore $\lesssim 2$ per le nubi locali. L'emissione γ mette in evidenza in tutte le regioni studiate una fase oscura del gas interstellare che non brilla alle lunghezze d'onda radio o millimetriche, la cui massa rappresenta $\sim 50\%$ di quella tracciata dal CO; l'origine dell'emissione γ da parte di gas oscuro è dimostrata dalla prima misura mai effettuata del suo spettro, che risulta ben correlato a quello dell'idrogeno atomico.

Dall'altro lato l'emissività per atomo di idrogeno serve per tracciare la distribuzione dei raggi cosmici in regioni lontane non accessibili con misure dirette. Mentre l'emissività locale risulta consistente con lo spettro dei raggi cosmici misurato in prossimità della Terra, non si osserva nessuna diminuzione significativa nella Galassia esterna malgrado il rapido decremento nella densità delle sorgenti putative di raggi cosmici. Le implicazioni per la loro origine e propagazione sono discusse in dettaglio.

I nostri modelli riproducono i dati del LAT nella maggior parte delle regioni considerate. Si rivela un eccesso esteso di emissione γ dura nei 100 pc centrali della regione attiva di formazione stellare del Cigno. La "bolla" γ riempie una cavità ionizzata, che apparentemente si estende dall'ammasso di stelle massicce Cyg OB2 in direzione del resto di supernova γ Cygni, e suggerisce la presenza di un eccesso di particelle di alta energia rispetto alle nubi che la circondano. I possibili meccanismi di accelerazione alla sua origine sono esaminati anche in riferimento all'associazione con emissione γ al TeV rivelata da Milagro.

RÉSUMÉ

L'émission γ diffuse Galactique provient des interactions des rayons cosmiques avec le gaz et le champ de rayonnement de basse énergie dans l'espace interstellaire. Elle représente la composante la plus brillante du ciel γ de haute énergie, lequel est observé depuis 2008 avec une sensibilité et une résolution angulaire sans précédent par le Large Area Telescope (LAT) à bord du télescope spatial *Fermi*. L'émission diffuse Galactique ne constitue pas seulement un fond intense et structuré qui doit être modélisé pour étudier les sources individuelles ou les composantes diffuses plus faibles, mais elle peut être utilisée pour sonder l'environnement interstellaire de la Voie Lactée.

Des études détaillées des observations γ du LAT dans des régions spécifiques de la Galaxie locale et externe sont présentées. Les données LAT sont comparées à des traceurs multi longueurs d'onde du milieu interstellaire, dont les raies radio et millimétriques du gaz et l'émission et l'extinction des poussières. L'impact de la profondeur optique du H I, souvent négligé auparavant, est examiné soigneusement et identifié comme la principale source actuelle d'incertitude dans l'interprétation des observations.

Les contraintes apportées par l'émission γ sur le recensement du gaz interstellaire sont discutées. Le rapport $X_{\rm CO} = N({\rm H_2})/W_{\rm CO}$ est déterminé dans plusieurs nuages. Il ne présente pas de gradient significatif dans le disque Galactique sur une distance de 3.5 kpc en rayon Galactocentrique mais des variations d'un facteur $\lesssim 2$ sont observées dans les nuages proches. L'émission γ révèle la présence un peu partout d'une phase sombre du gaz interstellaire qui ne brille pas aux longueurs d'onde radio/millimétriques et dont la masse représente $\sim 50\%$ de celle vue en CO. Pour la première fois on détermine son spectre γ qui suit étroitement celui du H I et confirme ainsi que l'émission associée provient d'un gaz.

D'autre part, l'émissivité trouvée par atome d'hydrogène sert à suivre la distribution des rayons cosmiques dans des endroits éloignés, non accessibles par des mesures directes. L'émissivité trouvée dans le gaz H I local est compatible avec les spectres des rayons cosmiques mesurés près de la Terre, mais nous n'observons pas de diminution significative dans la Galaxie externe malgré le déclin rapide de la densité volumique des sources potentielles de rayons cosmiques. Les conséquences sur l'origine et la propagation de ceux-ci sont discutées en détail.

Nos modèles reproduisent les données LAT dans la plupart des régions considérées. Ils révèlent une bulle étendue d'émission γ dure dans les 100 pc centraux de la région active de formation d'étoiles du Cygne. L'excès γ remplit une cavité ionisée, laquelle apparemment s'étend de l'amas d'étoiles massives Cyg OB2 en direction du reste de supernova γ Cygni, et il suggère la présence d'un excès de particules de haute énergie par rapport aux nuages circonvoisins. La relation avec l'émission γ au TeV mesurée par Milagro au même endroit et les différents processus d'accélération disponibles dans la région sont discutés pour en cerner l'origine.

ACKNOWLEDGEMENTS

I acknowledge the continuous throughout support I received over the past five years from Giovanni Busetto, Denis Bastieri and Riccardo Rando, who gave me the opportunity of undertaking this stimulating research work. My thanks to all the other present and former members of the *Fermi* LAT group in Padova, as well as to people I met in the Physics Department and the INFN section.

I am deeply indebted to Isabelle Grenier for sharing with me her endless knowledge, for the support she gave me and for the enthusiasm she put in our projects. I owe many thanks to the other members of the *Fermi* LAT group at the Service d'Astrophysique of CEA Saclay, especially to Jean-Marc Casandjian, Jean Ballet and David Landriu. I thank also all the people working there for their warm hospitality during my stay in France.

I acknowledge the support of the IDAPP program, which greatly contributed to the quality of my doctoral education and made possible my stay in France. I wish to thank especially Antonio Masiero for introducing me to the IDAPP network and Alessandra Tonazzo for her support at the Université Paris 7.

I am deeply indebted to the *Fermi* LAT collaboration: none of my achievements would have been possible without their huge effort to sustain the mission and the interpretation of the data. I want to thank especially the members of the Galactic sources, calibration & analysis and diffuse emission working groups, and in particular those who directly contributed to the works reported in this dissertation. My thanks to Gulli Jóhannesson and Seth Digel for reviewing the paper on the second quadrant; to Tsunefumi Mizuno for his invaluable work on the third quadrant, to Johann Cohen-Tanugi and Jim Chiang for the bug hunting in the Science Tools and to Andy Strong and Elliot Bloom for their critical comments on the paper. The Cygnus project required many different areas of expertise: I acknowledge the precious help I received from Damien Parent and Lucas Guillemot, the pulsar killers, Sylvain Bontemps for the extinction maps, Hide Katagiri for the study of the Cygnus Loop and Elena Orlando for the modeling of Cygnus OB2. I am grateful to the GALPROP team for the profitable cooperation over the development of this work. Many thanks to Bill Atwood for the useful discussions about residual backgrounds in LAT data and to the other folks of the isotropic background task force.

I wish to express my gratitude to Andy Strong and Thierry Montmerle for serving as rapporteurs for my thesis, and to Antonio Masiero and François Lebrun for accepting to take part to the jury.

I gratefully thank all my friends and my family for their support and their patience. To my parents, Giuseppe and Gabriella, who have always stood beside me, for so much my love.

Io stimo più il trovar un vero,
benché di cosa leggiera,
che 'l disputar lungamente delle massime questioni
senza conseguir verità nissuna.

— Galileo Galilei

INTRODUCTION

Galileo Galilei in 1609 first looked at the sky not by naked eye but instead using his telescope. This event in regarded as the foundation stone of modern Astronomy. A second revolution occurred in the 20$^{\text{th}}$ century, when the development of new instrumentation enabled astrophysicists to expand their field of investigation from visible light to the whole electromagnetic spectrum and to other messengers like cosmic rays (CRs), neutrinos and gravitational waves. Among the last windows of the electromagnetic spectrum opened, we find the most energetic form of light, γ-rays.

Following the first complete survey of the γ-ray sky by the *Compton Gamma-Ray Observatory*, since 2007 we entered in a renaissance of high-energy γ-ray Astrophysics with the launch of the *AGILE* satellite and the *Fermi Gamma-ray Space Telescope*. The *Fermi* Large Area Telescope (LAT) provides a continuous survey of the sky from 20 MeV to more than 300 GeV with unprecedented sensitivity and angular resolution.

This manuscript represents the fruit of the research I carried out in the *Fermi* LAT collaboration during the past three years. I focused my effort in understanding the performance of the telescope and the backgrounds for the study of γ-ray sources, especially Galactic diffuse γ-ray emission.

Indeed, the most evident feature of the LAT sky is our Galaxy, which shines in γ-rays because of interactions of CRs with gas in the interstellar medium (ISM) and low-energy interstellar radiation fields. But what for someone else is only a background, for me represented a treasure of knowledge about the interstellar environment of the Milky Way.

The interstellar space of our Galaxy is populated by CRs, the ISM and interstellar electromagnetic fields intimately bound together and with massive stars. Massive stars form out of the reservoir of matter provided by the ISM in its densest and coldest regions. They enrich their surroundings by emitting intense radiation and releasing nucleosynthesis products carried away in strong winds and powerful explosions at the end of their life. The latter process is thought to power as well the injection of CRs with energies $\lesssim 10^{15}$ eV in the interstellar space of the Galaxy.

CR Physics represented one of the most fertile fields of the 20$^{\text{th}}$ century Science. After the first pioneering studies, CR observations gave birth to subnuclear Physics in the '30s and the '40s. CR Physics reflourished in the second half of the century with the advent of spaceborne instruments, and once more toward the new millennium with the discovery that apparently most of the Universe is made from something unknown we call "dark matter" and "dark energy". The quest for new Physics needed to explain this mystery led to the foundation of the field known as Astroparticle Physics.

On the other hand the ISM is a system extremely rich in interesting Physics far from the local thermodynamical equilibrium, playing a fundamental role in the interplay between the interstellar environment and stars, which are the major constituents of the Galactic ecosystem.

Interstellar γ-ray emission is key to understand CR origin and propagation. It is also a tracer of total column densities in the ISM, which usefully complements gas and dust observations at other wavelengths. The core of the thesis is built around the analyses of three selected regions of the sky relevant for the understanding of the interstellar environment of the Milky Way. The first two of these studies led to publications, for which I gave a major contribution in both the analysis and the redaction phases. The papers are therefore integrated in the manuscript. The last analysis reported is still a work in progress, yet anticipating very exciting results.

Part I provides the reader with the fundamental pieces of information to understand the results presented in the thesis. Readers experienced in the field should skip whatever they already know or even go directly to the second part of the thesis.

Chapter 1 is an overview on *Fermi* LAT data analysis, which presents the γ-ray data and the analysis methods discussed in the following chapters.

Chapter 2 gives a general introduction on the interstellar environment of the Milky Way, with its three basic constituents, the ISM, CRs and electromagnetic fields.

Chapter 3 focuses on the main subject of the thesis, interstellar γ-ray emission. It illustrates the main open questions before the *Fermi* era and some early results obtained by the LAT collaboration, relevant or complementary to my work.

The major scientific outputs of my work are presented in Part II. The first three chapters report the analysis of the individual regions, the latter provides a summary of the results and their implications.

Chapter 4 is dedicated to the region of Cassiopeia and Cepheus in the second Galactic quadrant, where we observe some nearby conspicuous clouds of the Gould Belt, as well as interstellar complexes at larger distances in the outer region of the Milky Way.

Chapter 5 completes the study of the outer Galaxy, with the segment seen toward the third Galactic quadrant in the constellations of Canis Major and Puppis. LAT measurements are also compared with predictions by CR propagation models, and the implications are discussed.

Chapter 6 presents a global analysis of the γ-ray emission from the Cygnus region. The Cygnus complex, located in the tangent direction of the Local Spur, hosts a massive interstellar complex and is the region with the highest massive star-formation activity in the vicinities of the solar system.

Chapter 7 summarizes the results of my analysis efforts regarding interstellar emission and discusses their implications for the distribution of CRs in the Galaxy and its relations with the distribution of putative sources, remnants of massive stars after their explosive death, as well as for the census of the ISM.

Finally, Part III collects some technical material. It is intended to present some very specific personal contributions I gave to the analysis of LAT data with all their gory details.

Appendix A is a note about my work on residual backgrounds in LAT data, both from misclassified CR interactions and the Earth's atmospheric γ-ray emission. Residual backgrounds are a key issue to study the large-scale interstellar emission, therefore relevant to the analyses previously presented, but they are also of larger general interest for the analysis of LAT data.

Appendix B provides some details about the kinematic separation of ISM structures. In particular, I explain here in detail the novel method I developed for kinematic separation that I applied to the analyses presented in the thesis, based on physical structures of the ISM instead of rings as in most of the previous studies.

Appendix C illustrates the procedure for the linear fit of two sets of variables both affected by non-negligible uncertainties and not statistically independent, that I also used for the analyses previously reported.

To help the reader a list of acronyms used along the thesis is provided. Finally, the table of contents describes in detail the structure of the manuscript.

Part I

THE *FERMI* LARGE AREA TELESCOPE AND THE INTERSTELLAR ENVIRONMENT OF THE GALAXY IN γ-RAYS

TELESCOPE, n. A device having a relation to the eye
similar to that of the telephone to the ear,
enabling distant objects to plague us with a multitude of needless details.
Luckily it is unprovided with a bell summoning us to the sacrifice.

— Ambrose Bierce, The Devil's Dictionary

1 THE *FERMI* LARGE AREA TELESCOPE: DATA AND ANALYSIS

The Large Area Telescope (LAT) is the primary instrument on board the *Fermi Gamma-ray Space Telescope* (*Fermi*)[1], launched on June 11, 2008. The LAT is an imaging telescope detecting photons from 20 MeV to more than 300 GeV. The second instrument on board *Fermi* is the γ-ray burst monitor (GBM), dedicated to the study of transient phenomena in the 8 keV to 40 MeV energy range.

In this chapter I will introduce the reader to LAT data and their analysis. I will start with a short overview of the detector and data taking, then I will go through the analysis chain which associates to each event the best estimate of energy and arrival direction and reduces the backgrounds by about six order of magnitudes. The interpretation of data relies on the understanding of the instrument performance, which is modeled using both Montecarlo simulations and in-flight data. I will briefly describe the LAT performance and how it is modeled through Instrument Response Functions (IRFs). I will finally introduce the reader to the statistical technique mainly used to analyze LAT data, the likelihood analysis based on Poisson statistics, and to the high-level analysis environment developed by the LAT team.

This chapter is meant to provide the reader with a comprehensive introduction about LAT data and their analysis rather than presenting my work. Being involved in the activities of the LAT collaboration since the late preparatory phase before the launch, I took part to the verification of the LAT performance[2], to the validation of the analysis tools (§ 1.3.2) and to the studies of residual background contamination. Some technical notes about my personal contributions to the latter topic are included in Appendix A. Given the broad scope of the LAT Science, no attempt is made to review all the objectives of the mission. Those strictly related to my work are presented in Chapter 2 and Chapter 3.

1.1 LAT DATA

1.1.1 *The LAT on orbit*

Fermi is on orbit around the Earth, at $\sim$ 565 km with an inclination of 25.6° with respect to the Equator. After a check-out and commissioning phase the *Fermi* observatory started the nominal Science operations on August 13, 2008[3]. The primary observing mode for *Fermi* is a scanning mode, where the LAT observes the whole sky every two orbits ($\sim$ 3 hours). To achieve this purpose the LAT boresight on alternate orbits is pointed to $+50°$ from the zenith direction and towards the

1. http://fermi.gsfc.nasa.gov/; formerly known as *Gamma-ray Large Area Space Telescope* (*GLAST*).

2. I participated, e.g., to the definition of the standard performance plots shown later in § 1.1.2 and available at
http://www-glast.slac.stanford.edu/software/IS/glast_lat_performance.htm.

3. The LAT was operated in the standard Science operation mode almost continuously since August 4, 2008.

pole of the orbit and to -50° from the zenith on the subsequent orbit[4]. The orbit of *Fermi* has a precession period of $\sim$ 53.5 days. *Fermi* is occasionally operated in pointing mode to study interesting transient phenomena. Calibration runs, which may involve or not pointings, are also periodically performed.

The LAT detector

The LAT (Atwood et al., 2009) is an imaging, wide-field-of-view, γ-ray telescope, detecting photons from 20 MeV to more than 300 GeV. The LAT is a pair-tracking telescope, made from a 4×4 array of towers, with a converter-tracker and a calorimeter module. A segmented anticoincidence detector (ACD) covers the tracker array, and a programmable trigger and data acquisition system (DAQ) completes the instrument. Fig. 1.1 provides a schematic illustration of the LAT.

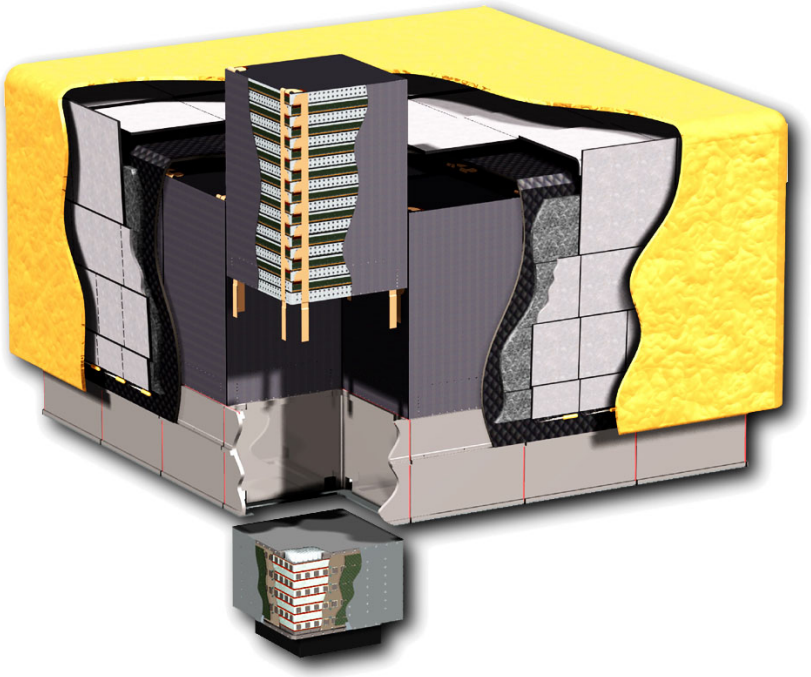

Figure 1.1: Schematic view of the LAT (Atwood et al., 2009): a tower (tracker and calorimeter module) is cut-away and partially exploded for display. The real telescope dimensions are 1.8 m$\times$1.8 m$\times$0.72 m.

High-energy γ-rays interact with matter mainly through production of $e^+ - e^-$ pairs. The LAT converter-tracker modules (Atwood et al., 2007) have therefore 16 planes of high-Z material (tungsten), which promote the conversion into pairs. The sensitive tracker apparatus consists of 18 (x, y) tracking planes, each with two layers (x and y) of single-sided silicon strip detectors. The first 16 planes are interleaved with the tungsten foils, the first 12 with a thickness of 0.03 radiation lengths (*thin* or *front* section) to maximize the angular resolution at low energies limiting the Coulomb scattering, the following 4 with a thickness of 0.18 radiation lengths (*thick* or *back* section) to maximize

4. The rocking angle used to be 35° at the beginning of the mission, and it was later increased to improve the battery performance, being its cooling more efficient if the bottom of the spacecraft points away from the Earth.

the conversion probability at high energies. The last two planes have no converter foils in order to accurately measure the entering point in the calorimeter. The aspect ratio of the tracker (height/width) is 0.4, allowing a large field of view (FoV) of 2.4 sr and ensuring that nearly all pair-conversion events will pass into the calorimeter. The self-triggering capability of the tracker is an important new feature of the LAT design that is possible because of the choice of silicon-strip detectors, which do not require an external trigger. In addition, all of the LAT instrument subsystems utilize technologies that do not use consumables, such as the gas of tracking spark chambers in previous high-energy γ-ray telescopes. The read-out electronics are described in Baldini et al. (2006).

Every calorimeter module has 96 CsI crystals doped with thallium, arranged in an eight-layer hodoscopic configuration with a total depth of ~ 8.6 radiation lengths, giving both longitudinal and transverse information about the energy deposition pattern. Crystals are read out by photodiodes at each side. The calorimeter provides the measurement of the energy deposited by the shower initiated by the $e^+ - e^-$ pairs, and also images the shower development, enabling the estimation of the energy leakage and the discrimination from hadronic showers. Each crystal provides three spatial coordinates: two discrete coordinates from the location of the crystal in the array and the third coordinate given by measuring the light yield asymmetry at the ends of the crystal along its long dimension.

The ACD is the first defense of the LAT against the large background given by charged CRs. In the LAT design it was required to provide an efficiency exceeding 0.997 for detection of singly charged particles entering the FoV of the telescope. With respect to previous pair-tracking γ-ray telescopes the LAT was designed to detect photons up to hundreds of GeV. It was therefore essential to avoid the "self-veto" effect, i.e. the rejection of γ-rays with energies $\gtrsim 10$ GeV because of the backsplash on the ACD of secondary particles produced in the calorimeter. For this purpose the LAT ACD is segmented into 89 plastic scintillator tiles providing spatial information that can be correlated with the signal from tracker and calorimeter modules. Scintillation light from each tile is recorded by wavelength shifting fibers embedded in the scintillator and connected at their ends to two photomultiplier tubes (PMTs). To minimize inefficiencies along one dimension adjacent tiles are overlapping; along the other gaps between tiles are covered by flexible scintillating fiber ribbons with $> 90\%$ detection efficiency. To protect the ACD from debris hitting its surface, it is covered by a light micrometeoroid shield (0.39 g cm^{-2}). A complete description of the ACD and its performance is given by Moiseev et al. (2007).

Data acquisition

The DAQ collects information from the subsystems, generate the instrument triggers (at a rate of $2 - 3$ kHz) and provides the first onboard filter reducing the rate of downlinked events to ~ 500 Hz, while the entire LAT instrument is connected to the satellite through the spacecraft interface unit.

The tracker and calorimeter modules of each tower are interfaced by a tower electronics module (TEM), generating tower-based triggers. At the entire instrument level a global unit collects signals from all the electronics module and distributes the clock signal, provides an

interface with the ACD, generates instrument-wide triggers based on the information received from the TEMs and the ACD interface and builds the events with the information received from the whole apparatus, sending them to the event processor units (EPUs).

The minimum read-out time per event is 26.5 μs, due to the transmission of the trigger signal between the different units. During the event read-out the different subsystems send a busy signal to the global unit, which generates the overall dead time and send it to Earth along with data.

The trigger is designed in order to minimize the deadtime due to background events. Triggers are generated by any of the TEMs, either if there is a signal over threshold for three planes in a row or an energy deposition threshold is exceeded in any of the calorimeter crystals (with two different thresholds for low-energy and high-energy events). Non-detector based trigger inputs are used for calibration and diagnostic purposes, either derived from a periodic clock or from an external request.

The two EPUs implement the onboard filtering aimed at reducing the contamination by charged particles. The events triggering the LAT are indeed mostly background due to CR interactions. The onboard analysis is designed in order to maximize the efficiency for γ-ray detection keeping the background within the bandwidth allowed for downlink. Note that all events exceeding a threshold of raw energy deposited in the calorimeter (in the range $10 - 20$ GeV) are downlinked at Earth for analysis since their rate is low.

The *Fermi* orbit crosses the Earth inner radiation belt in a region known as the South Atlantic Anomaly (SAA). The SAA hosts geomagnetically trapped particles with fluxes exceeding by several orders of magnitude those in the rest of the orbit. This hard radiation environment would lead to the saturation of the tracker electronics, with a drastic reduction of the livetime, and high currents in ACD PMTs exceeding the safe operation limits and producing a rapid deterioration. Therefore, the LAT does not take data during the passages in the SAA and bias voltages of the PMTs are lowered from 900 V to $\sim$ 400 V (Abdo et al., 20090). The perimeter delimiting the SAA was conservatively defined prior to launch, and re-evaluated in the commissioning phase, so that the turn-off leads to a loss in observation time of $\sim$ 13% of the total on-orbit time (Abdo et al., 20090).

1.1.2 *Reconstruction and classification*

Once data have been downlinked to the Earth the event analysis process starts, consisting in the determination of the direction and energy of the candidate γ-rays and the event classification necessary to largely reduce the backgrounds and tune the instrument performance. The whole event analysis chain was developed and strongly relies on detailed Montecarlo (MC) simulations of the instrument.

All the work presented in this thesis is based on the event analysis developed prior to launch known as `Pass 6` (or `P6`), which is described in some detail in the rest of the paragraph. The LAT team, thanks to the expertise accumulated with real data after the launch, is working on the definition of an analysis with improved event classification (`P7`) and a further analysis version redefining also the event reconstruction (`P8`).

The LAT Montecarlo Modeling

Central in the pre-launch phase for the design of the instrument and the development of the software infrastructures, the MC modeling of the LAT is fundamental for both the event analysis and the studies of the instrument performance.

LAT MC simulations make use of different γ-ray source models (including realistic representations of the γ-ray sky) and a full model of the backgrounds (e.g. charged CRs, neutrons, γ-ray emission from the Earth limb, see Ormes et al., 2007).

The LAT MC modeling is based on GLEAM (*GLAST* LAT Event Analysis Machine, see Boinee et al., 2003, for details). The simulation of events is based in particular on some tools of the Geant 4 MC toolkit (Allison et al., 2006).The instrument digitization is then modeled through parametrized calculations; after the launch on-orbit calibration data (Abdo et al., 20090) were used to convert the energy deposited in the active volumes to instrument signals. Then, an analogue of the onboard filter described above is applied and then events undergo the same analysis chain described below.

The MC modeling of the LAT was validated through an on-ground calibration with muons and a beam-test campaign performed on a calibration unit (CU), made from some subdetector modules identical to those used to build the LAT, including two complete tracker-calorimeter towers. The CU was exposed to photons (up to 2.5 GeV), electrons ($1 - 300$ GeV), hadrons (π and p, from a few GeV to 100 GeV) and ions (C, Xe, 1.5 GeV/n) in different irradiation facilities (see Baldini et al., 2007, for details). The beam test made possible the tuning of the detector modeling, as well as the choice of the G4 interaction models which best reproduce the real data [5]. It provided also the bounds to the systematic uncertainties on the absolute energy measurements, equivalent to $^{+5\%}_{-10\%}$ (Ackermann et al., 2010).

Tracking and energy reconstruction

Spatially adjacent hits in the tracker are combined in a cluster, determining a 3D position in the detector. Clusters are then combined to generate track hypotheses. Two different algorithms are used to generate tracks. The first method is based on the centroid and axis of the energy deposition in the calorimeter; the furthest cluster is chosen at random in the appropriate temporal window, the second one is searched for on the line connecting the putative first hit to the deposition centroid in the calorimeter; if the latter is found a track hypothesis is generated and populated using an adaptation of the Kalman filter (Frühwirth et al., 2000), propagating clusters to the following layer using a full covariance matrix which takes into account Coulomb scattering; the process is iterated over all the possible furthest clusters, until a track of sufficient quality is found after exploring at least two layers; the "longest, straightest" track found by the Kalman fit is retained as the best track (corresponding to the higher energy charged particle hypothetically produced by the γ-ray conversion), and after flagging the hits of the first track as used a second track-finding algorithm is

5. Notably, the LAT beam test led to discover that the Landau-Pomeranchuck-Migdal effect, affecting the development of electromagnetic showers in the calorimeter, was inaccurately implemented in the standard libraries; the problem was fixed in following versions of Geant 4.

invoked. The second method is used when calorimeter information is not sufficient for track finding (e.g. at low energies): it is a blind method analogous to the first one but the second cluster is chosen at random in the next closest layer to the calorimeter; multiple scattering errors are calculated assuming a minimum energy, namely 30 MeV.

After determining single tracks, the latter are combined into vertices. The best track is combined with a second one chosen among the others associated with the event. If the second track approaches the best one within a given distance, namely 6 mm, a vertex solution is generated. The next unused track is selected and the process repeated. Tracks which are not satisfactorily paired are assigned to a vertex by themselves. If calorimeter information is available a further solution, the "neutral energy" solution, is also possible: when a significant fraction of energy goes into neutral particles (γ-rays) during the conversion process or immediately thereafter (due e.g. to Bremsstrahlung) the tracks can point away from the direction of the infalling γ-ray, but the direction can be better reconstructed using the centroid of the energy deposition in the calorimeter.

The first step in the energy reconstruction is the conversion of the raw signals into energy deposition for each crystal end, providing the total energy and the position for each crystal, thus resulting in a 3D array of energies. The sum of the energies deposited provides the first raw estimate of the event energy, whereas the 3D centroid and moments of the energy deposition provide the direction of the shower. Further corrections are based on the track direction (or vertex direction) determined as described above using the tracker information. The trajectory is used to estimate the energy leakage out of the sides and back of the calorimeter and in internal gaps between the active volumes. Three different algorithms are used, based on a parametric correction using the barycenter of the shower, on a fit to the shower profile or on a maximum likelihood taking into account also the hits in the tracker. At low energies ($\lesssim 100$ MeV) a significant fraction of the energy can be deposited in the tracker, therefore this contribution is estimated from the tracker hits and added to the corrected calorimeter energy.

Event classification and background rejection

Event classification aims at selecting the best estimates of the event direction and energy among those available for the event and determining their accuracy, as well as at drastically reducing the backgrounds in the final data sample. All these purposes are achieved using a series of selection criteria and classification tree [6] (CT) generated probabilities (Breiman et al., 1984).

Using a CT the best energy estimate is chosen between the available options for each event, and using another CT the probability that the measured value is within 1σ from the true value is evaluated. For the estimate of the direction, at first a CT chooses between the vertex solution if available and the best one-track solution. Events are then divided into four subclasses, according to the conversion point, in the *front* or *back* section of the tracker, and to the vertexing properties, vertex or one-track events. For each of the subsets the probability that the

6. Automated algorithm which partitions a data set into classes generating complex event selection criteria

measured direction is within the 68% containment angle from the true arrival direction is evaluated by a CT, and the events are re-merged. At this point for each event there are a best energy and a best direction measurements, as well as the corresponding estimates of the accuracy of the measurements.

The background rejection is a fundamental task since the background events triggering the LAT exceed by 10^5 the celestial γ-rays. The on-board filter is configured in order to fit the available band for data downlink at the Earth while keeping the largest possible efficiency for γ-ray detection (reducing the signal-to-noise ratio at $\sim 1:300$). The background rejection at Earth aims at further reducing the backgrounds by almost three orders of magnitude. The main tool to achieve this purpose is the ACD used in conjunction with the measured tracks. Event with tracks pointing to hits in the ACD and to gaps in the ACD shield are discarded (the latter case provides an efficiency loss only at the level of $\sim 2\%$). Further constraints to reduce the backgrounds are based on the event topology in the tracker and the overall shower profile in tracker-calorimeter; they are used to grow some CTs which estimate the probability of an event being a celestial γ-ray or a background particle.

The various scientific objectives of the LAT Science require an appropriate tuning of the instrument performance and of efficiency/background contamination; a few event classes were defined prior to launch. The *Transient* class, suitable for studying localized, intense, transient phenomena, has the largest efficiency but a residual background at the level of the γ-ray detection rate. The *Diffuse* class[7] was the purest class, expected to achieve a background-rejection factor of the order of 10^6, while keeping an efficiency for γ-ray detection $\sim 80\%$. After launch the better understanding of the backgrounds led to the definition of a purer class, called *Dataclean*, especially developed to study the extragalactic γ-ray background (EGB, Abdo et al., 2010j). All the event classes have a residual background contamination. The reducible backgrounds are given by events which, in principle, could be identified as background and eliminated. The irreducible backgrounds are given by background particles interacting with the dead materials surrounding the instrument and producing a real γ-ray which enters the detector. Irreducible events constitutes the majority of residual backgrounds in the purest classes. For more details on residual backgrounds see Appendix A.

The event analysis finally results in a table, where each event is associated with an energy, a direction and some additional pre-computed quantities, as well as a flag which allows the user to select among the predefined event classes. LAT photon data[8] are publicly available through the *Fermi* Science Support Center (FSSC)[9], together with the orbital history of the telescope.

7. So called because it was specifically tuned to study diffuse γ-ray emission, even if after launch it was used also to study sources due to the backgrounds larger than expected for the *Source* class.

8. Only photon data are released, meaning that all the events in the public data sample meet the loose selection criteria of the *Transient* class.

9. http://fermi.gsfc.nasa.gov/ssc/

1.2 THE LAT INSTRUMENT RESPONSE FUNCTIONS

In high energy Astrophysics it is conventional to use for data analysis a high-level model of the instrument response through Instrument Response Functions (IRFs; e.g. Davis, 2001). This choice is motivated by two different purposes:

- providing the whole scientific community with a mean to interpret the data after direction and energy reconstruction and event classification;
- comparing data from different instruments in different energy ranges, to perform multiwavelength analyses.

The LAT IRFs were defined and parametrized prior to launch based on the MC simulations described in § 1.1.2. After launch the IRFs started being modified to take into account effects observed on-orbit, notably the losses of efficiency due to accidental coincidences and pile-up effects in the detector and other differences found between MC and on-orbit performance. The LAT IRF models developed by the LAT team are released along with data. (§ 1.3.2).

1.2.1 *Modeling the LAT performance*

Definition of the IRFs

The IRFs are defined by convention as a function R of true photon energy E' and direction $\hat{p}'$, measured photon energy E and direction $\hat{p}$ and time t, so that the differential count rate in the instrument phase space (reconstructed energy and direction) is given by the convolution of the source differential flux per unit area at the detector with the IRFs.

$$\frac{\mathrm{d}N}{\mathrm{d}t\,\mathrm{d}E\,\mathrm{d}\hat{p}}(E,\hat{p},t) = \int \mathrm{d}E'\mathrm{d}\hat{p}'\; R(E,\hat{p}|E',\hat{p}';t)\,\frac{\mathrm{d}N}{\mathrm{d}t\,\mathrm{d}E'\mathrm{d}\hat{p}'\mathrm{d}S}(E',\hat{p}',t) \tag{1.1}$$

The IRFs are canonically factorized into three functions, representing the efficiency, the angular resolution and the energy resolution plus a temporal scaling factor.

$$R(E,\hat{p}|E',\hat{p}';t) = T(t)A(E',\hat{p}')P(\hat{p}|E',\hat{p}')D(E|E',\hat{p}') \tag{1.2}$$

The scaling factor $T(t)$ accounts for temporal variations, such as instrument failures or the deterioration of instrument components. The lack of consumables (like the gas of spark chambers in previous high-energy γ-ray telescopes) makes the LAT performance very stable and therefore this term negligible.

The three functions usually called IRFs are then:

- the effective area, $A(E',\hat{p}')$, the detection efficiency for photons of true energy E' and arrival direction $\hat{p}'$ expressed as an area (i.e. the factor converting incident fluxes per unit area into differential count rates in the instrument regardless of the reconstructed energy E and direction $\hat{p}$);
- the Point Spread Function (PSF), $P(\hat{p}|E',\hat{p}')$, the probability density that a photon with energy E' and arrival direction $\hat{p}'$ has a reconstructed direction $\hat{p}$;
- the energy dispersion, $D(E|E',\hat{p}')$, the probability density that a photon with energy E' and arrival direction $\hat{p}'$ has a reconstructed energy E.

Representation of the IRFs

The LAT IRFs are determined primarily by the hardware design, the event reconstruction algorithms and the event classification and selection. The IRFs were modeled prior to launch using the MC simulation of the detector. The MC modeling consists in a dedicated massive simulation of γ-ray events and the subsequent derivation of the IRFs.

The effective area is represented as a table of scalars in several bins in energy and inclination angle with respect to the detector axis and separately for *front* and *back*-converting events. The representation of the PSF and energy dispersion is more complex: it involves the parametrization of the angular and energy distribution of events. This is done assuming some functional forms which approximately reproduce the observed distributions and determining the function parameters fitting data in several bins in energy and inclination angle.

The details of the representation (parametric functions, binning) varied among the different versions of the IRFs. Instead of focusing on the current version, for further details I address the interested reader to the dedicated web pages of the FSSC [10], which are continuously updated with the latest developments in the modeling of the LAT performance.

The latest pre-launch expectations for the LAT performance are described in Atwood et al. (2009), corresponding to the IRF sets known as `P6_V1` [11]. In the next paragraph I will overview the developments in the LAT IRF after launch and I will briefly discuss the current open issues.

1.2.2 *LAT Instrument Response Functions since launch and open issues*

The outcome of the on-orbit calibration campaign of the LAT (Abdo et al., 20090) was implemented in the LAT MC simulation, and so in the generation of the IRFs. Moreover, some unexpected effects became clear when comparing real data with MC simulations.

Hunting ghosts

Right after launch unexpected interactions between γ-ray and background events were observed, source of rate-dependent inefficiencies. Prior to launch these effects were thought to be negligible. A *ghost event* consists, e.g., in a background particle releasing energy in the sensitive volumes immediately before a real γ-ray triggers the LAT. See Fig. 1.2 for an example illustration. Those events may be discarded by the event classification algorithms trained on MC simulations unaffected by such effects, leading to a degradation of the instrument performance.

The real solution to these problems is the redefinition of the reconstruction analysis in order to correctly treat events with artifacts, which is under investigation by the LAT team (`P8` analysis). In the mean time, to allow unbiased studies of celestial sources the effects of ghosts are taken into account in the generation of the IRFs. Data frames are extracted from periodic trigger events, stored in bins of geomagnetic

10. http://fermi.gsfc.nasa.gov/ssc/data/analysis/documentation/Cicerone/Cicerone_LAT_IRFs/IRF_overview.html

11. The LAT IRFs are conventionally called after the event analysis version they refer to (`P#`), plus a number representing the version of the IRFs (`V#`), plus the event class (selection criteria used to build the data sample).

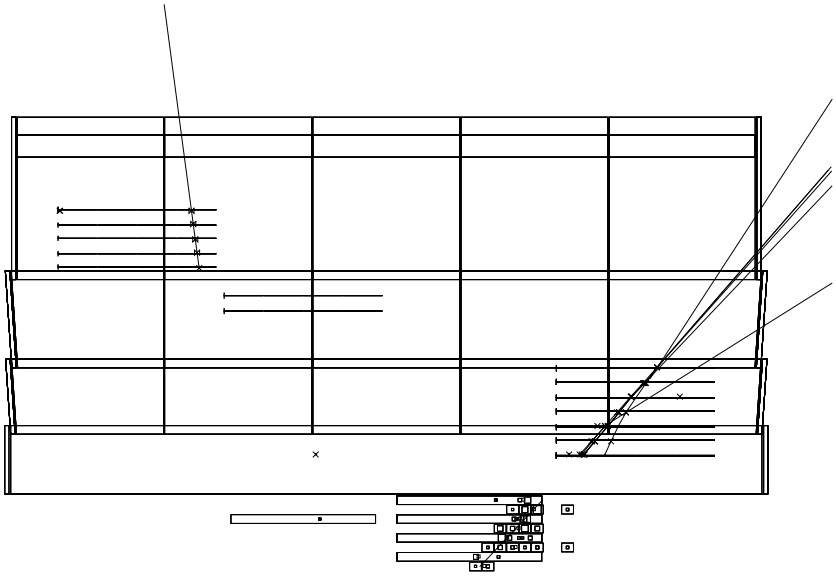

Figure 1.2: Example of a ghost event in the LAT (Rando et al., 2009): on the left a *ghost* track produced by the accidental time coincidence of a background particle hitting the LAT, on the right a candidate γ-ray. Only active volumes in tracker and calorimeter are shown; overlaid the candidate tracks.

latitude to correctly sample the LAT radiation environment, and randomly superimposed to MC generated events to simulate the effect of ghosts [12].

P6_V3_DIFFUSE IRFs

This "overlay" procedure led to the first IRF set taking into account on-orbit effects, called `P6_V3` (Rando et al., 2009), where the effective area is corrected for the *average* effect of pile-up and accidental coincidence effects in the LAT given its orbital characteristics. I will now shortly describe the performance of the LAT as depicted in this IRF set for the *Diffuse* events class, which were used for most of the analyses reported in this thesis, as well as for many published papers, notably the first-year LAT Catalog (1FGL; Abdo et al., 2010c). I address the readers to the LAT performance web page [13] for the latest developments.

Fig. 1.3 shows the effective area of the LAT, separately as a function of energy for normally incident photons and as a function of incidence angle for 10 GeV photons. The peak effective area, typically lying in the $1 - 10$ GeV energy range is greater than 8000 cm^2.

The relevant quantity in the standard survey mode is the effective area integrated over the FoV, called acceptance or *étendue*, which is shown in Fig. 1.4. The large acceptance of the LAT led to the collection of a data sample which already exceeds by more than one order of magnitude the statistics of previous γ-ray telescopes. Fig. 1.4 shows the intrinsic acceptance, regardless of orbital characteristics; to obtain the effective acceptance the curves have to be rescaled by the livetime fraction. It is interesting to note that the acceptance has a slower turn-

12. Note that most of the data frames are empty.
13. http://www-glast.slac.stanford.edu/software/IS/glast_lat_performance.htm

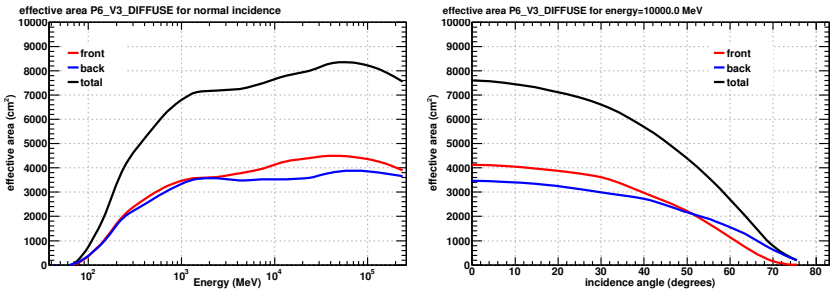

Figure 1.3: The LAT effective area as a function of energy for normally incident photons (left) and as a function of incidence angle for 10 GeV photons (right). The curves correspond to *front*-converting events (red), *back*-converting events (blue) and total (black).

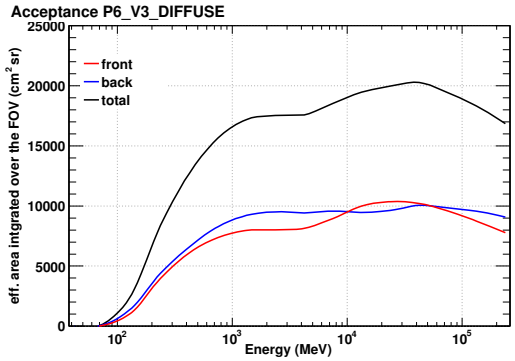

Figure 1.4: The LAT acceptance as a function of energy. The curves correspond to *front*-converting events (red), *back*-converting events (blue) and total (black).

on with respect to the normal effective area, highlighting the dependence of the FoV on energy.

Fig. 1.5 shows the angles for 68% and 95% event containments, as a function of energy and incidence angle as above. The PSF strongly

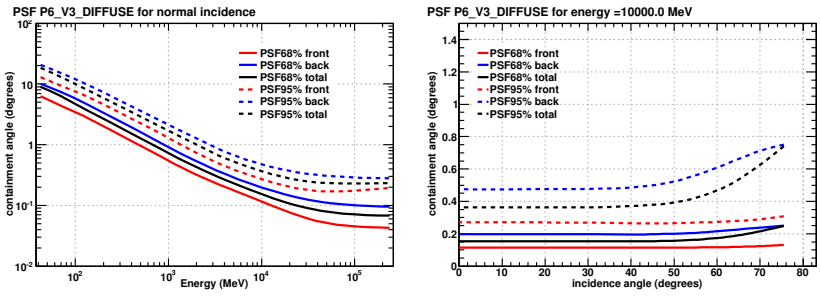

Figure 1.5: The 68% and 95% event containment angles as a function of energy for normally incident photons (left) and as a function of incidence angle for 10 GeV photons (right). The curves correspond to *front*-converting events (red), *back*-converting events (blue) and total (black).

depends on energy due mainly to Coulomb scattering in the tracker,

whereas the dependence on incidence angle is mild. As an illustrative number, we note that the 68% containment angle for *front*-converting events at 1 GeV is $\sim 0.6^\circ$, whereas the diameter of the full Moon in the sky is $\sim 0.5^\circ$. For comparison, the 68% containment angle at 1 GeV of EGRET, the predecessor of the LAT, was 1.7°. If compared to an ideal Gaussian case, the PSF has larger tails especially at energies $\gtrsim 10$ GeV. This can be appreciated looking at the ratio of the 95% to the 68% containment angle, shown in Fig. 1.6. This ratio would be 1.62 for the

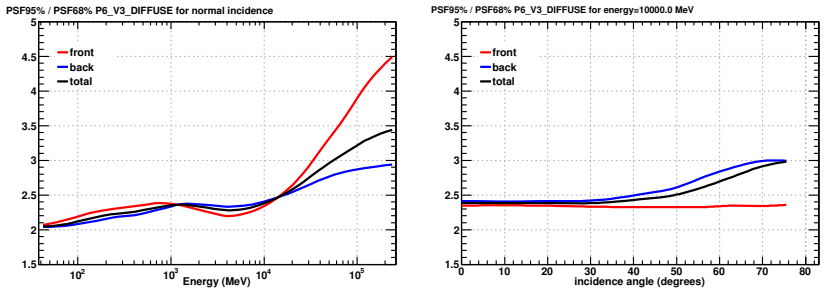

Figure 1.6: The ratio of 95% and 68% event containment angles as a function of energy for normally incident photons (left) and as a function of incidence angle for 10 GeV photons (right). The curves correspond to *front*-converting events (red), *back*-converting events (blue) and total (black).

ideal Gaussian case, while it is > 2 for the LAT PSF.

Fig. 1.7 shows $\Delta E/E$ for 68% event containment, which is a measure

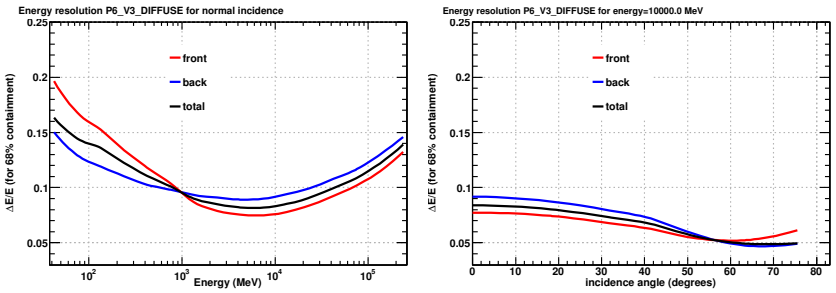

Figure 1.7: $\Delta E/E$ for 68% event containment as a function of energy for normally incident photons (left) and as a function of incidence angle for 10 GeV photons (right). The curves correspond to *front*-converting events (red), *back*-converting events (blue) and total (black).

of the instrument energy resolution. It is better than 15% over most of the LAT energy band.

The systematics affecting the LAT effective area were evaluated for this event class using bright pulsars (Rando et al., 2009), which provide us with a clean γ-ray sample thanks to the temporal properties of their emission. The conservative estimate of the systematics derived puts a 10% upper limit on the effective area uncertainties at 100 MeV, 5% at 562 MeV and 20% at 10 GeV. The bounds to the effective area uncertainties can be assumed to linearly vary with the logarithm of energy between these values.

IRFs beyond `P6_V3`

Further improvements are under development by the LAT team. There is a small dependence of the effective area on the azimuthal angle in the detector, at a few % level, which can affect observations of bright sources on day scales. This dependence can be modeled from the MC simulations and taken into account.

`P6_V3` IRFs take into account the *average* effect of pile ups and accidental coincidences in the LAT. The effect is indeed dependent on the trigger rate, or, equivalently, on the livetime fraction. The livetime-dependent correction to the effective area can be computed from MC simulations with *ghost* overlays and parametrized (also as a function of energy) with simple analytical formulas to re-weight the effective areas in the IRF convolution.

The experimental PSF at energies $\gtrsim 5$ GeV was found to be broader than expected from MC simulations. This was noticed in the distribution of events around bright sources, active galactic nuclei (AGN) and pulsars (PSR), and advertised as a source of systematics by the LAT collaboration (e.g. Abdo et al., 2010c). Part of the problem can be attributed to deficiencies of the MC simulation used to generate the IRFs; the LAT team is currently investigating the possibility of releasing an in-flight PSF, corrected to reproduce in-flight data, while trying to fix the mismatch between data and MC simulations.

As anticipated, small systematic discrepancies at the 5% level are observed between real events and MC for some variables related to the shower development in the tracker and the calorimeter, which are influencing the estimate of the efficiency. Also in this case the LAT collaboration is considering to use in-flight data to correct the effective area while investigating the origin of these discrepancies to reduce the final systematic uncertainties on the absolute fluxes.

1.3 LIKELIHOOD ANALYSIS OF LAT DATA

Because of the limited statistics, the presence of a bright and structured background given by interstellar emission and the angular resolution strongly varying with energy, yet always poor compared to other wavelengths, it is never possible to really isolate a source in high-energy γ-rays and statistical techniques have to be applied to study the GeV sky. In this section I review the most broadly used method, the likelihood analysis based on Poisson statistics, which was applied for the analyses described in this thesis. I will describe its basics features and how it is implemented in the LAT high-level analysis environment.

The likelihood analysis requires to assume a model of the signal detected by the telescope. Describing the sky at GeV energies is complicated by the dominance of diffuse γ-ray emission (see Chapter 3), which needs to be modeled together with individual sources.

1.3.1 *Likelihood analysis for photon-counting experiments*

Let us assume to have a model describing the observations supposed to be known except for a finite number of parameters. Let $M(E', \hat{p}', t; \{\alpha_k\})$ be the differential flux per unit area at the detector predicted by the model as a function of true photon energy E', true

photon arrival direction at the detector $\hat{p}'$, time t and of the unknown parameters $\{\alpha_k\}_{k=1,\ldots,m}$.

Using the definition of the IRFs in Eq. 1.1 we can derive the differential count rate J in the detector phase space (reconstructed energy E and direction $\hat{p}$) predicted by the model

$$J(E,\hat{p};\{\alpha_k\}) = \int \mathrm{d}t\,\mathrm{d}E'\mathrm{d}\hat{p}'\; R(E,\hat{p}|E',\hat{p}';t)\,M(E',\hat{p}',t;\{\alpha_k\}) \quad (1.3)$$

as a function of reconstructed energy E, reconstructed arrival direction $\hat{p}$ and of the unknown parameters $\{\alpha_k\}_{k=1,\ldots,m}$. The counts expected in a given energy range (E_1, E_2), solid angle Ω and time interval (t_1, t_2) are then obtained as the integral of the differential count rate in the detector.

$$\Lambda(\{\alpha_k\}) = \int_{t_1}^{t_2} \mathrm{d}t \int_{\Omega} \mathrm{d}\hat{p} \int_{E_1}^{E_2} \mathrm{d}E\; J(E,\hat{p};\{\alpha_k\}) \quad (1.4)$$

Given the low counting rates it is appropriate to use for the comparison the Poisson statistics, as originally proposed by Cash (1979). This method was successfully used for γ-ray studies over the years (e.g. Pollock et al., 1981; Mattox et al., 1996). If λ is the number of expected counts the probability density of observing n counts is

$$f(n,\lambda) = \frac{\lambda^n}{n!}\mathrm{e}^{-\lambda} \quad (1.5)$$

Expected counts can be compared with observed counts binned with a certain grid in arrival direction and energy. The likelihood is defined as the product for each pixel $\imath$ of the probability densities of observing $N_\imath$ counts given the expectation $\Lambda_\imath(\{\alpha_k\})$.

$$\mathscr{L}(\{\alpha_k\}) = \prod_\imath f[N_\imath, \Lambda_\imath(\{\alpha_k\})] \quad (1.6)$$

It is convenient to consider the logarithm of the likelihood.

$$\log\mathscr{L}(\{\alpha_k\}) = \sum_\imath N_\imath \log\Lambda_\imath(\{\alpha_k\}) - \sum_\imath \Lambda_\imath(\{\alpha_k\}) - \sum_\imath \log(N_\imath!) \quad (1.7)$$

The best-fit set of parameters $\{\overline{\alpha}_k\}$ is found maximizing the likelihood, or equivalently its logarithm [14], where the last term $\sum_\imath \log(N_\imath!)$ can be neglected since it is model independent. The likelihood becomes

$$\log\mathscr{L}(\{\alpha_k\}) = \sum_\imath N_\imath \log\Lambda_\imath(\{\alpha_k\}) - \Lambda_{\mathrm{tot}}(\{\alpha_k\}) \quad (1.8)$$

where $\Lambda_{\mathrm{tot}}(\{\alpha_k\})$ is the total number of counts predicted by the model.

The likelihood profile around the maximum provides an estimate of the statistical errors affecting the best-fit parameters. According to Cramer-Rao's disequation (Cramer, 1946; Rao, 1945) an upper limit to the covariance matrix terms is given by

$$\sigma^2_{ab} = \left[-\left.\frac{\partial^2 \log\mathscr{L}}{\partial\alpha_a\partial\alpha_b}\right|_{\{\overline{\alpha}_k\}} \right]^{-1} \quad (1.9)$$

In the case of limited statistics an unbinned likelihood method can be used. Let us think to use a grid fine enough that in each pixel the

14. Commonly used numerical codes minimize the opposite of the likelihood logarithm.

number of observed counts is either 0 or 1. Let P be the pixel set where $N_\iota = 1$, the likelihood logarithm is therefore simply

$$\log \mathscr{L}(\{\alpha_k\}) = \sum_{\iota \in P} \log \Lambda_\iota(\{\alpha_k\}) - \Lambda_{\rm tot}(\{\alpha_k\}) \tag{1.10}$$

In a small enough pixel $\Lambda_\iota(\{\alpha_k\}) = J(E_\iota, \hat{p}_\iota; \{\alpha_k\})\Delta t \Delta\hat{p}\Delta E$, so Eq. 1.10 yields

$$\begin{aligned} \log \mathscr{L}(\{\alpha_k\}) &= \sum_{\iota \in P} [\log J(E_\iota, \hat{p}_\iota; \{\alpha_k\}) + \log \Delta t + \log \Delta\hat{p} + \log \Delta E] + \\ &\quad -\Lambda_{\rm tot}(\{\alpha_k\}) = \\ &= \sum_{\iota \in P} \log J(E_\iota, \hat{p}_\iota; \{\alpha_k\}) + \log \Delta t^{N_{\rm obs}} + \log \Delta\hat{p}^{N_{\rm obs}} + \\ &\quad + \log \Delta E^{N_{\rm obs}} - \Lambda_{\rm tot}(\{\alpha_k\}) \end{aligned} \tag{1.11}$$

where $N_{\rm obs}$ is the total number of observed photons. Being the mid terms independent from the model they can be neglected for the likelihood maximization and Eq. 1.11 becomes

$$\log \mathscr{L}(\{\alpha_k\}) = \sum_{\iota \in P} \log J(E_\iota, \hat{p}_\iota; \{\alpha_k\}) - \Lambda_{\rm tot}(\{\alpha_k\}) \tag{1.12}$$

where the first summation can be practically computed looping over the energies and directions of the observed photons.

The quantitative comparison between different models using the likelihood analysis is not straightforward. There are some selected cases where the comparison can be performed using the likelihood ratio test (LRT). Let us consider the model $M(\{\alpha_k\}_{k=1,\dots,m})$, and let us assume $M_0(\{\alpha_k\}_{k=1,\dots,h})$ to be a simpler or more parsimonious model where $\{\alpha_k\}_{k=h+1,\dots,m}$ are fixed to given values ($m > h$). In the null hypothesis that $\{\alpha_k\}_{k=h+1,\dots,m}$ are set to the true values the Wilk's theorem (Wilk, 1938) predicts that the test statistics

$$\mathrm{TS} = 2\left(\log \overline{\mathscr{L}} - \log \overline{\mathscr{L}_0}\right) \tag{1.13}$$

where $\overline{\mathscr{L}}$ and $\overline{\mathscr{L}}_0$ are the maximum likelihood values found for the full model M and the simpler model M_0, respectively, is distributed asymptotically as a χ^2 with $m - h$ degrees of freedom [15]. When TS is large we reject the null hypothesis (the simpler model does not suffice to describe data) and we resort to the full model determining $\{\alpha_k\}_{k=h+1,\dots,m}$ from the likelihood fit. The confidence level at which the full model M describes data better than the simpler model M_0 is

$$\text{c.l.} = \int_0^{\rm TS} \mathrm{d}s\, \chi^2_{m-h}(s) \tag{1.14}$$

being $\int_{\rm TS}^{+\infty} \mathrm{d}s\, \chi^2_{m-h}(s)$ the chance probability that the test statistics is larger than the obtained value.

The LRT can be applied as long as the likelihood function met some regularity conditions and the two alternative models are *nested* (as detailed in Protassov et al., 2002). The regularity conditions require that $\log \mathscr{L}(\{\alpha_k\})$ is three times differentiable with respect to the α_k, that the derivatives are limited and the Hessian matrix is positive definite (for technical details see Protassov et al., 2002, Appendix A). Requiring the two models to be *nested* means that:

15. Neglecting terms of the order of $\mathscr{N}^{-1/2}$ or higher, where $\mathscr{N}$ is the number of pixels.

1. given $M(\{\alpha_k\}_{k=1,\ldots,m})$ it must be possible obtaining $M_0(\{\alpha_k\}_{k=1,\ldots,h})$ by setting $\{\alpha_k\}_{k=h+1,\ldots,m}$ to some fixed values (as obvious from our formulation);
2. the null values of the parameters $\{\alpha_k\}_{k=h+1,\ldots,m}$ must be in the interior (not on the boundary) of the set of possible values in the full model.

The first criterion implies that, e.g., we cannot use the LRT to discriminate among two different spectral models for a source, like a power law or a black-body spectrum. The second criterion is particularly important for added model components, e.g. to test if there is significant signal from a source over the expected backgrounds. To met the second criterion when adding the source to the model its flux should not forced to be > 0, but instead allowed to be negative, so that the null hypothesis (flux null) is in the interior of the possible values of the more complex model.

When such conditions are not met the test statistics is not guaranteed to follow the reference distribution and so it is not possible to calculate the false positive rate for a detection. For example Mattox et al. (1996) recognized such a problem in the analysis of EGRET point sources and subsequently re-calibrated their test statistics through MC simulations.

1.3.2 *The LAT high-level analysis environment*

The LAT collaboration developed a high-level analysis suite for studying LAT data, called the *Science Tools*, publicly available through the FSSC [16]. The *Science Tools* include tools to rapidly simulate LAT observations, to perform temporal analysis of pulsars, to select and explore LAT data, to perform the likelihood analysis described in § 1.3.1. We will concentrate on the latter two items, which are those relevant for our purpose.

Data selection

Beyond the event classification described in § 1.1.2 a further selection can be performed. Events can be selected in a specific region of the sky, energy range or temporal window (e.g. when a source is in a particular state), on the basis of the event class level or according to the conversion point in the detector (in the *front* or *back* section). Events can also be selected on the basis of the corresponding observing time intervals: good time intervals are, e.g., those when the LAT was taking data in the configurations suitable for scientific analysis (runs where the detector is specifically configured for calibration purposes are periodically taken) and the quality of the data was judged to be "good" by the monitoring scientists.

Dedicated selection criteria are required to limit the contamination by γ-rays produced in CR interactions with the Earth atmosphere. The Earth atmospheric emission is very bright for the LAT due to its proximity and largely anisotropic due to the pointing strategy. Atmospheric γ-rays are real γ-rays entering the LAT, which cannot be rejected using detector information apart from the arrival direction. The selection is therefore usually performed selecting events within a maximum zenith angle for the infalling direction, which is chosen on

16. http://fermi.gsfc.nasa.gov/ssc/data/analysis/documentation/Cicerone/

the basis of the LAT orbital characteristics and the region of the sky to be studied; for more details see Appendix A.

Likelihood analysis

The likelihood analysis is implemented through a series of subsequent steps. At first the livetimes are summed for each position on the sky as a function of inclination angle with respect to the detector axis. In this procedure good time intervals are chosen accordingly to the event selection criteria previously specified.

The cumulative livetimes are then used to precompute the exposures with procedures which differ according to the analysis strategy, binned or unbinned. Calculating the exposures always involves, roughly speaking, the integration of the effective area over the FoV weighted by the livetimes over a position-energy grid. This precomputed quantity is then used to calculate the convolution in Eq. 1.3.

Exposure maps are also a useful way to see how uniform is the survey performed by the LAT. As an example we show in Fig. 1.8 the exposure map corresponding to the first three months of sky survey (Abdo et al., 2009k). The coverage of the sky was uniform within 30%

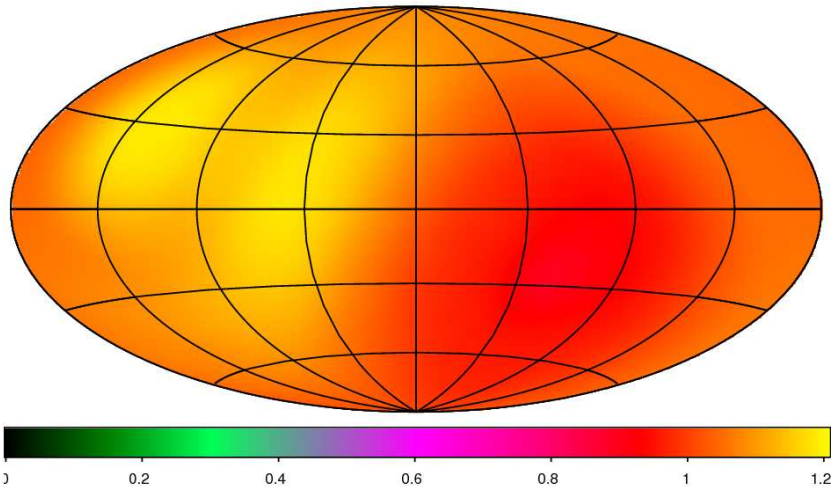

Figure 1.8: Exposure map at 1 GeV over the whole sky (Galactic coordinates in Aitoff projection) for the first three months of LAT observations (the data sample is described in Abdo et al., 2009k). The map is rescaled by the on-axis effective area, so that the scale gives the equivalent on-axis observing time for each point in the sky. The color scale is in units of Ms.

after only three months of survey, with a clear deficit around the south celestial pole due to the SAA.

In the convolution with the IRFs (Eq. 1.3) the energy dispersion is usually neglected to limit the computing time, since its impact is less important. This can be a source of systematic effects, especially if there is a strong dependence of the effective area on energy, notably at low energies.

After the convolution with the response functions the last step is the actual likelihood fitting. It is based on numerical minimization codes,

very often on `Minuit` [17]. The likelihood routines return as output the best-fit values of the model parameters and their statistical uncertainties derived from the likelihood profile (Eq. 1.9), as well as the maximum likelihood logarithm values associated to each model to perform the LRT (§ 1.3.1).

The analysis of LAT data as sketched in this Chapter has been leading to a wealth of new results in γ-ray astrophysics. Some of them, regarding diffuse emission are summarized in Chapter 3 (after a general introduction on the interstellar environment in the Galaxy in Chapter 2). The methods and analysis tools I introduced were used in particular to obtain the results presented in Part II.

17. http://wwwasdoc.web.cern.ch/wwwasdoc/minuit/minmain.html
http://seal.web.cern.ch/seal/MathLibs/Minuit2/html/index.html

2

THE INTERSTELLAR ENVIRONMENT IN THE GALAXY

Stars do not reside in empty space, but in a rich interstellar environment which is populated by extremely rarefied ordinary matter (the interstellar medium; ISM), by relativistic particles (the cosmic rays; CR) and by electromagnetic fields.

These basic constituents are, as we will see in the chapter, intimately bound together, with comparable energy densities and pressures. Furthermore they play a key role in the Galactic ecosystems, one of the most interesting aspects being probably the interplay between the interstellar environment and stars. New stars form out of the reservoir of matter given by the ISM, in its densest and coldest regions. During their life stars emit electromagnetic radiation in the interstellar space and enrich the matter locked in their interior in heavy elements. Part of this matter eventually returns to the ISM via powerful stellar winds or violent supernova explosions. The latter process is thought to power as well the injection of CRs in the interstellar space.

This chapter introduces the main constituents of the interstellar environment of the Milky Way. I will present the standard multiphase picture of the ISM, with particular emphasis on the tracers that allow us to determine its distribution. I will then give an overview on Galactic CRs, in particular on the direct measurements performed near the Earth and the theoretical and observational knowledge about their acceleration, propagation and interactions in the Galaxy. I will conclude with a brief description of the Galactic magnetic field and of the electromagnetic radiation with emphasis on that produced by CR during their propagation in the interstellar space.

The chapter has been inspired by the concept of interstellar environment as a part of the Galactic ecosystem proposed by Ferrière (2001).

2.1 THE INTERSTELLAR MEDIUM

To a terrestrial observer the Milky Way on clear nights appears as a faint luminous band across the sky. In the late 18^{th} century Herschel noticed that some regions along this band seemed devoid of stars. It was realized in the following century that these "holes" were due to the presence of discrete "clouds" of obscuring matter.

A breakthrough event was the discovery by Hartmann (1904) of stationary narrow absorption lines of ionized calcium (Ca II) in the spectrum of the binary δ Orionis, indicating the presence of cold ($T < 1000$ K) material located between the binary and the observer. The subsequent detection of absorption lines with multiple narrow peaks showing a sine-wave pattern compatible with the rotation of Galactic stars (this aspect is explained in detail in Appendix B), convinced the astronomers of the existence of a diffuse ISM.

To the current knowledge, the ISM accounts for $10\% - 15\%$ of the visible mass of the Galaxy and it has a highly inhomogeneous distribution. Roughly half of the ISM mass is located in discrete clouds occupying only a small fraction of the Galactic volume. These interstel-

lar clouds are made of very cold ($T = 10 - 20$ K) molecular gas and cold ($T = 30 - 100$ K) atomic gas. The rest of the interstellar matter spreads out between the clouds, under the form of warm atomic gas, warm ionized gas and hot ionized gas. The most relevant properties of these five "thermal phases" of the ISM are described in Table 2.1.

	T (K)	n (cm^{-3})	mass (%)	filling (%)
molecular	$10 - 20$	$> 10^3$	20	20
cold atomic	$30 - 100$	50	30	20
warm atomic	8000	0.5	45	25
warm ionized	$6000 - 12000$	0.1	< 10	25
hot ionized	$> 10^6$	< 0.003	< 1	20

Table 2.1: Some approximate characteristics of the thermal phases of interstellar gas: temperature, number density, approximate mass fraction, volume filling factor. Adapted from Ferrière (2001); Schlickeiser (2002); mass fractions for the neutral phases are deduced from Wolfire et al. (2003) assuming for atomic gas a cold fraction of 40% (Heiles and Troland, 2003); filling factors are taken from de Avillez and Breitschwerdt (2004) for the Galactic supernova rate.

The chemical composition of the ISM is similar to that of the solar system (Asplund et al., 2006): $\sim$ 92.5% by number (74% by mass) of hydrogen, $\sim$ 7.5% (25%) of helium and $\sim$ 0.12% (1.2%) of heavier elements, called in the jargon of the astrophysical community "metals". More than 50% of the metals are locked in solid dust grains (making from 0.5% to 1% of the total mass in the ISM). The dust is responsible for the obscuration and reddening of starlight.

In the following subsections, after providing an overall picture of the Galaxy, I will introduce the three chemical phases of the interstellar gas, atomic, molecular and ionized, with their main tracers. The last subsection is dedicated to interstellar dust.

2.1.1 *Overall picture of the Galaxy*

I anticipate here an overall picture of the Milky Way, illustrated also in Fig. 2.1. It is derived from a wide range of observations, including neutral hydrogen (see below 2.1.2), carbon monoxide (2.1.3), massive stars, globular clusters.

Galactic stars reside in four different systems (Robin et al., 2003): a thin and a thick disk, plus a inner bulge (or, according to recent proposals, a bar, see e.g. Churchwell and the Glimpse team 2005) and a spherical halo. The Milky Way extends over more than 60 kpc from its center (e.g. Kalberla and Dedes, 2008). The solar system resides in the disk at a radius of approximately [1] $R_\odot = 8.5$ kpc (Kerr and Lynden-Bell, 1986). The stars belonging to the disk rotate around the Galactic center in nearly circular orbits. The angular velocity at the Sun's orbit (the "solar circle") is approximately $V_\odot = 220$ km s^{-1} (Kerr and Lynden-Bell, 1986); the velocity is almost constant beyond the solar circle and slightly increases in the inner Galaxy (McClure-Griffiths and

1. We adopt the values of $R_\odot$ and $V_\odot$ recommended by the International Astronomical Union (IAU).

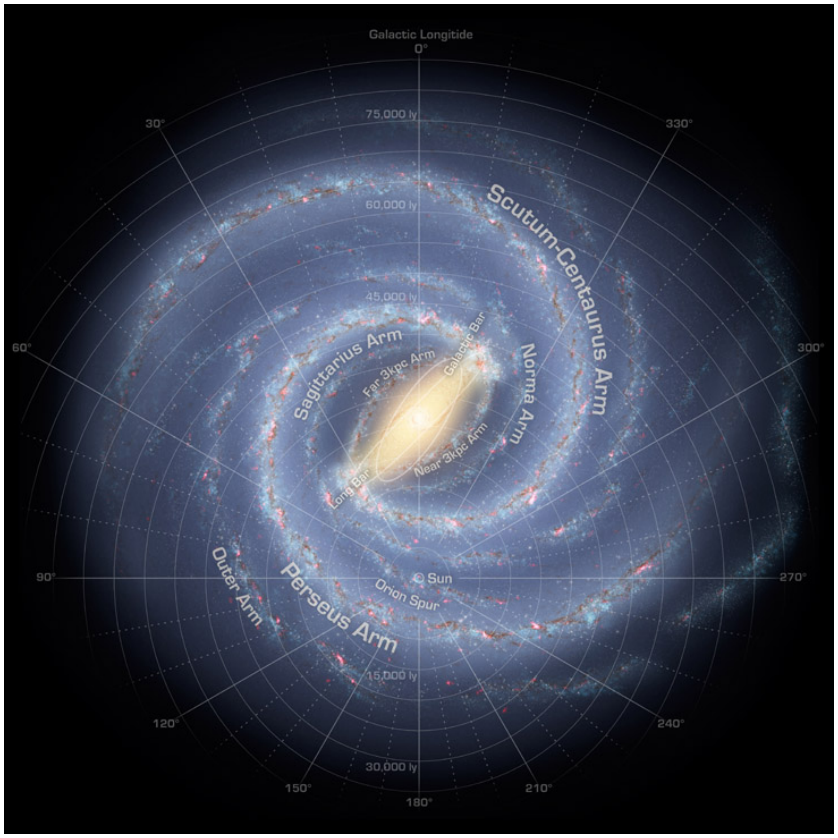

Figure 2.1: Artist's view of the Milky Way. The grid corresponds to polar coordinates in a reference frame centered at the Sun position, giving the radial distance in light years and the azimuthal angle w.r.t. the direction of the Galactic center, i.e. the Galactic longitude l. Names of the Galactic arms are also provided. Courtesy: NASA/JPL-Caltech/R. Hurt (SSC-Caltech).

Dickey, 2007). The neutral hydrogen line (see below § 2.1.2 and Appendix B) indicates the presence of a spiral structure, similar to that seen optically in external galaxies.

Spiral arms are named after the constellation where their direction is tangent to the line of sight for an observer on the Earth (their "tangent directions"). The Sun is located between the inner Sagittarius arm and the outer Perseus arm, near the inner edge of a short spur, called the Orion spur (because it is particularly evident in Orion), but also, due to its proximity to the Earth, the Local Arm (or Orion-Cygnus arm, because its tangent is crossing the solar circle in Cygnus; Mihalas and Binney 1981). Other major spiral arms are the Scutum-Centaurus arm and the Norma arm (that, in the segment located in the outer Galaxy, is often called the outer arm).

The solar system is embedded in a local structure, named the Gould Belt (after the pioneering observations by B. Gould). The Gould Belt (see e.g. Poppel, 1997; Perrot and Grenier, 2003) includes a flat local group of young stars and an associated interstellar superstructure of atomic and molecular gas. The distribution of the stars is tilted at about 17° to the Galactic plane. Current evidences suggest that the stars and most of the gas are in expansion. The size of the system is of

several hundred pc in the Galactic plane. The solar system is located inside an gas cavity, known as the Local Bubble (e.g. Lallement, 2009).

2.1.2 *Atomic gas*

Neutral atomic hydrogen, denoted H I, is not directly observable at optical wavelengths. Lines corresponding to electronic transitions between the ground state and excited states lie in the UV, with the Lyman α line (Lα, from $n = 2$ to $n = 1$) at a wavelength of 1216 Å.

The breakthrough event in the study of the neutral medium was the discovery by Ewen and Purcell (1951) of the 21 cm line of the H I atom hyperfine transition. This spin-flip line penetrates deeply into the ISM, tracing atomic gas throughout the Milky Way, and moreover, as explained in detail in Appendix B, the contribution from each segment along the line of sight can be separated thanks to the Doppler redshift due to the Galactic rotation.

Radially, the H I gas extends to > 60 kpc from the Galactic center. It lies in a roughly flat layer with a characteristic height of 230 pc. The thickness of the H I layer drops to $\lesssim 100$ pc within 3.5 kpc from the Galactic center, and it expands to almost 3 kpc in the outer Galaxy. This flaring, plausibly due to the steep decrease in the vertical gravitational field, is accompanied by a warping, such as in the first ($0° < l < 90°$) and second ($90° < l < 180°$) Galactic quadrants the midplane of the H I disk is above the Galactic plane, with a maximum displacement of ~ 4 kpc, and below the Galactic plane in the third ($-180° < l < -90°$) and fourth ($-90° < l < 0°$) quadrant, with a maximum displacement of ~ 1.5 kpc (Kalberla and Dedes, 2008).

The thermal state of interstellar hydrogen

While 21-cm emission spectra contains both narrow and broader peaks, absorption spectra observed against bright continuum sources show only narrow features. The conventional interpretation is that narrow peaks seen both in absorption and emission are produced by discrete cold ($T \simeq 30 - 100$ K) H I clouds, whereas the broader features are due to widespread warm gas, too warm to produce detectable 21-cm absorption [2]. In the outer Galaxy the average fraction of cold gas is $< 20\%$ (Dickey et al., 2009); it increases in the inner Galaxy to $< 40\%$ (Heiles and Troland, 2003).

The existence of two thermal phases of H I with comparable thermal pressures but different temperatures and particle densities was predicted theoretically by Field et al. (1969). The thermodynamic of interstellar gas is regulated by the equilibrium between heating and cooling. Heating processes (photoelectrons ejected from dust grains by FUV photons, ionization by low-energy CRs, direct ionization by FUV photons especially in the proximity of massive O and B stars) have rates proportional to the number density of the gas n, thus the heating rate is $n\Gamma$, with Γ independent from the temperature of the gas. Conversely, the main sources of cooling (collisionally excited line emission, collisional ionization and recombination of atoms and other minor contributors like thermal Bremsstrahlung) have rates, related to

2. The pure-absorption coefficient is independent from temperature, but the net-absorption coefficient, corrected for stimulated emission, is roughly inversely proportional to temperature, see below Eq. 2.14.

collisions, proportional to n^2, with a cooling curve depending on the temperature, so that the cooling rate is $n^2\Lambda(T)$.

The thermal equilibrium of the interstellar gas is thus determined by the shape of the cooling curve $\Lambda(T)$. For atomic gas the curve is fairly flat between a steep rise due to the C II 158-μm line around 100 K and another steep rise due to the Lα line around 8000 K (see e.g. Fig. 18.4 in Bowers and Deeming, 1984). This shape leads to two stable equilibria around $30 - 100$ K and several thousands K, that correspond for the neutral medium to the cold and the warm phases. A picture of a static ISM is only idealized and a large fraction of the mass (up to 50%) can be in transition between the two phases (see e.g. Wolfire et al., 2003; Heiles and Troland, 2003; Audit and Hennebelle, 2010).

The radiative transfer of the H I *line*

The 21-cm line, as we said, allows us to "count" H I atoms throughout the Milky Way. The measured quantities are the intensity of the line (often expressed in terms of a "brightness temperature", as we will see) and the Doppler shift, which is related to the velocity with respect to the local standard of rest (LSR). The determination of the position from the Doppler shift requires some assumptions about the motion of the Galaxy: some technical details about this procedure are presented in Appendix B.

The 21-cm line of H I corresponds to the spin-flip transition between a higher energy state in which the proton and electron spins are aligned, state 1, and a lower energy state in which they are opposite, the ground state or state 0. For gas in local thermodynamic equilibrium the relative level populations follows the Boltzmann equation

$$\frac{n_1}{n_0} = \frac{g_1}{g_0} \mathrm{e}^{-\Delta E_{10}/kT} \tag{2.1}$$

being T the thermodynamic temperature of the gas and g_1 and g_0 the multiplicities of the two states and n_1 and n_0 the number densities of the two populations.

The equation of radiative transfer is

$$\frac{\mathrm{d}I_\nu}{\mathrm{d}s} = -\kappa_\nu I_\nu + \jmath_\nu \tag{2.2}$$

with I_ν specific intensity at the frequency ν (W m^{-2} sr^{-1} Hz^{-1}), κ_ν absorption coefficient (m^{-1}) and $\jmath_\nu$ emission coefficient (W m^{-3} sr^{-1} Hz^{-1}). We can introduce the optical depth defined as

$$\mathrm{d}\tau_\nu \equiv \kappa_\nu \, \mathrm{d}s \tag{2.3}$$

so that Eq. 2.2 can be re-written as

$$\frac{\mathrm{d}I_\nu}{\mathrm{d}\tau_\nu} = -I_\nu + \frac{\jmath_\nu}{\kappa_\nu} \tag{2.4}$$

The source function $S_\nu = \jmath_\nu/\kappa_\nu$ for an optically thick medium with temperature T in local thermodynamic equilibrium is given by the black-body spectrum, i.e. in the Rayleigh-Jeans limit attained in the radio domain

$$S_\nu = \frac{2k\nu^2}{c^2} T \tag{2.5}$$

We define the "brightness temperature" T_B (called also "antenna temperature") as the equivalent black-body temperature which corresponds to the specific intensity measured by the telescope, i.e. in the Rayleigh-Jeans limit

$$I_\nu = \frac{2k\nu^2}{c^2} T_B(\nu) \tag{2.6}$$

If the gas is not in local thermodynamic equilibrium we can parametrize the relative level populations as

$$\frac{n_1}{n_0} = \frac{g_1}{g_0} \mathrm{e}^{-\Delta E_{10}/kT_S} \tag{2.7}$$

where we introduced T_S, the H I "spin temperature". Using Eq. 2.5, 2.6 and 2.7, Eq. 2.4 can be written as

$$\frac{\mathrm{d}T_B}{\mathrm{d}\tau_\nu} = -T_B(\nu) + T_S \tag{2.8}$$

The solutions of Eq. 2.8 have the form

$$T_B(\tau_\nu) = T_{\mathrm{bg}}\, \mathrm{e}^{-\tau_\nu} + \int_0^{\tau_\nu} \mathrm{d}\tau'_\nu\, T_S\, \mathrm{e}^{-(\tau_\nu - \tau'_\nu)} \tag{2.9}$$

with T_{bg} background temperature. Simple analytical solutions of Eq. 2.9 are found only under the approximation of a *uniform spin temperature*

$$T_B(\tau_\nu) = T_{\mathrm{bg}}\, \mathrm{e}^{-\tau_\nu} + T_S(1 - \mathrm{e}^{-\tau_\nu}) \tag{2.10}$$

Experimentally in fact we can determine

$$\Delta T_B(\tau_\nu) = T_B(\tau_\nu) - T_{\mathrm{bg}} = (T_S - T_{\mathrm{bg}})(1 - \mathrm{e}^{-\tau_\nu}) \tag{2.11}$$

In the limit of infinitely high optical depth, Eq. 2.11 yields $\Delta T_B = (T_S - T_{\mathrm{bg}})$; in general $T_B < T_S$. In the small optical depth limit, on one hand we can consider the case of a strong background source ($T_{\mathrm{bg}} \gg T_S$), where we observe an *absorption* line

$$\Delta T_B(\tau_\nu) = -\tau_\nu T_{\mathrm{bg}} \tag{2.12}$$

so we can estimate the optical depth τ_ν; on the other hand for a faint background source ($T_{\mathrm{bg}} \ll T_S$)[3] we observe an *emission* line, and Eq. 2.11 yields

$$\Delta T_B(\tau_\nu) = \tau_\nu T_S \tag{2.13}$$

which, we will see, is related to the column density of hydrogen atoms.

Indeed, the absorption coefficient can be derived from the number of atoms in the excited and ground state, and, recalling the definition of spin temperature in Eq. 2.7 can be written as (see e.g. Bowers and Deeming, 1984, Eq. 18.84)

$$\kappa_\nu = \frac{c^2}{8\pi\nu^2} \left(\frac{h\nu}{kT_S}\right) A_{10}\, n_1 \tag{2.14}$$

where A_{10} is Einstein's coefficient for spontaneous emission. Integrating Eq. 2.3 along the path to the observer allows us to obtain the optical

3. In the most common case the background is given by the cosmic microwave background (CMB), with $T_{\mathrm{bg}} = 2.66$ K at 21 cm.

depth as a function of the column density of H I atoms along a line of sight (eventually partitioned into different ranges as explained in Appendix B). If we express the frequencies as velocities with respect to the LSR we can obtain from Eq. 2.3 and 2.14

$$N(\mathrm{H\,I}) \equiv \int \mathrm{d}s\, n(\mathrm{H\,I}) = C \int T_S\, \tau(v)\, \mathrm{d}v \tag{2.15}$$

with $C = 1.823 \times 10^{18}$ atoms cm^{-2} (K km s^{-1})$^{-1}$.

The determination of $N(\mathrm{H\,I})$ requires to know (for each position, i.e. for each velocity) the spin temperature and the optical depth, whereas the only quantity measurable from the H I-line observations in emission is the brightness temperature ΔT_B. In the case of a uniform spin temperature T_S considered in Eq. 2.10 we can write

$$N(\mathrm{H\,I}) = -C T_S \int \ln\left(1 - \frac{\Delta T_B(v)}{T_S - T_{\mathrm{bg}}}\right) \mathrm{d}v \tag{2.16}$$

We note that, in the limit $T_S \to \infty$, $\Delta T_B(v)\mathrm{d}v$ is the column density of hydrogen atoms; combining Eq. 2.15 and 2.13 it is evident that $T_S \to \infty$ is equivalent to $\tau \to 0$, and it provides the lower limit on the column density of hydrogen atoms.

Fig. 2.2 shows the all-sky $N(\mathrm{H\,I})$ map integrated over the whole velocity range (in the optically thin approximation) from the Leiden/Argentine/Bonn (LAB) survey of the H I 21-cm line (Kalberla et al., 2005).

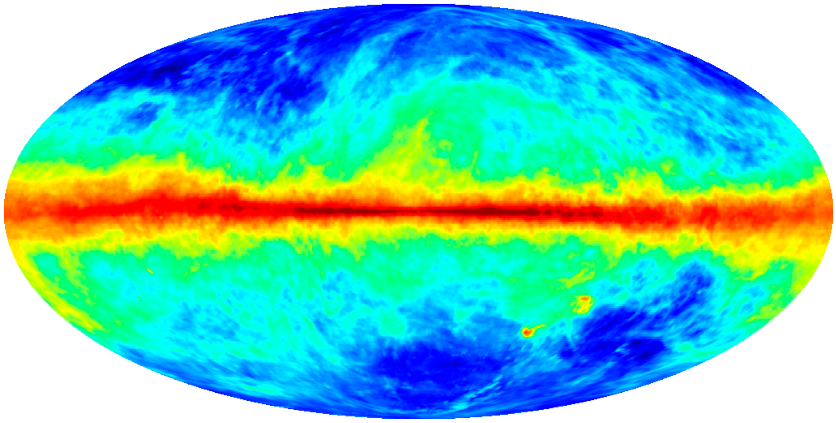

Figure 2.2: All-sky $N(\mathrm{H\,I})$ map integrated over the whole velocity range of the LAB survey (Kalberla et al., 2005) in the optically-thin approximation. Logarithmic scale from 10^{19} atoms cm^{-2} to 2×10^{22} atoms cm^{-2}. Aitoff projection in Galactic coordinates. Credit: Legacy Archive for Microwave Background Data Analysis (LAMBDA).

The key parameter to estimate the atomic column densities is thus the spin temperature T_S. Its determination is challenging, because it implies to measure both emission and absorption against bright continuum sources (Eq. 2.13 and 2.12), and the instrumental requirements to measure absorption spectra are more stringent. Large-scale averages of T_S are related to the mixture of the cold and neutral phase rather than to the temperature of gas. State-of-the-art measurements for the outer disk of the Milky Way (Dickey et al., 2009) indicate that the mixture of the cold and warm phases is a robust quantity, independent

from local properties of the interstellar environment, with $15-20\%$ of the atomic gas in cold clouds and the rest warm, corresponding to an average spin temperature of $250-400$ K. Lower average spin temperatures are observed in the inner Galaxy (Heiles and Troland, 2003).

2.1.3 *Molecular gas*

Interstellar molecules (CH, CH^+, and CN) were discovered in the late 1930s through their optical absorption lines. In the 1970s UV observations revealed the most abundant interstellar molecule, H_2 (Carruthers, 1970), and the next most abundant molecule, CO (Smith and Stecher, 1971). Observations of optical and UV absorption lines do not allow astronomers to probe the interior of dense clouds, because bright sources beyond them are obscured by the interstellar dust. The H_2 molecule itself cannot be directly observed because it is a homonuclear linear molecule with no permanent dipole moment, so that the low-energy excited levels correspond to quadrupole transitions with small probabilities and relatively high excitation energies.

Most of what we know comes from observations of the so-called "tracer" species, primarily ^{12}CO which is observed in its $J = 1 \rightarrow 0$ transition at a wavelength of 2.6 mm. In the limit of high densities the CO-line emission is dominated by collisional excitation and deexcitation. Early surveys (Scoville and Solomon, 1975; Burton et al., 1975) showed that most of the molecular gas is located in a ring at $\sim$ 4 kpc from the Galactic center, and they unveiled a strong molecular concentration in the inner region of the Galaxy, within 0.4 kpc. The first large-scale survey by Dame et al. (1987) brought to light the spiral-arm pattern of CO emission. Beyond the solar circle CO emission drops off rapidly. In the vertical direction CO emission has a characteristic height of ~ 90 pc.

High-resolution observations indicate that the molecular gas is contained in discrete clouds organized hierarchically from giant complexes (size of a few tens of pc and mass up to $10^6\ M_\odot$) down to small cores (size of a few pc and mass up to $10^3\ M_\odot$). An approximate power-law relation holds between cloud velocity dispersion and size (Larson, 1981). Fig. 2.3 shows the large-scale CO survey by Dame et al. (2001).

H_2 molecules are believed to form by recombination of hydrogen atoms on the surface of dust grains (Hollenbach and Salpeter, 1971). They can survive in vast numbers only in the interior of dark and translucent clouds, where they self shield from radiative dissociation by external UV photons, and cold enough to avoid collisional dissociation. The thermal state of molecular clouds results from the balance between heating by CRs and cooling by molecular line emission (§ 2.1.2).

The equilibrium of interstellar clouds

The equilibrium of interstellar clouds is a complicate phenomenon, which can be understood in terms of pressure (or energy) balance:

THERMAL PRESSURE the associated energy density is $u_{\rm th} = 3/2\,p$ (0.39 eV cm^{-3} for a typical value of $p/k = nT$ of 3000 cm^{-3} K)

RAM PRESSURE $u_{\rm ram} = 1/2\,\rho\langle v^2\rangle$ (1.3 eV cm^{-3} for typical values of $n = 10$ cm^{-3} and a linear velocity dispersion of 5 km s^{-1});

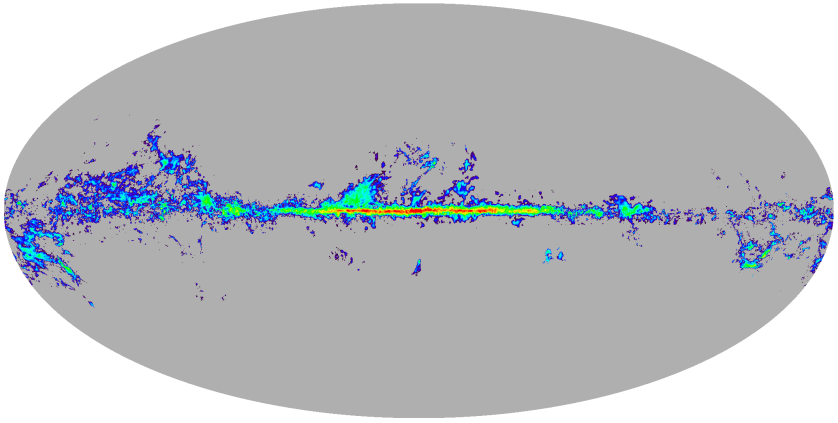

Figure 2.3: Large-scale map of W_{CO} (2.6 mm brightness temperature integrated over velocity) from (Dame et al., 2001). Logarithmic scale from 1.5 K km s^{-1} to 200 K km s^{-1}. Aitoff projection in Galactic coordinates. Credit: Legacy Archive for Microwave Background Data Analysis (LAMBDA).

MAGNETIC PRESSURE $u_B = B^2/8\pi$ (0.22 eV cm^{-3} for a typical value of $B = 3$ μG);

CR PRESSURE $u_{CR} \simeq 0.8$ eV cm^{-3};

STARLIGHT $u_{stars} \simeq 0.5$ eV cm^{-3};

COSMIC MICROWAVE BACKGROUND PRESSURE $u_{CMB} \simeq 0.26$ eV cm^{-3};

All of these sources of pressure have energy densities comparable within one order of magnitude, emphasizing the fact that the interstellar environment is a dynamic and complex system.

Molecular clouds are thought to be gravitationally bound on the basis of comparison between their masses, radii and velocity dispersions (e.g. Leung et al., 1982). However, their cores are likely to be unstable and sites of new star formation.

Interstellar molecular densities and molecular cloud masses

If we assume that a cloud is held in equilibrium against gravitational collapse by random turbulent motion (neglecting other sources of pressure) with a characteristic velocity dispersion σ_v, we can define a "virial mass" for the cloud

$$M_{vir} \propto \sigma_v^2 \frac{R}{G} \tag{2.17}$$

where R is the radius of the cloud itself and G is Newton's constant (the proportionality constant depends on the matter distribution in the cloud).

A commonly used method to derive cloud masses is using the velocity-integrated temperature of ^{12}CO

$$W_{CO} = \int T_B(v)\, \mathrm{d}v \tag{2.18}$$

as a mass tracer. Observations show that the CO luminosity

$$L_{CO} = d^2 \int W_{CO} \mathrm{d}\Omega \tag{2.19}$$

(with d distance to the cloud) is proportional to the virial mass of the cloud. This is equivalent to say that the H_2 column densities are proportional to W_{CO}. The conversion factor is known as X_{CO}

$$X_{CO} \equiv \frac{N(H_2)}{W_{CO}} \tag{2.20}$$

(Lebrun et al., 1983). The precise value of this conversion factor should depend on the density, temperature and metallicity of the gas.

Other independent techniques have been used to probe W_{CO} as molecular tracer and calibrate the X_{CO} ratio. One of them uses the optically thin line of ^{13}CO and correlates it with the visual extinction through nearby molecular clouds. The extinction measurements are converted into gas column density through a standard gas-to-dust ratio, to calibrate the conversion between the integrated intensity of ^{13}CO into $N(H_2)$. The average ratio of the integrated brightness temperature of ^{13}CO and ^{12}CO is then used to calibrate X_{CO} (Dickman, 1975).

More suitable to calibrate the W_{CO}-to-H_2-mass ratio over large scales is the use of total column density tracers like dust (e.g. Dame et al., 2001) or interstellar γ-ray emission produced by interactions of CRs with molecular clouds (§ 3.3.2).

All the methods agree within one order of magnitude around $X_{CO} \sim 2 \times 10^{20}$ cm^{-2} (K km s^{-1})$^{-1}$. None of them explains why the optically thick line of ^{12}CO is a good mass tracer. This can be justified if molecular cloud complexes consist of a large number of statistically similar optically thick clumps (cloudlets) that do not overshadow each other in the position-velocity space, and therefore W_{CO} is simply proportional to the number of cloudlets in the beam of the telescope (Morris and Rickard, 1982).

2.1.4 *Ionized gas*

Ionized gas in the ISM resides in two distinct thermal phases, warm and hot, which are thought to originate from different phenomena (irradiation by massive O and B stars and supernova explosions, respectively) and are traced thanks to different observations (mainly the hydrogen H_α line, free-free emission and pulsar dispersion measurements for the warm phase, UV lines from oxygen and nitrogen and the soft X-ray background for the hot phase).

Warm ionized gas

Massive O and B stars emit strong UV radiation, which, above an energy of 13.6 eV, can ionize hydrogen atoms. These stars are thus surrounded by "H II regions". The size of these regions is determined by the balance between photoionization and recombination. The equilibrium temperature has a typical value of $\sim$ 8000 K (Osterbrock, 1989).

In H II regions free electrons are accelerated in the field of ions, giving rise to radio/microwave continuum emission through thermal Bremsstrahlung known as free-free emission. Emission lines, found at optical, infrared and radio wavelengths are primarily due to radiative recombination of hydrogen and helium. In particular, the H_α Balmer line at 6563 Å arises from the transition between the electronic energy level $n = 3$ and $n = 2$. Since the rate per unit volume of recombinations into an excited hydrogen atom is proportional to $n_H n_e \propto n_e^2$, the

integrated intensity of the Balmer line is proportional to the "emission measure"

$$\mathrm{EM} = \int n_e^2 \, \mathrm{d}s \tag{2.21}$$

The presence of warm ionized gas outside well-defined H II region was first reported by Struve and Elvey (1938), who detected H_α and O II lines from extended regions in Cygnus and Cepheus. Because of the obscuration by interstellar dust, optical lines can probe only a limited region around the solar system. A much better tracer of the warm ionized gas are the signals from pulsars. Electromagnetic waves traveling through an ionized medium interact with free electrons so that their group velocity decreases with increasing wavelength. The periodic radio pulses emitted by pulsars show a spread in arrival time between low-energy and high-energy emission, which is directly proportional to the column density of free electrons between the source and the observer, i.e. the "dispersion measure"

$$\mathrm{DM} = \int n_e \, \mathrm{d}s \tag{2.22}$$

The large-scale structure of ionized gas derived from pulsar dispersion measurements (Cordes and Lazio, 2002) shows a thin-disk component arising from localized H II regions (roughly consistent with the stellar disk), plus a thick disk associated with the diffuse warm ionized medium, with a height > 1 kpc (the Reynolds layer). The spiral arm pattern is visible in the distribution of H II regions.

Hot ionized gas

The existence of a hot interstellar gas was suggested by the observations of broad UV absorption lines of ions formed only at high temperatures by the *Copernicus* satellite (Jenkins and Meloy, 1974) and a soft X-ray background supposed to be the free-free emission from hot interstellar plasma.

The soft X-ray background (around 0.25 keV) allow us to deduce a temperature of 10^6 K for the emitting gas (McCammon and Sanders, 1990). Observations by the *ROSAT* satellite highlighted a significant contribution from the Local Bubble, plus an absorbed contribution from the Galactic halo and an absorbed isotropic contribution possibly of extragalactic origin (Snowden et al., 1998).

Current observations do not allow us to map the large-scale structures of the hot interstellar gas, especially because of the difficulties in separating the true interstellar X-ray emission from the contribution by unresolved sources. It is now widely accepted that the hot interstellar gas originates from supernova explosions and, to a lesser extent, by powerful star winds (McKee and Ostriker, 1977).

2.1.5 *Dust*

The principal manifestation of interstellar dust is the obscuration, reddening and polarization of starlight. Classically the extinction is measured by comparing the spectra of pairs of stars with the same spectral type, one in a "clear" and one in an extinguished direction. It is conventional at UV to near IR to express the extinction in units of

magnitudes at given wavelengths, A_λ, normalized in terms of a "color excess" (or reddening) which expresses the selective extinction, e.g.

$$E(B-V) = A_B - A_V \tag{2.23}$$

Here A_B is the absorption in the photometric B band (4300 Å) and A_V in the V band (5500 Å). If the extinction curve has a universal form then there will be a simple relation between the color excess $E(B-V)$ and the absolute visual extinction, expressed in terms of extinction at a fiducial wavelength, usually A_V. This relation is often expressed in terms of a parameter called ratio of total to selective extinction

$$R_V = \frac{A_V}{E(B-V)} \tag{2.24}$$

where R_V has an average value for the diffuse ISM of 3.10 ± 0.05 (Wegner, 2003).

Assuming that the extinction is proportional to the total dust column densities, observations prove that the dust column density is well correlated with that of hydrogen, providing an indication that dust tends to follow the inhomogeneous clumpy distribution of the interstellar gas and that the dust-to-gas ratio is almost uniform in the cold and warm phases of the ISM (Jenkins and Savage, 1974).

The extinction curves, which show the wavelength dependence of interstellar extinction, contain several spectral features which provide clues on the nature and size of dust grains. The most prominent feature at $\sim$ 2175 Å is attributed to graphite particles. There are then evidences for the presence of amorphous silicates, polycyclic aromatic hydrocarbons (PAH) and organic refractory materials. The extinction curve suggests grain dimensions spanning from 5 nm to 1 μm. For further details see Draine (2003).

The stellar radiation heats dust grains up to over 20 K and it is then mostly re-emitted in the IR band. The dust thermal emission is thus an additional probe of the ISM, which took two major steps with the the *Infrared Astronomy Satellite* (*IRAS*) in the '80s and the *Cosmic Background Explorer* (*COBE*) at the end of the same decade. Schlegel et al. (1998) produced a combined all-sky map of dust column densities (Fig. 2.4) derived from its thermal emission combining the *IRAS* spatial resolution (5′) and the *COBE* quality calibration[4], showing a good correlation between gas and dust in the ISM.

Although dust represents but $\sim$ 1% of the ISM mass, it plays a key role in the chemical and energetic balance of the ISM. Dust grains serve as catalysts by allowing hydrogen atoms to recombine on their surfaces (Hollenbach and Salpeter, 1971) and they help to shield the resulting H_2 molecules from photodissociation by UV radiation (Shull and Beckwith, 1982). Then, dust provides a significant contribution to the heating of the ISM (ejecting photoelectrons) and to the cooling through collisional de-excitation of gas atoms and/or molecules (see 2.1.2) and PAH vibrational lines.

2.2 COSMIC RAYS

Highly energetic charged particles hit the Earth from the interstellar space. Since the first balloon experiments proved their extraterrestrial

4. The temperature correction based on *COBE* data has an angular resolution of 0.7°.

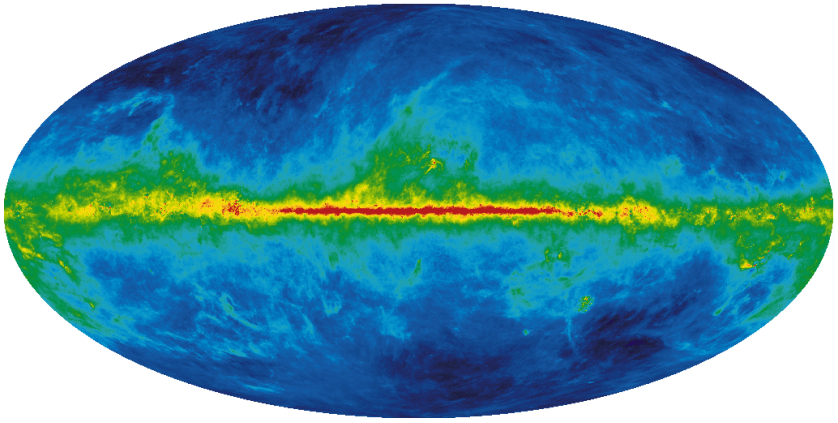

Figure 2.4: Map of dust column densities by Schlegel et al. (1998), expressed as color excess $E(B-V)$. Magnitudes in logarithmic scale from 0.004 to 6.3. Aitoff projection in Galactic coordinates. Credit: Legacy Archive for Microwave Background Data Analysis (LAMBDA).

origin (Hess, 1912), they were called cosmic rays (CRs). It took 20 years to prove, through the dependency of CR fluxes on the magnetic latitude, that they are made predominantly from charged particles (Compton, 1933).

CRs are detected over several decades in energy either by balloon and spaceborne experiments, or, at higher energies, by ground-based instruments. They are also believed to be at the origin of conspicuous observable phenomena: synchrotron radiation and interstellar γ-ray emission produced by CR interactions with the Galactic magnetic fields, radiation fields and the matter in the ISM (§ 2.3.2). Those phenomena are additional probes of CRs, providing information not only about CRs in the interplanetary space of the solar system but also about their properties throughout the Milky Way.

One century after their discovery CRs are still an intriguing puzzle. γ-ray observations of external galaxies indicate that CRs are Galactic in origin at energies below $\sim 10^{15}$ eV (§ 3.4). However, many questions are still open.

2.2.1 *Direct observations*

Direct measurements, either by balloon/spaceborne experiments or ground-based air-shower detectors, provide information on the CR composition, energy spectra and arrival directions. However, the low-energy part of the CR spectrum measured at the Earth is strongly influenced by the presence of the Sun. Extrasolar CRs with rigidity $R \lesssim 10$ GV have a Larmor radius smaller than the characteristic dimensions of magnetic field structures in the solar system interplanetary medium, and are swept out along the magnetic field lines. Low-energy CR densities observed at Earth are therefore lower than those in the interstellar space. This concept of *solar modulation* was first developed by Parker (1965). Solar modulation depends on the phase of the solar cycle, showing anticorrelation with the solar activity (Forbush, 1954). The Sun also produces energetic particles known as solar energetic particles. They are produced by solar flare eruptions, which

accelerate ions up to energies of several GeV and electrons up to ~ 100 MeV.

The CR spectrum extends over many decades in energy, with quite good agreement with a power law over different energy ranges (e.g. Cronin, 1999). The first break, the *knee*, occurs at $\sim 3 \times 10^{15}$ eV (fluxes of ~ 1 particle m^{-2} year^{-1}) and it is thought to mark the transition between the Galactic and extragalactic-dominated part of the CR spectrum. The second break, the *ankle*, occurs at $\sim 4 \times 10^{18}$ eV (fluxes of 1 particle km^{-2} year^{-1}); a cutoff is observed at $\sim 3 \times 10^{19}$ eV, plausibly due to the GZK mechanism (Abraham et al., 2008). Indeed, the CMB is supposed to suppress the proton fluxes above $\sim 10^{18}$ eV for pair photoproduction [$p + \gamma \rightarrow p + e^+ + e^-$], nuclei above $\sim 10^{18}$ eV through photonuclear collisions [$A + \gamma \rightarrow (A-1) + n$] and protons above $\sim 7 \times 10^{19}$ eV for photopion production [$p + \gamma \rightarrow p + \pi^0$] leading to a break, named GZK cutoff from the initials of the scientists who proposed these mechanisms: Greisen (1966); Zatsepin and Kuz'min (1966).

Charged CRs consist of $\sim$ 98% of nuclei and $\sim$ 2% of electrons and positrons. Around $10^8 - 10^{10}$ eV the hadronic component is given by $\sim$ 87% of protons, 12% of He and $\sim$ 1% of heavier nuclei (e.g. Schlickeiser, 2002). With respect to typical abundances in the solar system, CRs show a different composition. Given as reference the carbon abundance in CRs, hydrogen and helium are under-abundant, nuclei of the Li, Be, B group and sub-Fe group are overabundant by several orders of magnitude. Other discrepancies in the isotopic composition are observed, and a minor component made from antiparticles (antiprotons and positrons) is also present. We will see that this peculiar composition is related either to CR acceleration sites (§ 2.2.2) or to their propagation in the interstellar space (§ 2.2.3).

High isotropy is a distinctive characteristic of CRs observed at the Earth. The trajectories of charged particles are tangled by the interstellar magnetic fields that isotropize the angular distribution (§ 2.2.3). Data give an upper limit on the level of anisotropy in the energy range $10^{12} - 10^{14}$ eV of the order of 10^{-3} (Ambrosio et al., 2003). At lower energies the angular distribution is strongly affected by the solar modulation, whereas the statistics are too low at higher energies, providing anisotropy levels at most of a few % (Amenomori et al., 2005). Above a few EeV a possible association with nearby active galactic nuclei (AGNs) was recently observed by the *Auger* observatory (Abraham et al., 2007).

2.2.2 *Cosmic-ray acceleration*

The problem of understanding the origin of Galactic CRs is one of the most tenacious in high-energy Astrophysics. The only theory sufficiently well developed and able to fulfill many observational constraints is diffusive acceleration in strong shocks associated with supernova remnants (SNRs). The strongest indication is that the power required to maintain the Galactic CR population is estimated to be at most a moderate fraction of the energy input to the Milky Way from supernovae (SNe) explosions (Ginzburg and Syrovatskii, 1964). Other plausible sources in the Galaxy are too weak, with the possible exception of γ-ray bursts (GRBs). The SN explosion itself suffers from adiabatic energy losses, so the acceleration site must be located in the

subsequent SNR, and collisionless shock acceleration offers a plausible mechanism for this purpose (see e.g. Drury et al., 2001).

Collisionless shock acceleration

In tenuous astrophysical plasmas particles scatter collisionlessly against magnetic turbulences rather than against other particles. Sound speeds are considerably lower than easily obtainable bulk flow velocities, so shocks are expected to occur. Fermi (1949) proposed that collisionless shock acceleration is the mechanism most likely to be responsible for the origin of CRs.

Later in the '70s a series of independent works showed how a superthermal population of accelerated particles with a power-law momentum spectrum results from very general properties of a plasma shock traveling through a medium in which energetic particles are diffusing (Axford et al., 1977; Krymskii, 1977; Bell, 1978a,b; Blandford and Ostriker, 1978). These works showed that, under very general conditions, the steady-state power-law spectrum resulting from diffusive shock acceleration (DSA) is independent from the injection spectrum, the details of the interaction processes and the geometry of the shock. All these works employed the *test particle approach* in which the plasma shock is given and test particles were only allowed to interact with it.

It immediately became evident that accelerated particles were a dynamically important ingredient in the shock process itself (Axford et al., 1977). Nonlinear processes are expected to occur if acceleration is efficient (Jones and Ellison, 1991): plasma waves generated by energetic particle upstream, CR pressure on the unshocked material, CR-driven increase of the acceleration efficiency and compression ratio at the shock, energy losses due to CR escape.

Successes of SNR source models

DSA theories successfully reproduce a large range of observations. First of all nonlinear DSA naturally explains the CR spectrum up to the knee (e.g. Blasi et al., 2007). Additional probes of particle acceleration in SNRs are given by their multiwavelength spectrum.

Non-radiative shocks produce a zone where gas is not efficiently cooled after being shocked, and optical and UV lines are expected to be emitted in the layer of ionized gas present behind the shock. For partially neutral gas the most often observed line is Hα, which provides a measure of the pre-shock and post-shock proton kinetic temperature (Chevalier et al., 1980). The measured postshock temperature, in combination with the shock velocity, suggests that $> 50\%$ of the postshock pressure is produced by CRs (Helder et al., 2009).

X-ray observations of several SNRs show strong evidence for the presence of nonthermal emission: e.g. SN 1006 (Koyama et al., 1995), J1713.7−3946 (Koyama et al., 1997), Cas A (Allen et al., 1997) and again the observation of X-ray filaments in the remnant J1713.7−3946 (Cassam-Chenaï et al., 2004). The observation of X-ray filaments in SNR shells with a thickness of $\sim 10^{-2}$ pc is consistent with the idea of synchrotron-limited structure formation in strong magnetic fields (of the order of 100 μG), which suggests also the acceleration of hadrons up to PeV energies. The high magnetic fields have been confirmed by the strong-variability observed in J1713.7-3946 (Uchiyama et al., 2007). *Chandra* observations of the precursor upstream of the shock

in SN 1006 show good consistency with the predictions of nonlinear DSA, indicating amplifications of the magnetic field by a factor of ~ 10 at the shock (Morlino et al., 2010).

SNRs became an established source class for very high-energy (VHE) γ-ray astronomy, for a review see, e.g., Funk (2008): whereas the presence of nonthermal particle populations is obvious, the acceleration of CR hadrons was not unambiguously demonstrated, even if interactions between freshly accelerated hadrons and nearby molecular clouds is suggested by some of them (e.g. Aharonian et al., 2008). The *Fermi* Large Area Telescope, on orbit since 2008, is detecting high-energy γ-ray emission from several SNRs, hinting also to a hadronic origin (see e.g. Abdo et al., 2009f, 2010f,g).

Properties of Galactic SNRs

Given the outstanding role of SNRs in our picture of Galactic CRs I will overview their main properties in the following paragraphs.

The Galactic frequency of SNe is deduced from observations of external galaxies. From the results reported in Cappellaro et al. (1997), Ferrière (2001) derived a SN frequency of 1/48 years, in reasonably good agreement with historical observations (although only 5 SNe were observed during the last millennium, many more are expected to have occurred and obscured by interstellar dust) and with the independent estimate by Tammann et al. (1994), who estimate $\sim 85\%$ of them from massive progenitors.

The spatial distribution of SNRs is more uncertain. A summary of some observational results is shown in Figure 2.5. The distribution can be determined from radio observations of SNRs based on the surface brightness to diameter relation (Case and Bhattacharya, 1998), but the sparsity of the known SNR sample (36 objects for the estimate referenced) and observational biases make this determination very uncertain. PSRs are born in the same SN explosions as SNRs and their distributions are very well correlated in external Galaxies (Sasaki et al., 2004). Some derivations of the distribution in the Galaxy are available in the literature (e.g. Lorimer, 2004; Yusifov and Küçük, 2004), but even if the observed sample is larger, uncertainties in the dispersion measurements (§ 2.1.4) can bias the results. The massive OB stars, progenitors of SNe, can also be used as surrogate tracers of SNRs, as well as the H II regions they create in the ISM. In spite of the uncertainties, all these tracers point to a SNR distribution peaking in the inner Galaxy and with a dramatic drop beyond the solar circle. The same conclusion is drawn from observations of the ^{26}Al line, which traces the injection of explosive nucleosynthesis products into the ISM (Diehl et al., 2006).

Superbubbles as Galactic CR sources

SN explosions often show strong spatial and temporal correlations resulting from the concentration of the vast majority of SN progenitors into associations of massive type O and B stars (OB associations), formed on a short timescale from the collapse of a giant molecular cloud core. In these associations of massive stars tens of SN explosions can take place in a few million years. This results in a collective expansion, powered by both the SN explosions and the strong winds of Wolf-Rayet stars, which produces a bubble of hot tenuous plasma

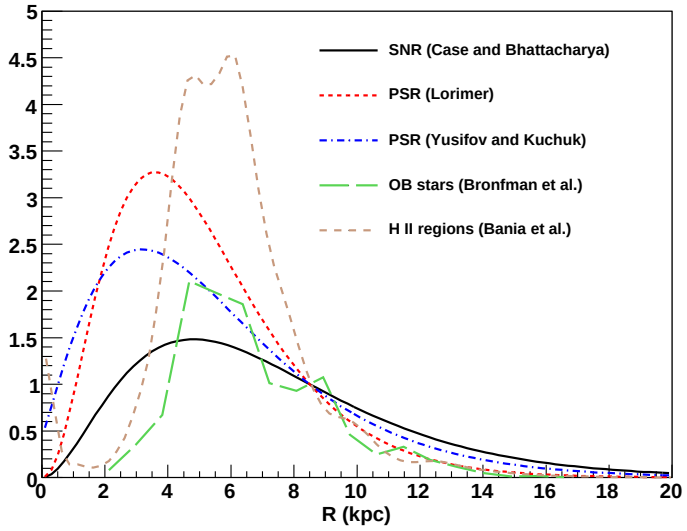

Figure 2.5: The distribution of SNRs in the Galaxy as a function of Galactocentric radius (R), as measured directly from the surface brightness to diameter relation (Case and Bhattacharya, 1998) and as traced indirectly from PSR dispersion measurements (Lorimer, 2004; Yusifov and Küçük, 2004) and from the IR luminosity of OB stars (Bronfman et al., 2000) and the distribution of H II regions (Bania et al., 2010). The units of the vertical axis are arbitrary, and all the distributions are normalized so that they are equal to 1 at the solar circle ($R_\odot = 8.5$ kpc).

known as "superbubble" (SB; Mac Low and McCray 1988). SBs have been considered as very plausible sites of nonthermal particle acceleration (Bykov and Fleishman, 1992; Higdon et al., 1998; Bykov and Toptygin, 2001; Binns et al., 2007). The energy contained in the SB magnetohydrodynamic (MHD) turbulence is thought to be converted into nuclei nonthermal energy via Fermi second order acceleration with an efficiency estimated as $\gtrsim 20\%$ (Bykov, 1999).

The first hint came with the observation of coincidences between *COS-B* γ-ray sources, SNRs and OB associations, leading to the SNOB scenario (Montmerle, 1979), where ions are first injected by winds of massive stars and then accelerated at higher energies by the shocks of nearby SNRs. Higher-sensitivity/resolution γ-ray observations by *CGRO* EGRET, however, found only a few sources spatially associated with OB associations.

Nowadays the SB scenario is supported mainly by isotopic abundances. The light isotopes ^{6}Li, ^{9}Be and ^{10}B are produced exclusively by spallation of heavier nuclei, notably C and O. The production by CR protons accelerated by isolated SNRs interacting with matter in the ISM of the early Galaxy was too inefficient to explain the observed abundances (Parizot and Drury, 1999), whereas the acceleration of particles out of the material inside SBs, enriched by the products of stellar nucleosynthesis ejected by SNe, can easily fulfill observational constraints (Parizot, 2001). This suggests that SB were the principal sources of CRs in the early Galaxy, and so probably nowadays. The acceleration of material enriched by the nucleosynthesis products ejected by Wolf-Rayet stars would explain also the Ne isotopic problem (the

^{22}Ne/^{20}Ne isotopic ratio in CRs is enhanced with respect to the local ISM by a factor $\sim$ 3), as well as other isotopic ratios like ^{58}Fe/^{56}Fe and ^{12}C/^{16}O (Binns et al., 2007). In addition, acceleration in SBs allows a higher-energy cutoff (Bykov and Toptygin, 2001; Ferrand and Marcowith, 2010), extending beyond the knee, and the average time between SN explosions of $\sim 3 \times 10^5$ years (Binns et al., 2007) is comparable to the decay time of ^{59}Ni ($\sim 7.5 \times 10^4$ years), providing a possible explanation for its lack in CRs (see later § 2.2.3).

2.2.3 *Propagation and interactions*

Propagation mechanisms

At present we believe that a diffusion model with the possible inclusion of convection and reacceleration in the ISM provides the most adequate description of CR transport in the Galaxy at energies $\lesssim 10^{17}$ eV. The CR propagation for a given particle species can be written in the general form (Strong et al., 2007)

$$\begin{aligned}\frac{\partial \psi}{\partial t}(\vec{r},p,t) &= q(\vec{r},p,t) + \vec{\nabla}\cdot\left(D_{xx}\vec{\nabla}\psi - \vec{V}\psi\right) + \frac{\partial}{\partial p}p^2 D_{pp}\frac{\partial}{\partial p}\frac{1}{p^2}\psi + \\ &- \frac{\partial}{\partial p}\left[\dot{p}\psi - \frac{p}{3}\left(\vec{\nabla}\cdot\vec{V}\right)\psi\right] - \frac{1}{\tau_f}\psi - \frac{1}{\tau_r}\psi \end{aligned} \quad (2.25)$$

where $\psi(\vec{r},p,t)$ is the CR density per unit of total particle momentum p at the position $\vec{r}$, $\psi(p)\mathrm{d}p = 4\pi p^2 f(\vec{p})\mathrm{d}p$ in terms of phase-space density $f(\vec{p})$ under the assumption of an isotropic momentum field; $q(\vec{r},p,t)$ is the source term including primaries injected by sources into the interstellar space and secondaries from spallation or decay; D_{xx} is the spatial diffusion coefficient, $\vec{V}$ the convection velocity; reacceleration is equivalent to diffusion in the momenta space and so described by the coefficient D_{pp}; $\dot{p}$ is the momentum gain or loss rate; τ_f and τ_r are the lifetimes for fragmentation and radioactive decay, respectively.

Diffusion explains why energetic CRs have highly isotropic distributions and why they are retained in the Galaxy. From the microscopic point of view the diffusion of CRs results from particle scattering on random MHD waves and discontinuities. If $r_g = pc/ZeB$ is the particle gyroradius and L ($\sim$ 100 pc) is the scale over which strong fluctuations of the magnetic fields are expected, in the regime where $r_g < L$ the diffusion coefficient can be estimated as $D_{xx} \approx (\delta B_{\rm res}/B)^{-2}\, v r_g/3$ (Strong et al., 2007), where $\delta B_{\rm res}$ is the amplitude of the random field at the resonant wave number $k_{\rm res} = r_g^{-1}$. The spectral energy density of interstellar turbulence has a power-law form $w(k)\mathrm{d}k \approx k^{-2+\delta}\mathrm{d}k$, with $\delta = 1/3$ over a wide range of wave numbers 10^{-20} cm$^{-1} < k < 10^{-8}$ cm^{-1} (Elmegreen and Scalo, 2004). This provides a diffusion coefficient

$$D_{xx} = D_0\,\beta\left(\frac{R}{R_0}\right)^{\delta} \quad (2.26)$$

with R_0 rigidity scale and $D_{xx} \approx 2 \times 10^{27}$ cm^{-2} s^{-1} for CRs with a rigidity $R < 10^8$ GV. The Kolmogorov-like spectrum ($\delta = 1/3$) may refer only to some part of the MHD turbulence, an exponent $\delta = 1/2$ typical for the Kraichnan-type turbulence may also apply to the ISM (Yan and Lazarian, 2004), and would translate into a dependence $R^{1/2}$. However, there is no general consensus that CR data are consistent with $\delta = 1/3$ nor $\delta = 1/2$, e.g. Maurin et al. (2010) suggest

$\delta \simeq 0.6 - 0.8$. The kinetic theory thus gives an approximate estimate of the diffusion coefficient and predicts a power-law dependence of diffusion on magnetic rigidity. The actual diffusion coefficient must be determined from CR data themselves.

The existence of galactic winds in many external galaxies may suggest that convective (or advective) transport is also important. Winds are common in galaxies and can be CR driven (Breitschwerdt and Komossa, 2000). Possible evidences for winds in our own Galaxy seem to be confined to the Galactic center region from X (Bland-Hawthorn and Cohen, 2003) and perhaps γ-ray observations (Su et al., 2010). Secondary-to-primary ratios and radioactive isotopes (see later) constrain the convective transport, but the results are controversial: e.g. Strong and Moskalenko (1998) derived a wind speed $\mathrm{d}V/\mathrm{d}z < 10\ \mathrm{km\ s^{-1}\ kpc^{-1}}$ (for a model where the wind speed increases linearly with distance from the plane), whereas Maurin et al. (2002) proposed a constant speed of $V = 15\ \mathrm{km\ s^{-1}}$.

The scattering of CR particles on randomly moving MHD waves leads also to stochastic reacceleration, often described as diffusion in the momenta space. The momentum diffusion coefficient D_{pp} is related to the spatial diffusion coefficient D_{xx} by the equation (Berezinsky, 1990; Schlickeiser, 2002)

$$D_{pp} \propto \frac{p^2 v_A^2}{D_{xx}} \tag{2.27}$$

where the Alfvén velocity v_A is the characteristic velocity of weak turbulences propagating in a magnetic field. Let us note that acceleration distributed in the interstellar space cannot serve as the main mechanism of CR acceleration in the energy range $1 - 100$ GeV/n, since high-energy particles would thusly spend a longer time in the Galaxy producing secondary-to-primary ratios increasing with energy contrarily to observations. That is the reason why this mechanism is usually referred to as reacceleration, to distinguish it from the primary acceleration discussed in 2.2.2.

Interaction processes and their products

Propagating in the interstellar space CRs loose their energy because of many different interaction processes (for an overview see Strong and Moskalenko, 1998, Appendix A and C). For CR nucleons energy losses are mainly due to ionization, Coulomb scattering, fragmentation and radioactive decay. For CR electrons the important processes are ionization, Coulomb scattering, Bremsstrahlung, Compton and synchrotron losses. Those interaction processes often lead to the production of secondaries (either CRs or electromagnetic radiation) which are a powerful probe to understand the interstellar environment itself.

CR electrons produce synchrotron radiation interacting with magnetic fields (§ 2.3.2). Furthermore they produce Bremsstrahlung radiation in the γ-ray domain via interactions with the matter in the ISM. Another major contributor to the secondary γ-radiation is the inverse Compton (IC) scattering off CR electrons of photons of the low-energy interstellar radiation field (ISRF; see below § 2.3.2).

Nucleon-nucleon interactions are of great interest: they lead to the production of secondaries like nucleons (both stable and unstable), antinucleons and mesons, with final products like γ-rays, $e^{\pm}$ and neu-

trinos. Their spectra have been calculated with analytical or semi-analytical methods (e.g. Stecker, 1970; Badhwar et al., 1977; Dermer, 1986a,b), and nowadays can be derived from state-of-the-art particle Physics codes (e.g. Kamae et al., 2006). An open issue is the contribution from particles other than protons in both CRs and the ISM, which is often expressed as a "nuclear enhancement factor" with respect to the pure *p-p* interactions. In the literature values span from 1.45 (Dermer, 1986a,b) to 1.68 (Gaisser and Schaefer, 1992), up to $1.8 - 2$ as recently proposed by Mori (2009). These discrepancies should be investigated in detail in the future.

Constraints from direct CR measurements

Stable secondaries to primary ratios bring information on the number of interactions which primaries underwent during their propagation, and so, indirectly on the propagation mechanisms. The reference ratio is always B/C because boron is entirely of secondary origin, the measurements are good up to high energies and the cross sections for its production from C, N and O are well known. Practically, the B/C ratio is used to constrain the diffusion coefficient D_0 and the power-law dependence on rigidity (Eq. 2.26). Convection implies an energy independent escape from the Galaxy and so a decrease in diffusion at low energies. Reacceleration affects as well the energy dependence of the B/C ratio and it has been shown (e.g. Strong and Moskalenko, 1998) that it provides a natural way to explain observations without introducing an ad-hoc break in the power-law index of Equation 2.26 consistently with Kolmogorov-like MHD turbulence ($\delta = 1/3$). The solution is not unique, see e.g. Maurin et al. (2002) for an alternative scenario.

Unstable secondaries to primary ratios are a radioactive clock which provides information about the residence time of CRs in the Galaxy. ^{10}Be is the longest lived and best measured unstable secondary. The ^{10}Be/^{9}Be ratio indicates residence times of the order $10^7 - 10^8$ years. In diffusive halo models, together with the B/C ratio, this provides a height for the propagation halo $\sim 4 - 20$ kpc (Strong and Moskalenko, 1998). The Local Bubble (§ 2.1.1) can influence this determination, since secondaries might be underproduced in the gas-depleted region around the Sun leading to an overestimate of the propagation volume (Donato et al., 2002).

Three isotopes produced in explosive nucleosynthesis by SNe, ^{59}Ni (decay time 7.5×10^4 years), ^{57}Co (0.74 years) and ^{56}Ni (6 days), decay only by electron capture. If acceleration occurs before they decay, the decay is then suppressed. ^{59}Ni is not observed. Wiedenbeck et al. (2000) showed that the delay between synthesis and acceleration is long compared to ^{59}Ni decay time, $\geq 10^5$ years. This demonstrates that CRs do not come from SN ejecta during their explosions, but from subsequent acceleration of matter in the SNR expansion and may support the SB scenario (§ 2.2.2). The implications of electron-capture isotopes for reacceleration are not clear yet (Strong et al., 2007).

Antiprotons were the subject of active debate since their discovery by Golden et al. (1979). There is now a consensus that most of them are of secondary origin (Mitchell et al., 1996), produced by nucleon-nucleon interactions in the ISM, as recently confirmed by Adriani et al. (2010). Despite numerous efforts, however, published estimates of expected

$\bar{p}$ fluxes differ significantly (Orito et al., 2000), due to uncertainties in cross-sections, propagation and solar modulation.

Positrons in CRs are more problematic. Recent measurements of the $e^+/(e^+ + e^-)$ ratio (Adriani et al., 2009a) showed a rise above 10 GeV which is difficult to reconcile with a pure secondary origin. Many different solutions have been proposed, including a contribution from processes involving dark matter particles, from nearby sources like SNRs or PSRs, interactions of freshly accelerated CRs with nearby interstellar clouds (see e.g. Grasso et al., 2009, and references therein).

Other powerful probes of CRs in the Galaxy are given by electromagnetic radiation produced by interactions with gas in the ISM and electromagnetic fields, notably the synchrotron radiation produced by electrons tangled by the magnetic field and the interstellar γ-ray emission (§ 2.3.2). They offer the unique opportunity to study CR properties throughout the Galaxy beyond direct measurements performed near the Earth.

Propagation codes: GALPROP

CR propagation and interactions have been attacked with many approaches. Leaky box models use the simple picture of CRs injected by sources distributed uniformly over some volume with a position-independent matter and radiation density. More sophisticated two-zone models make use of a disc, where CRs are injected, and a propagation halo with a lower gas/radiation density. Recent advances in computing power allowed realistic models of the Galaxy to be used for the numerical solution of the propagation equation 2.25.

The numerical explicit approach has been exploited by some authors (e.g. Maurin et al., 2002; Evoli et al., 2008), but the most successful implementation up to now is given by the Galactic propagation (GALPROP) package [5]. It is the only code which simultaneously reproduces observational data of many kinds related to CR origin and propagation, including charged species, synchrotron emission and interstellar γ-radiation. It has therefore been adopted as reference propagation model by the *Fermi* LAT collaboration (e.g. Abdo et al., 2009c) and largely used for the work reported in this thesis. I present here a short description of GALPROP and I refer the reader to the review by Strong et al. (2007) for further details.

GALPROP numerically solves the propagation equation 2.25 on a spatial grid, either in two dimensions assuming cylindrical symmetry or in full three dimensions. The propagation volume is described by a radius and a halo height, beyond which free escape is assumed. The solution is found iteratively until a steady solution is reached, including secondaries and tertiaries. The parameters of Eq. 2.25 are given as input. The distribution of CR sources, parameters of the injection spectra and isotopic composition are also given as input. Cross sections are based on extensive compilations and parametrizations (see e.g. Mashnik et al., 2004). The model uses realistic distributions of the gas in the ISM based on H I, CO and infrared surveys as well as a detailed model of the interstellar radiation field (ISRF) based on the calculation by Porter et al. (2008). Let us note, however, that most of the Galactic luminosity comes from the most luminous massive stars, which are rare;

5. http://galprop.stanford.edu.

they could produce a clumpiness in the IC γ-ray emission detectable by *Fermi* (Orlando and Strong, 2007).

The main limitation of GALPROP is given by the assumption of isotropic diffusion: locally the diffusion is strongly anisotropic along the magnetic fields lines; over scales $\gtrsim 100$ pc diffusion becomes isotropic because of the strong fluctuations of the magnetic field, whose random component is several times higher than the average field strength. Therefore GALPROP models apply only to large scale properties of Galactic CRs ($\gtrsim 100$ pc). As any other models based on the diffusion approximation, GALPROP is limited below the knee, $\leq 10^{17}$ eV, since above this energy the trajectories of individual particles should be considered.

2.3 INTERSTELLAR ELECTROMAGNETIC FIELDS

The interstellar space in our Galaxy is populated by electromagnetic fields intimately bound with stars, the ISM and CRs. A large-scale magnetic field is observed through the polarization of starlight, Zeeman splitting of radio lines and Faraday rotation of polarized radio signals. The Milky Way shines from radio to γ-rays. Most of this radiation is given by starlight, partially absorbed and reprocessed by dust grains, but continuum emission at lower and higher energies is dominated by interstellar processes related to CR propagation giving rise to synchrotron emission observed in the radio domain and diffuse γ-ray emission.

2.3.1 *The Galactic magnetic field*

The presence of interstellar magnetic fields in our Galaxy was first revealed by the linear polarization of starlight (Hall, 1949), later explained in terms of selective extinction by elongated dust grains partially aligned because of a magnetic field (Davis and Greenstein, 1951).

Stellar polarimetry provides information only on the direction of the magnetic fields, its strength can be estimated thanks to the Zeeman splitting of radio lines (mainly the two circularly polarized components of the 21-cm line of H I) or Faraday rotation of polarized radio signals (either from pulsars or extragalactic continuum sources).

Zeeman splitting occurs when the 21-cm radiation travels through regions with a magnetic field, so that we observe two circularly polarized components with an energy spread

$$\Delta E = \mu_B B \Delta m \tag{2.28}$$

where μ_B is the Bohr magneton and Δm is the difference of magnetic quantum number between the two states ($\Delta m = 2$ since the circularly polarized components are produced by electrons with $m = \pm 1$). In this case Zeeman-splitting measurements are biased towards regions with high H I densities and small line widths, so cold H I clouds. The Zeeman effect has now been observed also for the OH and H_2O lines in molecular clouds (Crutcher et al., 1987; Fiebig and Guesten, 1989), providing values of $10 - 100$ μG up to 5×10^4 μG in dense cloud cores ($n \simeq 10^{10}$ cm^{-3}).

Faraday rotation occurs when a polarized radio wave passes through a plasma. Counterclockwise rotation occurs if the magnetic field is oriented toward the observer, clockwise if the field points away from the

observer. The rotation angle $\Delta\chi = \lambda^2 \mathrm{RM}$ increases with the wavelength λ squared and the "rotation measure"

$$\mathrm{RM} = \int n_e B_{\parallel} \mathrm{d}s \tag{2.29}$$

where n_e is the number density of free charges. The rotation measure can be combined with the dispersion measure (Eq. 2.22), which provides an estimate of the column density of ionized gas, to extract the average intensity of the magnetic field in the direction parallel to the observer. Thus, Faraday-rotation measurements sample regions of ionized gas.

The strength of the large-scale magnetic field averaged over 1 kpc around the solar system is ~ 6 μG from radio synchrotron measurements (see later). Beyond the small-scale features revealed by Faraday rotation and radio polarization, the overall field structure in the Galaxy is still under debate (e.g. Beck, 2009a). In nearby galaxies random fields are concentrated in spiral arms, whereas ordered fields are stronger in interarm regions and follow the orientation of adjacent arms.

The interstellar magnetic field is coupled with the matter in the ISM through its ionized component (and as a whole thanks to ion-neutral collisions, Spitzer 1958). At large scales the magnetic field helps to support interstellar gas against gravitational collapse (§ 2.1.3) and it confines CRs in the Galactic halo. On smaller scales the interstellar magnetic field affects all kind of turbulent motions in the ISM, like SNR expansion, and it supports dense molecular clouds against gravitational collapse (2.1.3).

The origin of the interstellar magnetic field is still mysterious. The most likely scenario is a hydromagnetic dynamo: the motion of a conducting fluid in a magnetic field generate electric currents which amplify an original magnetic field, provided perhaps by a pre-existing intergalactic field. Parker (1992) proposed that the dynamo mechanism might be CR-driven.

2.3.2 *Interstellar radiation*

The space between stars is also populated by photon fields. The Galactic interstellar radiation field (ISRF) spanning the window from IR to UV is the result of emission by stars, and the subsequent scattering, absorption and reemission by dust in the ISM. The spectrum of the ISRF can be approximately described by the combination of some diluted blackbody distributions (*graybody* distributions), each characterized by a photon energy density and a temperature.

Beyond thermal emission from dust, peaking in the IR domain (§ 2.1.5), other interstellar processes are also present: lines from atomic or molecular transitions of interstellar gas (§ 2.1) and radioactive decays (see e.g. Cassé et al., 1999), and continuum emission due to free-free emission from ionized gas (§ 2.1.4) and CR-related processes. CR propagation in the Galaxy gives rise to diffuse continuum emission through synchrotron radiation, peaking in the radio domain, and in the γ-ray band due to interactions with interstellar matter and low-energy interstellar radiation (§ 2.2.3). The latter phenomena will be overviewed in the following paragraphs.

Synchrotron radiation

The rapid spiraling motion of CR electrons about magnetic field lines generate nonthermal radiation, termed synchrotron radiation, over a broad range of radio frequencies. The synchrotron emissivity depends on both the magnetic field strength and the spectrum of CR electrons, but unfortunately neither quantity is reliably known.

The only all-sky map available is the well-known compilation by Haslam et al. (1981) at 408 MHz (Fig. 2.6), combining good angular resolution and low contamination by thermal emission. On small

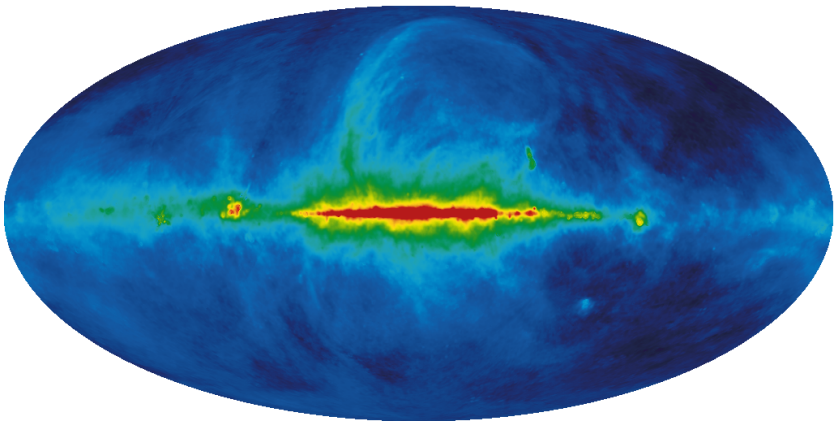

Figure 2.6: The 408 MHz map by Haslam et al. (1981). Brightness temperature in logarithmic scale from 10 to 250 K. Aitoff projection in Galactic coordinates. Credit: Legacy Archive for Microwave Background Data Analysis (LAMBDA).

scales the map is probably dominated by SNRs. On the large scale we can see the emission from CR electrons propagating through the Galaxy as well as large features known as radio loops (Berkhuijsen et al., 1971), which are thought to be old nearby SNRs.

The synchrotron spectral index at a frequency ν for a population of electrons with power-law spectrum of index γ is $\beta_\nu = (\gamma - 1)/2$ (e.g. Rybicki and Lightman, 1986, Eq. 6.22b), so the observed β_ν ranging from $0.6 - 1$ increasing with energy implies $\gamma = 2.4 - 3$ increasing with energy for CR electrons in our Galaxy.

Radio continuum observations of other galaxies provide a complementary view on CR electrons. The edge-on galaxies, like NGC891 (Allen et al., 1978; Heald et al., 2006; Beck, 2009b), show a nonthermal halo extending to several kpc, giving credence to the idea of a large propagation halo also for our Galaxy (§ 2.2.3).

Interstellar gamma-ray emission

Interstellar γ-radiation is produced by interactions of CRs during their propagation in the interstellar space (§ 2.2.3):

- CR nucleons inelastically collide with nucleons in the ISM, producing π^0 mesons which then decay into γ-rays;
- CR electrons and positrons interact with the gas in the ISM emitting Bremsstrahlung radiation;
- CR electrons and positrons produce γ-rays upscattering on low energy photons of the low-energy Galactic ISRF and the cosmic microwave background (CMB).

Since the Galaxy is transparent to high-energy γ-rays up to hundreds of TeV, the interstellar emission is a tracer of CR densities throughout the Galaxy and also of the total column densities of the ISM, complementary to gas and dust tracers at other wavelengths (§ 2.1). This subject will be addressed in next Chapter 3. A wealth of new information on this regard has been recently provided by *Fermi* LAT data (Chapter 1).

3

HIGH-ENERGY INTERSTELLAR γ-RAY EMISSION AT THE DAWN OF THE *FERMI* ERA

The sky at GeV energies (Fig. 3.1) is dominated by diffuse emission: a Galactic component, produced by interactions between high-energy CRs and interstellar gas and low-energy photons (§ 2.2.3), an isotropic component, whose origin is still unclear, and a contribution from unresolved sources.

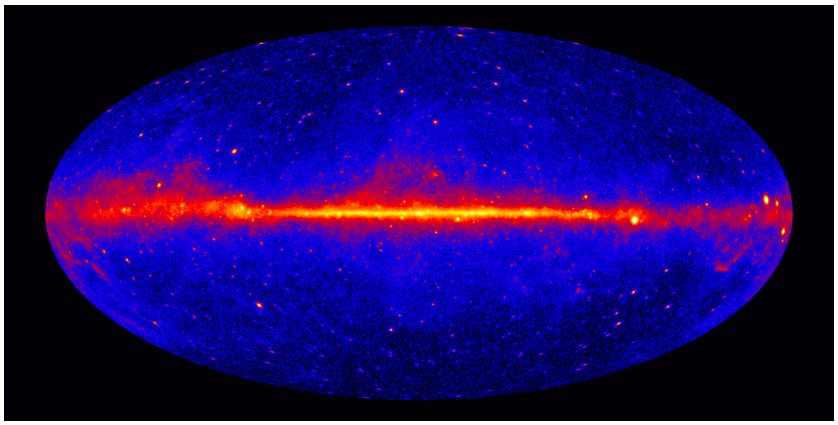

Figure 3.1: LAT count map for events in the *Diffuse* class with energies > 1 GeV accumulated over two years of normal Science operations. The map is binned on a grid of 0.1°, and the colour scales logarithmically with the number of counts per pixel from 1 to 500. Aitoff projection in Galactic coordinates. The skymap can be compared with those at other wavelengths presented in Chapter 2.

Understanding and modeling diffuse emission is fundamental for interpreting high-energy γ-ray observations. Interstellar emission also offers a unique probe of the interstellar environment of the Milky Way: since the Galaxy is transparent to high-energy γ-rays up to hundreds TeV, diffuse γ-ray emission traces CRs throughout the Milky Way, beyond direct measurements performed near the Earth, and it is also a tracer of the total column densities in the ISM, which usefully complements gas and dust tracers at other wavelengths.

In this chapter I will give a general introduction about diffuse γ-ray emission, with emphasis on the Galactic component, and I will also briefly overview the historical observations of interstellar emission, from the first detection of high-energy γ-ray emission associated with the Galactic plane in the '60s, to the predecessor of the LAT, the EGRET telescope on board the *Compton Gamma-ray Observatory* (*CGRO*). I will then discuss the legacies of the EGRET era. The most important was the "GeV excess", an excess of emission above 1 GeV with respect to expectations based on locally measured CR spectra. I will overview the interpretations proposed and how LAT observations at intermediate Galactic latitudes are inconsistent with EGRET results, suggesting an instrumental origin for the excess. Other important open issues were left from the EGRET era and are currently investigated using LAT data.

THE DISTRIBUTION OF CRS IN THE GALAXY Are the CR spectra measured at Earth representative of the Galactic population? How do CR densities relate with putative sources?

THE CALIBRATION OF MOLECULAR MASSES, How does γ-ray emission constrains the X_{CO} ratio? Are there any variations on the Galactic scale or from cloud to cloud?

THE DARK GAS, How much interstellar gas is missing in our census mainly based on the H I and CO lines? What is the nature of the gas not shining at those wavelengths?

My personal contributions to such field are presented in Part II.

I will also overview the observations of external galaxies (not hosting active nuclei): only one, the Large Magellanic Cloud (LMC), was detected by EGRET, but the LAT has proven to be capable to study some of them, providing complementary information on CR acceleration, propagation and their interplay with the ISM.

3.1 THE DIFFUSE γ-RAY SKY

3.1.1 *Diffuse γ-ray emission*

Continuum interstellar γ-ray emission is produced in our Galaxy (as well as in external galaxies) by interactions involving high-energy CRs (§ 2.2.3):

- nucleon-nucleon interactions with the gas in the ISM, leading to γ-ray emission through π^0 production and decay;
- electron Bremsstrahlung due to interactions with the gas in the ISM;
- inverse Compton (IC) emission from CR electrons (and positrons) interacting with the CMB and the low-energy interstellar radiation field (ISRF).

We will concentrate on this component along the rest of the chapter.

A weaker component is observed with almost isotropic distribution over the sky, and thus is thought to be extragalactic in origin and usually referred to as the extragalactic γ-ray background (EGB). The first determination of its spectrum based on LAT data is reported in Abdo et al. (2010j). Its nature is still unclear. A large fraction is attributed to unresolved sources, $\sim$ 20% to active galactic nuclei (AGN) according to Abdo et al. (2010k) and another significant fraction to normal galaxies [1]. Apart from the contribution by unresolved sources, many processes which might produce *truly diffuse* extragalactic emission have been proposed (for a review see e.g. Dermer, 2007), for example large-scale structure formation, interactions of ultra-high-energy CRs with the extragalactic low-energy background radiation, annihilation or decay of cosmological dark matter. On the other hand, interactions of CRs with debris at the outer frontier of the solar system might partially contribute to the spectrum of the EGB derived in past studies (Moskalenko and Porter, 2009).

Unresolved sources are contributing not only to the EGB, but also to the Galactic diffuse emission, due to the low sensitivity of γ-ray telescopes. Pulsars are the most obvious candidates, being the brightest sources of the galactic GeV sky and given that less than one hundred

1. The limited number of detections of normal galaxies at GeV energies (see later § 3.4) makes the estimate still highly uncertain.

have been detected in γ-rays (Abdo et al., 2010l) to be compared to the thousands known in radio. The contribution by unresolved sources to the low-latitude emission measured by EGRET was evaluated to be of the order of 10% (Casanova and Dingus, 2006; Strong, 2007).

Exotic processes have also been proposed as sources of Galactic interstellar γ-ray emission, notably the annihilation or decay of dark matter particles (see 3.2.1 for some examples), but up to now no conclusive evidence for such an exotic component has been found.

3.1.2 *Historical Overview*

The first observations of interstellar γ-ray emission date back to the '60s with the detection of high-energy γ-ray emission associated with the Galactic plane by *OSO 3* (Clark et al., 1968) and *SAS-II* (Fichtel et al., 1978). The correlation with Milky Way structures, notably the tangent points of the spiral arms, suggested that the diffuse emission was originated by interactions between CRs and the ISM. Early models developed to interpret those observations assumed a dynamical balance between CR and ISM densities (Bignami and Fichtel, 1974).

The breakthrough came with the *COS-B* satellite (1975-1982), whose observations in the 50 MeV$-$5 GeV energy range highlighted the correlation between γ-ray emission and ISM tracers and provided the first informations on the large scale properties of CRs (for a review see Bloemen, 1989). γ-ray measurements established the use of CO as a surrogate tracer of H_2 and were able to constrain the X_{CO} conversion factor (§ 2.1.3, see e.g. Lebrun et al. 1983). The gradient of CR densities on the Galactic scale was shown to be flatter than the distribution of SNRs or PSRs (Strong et al., 1988).

The *Compton Gamma-ray Observatory* (*CGRO*, 1992-1999), fully covered the energy range 1 MeV$-$30 GeV thanks to its two instruments COMPTEL (Imaging Compton Telescope,1 MeV$-$30 MeV) and EGRET (Energetic Gamma-ray Experiment Telescope, 20 MeV$-$30 GeV). *CGRO* data led to many in-depth studies, but also left many open questions about the origin of the interstellar emission, the properties of Galactic CRs and the census of the ISM that I will overview later in the chapter.

The last years have seen a dramatic extension of the energy window. The *INTEGRAL* (*International Gamma-Ray Astrophysics Laboratory*) observatory provided a new view below 1 MeV: whereas the soft γ-ray emission below $\sim$ 50 keV was finally proven to originate from unresolved sources (Lebrun et al., 2004), in the sub-MeV energy range a diffuse emission of plausible IC origin is observed (Porter et al., 2008). Ground-based instruments started exploring TeV energies. The HESS (High-Energy Stereoscopic System) telescope carried out a survey of the Galactic plane above 200 GeV, detecting γ-ray emission spatially correlated with a complex of giant molecular clouds in the central 200 pc of the Milky Way (Aharonian et al., 2006). The Milagro experiment detected diffuse emission at TeV energies from the Cygnus region, possibly associated with the distribution of interstellar matter (Abdo et al., 2007).

The *Fermi* Large Area Telescope (LAT; Chapter 1), on orbit since 2008, brought a wealth of new information, partially answering some open questions of the EGRET era that we will overview in the rest of the Chapter.

3.2 THE EGRET GEV EXCESS

3.2.1 *EGRET observations: The GeV excess*

Hunter et al. (1997) reported that the spectrum of diffuse emission measured by EGRET on the Galactic plane ($b \leq 10°$) above ~ 1 GeV was larger by a factor $\sim 60\%$ than expected from locally measured CR spectra. They compared EGRET data with a model based on the assumption of dynamical balance between CRs and ISM densities and on realistic distributions of interstellar matter and radiation. The excess was later confirmed over the whole sky and for explicit propagation models (§ 2.2.3), see e.g. Strong et al. (2004a). It was noticed also for single components, notably in the emission from local atomic clouds (Digel et al., 2001). Many different interpretations were proposed to explain the "GeV excess":

- problems in the absolute calibration of the EGRET instrument;
- discrepancies between the locally measured CR spectra and those present on the Galactic scale or even in the local interstellar space;
- contributions from exotic processes, notably involving dark matter particles;
- limitations of the theory of π^0 production or IC emission (which are thought to be the dominant processes above 1 GeV);
- contributions from unresolved sources.

The latter hypothesis was unlikely due to the uniformity of the GeV excess over the whole sky and the quite good agreement between expectations and EGRET measurements below 1 GeV. The theory of π^0 production was largely revisited after the discovery of the EGRET GeV anomaly, without leading to significant changes in the spectral shape with respect to previous estimates (e.g. Mori, 1997; Kamae et al., 2006; Mori, 2009). The IC component was also re-evaluated in the light of explicit CR propagation models and improved models of the ISRF, but expectations based on locally measured CR spectra were still deficitary above ~ 1 GeV if compared with EGRET data (Strong et al., 2000).

Problems in the absolute calibration of the EGRET instrument (Thompson et al., 1993) were considered a viable possibility. Above ~ 1 GeV uncertainties are large due to the effect of self-vetoing caused by the back-splash of charged particles on the anticoincidence shield after shower generation in the tracker/calorimeter. Since the relative excess was observed at the same level over the whole sky independently from any parameters like the line-of-sight density of gas, Stecker et al. (2008) concluded that this was the most likely explanation of the GeV excess.

Many authors proposed that CR spectra measured at the Earth may be not representative of those in the Galactic interstellar space. Some of them tried to reproduce the GeV excess invoking only a harder nucleon spectrum (e.g. Mori, 1997; Gralewicz et al., 1997), but this interpretation is ruled out by the $\bar{p}/p$ spectrum (Moskalenko et al., 1998). Variations in the electron spectrum are more likely, because of rapid energy losses via synchrotron emission and IC interactions and the stochastic nature of sources both in space and time (e.g. Porter and Protheroe, 1997; Pohl and Esposito, 1998; Aharonian and Atoyan, 2000). Strong et al. (2004a) sought an *optimized model* based on the GALPROP code (§ 2.2.3), able to reproduce EGRET data over the whole sky and still consistent (within the quite large uncertainties) with direct CR measurements. They invoked a steepening of the electron spectrum and

a renormalization by a factor of about 4 relatively to the locally observed spectrum, justified by the large uncertainties discussed above. They also scaled the proton spectrum by a factor 1.8 and modified the low-energy spectral shape (being still consistent with $\bar{p}$ data). This *optimized model* was not claimed to be a unique solution, but instead to represent the possibility of a model consistent with EGRET data and all the other relevant observations related with CR propagation.

Many authors (e.g. Bergström et al., 1998; Bertone et al., 2002; Hooper and Dingus, 2002) investigated the possibility that the EGRET GeV excess was due to a signal from dark matter annihilation or decay. As an example, de Boer et al. (2005) developed a model where the excess was explained as annihilation signal of non-relativistic weakly interacting massive particles (WIMPs) with a mass of $50 - 100$ GeV distributed in the Galaxy with a spherical isothermal profile with substructures in the Galactic plane in the form of toroidal rings at 4 and 14 kpc from the center, claimed to be also improving the consistency between expectations and the observed Galactic rotation curve.

3.2.2 *LAT observations at intermediate Galactic Latitudes*

Once the LAT started scientific operations, the first efforts to solve the GeV excess puzzle involved the study of diffuse γ-ray emission at intermediate Galactic latitudes, where most of the emission is thought to arise from processes involving nearby gaseous complexes. Indeed, on the Galactic plane we observe the superposition of signals coming from the local interstellar space and far away regions (either the inner or the outer Galaxy according to the longitude range). On the other hand, at high Galactic latitudes, data are dominated by the EGB, the residual background from misclassified charged CR interactions in the LAT (§ 1.1.2) and IC emission which is sampling a wider region along the line of sight, given the small scale-height of interstellar gas ($0.2 - 1$ kpc, § 2.1.2) compared with the CR propagation halo ($4 - 20$ kpc, § 2.2.3) and the uniform target provided by the CMB.

Comparison with a propagation model

LAT measurements for $10^\circ \leq |b| \leq 20^\circ$ and energy between 100 MeV and 10 GeV were reported in Abdo et al. (2009c). The γ-ray spectrum measured by the LAT is compared with that measured by EGRET in Fig. 3.2. For both telescopes uncertainties are dominated by instrumental systematics. The standard 13% systematics are assumed for EGRET (Esposito et al., 1999). LAT intensities were calculated using the post-launch IRFs `P6_V3` (§ 1.2.2).

Fig. 3.3 compares LAT intensities (as shown in Fig. 3.2) with a GALPROP model for the Galactic diffuse emission (§ 2.2.3), which is an updated version of the *conventional model* (i.e. an *a priori* model not consistent with the EGRET GeV excess) by Strong et al. (2004a) plus a source component and an unidentified isotropic background fitted to the LAT data with the Galactic diffuse model fixed. The source component was built taking sources at the positions given in the internal 3-month point-source list for $10^\circ \leq |b| \leq 20^\circ$ and fitting their intensities independently in 3 energy bins per decade. The unidentified isotropic background was obtained fitting to LAT data for $|b| > 30^\circ$ the Galactic diffuse emission model described above, point sources in the

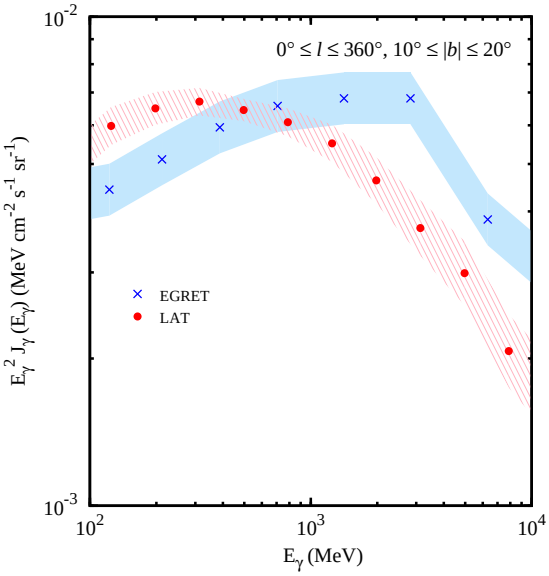

Figure 3.2: γ-ray emission intensity averaged over all Galactic longitudes for $10° \le |b| \le 20°$ (Abdo et al., 2009c). Red points: LAT data; blue points: EGRET data. Systematic uncertainties for both telescopes are shown as hatched bands.

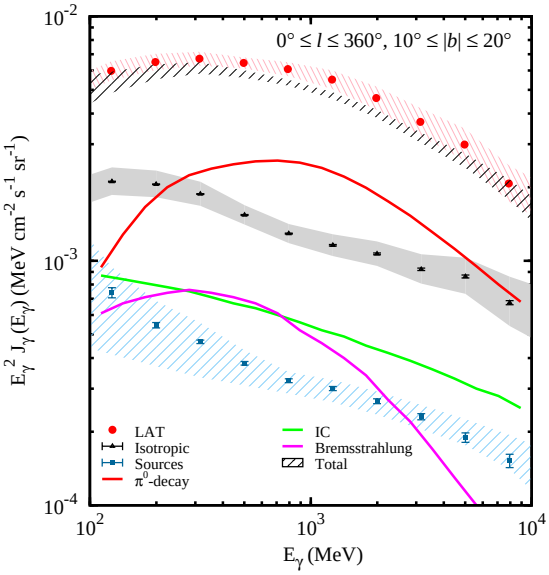

Figure 3.3: LAT intensities at $10° \le |b| \le 20°$ (red points/band) compared with the model for the Galactic diffuse emission, the contribution from sources and the unidentified isotropic background; the total model is represented by the hatched black band (Abdo et al., 2009c).

internal 3-month point-source list and an isotropic term independently in 5 energy bins per decade. At this early stage no effort was put into separating its different components, so the isotropic spectrum shown in Fig. 3.3 is a mixture of residual background from misclassified CR

interactions in the LAT (§ 1.1.2), the EGB (later determined from LAT data, Abdo et al. 2010j) and potentially other foreground components not modeled. Here, using the high-latitude region ($|b| > 30°$) minimizes the contamination by the bright Galactic ridge and therefore the systematic uncertainties.

The intensity scales of the LAT and EGRET have been found to be different with the LAT-measured spectra softer (Fig. 3.2). The same effect is seen in the spectrum of bright point sources like the Vela pulsar (Abdo et al., 2009e), pointing to an instrumental origin of the differences between the two telescopes. On the other hand the LAT-measured spectrum is approximately consistent with the *a priori* model of the Galactic diffuse emission. Observations of intermediate Galactic latitudes do not confirm the EGRET GeV excess and show that the basic processes for the production of diffuse emission are understood. There are, however, discrepancies between model and data that highlight limitations of the model susceptible of further improvements.

Local H I *emissivity*

As mentioned above, the EGRET GeV excess was affecting single components of the diffuse γ-ray emission, notably that associated with nearby H I clouds (Digel et al., 2001). If not an instrumental artifact, this was interpreted as an evidence either of problems in the theory of π^0 production (which dominates emission from gas above a few hundreds MeV) or of discrepancies between directly measured CR spectra and those in the local interstellar space.

This issue was investigated thanks to the measurement of the H I emissivity (γ-ray emission rate per hydrogen atom) associated with atomic clouds at intermediate latitudes in the third Galactic quadrant ($200° < l < 260°$ and $22° < |b| < 60°$; Abdo et al. 2009g). This region was chosen because it samples interstellar complexes within $\sim$ 1 kpc from the Sun (the scale height of the H I layer is $\sim$ 230 pc and it starts flaring outside the solar circle, § 2.1.2), and it is also free from known molecular clouds (therefore the H I 21-cm line traces the total gas column densities). Let us also note that the IC emission in this region is expected to be small, $\sim$ 10% of the total, and the tenuous diffuse clouds have mass column densities well determined from the 21-cm line intensities, without significant uncertainties due to the optical depth (§ 2.1.2).

Point sources were masked in 1° circular regions around positions in the internal 6-month point source list, and their spill-over was subtracted from γ-ray intensities as well as the contribution due to IC emission (as estimated using GALPROP, § 2.2.3). The residual γ-ray emission was correlated with $N(\mathrm{H\,I})$ column densities derived from the LAB survey [2] (Kalberla et al., 2005) convolved with the LAT PSF, in 13 logarithmic bins between 100 MeV and $\sim$ 10 GeV and over a spatial grid of order 7 ($\sim 0.5° \times 0.5°$) in HEALPix pixelization (Górski et al., 2005).

A good linear correlation between γ-ray intensities and $N(\mathrm{H\,I})$ column densities was observed. The offset is an estimate of the isotropic background (see previous paragraph), whereas the slope of the linear relation provides in each energy bin the H I emissivity.

2. $N(\mathrm{H\,I})$ column densities were derived for a uniform spin temperature of 125 K, but, as we explained, this assumption has a negligible impact for the low-density clouds under study.

The H I emissivity spectrum is compared in Fig. 3.4 with expecta-

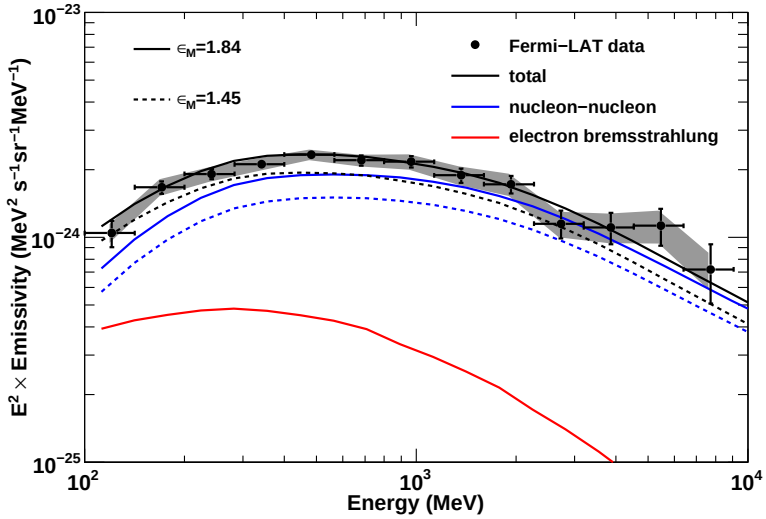

Figure 3.4: Differential γ-ray emissivity of local atomic hydrogen compared with expectations based on locally measured CR spectra (Abdo et al., 2009g). The nucleon-nucleon component (and therefore the total) are shown for different values of the nuclear enhancement factor ϵ_M (§ 2.2.3). LAT data are shown in black: horizontal and vertical bars represent the energy bin widths and the statistical errors, respectively; the shadowed band represents the systematic uncertainties in the event selection efficiency (Abdo et al., 2009g).

tions based on the locally measured CR spectra. The electron Bremmstrahlung component is evaluated using the standard routine implemented in GALPROP (§ 2.2.3); the nucleon-nucleon component is calculated using the $p - p$ emissivities estimated by Kamae et al. (2006) and the extreme values of the nuclear enhancement factor found in the literature, 1.45 (Dermer, 1986a,b) and 1.84 (from Mori, 2009, § 2.2.3). The H I emissivity spectrum is consistent with expectations for CRs interacting with the interstellar gas and it indicates that CR spectra in the local interstellar space are similar within $\sim 10\%$ to those directly measured at the Earth. The γ-ray emissivity of local interstellar matter above 100 MeV is estimated to be $(1.63 \pm 0.05) \times 10^{-26}$ s^{-1} sr^{-1}.

3.3 EGRET LEGACIES BEYOND THE GEV EXCESS

3.3.1 *The cosmic-ray distribution in the Galaxy*

Interstellar γ-ray emission is a unique probe of CR densities throughout the Galaxy and it is therefore a fundamental piece of information to understand the CR origin and propagation in the interstellar space.

Since the early *SAS-II* and *COS-B* years, the diffuse emission from the Milky Way was taken as evidence of a broad distribution of CRs through the Galaxy. The association between structures seen in the interstellar γ-ray emission and those known at other wavelengths, like the tangent points of the spiral arm, lead to the development of models based on a dynamical balance between CR and ISM densities (e.g. Bignami and Fichtel, 1974), tentatively justified by CR trapping by the

enhanced magnetic fields in interstellar clouds or by the association between putative CR sources and the placental clouds where they were born.

Strong et al. (1988) analysed the radial distribution of γ-rays in the final *COS-B* database using H I and CO data covering the entire Galactic plane (following the studies of selected regions by Bloemen et al. 1984, 1986). Thanks to the kinematic separation of H I and CO lines (Appendix B), they separated through a maximum likelihood fit (§ 1.3.1) the γ-ray emission arising from gas complexes in different ranges of Galactocentric distance (rings). This analysis yielded a maximum variations of the H I emissivity from the solar circle to the inner Galaxy of about a factor 2, much shallower than the gradient of SNRs or PSRs. On the basis of a simple diffusion model Bloemen (1989) concluded that the *gradient problem* was an indication either of limitations of the measured distributions of putative CR sources in the Galaxy or of a large propagation halo (e.g. Stecker and Jones, 1977). The *COS-B* result was later confirmed by Strong and Mattox (1996) repeating the ring-analysis with the Phase $1 + 2$ EGRET survey.

The development of numerical explicit models lead to a new era in this field. Strong et al. (2004b) sought a GALPROP model able to approximately reproduce EGRET data (in particular longitude and latitude profiles) using a population of CR sources smoothly distributed with the radial profile of PSRs (Lorimer, 2004) but assuming a large variation (by a factor 10) of $X_{\rm CO}$ from the inner to the outer Galaxy (see later § 3.3.2). Yet, this was not explaining the large gradient found by Strong and Mattox (1996) for the H I emissivity, which plays a prominent role being H I the only ISM component whose mass column densities are determined directly from radio observations (§ 2.1.2). Later, Evoli et al. (2008) used their code for CR propagation, DRAGON, to show that the agreement with EGRET longitude/latitude profiles can be obtained with a constant $X_{\rm CO}$ ratio (except for the Galactic bulge), but assuming a non-uniform CR diffusion coefficient as can be expected for theoretical reasons if energy equipartition holds between CR densities and magnetic field fluctuations (naturally if the Galactic magnetic field is generated by a CR-driven dynamo, see § 2.3.1).

A privileged target for gradient studies is given by the outer Galaxy, since the kinematic distance of gas lines is unambiguously determined outside the solar circle (Appendix B). The first analysis of *COS-B* data (Bloemen et al., 1984) was inconclusive, also due to the lack of CO data for the outer Galaxy at that time. The ring-analysis of EGRET data was performed in detail for two regions in the second (Digel et al., 1996) and third Galactic quadrant (Digel et al., 2001) with good kinematic separation between the different structures seen along the line of sight, but the limited statistics did not make possible firm conclusions to be drawn yet. I investigated the CR gradient in the outer Galaxy with a more accurate separation technique (not based on rings but instead on physical structures of the ISM, Appendix B) using LAT data: the results are reported in Chapter 4 for the second quadrant and Chapter 5 for the third one.

An important limitation of all the ring-analyses mentioned above is that they assume an axisymmetric distribution of CR densities in the Galaxy, neglecting Galactic structures like the spiral arms. The same assumption is often made for numerical explicit models, notably the bidimensional setup of GALPROP. On the other hand, since the dawn

of γ-ray astronomy, the association between Galactic structures and interstellar emission was suggested CR densities to follow the spiral arms (Bignami and Fichtel, 1974). This issue potentially could be resolved thanks to γ-ray observations, e.g., unveiling a contrast in γ-ray emissivities between spiral arms and the interarm regions. EGRET data did not lead to firm conclusions on this regard (Digel et al., 2001); I investigated this issue with LAT data by considering the interarm region present in the third Galactic quadrant between the local spur and the Perseus spiral arm (Chapter 5) and the massive interstellar complex in the Cygnus region (Chapter 6).

3.3.2 *The calibration of molecular masses*

As anticipated in § 2.1.3, interstellar γ-ray emission can be used to calibrate the $X_{CO} \equiv N(H_2)/W_{CO}$ ratio (Eq. 2.20). Let us assume to be able to determine from γ-ray observations the emissivity per H I atom, q_{HI}, and the emissivity per W_{CO} unit, q_{CO}, for the same cloud. If the same CR fluxes thread the atomic and molecular part of the cloud, since the molecular binding energy is negligible with respect to the energetics of the γ-ray production processes we expect that the emissivity per H_2 molecule is twice as the emissivity per H I atom. Therefore the quantity

$$X_\gamma = \frac{q_{CO}}{2\, q_{HI}} \tag{3.1}$$

is an estimate of X_{CO} (Lebrun et al., 1983).

X_γ is regarded as a reliable estimate of X_{CO} because it directly probes masses in the ISM, being the γ-ray flux proportional to column-densities of target gas[3], and it is independent from the chemical and thermodynamic status of the gas. On the other hand it is affected by possible systematics, either due to variations of CR densities over the same interstellar complex:

- the enhancement of CR densities in molecular clouds due to the trapping by the enhanced magnetic fields or to the association of CR sources with clouds (e.g. Gabici et al., 2009);
- the depletion of CR densities in the densest molecular cores due to an incomplete penetration (e.g. Gabici et al., 2007);

or to resolution problems:

- the presence of unresolved γ-ray sources with distribution similar to that of molecular gas;
- the IC interstellar γ-ray emission which might mimic the spatial distribution of clouds if high-energy electrons are confined around their sources associated with clouds;
- the similarity between H I and CO structures, becoming more severe for structures at larger distances from the Earth.

Let us also note that X_γ is, strictly speaking, an estimate of $X_{CO} \equiv N(H_2)_{CO}/W_{CO}$, being $N(H_2)_{CO}$ the column density of molecular hydrogen associated with CO emission (in fact, directly proportional to W_{CO}), not of the total molecular masses[4] (see later § 3.3.3).

3. Other methods are more indirect, invoking the proportionality between molecular masses and extinction (due to dust) or kinetic energy of the turbulent motion (which neglects non-turbulent –e.g. magnetic– support).

4. Contrarily to other estimates, such as the virial mass which measures the total gravitationally-bound mass.

Early models of interstellar γ-ray emission assumed X_{CO} constant over the whole Galaxy. Strong et al. (1988), from the ring-analysis of *COS-B* observations of the entire Galactic plane, obtained an estimate[5] $X_\gamma = (1.9 \pm 0.2) \times 10^{20}$ cm^{-2} (K km s^{-1})$^{-1}$. Strong and Mattox (1996) confirmed this result, obtaining from the ring-analysis of EGRET data the same value $(1.9 \pm 0.2) \times 10^{20}$ cm^{-2} (K km s^{-1})$^{-1}$. Using their model based on the dynamical balance between CR and ISM densities, Hunter et al. (1997) obtained from EGRET data a comparable value of $X_\gamma = (1.56 \pm 0.05) \times 10^{20}$ cm^{-2} (K km s^{-1})$^{-1}$.

However, during the '90s, several evidences came out that X_{CO} might vary over the Galaxy. Digel et al. (1990) reported the CO observations of molecular clouds in the outer arm of the Galaxy, with a X_{CO} ratio from virial masses 4 ± 2 times larger than in the inner Galaxy. Sodroski et al. (1995) derived from *COBE* DIRBE data a X_{CO} ratio within 400 pc from the Galactic center a factor $3 - 10$ lower than in the inner Galaxy. Combining their findings with the results previously discussed, they proposed that X_{CO} increases by more than one order of magnitude from the Galactic center to the outer Galaxy. Israel (1997) estimated from the far-IR surface brightness of several external galaxies a varying X_{CO} ratio, depending on both the ambient radiation field intensity and metallicity. This result was interpreted as the consequence of radiative photodissociation of CO and the poor self-shielding in low-metallicity environments. This interpretation would naturally lead for the Milky Way to a X_{CO} ratio increasing with Galactocentric radius.

The X_{CO} values derived from EGRET data for some selected clouds or complexes within a few kpc from the Sun seemed to support this idea (for a synthesis see Digel et al., 1996, 2001). As anticipated in § 3.3.1, Strong et al. (2004b) proposed a heuristic model of X_{CO} as a function of Galactocentric radius, R, designed to approximately reproduce the EGRET longitude/latitude profiles with a CR source distribution derived from PSRs thanks to an increase in the W_{CO}-to-$N(H_2)$ conversion factor by an order of magnitude from the inner to the outer Galaxy. A summary of the situation at the end of the EGRET era is given in Figure 3.5. The works reported in Part II allowed us to determine X_{CO} in some selected regions within a few kpc from the solar system, toward the outer Galaxy, shedding new light on the problem of the calibration of molecular masses.

3.3.3 *Dark gas*

For many years the modeling of γ-ray emission from interstellar gas was based on the 21-cm line of H I and on the 2.6-mm line of ^{12}CO. Yet, this combination was not guaranteed to provide an exhaustive census of the ISM. Grenier et al. (2005) showed that EGRET data were pointing to the presence of some "dark gas", i.e. neutral gas not properly traced by the H I and CO lines, in all the nearby clouds of the Gould Belt.

Their method was based on the comparison between a wide collection of gas tracers: the H I and CO cartographies, γ-ray data by EGRET and dust tracers (see § 2.1.5), namely thermal emission at 3000 GHz and 94 GHz and the color excess $E(B-V)$ map by Schlegel et al. (1998). The thermal emission at 94 GHz (tracing to cold dust at $\sim$ 10 K) and

5. The original result in Strong et al. (1988), $(2.3 \pm 0.3) \times 10^{20}$ cm^{-2} (K km s^{-1})$^{-1}$, was rescaled by 1.22 to take into account the calibration correction to be applied to data by Dame et al. (1987) according to Bronfman et al. (1988).

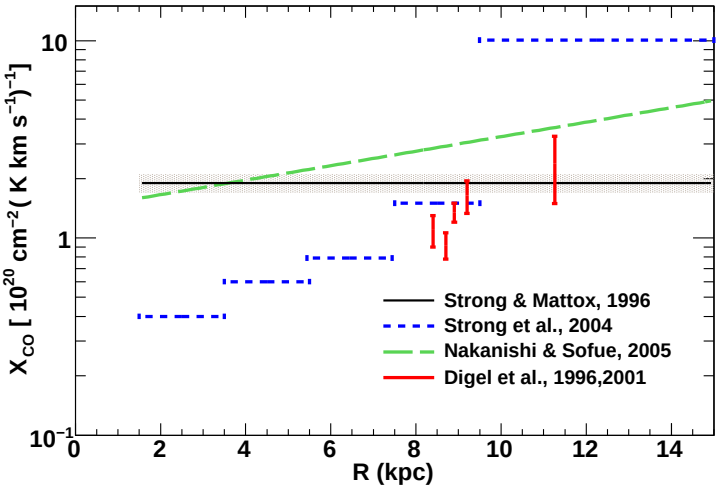

Figure 3.5: X_{CO} as a function of Galactocentric radius R. Black horizontal line: the constant value derived from EGRET observations of the entire Galactic plane by Strong and Mattox (1996); statistical uncertainties are represented as a shadowed band. Red points: values for selected clouds or complexes derived from EGRET data as summarized in Digel et al. (1996, 2001). Blue step function: the model used in Strong et al. (2004b). For reference we also give as a green dashed line the conversion function by Nakanishi and Sofue (2006), based mainly on virial masses.

the $E(B-V)$ map both showed extensive coherent regions with large dust-to-gas excesses bridging the nearby CO clouds and their atomic envelopes. These excesses were correlated as well with excesses seen in γ-ray emission, which is a tracer of gas mass independent of its chemical and thermodynamic state. These excesses were not correlated with free-free emission regions (ionized gas, § 2.1.4) or structures in the 408 MHz emission (concentrations of CR electrons, § 2.3.2). Given the negligible contribution expected from IC scattering off CR electrons of the thermal emission from dust itself, the most likely explanation was the presence of gas unaccounted for by the H I and CO surveys.

The interstellar γ-ray emission, however, cannot discriminate between molecular and atomic gas, so the chemical state of the dark gas is not clear yet. The existence of molecular gas not traced by the 2.6-mm line is largely accepted, both from observational evidences and theoretical modeling. Magnani et al. (2003) found in a translucent cloud a poor correlation between the distribution of CH (methylidyne) and CO, but, on the other hand, a good correlation between CH and the $E(B-V)$ color excess, and they suggested the same to hold for the translucent envelopes of giant molecular clouds. Papadopoulos et al. (2002) showed how H_2 formation likely occurs in metal-poor environments (like the outer Galaxy or the outer layers of molecular clouds) where the threshold for CO detection is not reached. Wolfire et al. (2010) calculated that the fraction of dark molecular gas is expected to be remarkably constant, ~ 0.3 for clouds down to $\overline{A}_V \simeq 8$, and insensitive to the incident UV radiation field and the density distribution in the cloud; they predicted that the dark fraction increases with decreasing $\overline{A}_V$.

On the other hand, our treatment of the radiative transfer of the H I line is only approximative and very often based on the assumption of a uniform spin temperature (§ 2.1.2). Studies of interstellar γ-ray emission were almost always based on the assumption of a uniform $T_S = 125$ K (e.g. Bloemen et al., 1984), whereas cold atomic clouds often shows $T = 40 - 70$ K (e.g. Heiles and Troland, 2003). This might lead to a significant underestimate of $N(\mathrm{H\,I})$ in the cold atomic envelopes of molecular clouds, and therefore a contribution to the dark gas observed through its gamma-ray emission.

The EGRET era left many open questions also on the dark gas. At first, the fact that the γ-ray emission and dust correlated excesses were due to dark gas was based on their spatial distribution and on the lack of other plausible emission mechanisms. In Chapter 4 we will derive from LAT data the γ-ray emissivity associated to dust residuals over an energy range of two decades for the clouds of Cassiopeia and Cepheus, and we will show that it linearly scales with the emissivity of atomic gas; the same underlying physical mechanism must originate γ-ray emission associated with H I and cold dust residuals, which are indeed a tracer of dark gas. Secondarily, the dark clouds were resolved in the EGRET era only for nearby complexes away from the Galactic plane. Resolving the dark clouds in the Galactic disk, with dust temperature gradients near massive-star forming regions, along crowded lines of sight is a difficult task. We undertook this challenge in Chapter 6 for the Cygnus region, also detecting a dust/γ-ray excess with a spectrum equivalent to that of H I in the 100 MeV-100 GeV energy range.

Our results for the clouds of Cassiopeia and Cepheus were found to be in remarkable good agreement with their theoretical predictions by Wolfire et al. (2010). In the mean time the *Herschel* satellite detected warm molecular gas through the C II line for 29 clouds in the Milky Way not showing CO emission (Langer et al., 2010) and through excesses in the far IR emission from the Large Magellanic Cloud (LMC), situated at the transition between H I and CO clouds (Roman-Duval et al., 2010). Many more results are expected to come as we accumulate LAT data, as well as data from *Herschel* and *Planck*.

3.4 INTERSTELLAR γ-RAY EMISSION FROM EXTERNAL GALAXIES

3.4.1 *EGRET observations*

Observations of external galaxies usefully complement the studies of interstellar γ-ray emission from the Milky Way. In particular, face-on galaxies offer the opportunity to map the distribution of CR densities without ambiguities due to confusion along the line of sight, which severely limits the understanding of our own Galaxy, observed from inside. This possibility, however, is often limited by the poor angular resolution of γ-ray instruments.

Emission from external galaxies was intensively searched using EGRET data. Particular consideration was given to the Magellanic clouds due to their proximity ($\sim$ 50 kpc), their large angular dimension ($> 5^\circ$) and the small viewing angle at the Earth ($\sim 30^\circ$). However, the low fluxes at the Earth made possible just one detection of a normal (not hosting an active nucleus) galaxy, the Large Magellanic Cloud (LMC; Sreekumar et al. 1992). At the beginning of the mission the LMC was detected (as a point source) with an integrated flux of $(1.9 \pm 0.4) \times 10^{-7}$

cm^{-2} s^{-1}. The flux was recognized to be consistent with the idea of dynamical coupling between CR with ISM densities.

Further searches for emission from the Small Magellanic Cloud (SMC) did not lead to the detection of significant signal. Lin et al. (1996) set an upper limit on the flux above 100 MeV of 0.4×10^{-7} cm^{-2} s^{-1}, well below the value expected from dynamical balance principles, already lower than the flux expected for CR densities measured in the Milky Way. They argued that this was proving the galactic origin for CRs below several hundreds GeV. Lin et al. (1996) gave also an upper limit on the flux associated with NGC 253 (one of the nearest galaxies not belonging to the local group, at 3.4 Mpc from the Earth) of 1.0×10^{-7} cm^{-2} s^{-1}.

The LAT brought a new quality to the subject, resolving the LMC as an extended source and detecting high-energy γ-ray emission from a few other galaxies, either from the local group, SMC (which was also resolved as extended source) and M31, or characterized by starbust activity, like M82 and NGC 253.

3.4.2 *LAT observations of the local group of galaxies*

The Milky Way is part of a local group of galaxies, the most massive members being the Milky Way itself, the Andromeda galaxy (M31) and the Triangulum galaxy (M33). Including dwarf galaxies, the local group is made from more than 30 galaxies. The Milky Way is the gravitational center of a subgroup including the aforementioned Magellanic clouds and several dwarfs. Due to their proximity they are a privileged target of investigation for the LAT.

Let us mention that γ-ray emission from the satellite dwarfs of the Milky Way was intensively searched because they are objects with a very high mass to luminosity ratio, low rate of massive-star formation and consequent lack of plausible conventional sources of γ-rays. They are therefore ideal targets for the detection of γ-ray signatures of dark matter particles. No significant emission was found yet (Abdo et al., 2010h; Scott et al., 2010).

The LMC

The LMC is relatively active, hosting SNRs, superbubbles and massive star-forming regions, and it was already detected as a high-energy γ-ray source by EGRET. The LAT was able to spatially resolve the galaxy enabling the mapping of its CR densities (Abdo et al., 2010i), and in particular revealing the massive star-forming region of 30 Doradus as a bright γ-ray source.

Through the use of geometric templates the γ-ray emission was shown to be rather extended than the sum of some discrete point sources. No significant pulsation was detected in γ-rays from the known pulsars. These findings suggest that a large part of the γ-ray luminosity is due to interstellar processes as in the Milky Way according to our picture.

The γ-ray emission from the LMC shows little or no correlation with tracers of the gas mass, H I and CO. On the other hand a remarkably good correlation was found with H_α emission. The H_α line is a tracer of the ionized gas (§ 2.1.4), which represents but a small fraction (1%) of the ISM in the LMC. However, the distribution of ionized gas can

be thought to indirectly trace the massive-star forming regions, and therefore putative CR sources. This is analogous to the results obtained for the Cygnus region in the Galaxy (Chapter 6).

The tight correlation between massive star-forming regions and γ-ray emission supports the idea that CR acceleration occurs in SNRs or superbubbles, but also suggest a small propagation length for CR protons, of the order of ~ 200 pc, much smaller than the estimates for the Milky Way.

The flux measured above 100 MeV for the LMC is $(2.6 \pm 0.2) \times 10^{-7}$ cm^{-2} s^{-1}, slightly higher that the value reported by EGRET, which, however, derived the flux under the hypothesis of point-like source. Even assuming that all the γ-ray emission from the LMC is due to interstellar processes the average emissivity is $(6.9 \pm 2.4) \times 10^{-27}$ s^{-1} sr^{-1} per H atom, ~ 2 smaller than the value measured by the LAT for the local interstellar space (the value might be smaller if part of the emission is attributed to sources). This implies CR densities around 30% of those observed in the Milky Way [6].

The map of γ-ray emissivities which can be derived from LAT data shows a good correlation with Wolf-Rayet stars and supergiant shells, supporting again the idea that CRs are accelerated in massive star-forming regions.

The SMC

The LAT detected also γ-ray emission from the SMC with an extension around 3° (Abdo et al., 2010b). Contrarily to the LMC, the correlation between γ-ray emission and both H I density and Hα emission is rather good, not showing any remarkable coupling with star formation activity.

The integrated flux above 100 MeV amounts to $(3.7 \pm 0.7) \times 10^{-8}$ cm^{-2} s^{-1}, which, if entirely attributed to interstellar emission, would lead to an average emissivity per H atom of $(2.5 \pm 0.5) \times 10^{-27}$ s^{-1} sr^{-1}, a factor of $6 - 7$ lower than in the vicinities of the solar system and a factor 2 lower than in the LMC. However, for such a low-mass galaxy, a large fraction of the signal might be due to the contribution from sources rather than to interstellar processes (in our Galaxy the source contribution is thought to be $< 10\% - 30\%$), so the emissivity might be even lower.

Given the star formation activity similar to the LMC, the lower emissivity is more likely due to different properties of CR transport (e.g. a smaller confinement volume) rather than to a lower injection rate.

M31 & M33

The two most massive members of the local group are Andromeda (M31) and the Triangulum Galaxy (M33). In two years of observations the LAT detected at 5σ γ-ray emission associated with M31 (Abdo et al., 2010d), with a flux integrated above 100 MeV of $(9.1 \pm 1.9_{\rm stat} \pm 1.0_{\rm syst}) \times 10^{-9}$ cm^{-2} s^{-1}, implying average CR densities 0.35 ± 0.25 of those in the Milky Way as estimated by Strong et al. (2010).

No significant emission was found in the direction of M33: the upper limit on the flux integrated above 100 MeV at 95% confidence level is 5.1×10^{-9} cm^{-2} s^{-1} (Abdo et al., 2010d).

6. The value of 30% is calculated through a simple one zone model for the LMC, for details see Abdo et al. (2010i).

3.4.3 *Beyond the local group*

Outside the local group of galaxies, the best candidates for a LAT detection are starbust galaxies with large star formation rates, and thus a plausibly large γ-ray luminosity. The first objects studied were M82 and NGC 253. Together with the galaxies of the local group, they revealed an unexpected correlation between γ-ray luminosity and star formation rate over a wide dynamical range.

M82 and NGC 253

Steady point-like emission positionally coincident with M82 and NGC 253 was detected by the LAT after 11 months of observations (Abdo et al., 2010a). On the other hand, γ-ray emission at energies > 200 GeV from the same galaxies was reported by The VERITAS Collaboration (2009) and the HESS collaboration (Acero et al., 2009), respectively.

The γ-ray luminosities measured by the LAT are $2-4$ times larger than that of the Milky Way, suggesting a connection between star-formation rate and enhanced CR densities. The contribution from sources must be taken into account, however, to draw firm conclusions.

The γ-ray luminosity-star formation rate relation

From the flux F_γ measured for a galaxy we can derive its luminosity $L_\gamma = 4\pi d^2 F_\gamma$ (with d distance from the Earth). In Fig. 3.6 the γ-ray luminosity for all the external galaxies detected by the LAT so far (and the upper limit for M33) is compared with their star formation rate (SFR).

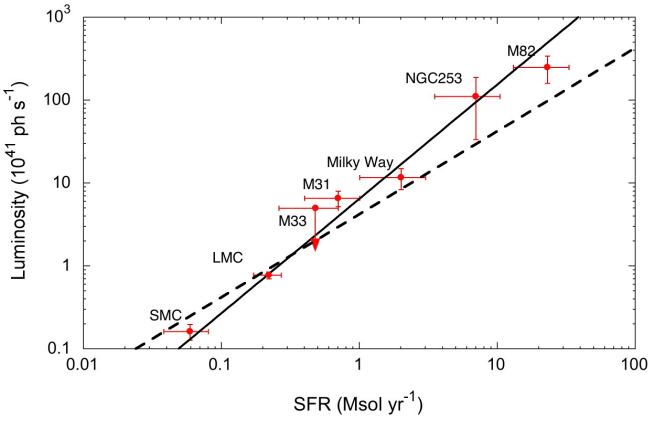

Figure 3.6: γ-ray luminosity versus star formation rate for the Milky Way and external galaxies studied so far with LAT data (Abdo et al., 2010d). The solid line shows the best-fit linear relation, whereas the dotted line is the best-fit power-law function for the experimental points.

There is a correlation between L_γ and SFR which is not clearly understood yet. The sample is too limited to draw firm conclusions, but this correlation seems to be analogous to the correlation observed between radio and far infrared (FIR) luminosities for galaxies (e.g. Murphy et al., 2006). The radio-FIR correlation is thought to express a link

between CRs and star formation, possibly because of electron calorimetry[7]. The hadronic component is dominant in the CR composition of the Milky Way, but it is unlikely to explain the L_γ-SFR correlation in terms of hadron calorimetry, since state-of-the-art propagation models depict our Galaxy as a very inefficient hadron calorimeter (Strong et al., 2010). The correlation might relate to the leptonic component of interstellar γ-ray emission, if this accounted for a significant fraction of the observed L_γ (consistently with some models for the Milky Way in Strong et al., 2010).

7. In the astrophysical jargon we say that a galaxy is an electron calorimeter if all the energy injected in the form of CR electrons is dissipated within the galaxy.

Part II

ANALYSES AND RESULTS

Then one day I started writing,
not knowing that I had chained myself for life
to a noble but merciless master.
When God hands you a gift, he also hands you a whip;
and the whip is intended solely for self-flagellation.

— Truman Capote, Music for Chameleons

4

INTERSTELLAR GAMMA-RAY EMISSION FROM THE OUTER GALAXY: THE SECOND GALACTIC QUADRANT

The outer Galaxy is a privileged target for studying large-scale properties of interstellar γ-ray emission because the Doppler shift-distance relation for radio/mm-wave lines of interstellar gas is single valued (§ B.1). It was therefore studied in detail with data from past telescopes (§ 3.3.1). Lines of sight in the proximities of the Galactic anticenter are problematic because of the loss of kinematic resolution (§ B.1), so two separate regions in the second and third Galactic quadrant are usually considered, where the velocity gradient is very steep and subsequently the kinematic separation very good.

I started studying the region of Cassiopeia and Cepheus in the second Galactic quadrant ($100° \leq l \leq 145°$), where some conspicuous nearby clouds of the Gould Belt resides, as well as interstellar complexes at larger distances up to the outer spiral arm. To separate the different structures seen along the line of sight I developed a novel kinematic separation procedure, based on the physical structures of the ISM rather than on rings as in most of previous studies (see § B.2). The results presented in the paper (§ 4.1) offered the opportunity to study the gradient of γ-ray emissivities of atomic gas toward the outer Galaxy and provided also constraints on the census of the ISM: on the gradient of the X_{CO} ratio from the Gould Belt to the Perseus arm and on the amount of dark gas in the nearby well-resolved clouds.

In the following study of the third quadrant (Chapter 5) we discovered that the most important source of uncertainties in this analysis method is due to the H I spin temperature (§ 2.1.2). This does not alter substantially the results presented in the paper, but I re-evaluate the uncertainties in § 4.2.

4.1 ATTACHMENT: THE SECOND QUADRANT PAPER

I attach here the paper published as Abdo et al. (2010e).

The Astrophysical Journal, 710:133–149, 2010 February 10 doi:10.1088/0004-637X/710/1/133

FERMI OBSERVATIONS OF CASSIOPEIA AND CEPHEUS: DIFFUSE GAMMA-RAY EMISSION IN THE OUTER GALAXY

A. A. Abdo[1,2], M. Ackermann[3], M. Ajello[3], L. Baldini[4], J. Ballet[5], G. Barbiellini[6,7], D. Bastieri[8,9], B. M. Baughman[10], K. Bechtol[3], R. Bellazzini[4], B. Berenji[3], E. D. Bloom[3], E. Bonamente[11,12], A. W. Borgland[3], J. Bregeon[4], A. Brez[4], M. Brigida[13,14], P. Bruel[15], T. H. Burnett[16], S. Buson[9], G. A. Caliandro[17], R. A. Cameron[3], P. A. Caraveo[18], J. M. Casandjian[5], C. Cecchi[11,12], Ö. Çelik[19,20,21], A. Chekhtman[1,22], C. C. Cheung[1,2], J. Chiang[3], S. Ciprini[12], R. Claus[3], J. Cohen-Tanugi[23], L. R. Cominsky[24], J. Conrad[25,26,52], C. D. Dermer[1], F. de Palma[13,14], S. W. Digel[3], E. do Couto e Silva[3], P. S. Drell[3], R. Dubois[3], D. Dumora[27,28], C. Farnier[23], C. Favuzzi[13,14], S. J. Fegan[15], W. B. Focke[3], P. Fortin[15], M. Frailis[29], Y. Fukazawa[30], S. Funk[3], P. Fusco[13,14], F. Gargano[14], N. Gehrels[19,31,32], S. Germani[11,12], G. Giavitto[6,7], B. Giebels[15], N. Giglietto[13,14], F. Giordano[13,14], T. Glanzman[3], G. Godfrey[3], I. A. Grenier[5], M.-H. Grondin[27,28], J. E. Grove[1], L. Guillemot[27,28,33], S. Guiriec[34], A. K. Harding[19], M. Hayashida[3], D. Horan[15], R. E. Hughes[10], M. S. Jackson[26,35], G. Jóhannesson[3], A. S. Johnson[3], W. N. Johnson[1], T. Kamae[3], H. Katagiri[30], J. Kataoka[36], N. Kawai[37,38], M. Kerr[16], J. Knödlseder[39], M. Kuss[4], J. Lande[3], L. Latronico[4], M. Lemoine-Goumard[27,28], F. Longo[6,7], F. Loparco[13,14], B. Lott[27,28], M. N. Lovellette[1], P. Lubrano[11,12], A. Makeev[1,22], M. N. Mazziotta[14], J. E. McEnery[19,32], C. Meurer[25,26], P. F. Michelson[3], W. Mitthumsiri[3], T. Mizuno[30], C. Monte[13,14], M. E. Monzani[3], A. Morselli[40], I. V. Moskalenko[3], S. Murgia[3], P. L. Nolan[3], J. P. Norris[41], E. Nuss[23], T. Ohsugi[30], A. Okumura[42], N. Omodei[4], E. Orlando[43], J. F. Ormes[41], D. Paneque[3], V. Pelassa[23], M. Pepe[11,12], M. Pesce-Rollins[4], F. Piron[23], T. A. Porter[44], S. Rainò[13,14], R. Rando[8,9], M. Razzano[4], A. Reimer[3,45], O. Reimer[3,45], T. Reposeur[27,28], A. Y. Rodriguez[17], F. Ryde[26,35], H. F.-W. Sadrozinski[44], D. Sanchez[15], A. Sander[10], P. M. Saz Parkinson[44], C. Sgrò[4], E. J. Siskind[46], P. D. Smith[10], G. Spandre[4], P. Spinelli[13,14], J.-L. Starck[5], M. S. Strickman[1], A. W. Strong[43], D. J. Suson[47], H. Takahashi[30], T. Tanaka[3], J. B. Thayer[3], J. G. Thayer[3], D. J. Thompson[19], L. Tibaldo[5,8,9], D. F. Torres[17,48], G. Tosti[11,12], A. Tramacere[3,49], Y. Uchiyama[3], T. L. Usher[3], V. Vasileiou[20,21], N. Vilchez[39], V. Vitale[40,50], A. P. Waite[3], P. Wang[3], B. L. Winer[10], K. S. Wood[1], T. Ylinen[26,35,51], and M. Ziegler[44]

[1] Space Science Division, Naval Research Laboratory, Washington, DC 20375, USA
[2] National Research Council Research Associate, National Academy of Sciences, Washington, DC 20001, USA
[3] W. W. Hansen Experimental Physics Laboratory, Kavli Institute for Particle Astrophysics and Cosmology, Department of Physics and SLAC National Accelerator Laboratory, Stanford University, Stanford, CA 94305, USA
[4] Istituto Nazionale di Fisica Nucleare, Sezione di Pisa, I-56127 Pisa, Italy
[5] Laboratoire AIM, CEA-IRFU/CNRS/Université Paris Diderot, Service d'Astrophysique, CEA Saclay, 91191 Gif sur Yvette, France; isabelle.grenier@cea.fr
[6] Istituto Nazionale di Fisica Nucleare, Sezione di Trieste, I-34127 Trieste, Italy
[7] Dipartimento di Fisica, Università di Trieste, I-34127 Trieste, Italy
[8] Istituto Nazionale di Fisica Nucleare, Sezione di Padova, I-35131 Padova, Italy; luigi.tibaldo@pd.infn.it
[9] Dipartimento di Fisica "G. Galilei," Università di Padova, I-35131 Padova, Italy
[10] Department of Physics, Center for Cosmology and Astro-Particle Physics, The Ohio State University, Columbus, OH 43210, USA
[11] Istituto Nazionale di Fisica Nucleare, Sezione di Perugia, I-06123 Perugia, Italy
[12] Dipartimento di Fisica, Università degli Studi di Perugia, I-06123 Perugia, Italy
[13] Dipartimento di Fisica "M. Merlin" dell'Università e del Politecnico di Bari, I-70126 Bari, Italy
[14] Istituto Nazionale di Fisica Nucleare, Sezione di Bari, 70126 Bari, Italy
[15] Laboratoire Leprince-Ringuet, École polytechnique, CNRS/IN2P3, Palaiseau, France
[16] Department of Physics, University of Washington, Seattle, WA 98195-1560, USA
[17] Institut de Ciencies de l'Espai (IEEC-CSIC), Campus UAB, 08193 Barcelona, Spain
[18] INAF-Istituto di Astrofisica Spaziale e Fisica Cosmica, I-20133 Milano, Italy
[19] NASA Goddard Space Flight Center, Greenbelt, MD 20771, USA
[20] Center for Research and Exploration in Space Science and Technology (CRESST) and NASA Goddard Space Flight Center, Greenbelt, MD 20771, USA
[21] Department of Physics and Center for Space Sciences and Technology, University of Maryland Baltimore County, Baltimore, MD 21250, USA
[22] George Mason University, Fairfax, VA 22030, USA
[23] Laboratoire de Physique Théorique et Astroparticules, Université Montpellier 2, CNRS/IN2P3, Montpellier, France
[24] Department of Physics and Astronomy, Sonoma State University, Rohnert Park, CA 94928-3609, USA
[25] Department of Physics, Stockholm University, AlbaNova, SE-106 91 Stockholm, Sweden
[26] The Oskar Klein Centre for Cosmoparticle Physics, AlbaNova, SE-106 91 Stockholm, Sweden
[27] CNRS/IN2P3, Centre d'Études Nucléaires Bordeaux Gradignan, UMR 5797, Gradignan, 33175, France
[28] Université de Bordeaux, Centre d'Études Nucléaires Bordeaux Gradignan, UMR 5797, Gradignan, 33175, France
[29] Dipartimento di Fisica, Università di Udine and Istituto Nazionale di Fisica Nucleare, Sezione di Trieste, Gruppo Collegato di Udine, I-33100 Udine, Italy
[30] Department of Physical Sciences, Hiroshima University, Higashi-Hiroshima, Hiroshima 739-8526, Japan
[31] Department of Astronomy and Astrophysics, Pennsylvania State University, University Park, PA 16802, USA
[32] Department of Physics and Department of Astronomy, University of Maryland, College Park, MD 20742, USA
[33] Max-Planck-Institut für Radioastronomie, Auf dem Hügel 69, 53121 Bonn, Germany
[34] Center for Space Plasma and Aeronomic Research (CSPAR), University of Alabama in Huntsville, Huntsville, AL 35899, USA
[35] Department of Physics, Royal Institute of Technology (KTH), AlbaNova, SE-106 91 Stockholm, Sweden
[36] Waseda University, 1-104 Totsukamachi, Shinjuku-ku, Tokyo 169-8050, Japan
[37] Department of Physics, Tokyo Institute of Technology, Meguro City, Tokyo 152-8551, Japan
[38] Cosmic Radiation Laboratory, Institute of Physical and Chemical Research (RIKEN), Wako, Saitama 351-0198, Japan
[39] Centre d'Étude Spatiale des Rayonnements, CNRS/UPS, BP 44346, F-30128 Toulouse Cedex 4, France
[40] Istituto Nazionale di Fisica Nucleare, Sezione di Roma "Tor Vergata," I-00133 Roma, Italy
[41] Department of Physics and Astronomy, University of Denver, Denver, CO 80208, USA

[42] Department of Physics, Graduate School of Science, University of Tokyo, 7-3-1 Hongo, Bunkyo-ku, Tokyo 113-0033, Japan
[43] Max-Planck Institut für extraterrestrische Physik, 85748 Garching, Germany
[44] Santa Cruz Institute for Particle Physics, Department of Physics and Department of Astronomy and Astrophysics, University of California at Santa Cruz, Santa Cruz, CA 95064, USA
[45] Institut für Astro-und Teilchenphysik and Institut für Theoretische Physik, Leopold-Franzens-Universität Innsbruck, A-6020 Innsbruck, Austria
[46] NYCB Real-Time Computing Inc., Lattingtown, NY 11560-1025, USA
[47] Department of Chemistry and Physics, Purdue University Calumet, Hammond, IN 46323-2094, USA
[48] Institució Catalana de Recerca i Estudis Avançats (ICREA), Barcelona, Spain
[49] Consorzio Interuniversitario per la Fisica Spaziale (CIFS), I-10133 Torino, Italy
[50] Dipartimento di Fisica, Università di Roma "Tor Vergata," I-00133 Roma, Italy
[51] School of Pure and Applied Natural Sciences, University of Kalmar, SE-391 82 Kalmar, Sweden
Received 2009 October 18; accepted 2009 December 18; published 2010 January 15

ABSTRACT

We present the analysis of the interstellar γ-ray emission measured by the *Fermi* Large Area Telescope toward a region in the second Galactic quadrant at $100^\circ \leqslant l \leqslant 145^\circ$ and $-15^\circ \leqslant b \leqslant +30^\circ$. This region encompasses the prominent Gould Belt clouds of Cassiopeia, Cepheus, and the Polaris flare, as well as atomic and molecular complexes at larger distances, like that associated with NGC 7538 in the Perseus arm. The good kinematic separation in velocity between the local, Perseus, and outer arms, and the presence of massive complexes in each of them, make this region well suited to probe cosmic rays (CRs) and the interstellar medium beyond the solar circle. The γ-ray emissivity spectrum of the gas in the Gould Belt is consistent with expectations based on the locally measured CR spectra. The γ-ray emissivity decreases from the Gould Belt to the Perseus arm, but the measured gradient is flatter than expectations for CR sources peaking in the inner Galaxy as suggested by pulsars. The $X_{\rm CO} = N({\rm H}_2)/W_{\rm CO}$ conversion factor is found to increase from $(0.87 \pm 0.05) \times 10^{20}$ cm^{-2} (K km s^{-1})$^{-1}$ in the Gould Belt to $(1.9 \pm 0.2) \times 10^{20}$ cm^{-2} (K km s^{-1})$^{-1}$ in the Perseus arm. We derive masses for the molecular clouds under study. Dark gas, not properly traced by radio and microwave surveys, is detected in the Gould Belt through a correlated excess of dust and γ-ray emission: its mass amounts to $\sim$50% of the CO-traced mass.

Key words: cosmic rays – gamma rays: diffuse background – ISM: clouds

Online-only material: color figures

1. INTRODUCTION

Galactic interstellar γ-ray emission is produced through the interactions of high-energy cosmic rays (CRs) with the gas in the interstellar medium (ISM; via pion production and Bremsstrahlung) and with the interstellar radiation field (via inverse Compton, IC, scattering). Thus, since early studies with the COS-B satellite, diffuse γ rays were recognized to be a tracer of the CR densities and of ISM column densities in the Galaxy (Lebrun et al. 1983; Strong et al. 1988; Bloemen 1989).

The interpretation of the observed emission is often based on two radio tracers of the interstellar gas: the 21 cm line of the hyperfine transition of atomic hydrogen (H I) is used to derive its column density N(H I); the 2.6 mm line of the rotational transition $J = 1 \rightarrow 0$ of CO is used to trace the molecular gas. The molecular phase of the ISM is composed mainly of H_2 which cannot be traced directly in its cold phase. It has long been verified, primarily using virial mass estimates, that the brightness temperature of CO integrated over velocity, $W_{\rm CO}$, roughly scales with the total molecular mass in the emitting region (see, e.g., Solomon & Barret 1991). The conversion factor that transforms $W_{\rm CO}$ into H_2 column density is known as $X_{\rm CO} = N({\rm H}_2)/W_{\rm CO}$ (Lebrun et al. 1983).

The $X_{\rm CO}$ conversion factor has often been assumed to be uniform across the Galaxy. We now have evidence, however, that it should increase in the outer Galaxy: from virial masses (Digel et al. 1990), from COBE/DIRBE studies (Sodroski et al. 1995, 1997), and from the measurement of the Galactic metallicity gradient (Israel 1997, 2000). A precise estimate of the $X_{\rm CO}$ gradient is necessary to measure the masses of distant H_2 clouds, but it also impacts the derivation of the distribution of CR sources from γ-ray observations (Strong et al. 2004b).

For many years, supernova remnants (SNRs) have been considered the best candidates as CR sources. We have recently detected possible signatures of hadron acceleration in SNRs thanks to γ-ray observations in the TeV (Albert et al. 2007; Aharonian et al. 2008; Acciari et al. 2009) and GeV domain (Abdo et al. 2009d). However, the origin of Galactic CRs is still mysterious and, on the other hand, the distribution of SNRs in the Galaxy is very poorly determined (Case & Bhattacharya 1998), leading to large uncertainties in the models of diffuse γ-ray emission. The γ-ray emissivity gradient of the diffuse H I gas can provide useful constraints on the CR-density distribution.

Since the Doppler shift of the radio lines allows kinematic separation of different structures along a line of sight, it is possible to constrain the γ-ray emissivities and the subsequent $X_{\rm CO}$ ratios in specific Galactic regions. The performance of the previous γ-ray telescopes did not allow very precise measurements beyond the solar circle (Digel et al. 1996, 2001). The situation has recently been improved with the successful launch of the *Fermi Gamma-ray Space Telescope* on 2008 June 11. The Large Area Telescope (LAT) on board the *Fermi* mission (Atwood et al. 2009) has a sensitivity more than an order of magnitude greater than the previous instrument EGRET on board the *Compton Gamma-ray Observatory* and a superior angular resolution.

We present here the analysis of the interstellar γ radiation measured by the *Fermi* LAT in a selected region of the second Galactic quadrant, at $100^\circ \leqslant l \leqslant 145^\circ$, $-15^\circ \leqslant b \leqslant +30^\circ$, during the first 11 months of the science phase of the mission. The region was chosen because here the velocity gradient with Galactocentric distance is very steep, resulting in good

[52] Royal Swedish Academy of Sciences Research Fellow, funded by a grant from the K. A. Wallenberg Foundation.

kinematic separation which allows four different regions to be defined along each line of sight: the nearby Gould Belt, the main part of the local arm, and the more distant Perseus and outer spiral arms. Among the most conspicuous clouds, one finds Cassiopeia, the Cepheus, and Polaris flares in the Gould Belt (Perrot & Grenier 2003; Heithausen & Thaddeus 1990; Grenier et al. 1989), the most massive molecular complex in the Perseus arm associated with NGC 7538 and Cas A (Ungerechts et al. 2000), and the off-plane molecular cloud in the Perseus arm associated with NGC 281 (Sato et al. 2007). These prominent cloud complexes are well suited to probe CRs and the ISM. The motivations of this work are both to provide improved constraints for diffuse emission models to be used in the detection and analysis of LAT sources and to reach a better comprehension of the physical phenomena related with diffuse γ-ray emission in the outer Galaxy.

2. INTERSTELLAR GAS

Here, we describe the preparation of the maps tracing the column densities of the different components of the ISM, used in the following section to analyze LAT data.

2.1. Radio and Microwave Data

2.1.1. H I

Column densities $N(\mathrm{H\,I})$ of atomic hydrogen have been derived using the LAB H I survey by Kalberla et al. (2005). The LSR velocity[53] coverage spans from -450 km s^{-1} to +400 km s^{-1} with a resolution of 1.3 km s^{-1}. The survey angular resolution is about 0.°6. Owing to the strong absorption against the radio continuum emission of the Cas A SNR, the H I column densities within 0.°5 from its position were determined by linear interpolation of the adjacent lines.

The column densities have been derived by applying an optical depth correction for a uniform spin temperature T_S = 125 K, in order to directly compare our results with previous studies (like Digel et al. 1996). There is not general agreement in the literature about the values of the spin temperature in the atomic phase of the ISM. From observations of the 21 cm line of H I seen in absorption, Mohan et al. (2004a, 2004b) derived for our region values of T_S varying from $\sim$50 K to $\gtrsim$ 2000 K, with a mean value $\sim$125 K. Recently, Dickey et al. (2009), on the basis of other H I absorption surveys, reported a mean value in the second Galactic quadrant T_S = 250 K, almost constant with Galactocentric radius. The maximum difference between the values of $N(\mathrm{H\,I})$ obtained with T_S = 125 K and those obtained in the optically thin approximation (corresponding to the lower possible amount of gas or to the limit of very high spin temperature) is 30%–40%, whereas the maximum difference between T_S = 250 K and optically thin approximation is 10%–15%. The optical depth correction is nonlinear, so assessing the effects of the approximation is not trivial: in particular we note that the uncertainties are larger where the gas density is higher and that assuming lower values for T_S, we obtain structured excesses in modeled diffuse γ-ray intensities following the shape of the clouds.

The systematic errors are even larger in the Galactic plane where self absorption phenomena become important, especially in the Perseus arm where the subsequent uncertainties of derived $N(\mathrm{H\,I})$ can reach 30% (Gibson et al. 2005).

[53] Local standard of rest velocity, i.e., the velocity in a reference frame following the motion of the solar system.

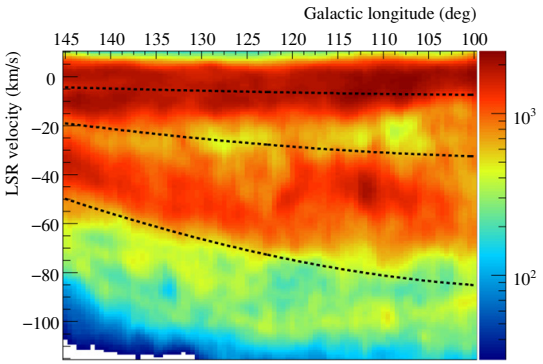

Figure 1. H I longitude–velocity diagram obtained by integrating the brightness temperature in Kalberla et al. (2005) for $|b| < 10°$. The color scale is logarithmic in units of deg K. The three curves bound the preliminary Galactocentric rings used for analysis. At R = 8.8 kpc, R = 10 kpc, and R = 14 kpc (from top to bottom) they roughly separate the Gould Belt, local arm, Perseus, and outer arm. The separation between the Gould Belt and main part of the local arm is hard to distinguish in this diagram.

(A color version of this figure is available in the online journal.)

2.1.2. CO

Intensities W_{CO} of the 2.6 mm line of CO have been derived from the composite survey of Dame et al. (2001), with sampling every 0.°125 near the Galactic plane and in the Gould Belt clouds, supplemented with observations at 0.°25 sampling for high-latitude clouds (>5°), covering in particular the region of NGC 281.

Lines of sight not surveyed in CO were restored by linear interpolation of adjacent directions where possible; otherwise they were assumed to be free of significant CO emission. CO data have been filtered with the moment-masking technique in order to reduce the noise while keeping the resolution of the original data and retaining the edges of the CO clouds (see, e.g., Dame et al. 2001, Section 2.3). Preserving the faint CO edges is important to help decrease the degree of spatial correlation that naturally exists between the $N(\mathrm{H\,I})$ and W_{CO} maps of a given cloud complex because of the ISM multi-phase structure.

2.2. Kinematic Separation of the Galactic Structures

Our aim is to separately determine the γ-ray emission from the different Galactic structures present along the line of sight in the second quadrant:

1. the very nearby complexes in the Gould Belt, within $\sim$300 pc from the solar system;
2. the main part of the local arm, typically $\sim$1 kpc away;
3. the Perseus arm, 2.5–4 kpc away;
4. the outer arm and beyond.

The separation between the Gould Belt and local-arm components is important to probe for a possible change in CR densities between the quiescent nearby clouds of Cassiopeia and Cepheus that produce few low-mass stars, and the more active regions of the local arm which shelter several OB associations (Grenier et al. 1989).

The good kinematic separation of the interstellar gas in this part of the sky is illustrated in Figure 1. The separation of the structures along the line of sight was achieved through a three-step procedure:

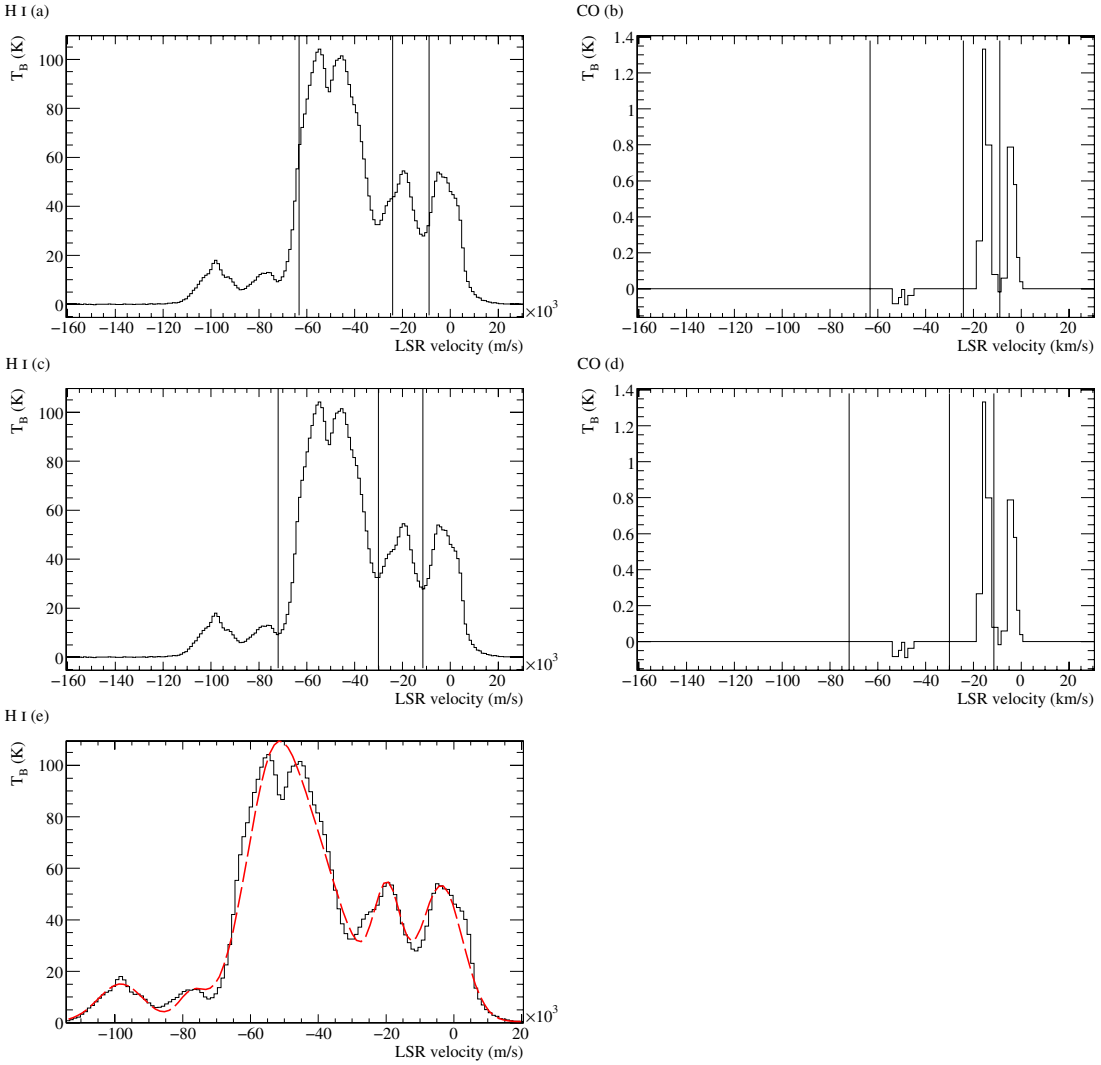

Figure 2. Example of the separation procedure described in Section 2.2 for the direction $l = 133°$, $b = 0°$. Each plot shows the brightness temperature T_B for H I or CO as a function of LSR velocity. Vertical lines correspond to the boundaries Gould Belt–local arm, local arm–Perseus arm, Perseus arm–outer arm (from right to left). The three rows correspond to (1) preliminary ring boundaries (panels (a) & (b)), (2) "physical" boundaries (panels (c) & (d)), and (3) Gaussian fitting of the H I line (panel (e)).

(A color version of this figure is available in the online journal.)

1. preliminary separation based on Galactocentric rings;
2. transformation of the ring-velocity boundaries into "physical" boundaries based on the (l, b, v) coherence of clouds, and production of $N(\mathrm{H\,I})$ and W_{CO} maps;
3. correction of the $N(\mathrm{H\,I})$ maps for the spill-over between adjacent regions.

The three steps are described in detail below. In Figure 2, the procedure is illustrated for an example direction at $l = 133°$, $b = 0°$.

The preparation of the gas maps started from preliminary velocity boundaries given in terms of Galactocentric rings that roughly encompass the Gould Belt for $R < 8.8$ kpc, the main part of the local arm at 8.8 kpc $< R <$ 10 kpc, the Perseus arm at 10 kpc $< R <$ 14 kpc, and the outer arm for $R >$ 14 kpc. Following IAU recommendations, we adopted a flat rotation curve with $R_\odot = 8.5$ kpc and a rotation velocity of 220 km s^{-1} at the solar circle. The confusion that is apparent in the longitude–velocity (l, v) diagram of Figure 1 between the Gould Belt and local-arm components results from the integration over latitude and is much reduced in the actual (l, b, v) cube which is used to construct the maps. The presence of two different components is evident in the example direction of Figure 2: the first component peaks at $v \sim 0$ km s^{-1} (Gould Belt), the second one at $v \sim -15$ km s^{-1} (local arm).

Starting from this preliminary separation, the ring-velocity boundaries were adjusted for each line of sight to better separate structures on the basis of their coherence in the (l, b, v) phase space. For each line of sight, every boundary was moved to the nearest minimum in the H I spectrum, or, if a minimum was not found, to the nearest saddle. The shifts are typically of the order of 1–10 km s^{-1} (see Figures 2(c) and (d)). The adjusted boundaries were used to calculate N(H I) and $W_{\rm CO}$ in each region.

The broad H I clouds can easily spill-over from one velocity interval into the next. To correct for this cross-contamination between adjacent intervals, for each line of sight the H I spectrum has been fitted by a combination of Gaussians (see Figure 2(e)). The overlap estimated from the fit was used to correct the column density N(H I) calculated in a specific interval from the spill-over from the adjacent regions. The correction on N(H I) is typically of the order of 1%–10%, although it can reach 20%–30% in regions corresponding to the frontier between clouds in the Gould Belt and in the main part of the local arm.

This separation scheme provides more accurate estimates of the actual gas mass in a specific region and helps with separating structures. The resulting maps are shown in Figure 3. They exhibit a low level of spatial degeneracy between the cloud complexes found in the four regions along these directions. Hence, we can model the observed γ-ray flux as a combination of contributions coming from CR interactions in the different regions. The correlation between the H I and CO phases in each region is unavoidable, but not tight enough to hamper the separation between the γ-ray emission from the two phases. No significant CO emission is found in the outer-arm region, so the corresponding map was removed from the analysis.

2.3. Interstellar Reddening

An excess of γ rays (observed by EGRET) correlated with an excess of dust thermal emission was found over the N(H I) and $W_{\rm CO}$ column-density maps in all the nearby Gould Belt clouds by Grenier et al. (2005). Therefore, they reported a considerable amount of "dark" gas, i.e., neutral gas not properly traced by H I and CO, at the interface between the two radio-traced phases. The chemical state of the additional gas has not been determined yet, leaving room for H_2 poorly mixed with CO or to H I, overlooked, e.g., because of incorrect assumptions about the spin temperature for optical depth corrections or H I self absorption (see Section 2.1.1).

Following the method proposed by Grenier et al. (2005), we have prepared a map to account for the additional gas. The map is derived from the $E(B-V)$ reddening map of Schlegel et al. (1998), which provides an estimate of the total dust column densities across the sky. Point sources (corresponding to *IRAS* point sources) were removed and the corresponding pixels were set to the average value of the adjacent directions. In order to subtract the dust components correlated with N(H I) and $W_{\rm CO}$, the reddening map was fitted with a linear combination of the same set of N(H I) and $W_{\rm CO}$ maps for the Gould Belt and local, Perseus, and outer-arm regions described above. A detailed discussion of the results of the fit goes beyond the scope of the present work, so it is deferred to another paper (A. A. Abdo et al. 2010, in preparation), which will address the results over several interstellar complexes in the Gould Belt and will compare them with γ-ray measurements by the LAT.

The resulting $E(B-V)_{\rm res}$ residual map, obtained by subtracting from the $E(B-V)$ map the best-fit linear combination of our set of N(H I) and $W_{\rm CO}$ maps, is shown in Figure 4. The residuals typically range from -1 to +1 magnitude. Unlike in Grenier et al. (2005), both positive and negative residuals have been considered in the analysis of the γ-ray data. Residuals hint at limitations in the gas radio tracers as well as in the $E(B-V)$ map. Positive residuals can correspond to a local increase in the dust-to-gas ratio and/or to the presence of additional gas not properly accounted for in the N(H I) and $W_{\rm CO}$ maps. The latter explanation is supported by the significant correlation we will find between the $E(B-V)_{\rm res}$ map and the LAT γ-ray data (see Section 4.2.2). Figure 4 shows that at $|b| > 5^\circ$ the $E(B-V)_{\rm res}$ map is dominated by positive residuals forming structured envelopes around the CO clouds. Small negative residuals are systematically seen toward the CO cores. They may be due to a decrease in dust temperature in the denser, well shielded, parts of the molecular complexes, or to local variations of the dust-to-gas ratio. Further comparison with dust extinction tracers is needed to investigate this effect. Positive and negative residuals appear at low latitude, but, because of the pile-up of dust clouds with different temperatures along the line of sight, the temperature correction, applied by Schlegel et al. (1998) to the thermal emission to produce the $E(B-V)$ map, is not as valid near the plane as in well-resolved local clouds off the plane, in particular toward bright star-forming regions. These effects may cause the clusters of negative residuals at $|b| < 5^\circ$. We note that the positive residuals along the plane are not well correlated with the amount of self-absorbed H I found in the second quadrant (Gibson et al. 2005). The most conspicuous self-absorbed H I cloud in fact corresponds to the negative residuals seen at $130^\circ < l < 140^\circ$.

By construction, the $E(B-V)_{\rm res}$ map compensates for the limitations of the radio tracers, both by revealing non-emitting gas and by correcting the approximations applied to handle the radiative transfer of the radio lines. In particular the $E(B-V)_{\rm res}$ map depends on the optical depth correction applied to the N(H I) maps. We note that different choices of the H I spin temperature, from the optically thin case down to 250 and 125 K, change the $E(B-V)$ residuals by up to 0.2–0.3 mag on the plane and 0.1 mag at $|b| > 5^\circ$. Off the plane, the shape of the large structures of positive residuals around the Gould Belt clouds hardly changes.

The strong correlation between $E(B-V)$ residuals and γ-ray data, which will be shown in Section 4.2.2, proves that the interstellar reddening is in many directions a better tracer of the total gas column densities than the combination of H I and CO. Therefore, we will use the $E(B-V)_{\rm res}$ map to correct the standard radio and microwave tracers, very suitable for the aims of this work since, unlike reddening, they carry distance information.

3. GAMMA-RAY ANALYSIS

3.1. LAT Data

The *Fermi* LAT is a pair-tracking telescope (Atwood et al. 2009), detecting photons from ~20 MeV to more than 300 GeV. The tracker has 18 (x, y) layers of silicon microstrip detectors interleaved with tungsten foils to promote the conversion of γ rays into electron–positron pairs (12 thin foils of 0.03 radiation lengths in the front section plus 4 thick foils of 0.18 radiation lengths in the back section; the last two layers have no conversion foils). The tracker is followed by a segmented CsI calorimeter to determine the γ-ray energy. The whole system is surrounded by a scintillator shield to discriminate the charged CR background. The instrument design and the analysis result

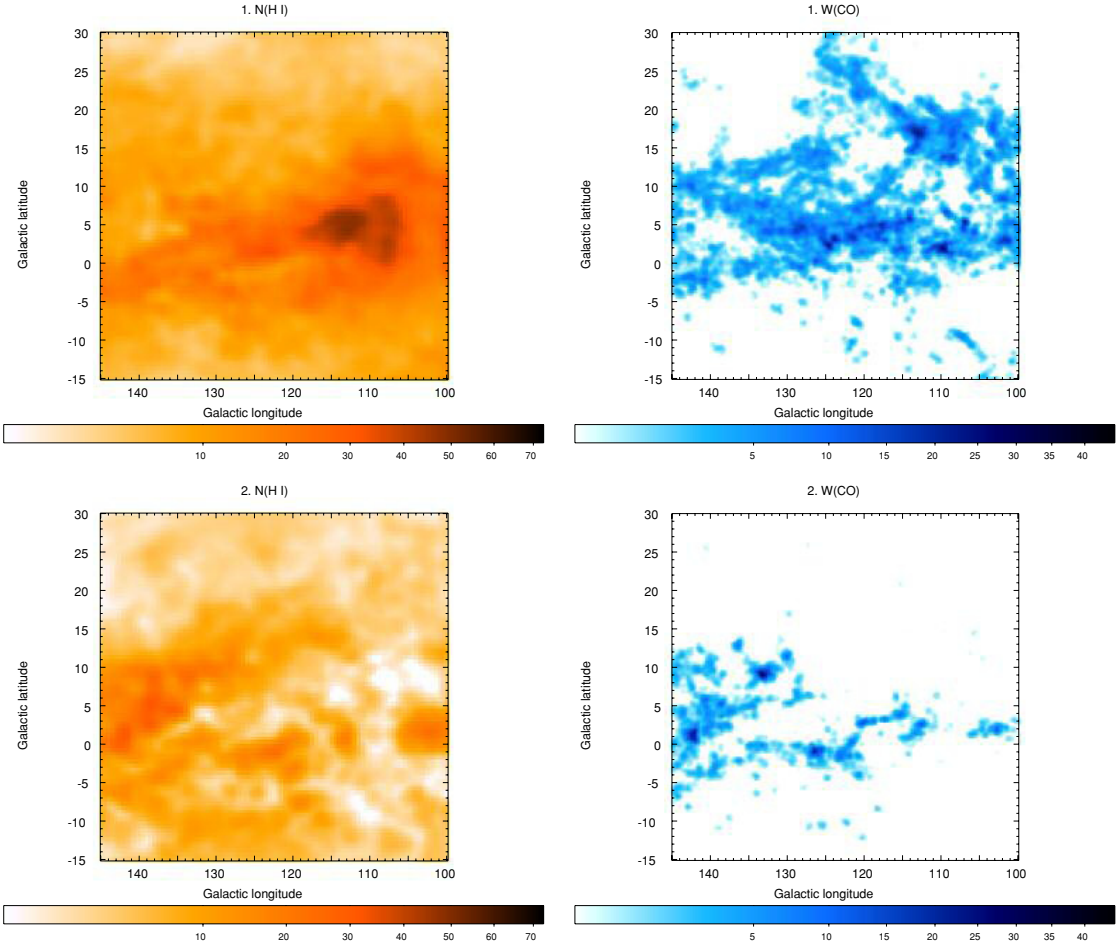

Figure 3. Maps of $N(\mathrm{H\,I})$ (units of 10^{20} atoms cm^{-2}) and W_{CO} (units of K km s^{-1}). Regions: (1) Gould Belt, (2) local arm, (3) Perseus arm, and (4) outer arm. The maps have been smoothed for display with a Gaussian with $\sigma = 1^{\circ}$. Data sources are described in the text.
(A color version of this figure is available in the online journal.)

in a peak effective area of ∼8000 cm^2 (∼6 times greater than EGRET), a field of view of ∼2.4 sr (∼5 times greater than EGRET), and a superior single photon angular resolution (for front converting photons, the 68% containment angle at 1 GeV reaches ∼0.°6 with respect to ∼1.°7 for EGRET).

Data were obtained during the period 2008 August 4–2009 July 4. The *Fermi* observatory was operated in scanning sky survey mode, rocking 35° north and south of the zenith on alternate orbits, apart from calibration runs that are excluded from the analysis. We used the data set prepared for the construction of the First Year Catalog of LAT sources (A. A. Abdo et al. 2010, in preparation), excluding brief time intervals corresponding to bright γ-ray bursts. It uses the *Diffuse* event selection, which has the least residual CR background contamination (Atwood et al. 2009). We also selected events on the basis of the measured zenith angle to limit the contamination from interactions of CRs with the upper atmosphere of the Earth. Owing to these interactions, the limb of the Earth is a very bright γ-ray source, seen at a zenith angle of ∼113° at the 565 km nearly circular orbit of *Fermi*. Since our region is close to the north celestial pole it is often observed at large rocking angles. In order to reduce the Earth albedo contamination, we accept for analysis here only events seen at a zenith angle <100°. The exposure is only marginally affected (because the detection efficiency dramatically decreases at large inclination angles), but the background rate is significantly reduced.

3.2. Model for Analysis

The analysis scheme used since the COS-B era (Lebrun et al. 1983; Strong et al. 1988; Digel et al. 1996) is based on a very simple transport model. Assuming that the ISM is transparent to γ rays, that the characteristic diffusion lengths for CR electrons and protons exceed the dimensions of cloud complexes, and that CRs penetrate clouds uniformly to their cores, the γ-ray intensity I (cm^{-2} s^{-1} sr^{-1}) in a direction (l, b) can be modeled to first order as a linear combination of contributions

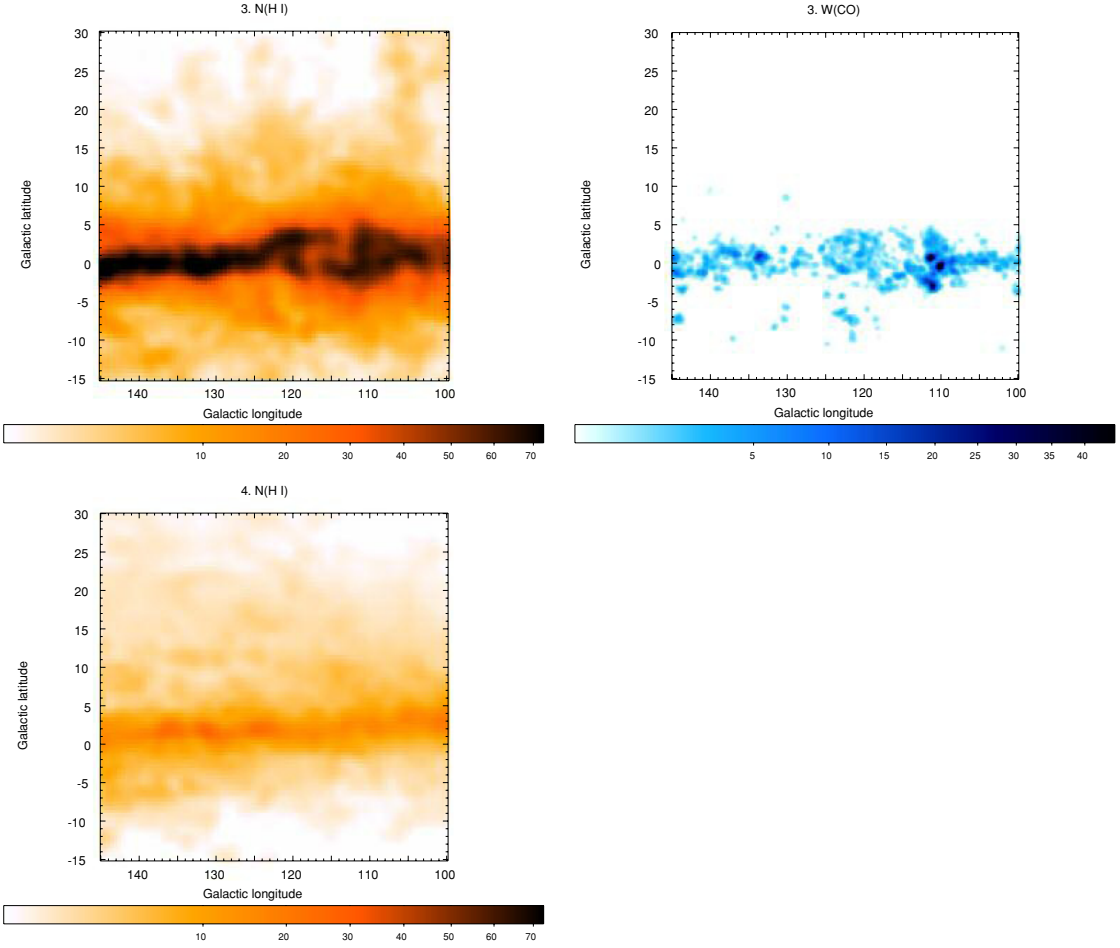

Figure 3. (Continued)

coming from CR interactions with the different gas phases in the various regions along the line of sight. We add the contribution from point-like sources and an isotropic intensity term. Several processes are expected to contribute to the latter, notably the extragalactic γ-ray background and the residual instrumental background from misclassified interactions of charged CRs in the LAT. The IC emission is also expected to be rather uniform across this small region of the sky. We used the current best models of IC emission to verify that it is statistically not distinguishable from an isotropic background over the small region of interest, at large angular distance from the inner Galaxy (see Section 3.4). The present analysis does not aim to provide meaningful results for the extragalactic background and the IC emission which will be addressed in forthcoming publications (Abdo et al. 2010, A. A. Abdo et al. 2010, in preparation).

In the absence of suitable tracers for the diffuse ionized gas (primarily H II), the derived γ-ray emissivities for neutral gas will be slightly overestimated. However, the ionized gas is contributing to $\sim$10% of the total mass and, because of its large scale height of $\sim$1 kpc above the plane (Cordes & Lazio 2002), part of its γ-ray emission will be overtaken by the isotropic term in the fit to the LAT data. So, the bias on the neutral gas emissivities should be small.

Therefore, the γ-ray intensity I, integrated in a given energy band, is modeled by Equation (1).

$$I(l,b) = \sum_{\iota=1}^{4} \left[q_{\mathrm{H\,I},\iota} \cdot N(\mathrm{H\,I})(\mathrm{l,\,b})_\iota + \mathrm{q}_{\mathrm{CO},\iota} \cdot \mathrm{W}_{\mathrm{CO}}(\mathrm{l,\,b})_\iota \right] + q_{\mathrm{EBV}} \cdot E(B-V)_{\mathrm{res}}(l,b) + I_{\mathrm{iso}} + \sum_J S_J \cdot \delta^{(2)}(l-l_J, b-b_J). \quad (1)$$

The sum over ι represents the combination of the four Galactic regions. The free parameters are the emissivities of H I gas, $q_{\mathrm{H\,I},\iota}$ ($\mathrm{s^{-1}\ sr^{-1}}$), per unit of W_{CO} intensity, $q_{\mathrm{CO},\iota}$ ($\mathrm{cm^{-2}\ s^{-1}\ sr^{-1}}$ ($\mathrm{K\ km\ s^{-1}}$)$^{-1}$), and per unit of $E(B-V)$ residuals, q_{EBV} ($\mathrm{cm^{-2}\ s^{-1}\ sr^{-1}\ mag^{-1}}$). I_{iso} ($\mathrm{cm^{-2}\ s^{-1}\ sr^{-1}}$) is the isotropic background intensity. The contribution from point sources is

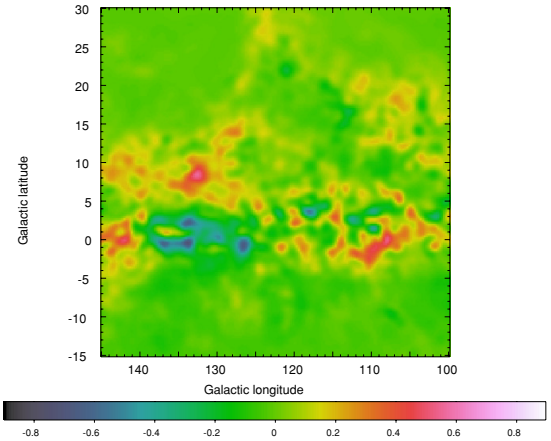

Figure 4. $E(B-V)_{\rm res}$ map: map of the reddening residuals obtained after subtraction of the parts linearly correlated with the combination of N(H I) column densities and $W_{\rm CO}$ intensities found in the four regions along the line of sight (Gould Belt, local, Perseus, and outer arms). The positive residuals surrounding CO clouds off the plane outline the potential dark-gas envelopes of the Gould Belt clouds. The map has been smoothed for display with a Gaussian with $\sigma = 1^\circ$.

(A color version of this figure is available in the online journal.)

represented by the sum over j, where S_j is the integrated flux (cm^{-2} s^{-1}) of the source lying at the position (l_j, b_j).

3.3. Analysis Procedure

3.3.1. Method

We used the standard LAT analysis environment provided by the *Fermi Science Tools*.[54] The γ-ray statistics are large enough to model the spectral shape of each component as a power law in relatively narrow energy bands. This assumption, together with the iterative procedure described below in Section 3.3.2, allows the exposures and the convolution with the energy-dependent point-spread function (PSF) to be computed without forcing an a priori spectral index. The *Science Tools* provide a full convolution of the maps with the energy-dependent PSF. The *Science Tools* are also very flexible in the description of point sources (number, location, spectra). We used the `P6_V3` post launch instrument response functions (IRFs), which take into account the loss of detection efficiency due to pile-up and accidental coincidence effects in the LAT (Rando et al. 2009).

LAT data have been analyzed using a binned maximum-likelihood procedure with Poisson statistics, on a spatial grid with 0.°5 spacing in Cartesian projection. The higher energy range we have investigated starts at a few GeV, where the 68% containment angle is ∼0.°5 for events converting in the front section of the tracker (about a factor 2 larger for back converting events), so we cannot resolve details smaller than this in the γ-ray maps. This resolution is commensurate with that of the H I and $E(B-V)$ maps.

The analysis was performed for five contiguous energy bands: 200 MeV–400 MeV, 400 MeV–600 MeV, 600 MeV–1 GeV, 1 GeV–2 GeV, and 2 GeV–10 GeV. The energy bands were chosen wide enough to obtain stable results for the fit parameters, because large statistical fluctuations might hamper the separation of the different maps. Below 200 MeV the broad PSF does not allow an effective separation of the different maps. We are confident that between 0.2 and 10 GeV the interstellar γ-ray emission from the gas dominates over the instrumental foregrounds. The count maps in the five energy bands are shown in Figure 5.

3.3.2. Point Sources

The inclusion of sources in the analysis model is a non-trivial task because the likelihood maximization procedure (based on the optimization engine `Minuit2`[55]) is stable up to a few tens of free parameters. The sources have thus been added following an iterative procedure.

The sources were taken from the 11 month source list, which will be the basis for the First Year Catalog of LAT sources in preparation (A. A. Abdo et al. 2010, in preparation). The sources were added following the detection significance (TS) in the 11 month source list.[56] The sources were added as point-like sources keeping their positions at those given in the list while letting their power-law spectra to vary independently in each energy band. No further attempts were made in this analysis to improve the spectral modeling or to account for possible extension.

The inclusion of the sources went through the following steps, where the parameters of the diffuse emission model were always let free.

1. We started with no point sources in the model.
2. We added nine sources detected with TS > 600 (hereafter bright sources). They were added to the sky model 3 at a time in order of decreasing TS, freezing at each step the previous source spectra and fitting the last three, while the diffuse parameters were always let free. Among bright sources, for the six sources lying in the region under study, we let their fluxes and spectral indexes free; for three sources lying just outside (<5°) the region boundaries, we fixed their parameters at the values determined in the 11 month source list. These bright sources were already reported in the LAT Bright Source List (Abdo et al. 2009b): two of them are firmly identified as pulsars (0FGL J0007.4+7303 or LAT PSR J0007+7303, and 0FGL J2229.0+6114 or PSR J2229+6114), one as a γ-ray binary (0FGL J0240.3+6113 or LSI+61 303), and the others are associated with blazars.
3. We then added 52 more sources in the 11 month source list within the region boundaries with TS between 600 and ≃ 25 (out of them 22 where detected with TS > 100); they were added in several groups of six or five sources, with a procedure analogous to that used to handle bright sources, but only their integrated fluxes were allowed to be free, whereas the spectral indexes were fixed at the values in the source list.
4. Finally, the analysis was repeated with all the sources, letting free only the parameters of the diffuse model and of the bright sources.

The iterative procedure allows verification that only the bright sources can affect the diffuse parameters: the latter do not significantly change when less significant sources (TS < 600) are added to the model. This does not apply to $I_{\rm iso}$ and $q_{\rm H\,I,\,4}$: we

[54] http://fermi.gsfc.nasa.gov/ssc/data/analysis/documentation/Cicerone/

[55] http://wwwasdoc.web.cern.ch/wwwasdoc/minuit/minmain.html

[56] The test statistic, TS, is defined as TS = $2(\ln \mathcal{L} - \ln \mathcal{L}_0)$, where $\mathcal{L}$ and $\mathcal{L}_0$ are the maximum-likelihood values reached with and without the source, respectively.

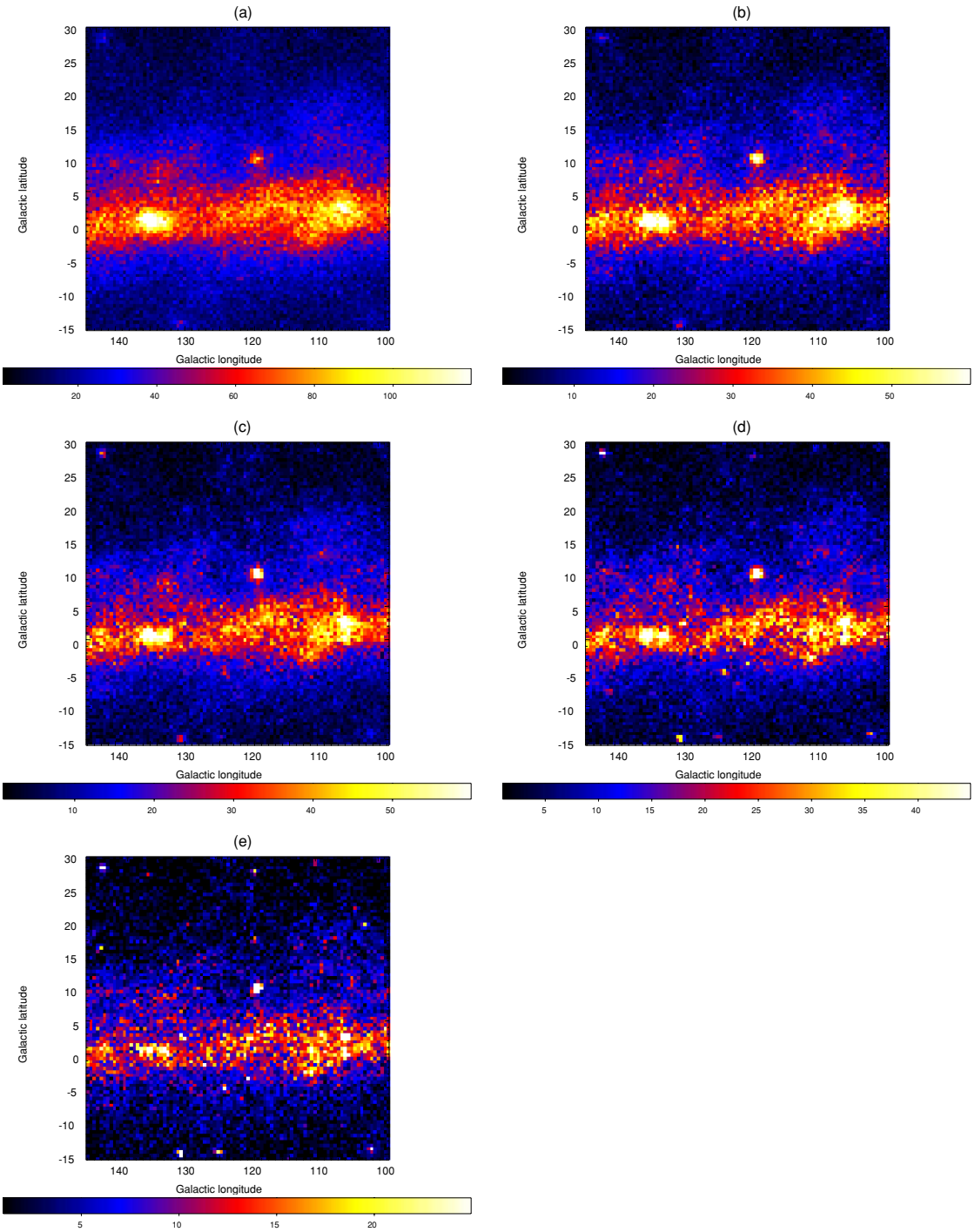

Figure 5. Gamma-ray count maps in the five energy bands: (a) 200–400 MeV, (b) 400–600 MeV, (c) 600 MeV–1 GeV, (d) 1–2 GeV, and (e) 2–10 GeV. (A color version of this figure is available in the online journal.)

note that their values keep decreasing as we add new sources down to TS $\sim$ 25. We argue that the isotropic intensity generally absorbs point sources off the plane that are not included in the analysis; as said before we are not trying to give a physical interpretation of $I_{\rm iso}$. On the other hand, given the low linear resolution in distant clouds of the outer arm and the subsequent lack of pronounced features in the map (see Figure 3), point sources at very low latitude ($|b| \lesssim 3^\circ$) can strongly bias the value of the corresponding H I emissivity, $q_{\rm H\,I,\,4}$, as separating them from the clumpy ISM emission near the plane in 0.°5 maps is difficult. Therefore, we consider this parameter only as an upper limit to the real gas emissivity in the outer arm.

3.4. Fit Results

The quality of the final fits is illustrated in the residual maps of Figure 6. The residuals, i.e., observed counts minus model-predicted counts, are expressed in standard deviation units (square root of model-predicted counts). The maps show no excesses below -4σ or above $+7\sigma$.

The best-fit parameters obtained in the five energy bands are given in Table 1, where the uncertainties correspond only to statistical errors. We have also evaluated the systematic errors due to the uncertainties on the event selection efficiency. From the comparison between Monte Carlo simulations and real observations of the Vela pulsar, they are evaluated to be 10% at 100 MeV, 5% at 500 MeV, and 20% at 10 GeV, scaling linearly with the logarithm of energy between these values. These uncertainties were parameterized into two sets of IRFs encompassing the most extreme scenarios. The last step of the analysis has been repeated using these two IRF sets and the results are assumed to bracket the systematic errors due to the event selection efficiency (shown as shaded gray areas in the following figures). Only the last step was considered, because we previously verified that only bright sources impact the parameters of the diffuse emission model.

We also verified the impact of the isotropic approximation for the IC emission, repeating the last step of the analysis including a recent model based on the GALPROP CR propagation code (see, e.g., Strong & Moskalenko 1998; Strong et al. 2004a; Porter et al. 2008). The values obtained for the parameters of the diffuse emission model were compatible with the previous results, except for the isotropic intensity.

Other systematic uncertainties will be addressed in the discussion section.

4. DISCUSSION

4.1. Emissivity Per H I Atom and Cosmic-ray Spectra

4.1.1. Consistency with Other Measurements

In Figure 7, we report the emissivity spectra per H I atom measured in the Gould Belt, the main part of the local arm and the Perseus arm. The inclusion of the $E(B-V)_{\rm res}$ map in the fit does not have a strong impact on the emissivities of the broadly distributed H I gas, which decrease by less than 10% considering the interstellar reddening in analysis.

The results we obtained in the Gould Belt and local-arm regions are consistent below 1 GeV with the measurement by Digel et al. (1996), obtained from EGRET observations of the region of Cepheus and Polaris. Above 1 GeV LAT measurements are $\sim$40% lower than those by EGRET. We will see below in Section 4.1.3 that LAT measurements are consistent with the a priori expectations for the local H I emissivity: this result confirms that, as was already deduced from LAT observations of broader regions of the sky (Abdo et al. 2009e), LAT measurements are not consistent with the GeV excess seen by EGRET, which was noticed also as an excess above 1 GeV in the emissivity of nearby H I complexes, as discussed in Digel et al. (2001).

Our spectra of the emissivity per H I atom are consistent with the results of an independent analysis carried out on LAT data to determine the local H I emissivity in a midlatitude region of the third Galactic quadrant (Abdo et al. 2009c). The latter analysis investigated a different region of the sky, but encompassing H I complexes at $\lesssim$1 kpc from the solar system, mostly located in a segment of the local arm. If we compare the present results in the main part of the local arm with those by Abdo et al. (2009c) we have excellent agreement. Therefore, we have verified that CR proton densities smoothly vary on a few kpc scale around the solar system.

4.1.2. Physical Model

We further compare our results with the predictions by GALPROP, a physical model of CR propagation in the Galaxy (see, e.g., Strong & Moskalenko 1998; Strong et al. 2004a, 2007). GALPROP solves the propagation equation for all CR species, given a CR source distribution and boundary conditions. Current GALPROP models assume a Galactocentric source distribution derived from that of pulsars (Strong et al. 2004b). The distribution used by the model adopted for this work, called `54_71Xvarh7S`, is given by Equation (2),

$$f(R) \propto \left(\frac{R}{R_\odot}\right)^{\alpha} \exp\left[-\beta\left(\frac{R-R_\odot}{R_\odot}\right)\right], \qquad (2)$$

with $\alpha = 1.25$, $\beta = 3.56$, and $R_\odot = 8.5$ kpc. A truncation is applied at $R = 15$ kpc because we do not expect many CR sources in the outermost Galaxy. This choice of parameters results in a slightly flatter radial profile of CR densities than with the pulsar distribution.

The GALPROP model `54_71Xvarh7S` is tuned to reproduce the in situ measurements of CR spectra at the solar circle. The proton spectrum is derived from a compilation of direct measurements (Alcaraz et al. 2000; Sanuki et al. 2000; Shikaze et al. 2007). The model includes the CR electron spectrum recently measured by the LAT (Abdo et al. 2009a).

Once the propagation equation is solved, GALPROP computes the emissivity for stable secondaries, in particular γ rays. The electron Bremmstrahlung component is evaluated using the formalism by Koch & Motz (1959) as explained in Strong et al. (2000). The emissivity due to p–p interactions is evaluated using the inclusive cross sections as parameterized by Kamae et al. (2006). Following the method by Dermer (1986a, 1986b), the p–p emissivity is increased to account for interactions involving CR α particles and interstellar He nuclei. This method provides an effective enhancement with respect to pure p–p emissivities, often named the nuclear enhancement factor, of $\epsilon_{\rm N} \simeq 1.45$. More recent calculations by Mori (2009), however, report values as large as $\epsilon_{\rm N} \simeq 1.75$–2 due to different CR spectral formulae (Honda et al. 2004), different ISM abundances and the inclusion of heavier nuclei both in CRs and in the ISM. Further theoretical developments are required to better constrain $\epsilon_{\rm N}$, extending the predictions from γ rays to other relevant messengers like antiprotons (Adriani et al. 2009).

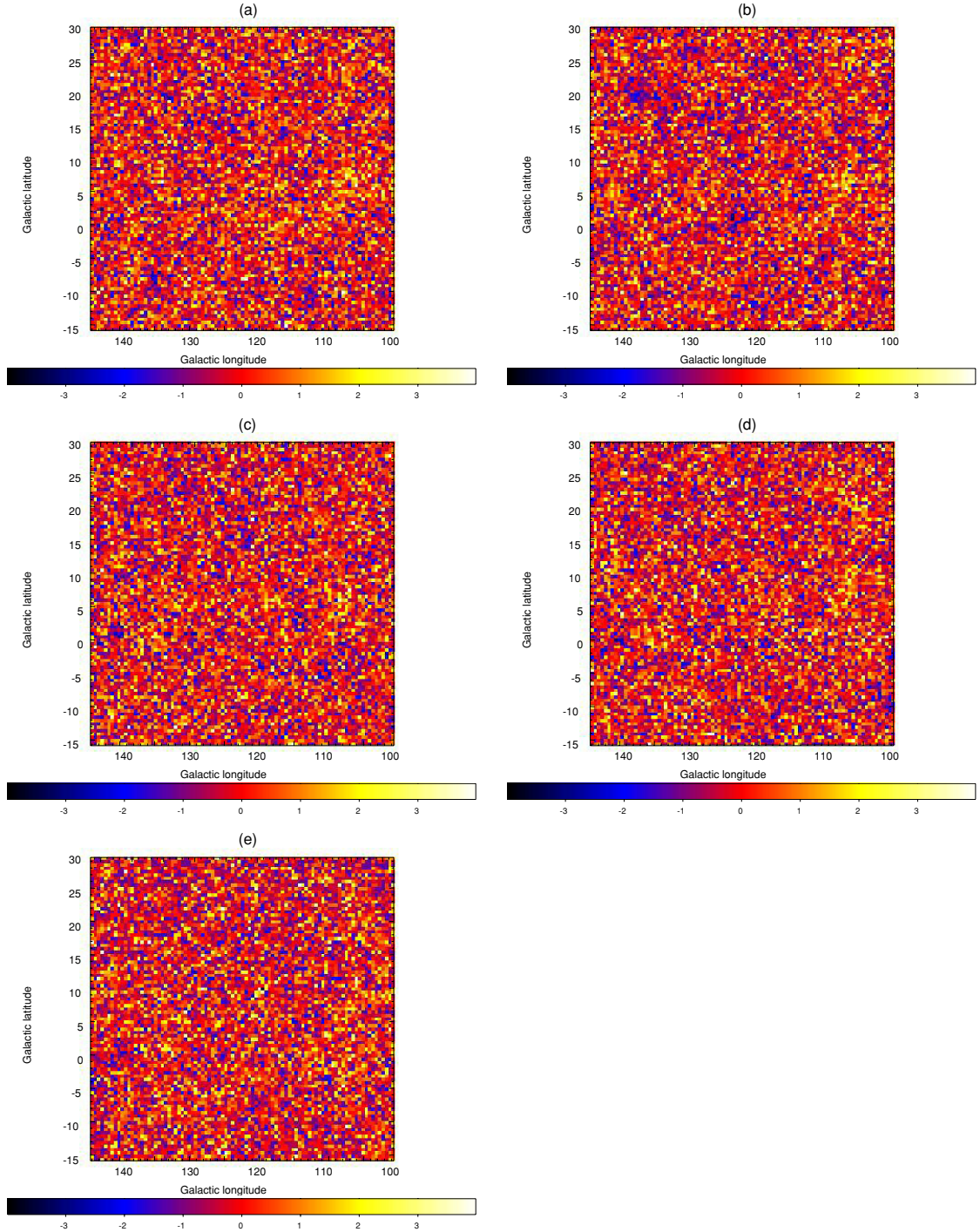

Figure 6. Gamma-ray residual maps in the same energy bands as in Figure 5. The residuals, i.e., observed counts minus model-predicted counts, are in units of the square root of the model-predicted counts (truncated between −4 and +4 for display).

(A color version of this figure is available in the online journal.)

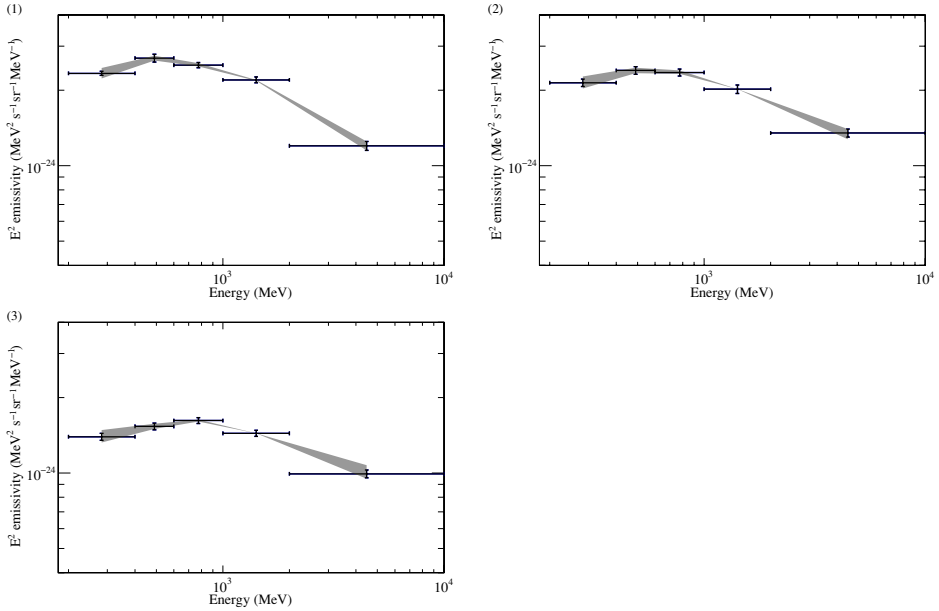

Figure 7. Emissivity spectra per H I atom as measured in the Gould Belt (1), local arm (2), and Perseus arm (3) clouds. Horizontal bars mark the energy bands, vertical bars show the statistical uncertainties on the measurement. The shaded areas represent the systematic errors due to the uncertainties on the event selection efficiency.

Table 1
Parameters of the Diffuse Emission Model Obtained from the Fit to LAT Data

Parameter [a,b]	0.2–0.4 GeV	0.4–0.6 GeV	0.6–1 GeV	1–2 GeV	2–10 GeV
$q_{\mathrm{H\,I},1}$	0.584 ± 0.011	0.224 ± 0.008	0.168 ± 0.004	0.110 ± 0.003	0.048 ± 0.002
$q_{\mathrm{CO},1}$	1.09 ± 0.04	0.367 ± 0.017	0.318 ± 0.013	0.198 ± 0.008	0.102 ± 0.005
$q_{\mathrm{H\,I},2}$	0.536 ± 0.018	0.200 ± 0.007	0.157 ± 0.005	101 ± 0.004	0.054 ± 0.002
$q_{\mathrm{CO},2}$	1.67 ± 0.17	0.47 ± 0.06	0.44 ± 0.04	0.26 ± 0.03	0.087 ± 0.014
$q_{\mathrm{H\,I},3}$	0.349 ± 0.011	0.128 ± 0.004	0.108 ± 0.003	0.072 ± 0.002	0.0397 ± 0.0014
$q_{\mathrm{CO},3}$	1.17 ± 0.15	0.52 ± 0.06	0.37 ± 0.04	0.24 ± 0.03	0.115 ± 0.016
$q_{\mathrm{H\,I},4}$	0.33 ± 0.04	0.101 ± 0.017	0.114 ± 0.013	0.103 ± 0.009	0.032 ± 0.005
q_{EBV}	16.7 ± 1.0	6.0 ± 0.4	3.49 ± 0.27	2.28 ± 0.18	0.80 ± 0.11
I_{iso}	4.67 ± 0.10	1.19 ± 0.04	0.92 ± 0.03	0.63 ± 0.02	0.371 ± 0.0017

Notes.
[a] Units: $q_{\mathrm{H\,I},i}$ (10^{-26} s^{-1} sr^{-1}), $q_{\mathrm{CO},i}$ (10^{-6} cm^{-2} s^{-1} sr^{-1} (K km s^{-1})$^{-1}$), q_{EBV} (10^{-6} cm^{-2} s^{-1} sr^{-1} mag^{-1}), I_{iso} (10^{-6} cm^{-2} s^{-1} sr^{-1}).
[b] The subscripts refer to the different regions under analysis: (1) Gould Belt, (2) local arm, (3) Perseus arm, and (4) outer arm and beyond.

4.1.3. Emissivity in the Gould Belt

In Figure 8, we compare the emissivity spectrum per H I atom we measured in the Gould Belt with the GALPROP predictions. We find the latter to be ≃50% lower at all energies. As we have just discussed, a large part of this excess (∼30%) can be explained by the uncertainties in the contribution from interactions involving CR and ISM nuclei other than protons. The remaining ∼20% excess can be explained by systematic uncertainties in the CR proton spectra at the Earth (∼20%), the N(H I) column-density derivation, and the kinematical separation of emission from the outer Galaxy.

The H I emissivity in the Gould Belt clouds (within 300 pc from the solar system) is thus consistent with the hypothesis that the gas is interacting with CRs with the same spectra measured at Earth. Figure 8 shows the GALPROP model scaled by +50% to highlight that the spectral shape is in good agreement with our results.

The H I spin temperature of 125 K (chosen to have a straightforward comparison with earlier analyses) is among the lowest values reported in the literature. A higher temperature would imply a higher emissivity, therefore a larger discrepancy with the GALPROP model (e.g., $q_{\mathrm{H\,I},1}$ increases by another 5%–10% if we take $T_S = 250$ K as recently suggested by Dickey et al. 2009).

4.1.4. H I Emissivity Gradient

It is evident from Figure 7 that the H I emissivity decreases from the Gould Belt to the Perseus arm, as expected from the declining distribution of candidate CR sources in the outer Galaxy. Figure 9 shows the emissivity ratios between the more distant regions and the Gould Belt. Systematic errors due to the event selection efficiency are not relevant for these ratios, because the emissivity spectra are similar.

The emissivity spectrum in the local arm is 10% lower than in the Gould Belt. The GALPROP model predicts such a decrease because of the change in Galactocentric radius from the solar circle to the main part of local arm, located in this direction at ∼9.5 kpc.

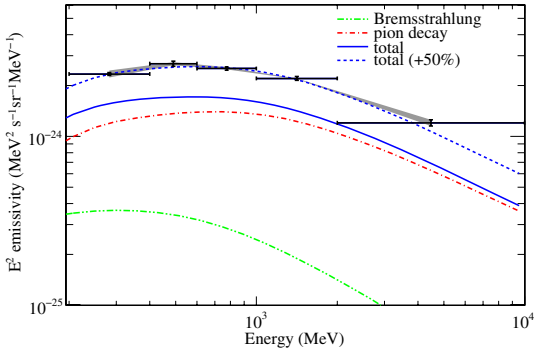

Figure 8. H I emissivity spectrum in the Gould Belt, as shown in Figure 7. The curves represent the predictions by GALPROP `54_71Xvarh7S`. The total emissivity from the model has been increased by 50% to reproduce our measurements.

(A color version of this figure is available in the online journal.)

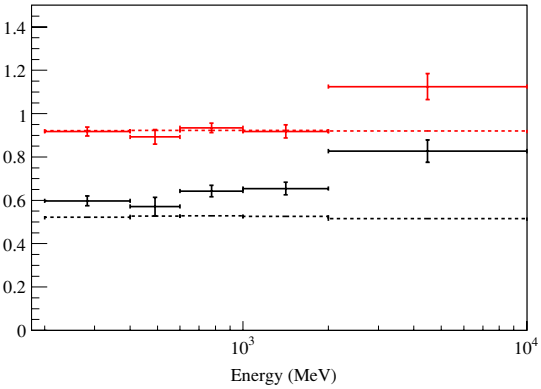

Figure 9. Emissivities measured in the Perseus arm—black—and in the local arm—light (red)—relative to those in the Gould Belt. Horizontal bars mark the energy ranges, vertical bars show statistical uncertainties. The dashed lines represent the GALPROP predictions.

(A color version of this figure is available in the online journal.)

A further decline in $q_{\rm H\,I}$ is expected between the local and Perseus arms, but Figure 9 shows that the measured $q_{\rm H\,I}$ gradient is significantly shallower than the GALPROP prediction. In Figure 10, we compare the H I emissivity integrated above 200 MeV predicted by GALPROP as a function of Galactocentric radius with the values we measured in the four regions defined for analysis, drawing the same conclusion. In this figure, we report the emissivity found in the outer arm, though considered only as an upper limit because its determination is probably affected by faint sources (see Section 3.3.2).

The discrepancies between the measured and predicted gradients may be due to the large uncertainty in the CR source distribution. The SNR radial distribution across the Galaxy is very poorly determined because of the small sample available and large selection effects (Case & Bhattacharya 1998). Distance and interstellar dispersion uncertainties also bias the pulsar distribution, in spite of the larger sample available (Lorimer 2004). On the other hand, the CR diffusion parameters, derived from local isotopic abundances in CRs, may not apply to the whole Galaxy, as suggested by Taillet & Maurin (2003). Self-absorption can also lead to a significant underestimate of

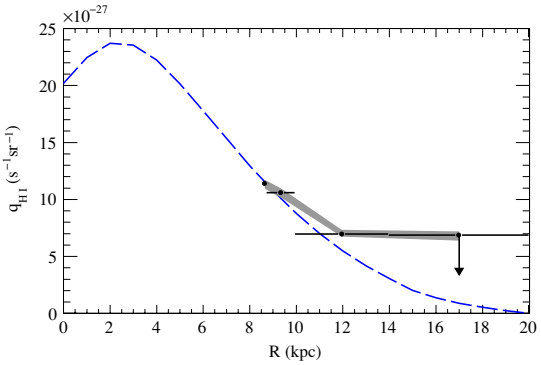

Figure 10. Radial profile with Galactocentric radius of the H I emissivity integrated between 200 MeV and 10 GeV. Black dots/horizontal bars mark the ranges in kinematic distance encompassing the Gould Belt, the main part of the local arm, the Perseus and outer arms (from left to right). Statistical uncertainties on $q_{\rm H\,I}$ are smaller than the dot dimensions. The gray shaded area shows the systematic uncertainties on the event selection efficiency. The (blue) dashed line is the GALPROP prediction scaled up by 50%.

(A color version of this figure is available in the online journal.)

N(H I) in the Perseus arm (Gibson et al. 2005), and thus to an overestimate of its γ-ray emissivity. Therefore, further investigation is needed to better understand the radial profile of the H I emissivity.

In Figure 7, the H I emissivity spectrum in the Perseus arm appears harder than expectations, thus suggesting that primary CR spectra vary across the Galaxy. We cannot, however, rule out energy-dependent systematic effects due to the separation power provided by the LAT PSF which strongly varies with energy, or a hardening due to contamination by hard unresolved point sources, like pulsars, clustering in the Perseus-arm structures.

4.2. Cloud Masses

4.2.1. CO

Because the γ-ray emission from molecular clouds is primarily due to H_2 and the molecular binding energy is negligible with respect to the energy scale of the γ radiation processes, the emissivity per H_2 molecule is twice the emissivity per H I atom. Under the hypothesis that the same CR flux penetrates the H I and CO phases of a cloud, we can assume that $q_{{\rm CO},\,i} = 2\,X_{{\rm CO},\,i} \cdot q_{{\rm H\,I},\,i}$ in each region to derive the CO-to-H_2 conversion factor, $X_{\rm CO}$.

We have performed a maximum-likelihood linear fit $q_{{\rm CO},\,i} = X_{{\rm CO},\,i} \cdot 2q_{{\rm H\,I},\,i} + \overline{q}_i$ between the $q_{{\rm CO},\,i}$ and $q_{{\rm H\,I},\,i}$ values found in the various energy bands for each region. We have taken into account the errors and covariances obtained from the γ-ray fits for both $q_{\rm H\,I}$ and $q_{\rm CO}$. Systematic errors due to the event selection efficiency do not affect the derivation of the $X_{\rm CO}$ slope because the H I and CO emissivities have similar spectra. The results are shown in Figure 11, and the best-fit parameters are reported in Table 2. We observe a good linear correlation between $q_{\rm H\,I}$ and $q_{\rm CO}$ that lends support to the assumption that CRs penetrate molecular clouds uniformly to their cores (still under debate; see, e.g., Gabici et al. 2007).

Figure 12 shows the $X_{\rm CO}$ variation with Galactocentric radius. Our measurements are consistent with previous γ-ray estimates in this region of the sky (Digel et al. 1996), but they are more precise, especially in the outer Galaxy. For the segment of the Perseus arm near NGC 7538, we have lowered the statistical uncertainty from ~40% to 10%. The results suggest

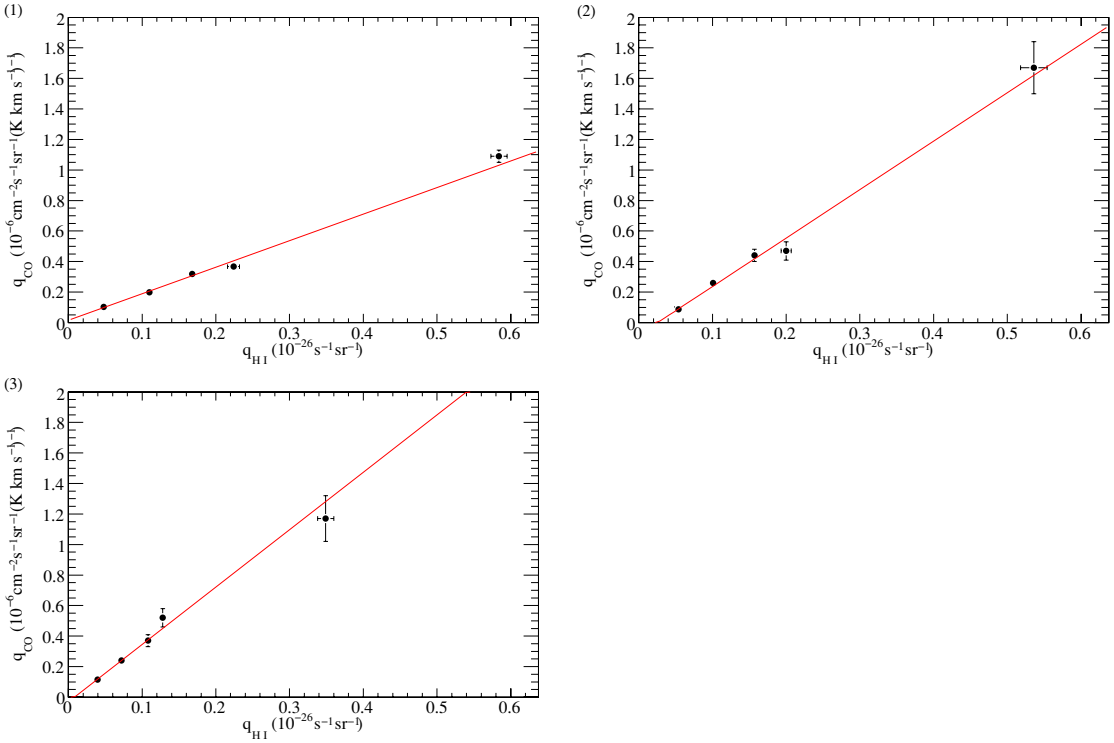

Figure 11. Correlation between the H I and CO emissivities obtained in the five energy bands for each region under analysis: (1) Gould Belt, (2) local arm, and (3) Perseus arm. Error bars show the statistical uncertainties on $q_{\mathrm{H\,I},i}$ and $q_{\mathrm{CO},i}$. The (red) lines give the best linear fits.
(A color version of this figure is available in the online journal.)

Table 2
Results of the Linear Fits between the H I and CO Emissivities in the Different Regions (1: Gould Belt, 2: local arm, 3: Perseus arm):
$q_{\mathrm{CO},i} = X_{\mathrm{CO}\,i} \cdot 2q_{\mathrm{H\,I},i} + \overline{q}_i$

Region	X_{CO}[a]	$\overline{q}$[b]
1	0.87 ± 0.05	0.015 ± 0.012
2	1.59 ± 0.17	−0.08 ± 0.03
3	1.9 ± 0.2	−0.03 ± 0.03

Notes.
[a] Units: 10^{20} cm^{-2} (K km s^{-1})$^{-1}$).
[b] Units: 10^{-6} cm^{-2} s^{-1} sr^{-1} (K km s^{-1})$^{-1}$.

an increase of X_{CO} in the outer Galaxy, as expected from the metallicity gradient (see, e.g., Rolleston et al. 2000). The X_{CO} measurements in external galaxies indeed show a metallicity dependence possibly caused by CO photodissociation and poor self-shielding in low-metallicity environments (Israel 1997, 2000).

Contamination from unresolved point sources with a spatial distribution closely related to that of the clouds is expected in star-forming regions which can produce young pulsars, SNRs, and massive binaries. This effect is unlikely in the Gould Belt clouds (Cassiopeia, Cepheus, and Polaris), first because they form few high-mass stars, second because of the good linear resolution of the γ-ray maps of these nearby clouds. Their proximity ($\lesssim$300 pc) and the $\sim$0.°5 angular resolution of the LAT in the higher energy band imply a linear resolution $\lesssim$3 pc, which allows an efficient separation between diffuse emission and point sources. The contamination by point sources is limited for similar reasons in the nearby local arm, $\lesssim$1 kpc away, but it cannot be clearly ruled out in the Perseus-arm clouds which are known to form massive star clusters (see, e.g., Sandell & Sievers 2004).

We cannot exclude separation problems between the γ-ray emission from the CO cores and their surrounding H I envelopes. The separation, based on the spatial distribution of the different phases, becomes less efficient with increasing distance due to the lower linear resolution. Moreover, we have verified that the presence of γ rays associated with the dark-gas envelopes around the CO cores affects the determination of the CO-to-H_2 factor in more distant, not so well-resolved, clouds (whereas the impact is negligible in the closer clouds). Excluding the $E(B-V)_{\mathrm{res}}$ map from the model yields a $\sim$30% increase of X_{CO} in the Perseus arm. Unfortunately, the $E(B-V)_{\mathrm{res}}$ map is not reliable near the plane because of the confusion along the line of sight that prevents an adequate temperature correction and the removal of clusters of IR point sources, so this difference has to be considered as a systematic error on X_{CO} in the Perseus arm.

Whether the present X_{CO} gradient can be fully attributed to the metallicity gradient, or partially to unresolved sources, H I and CO separation problems, or gas not traced by H I and CO, needs further investigation, primarily at higher resolution when more high-energy LAT data become available to profit from the better angular resolution. For the moment, the fact that the present X_{CO} determination does not depend on energy (see Figure 11)

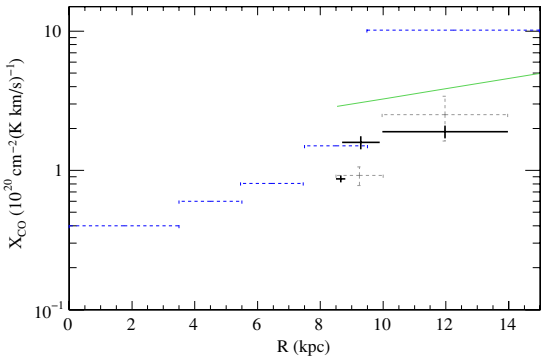

Figure 12. X_{CO} as a function of Galactocentric radius. The solid-line (black) points represent our measurements: horizontal bars mark the ranges of kinematic distance encompassing the Gould Belt and the local and Perseus arms (from left to right), vertical bars show the statistical uncertainties on X_{CO} (errors are statistical only; possible systematics are discussed in the text in Section 4.2.1). Dashed (blue) lines represent the values used in GALPROP by Strong et al. (2004b). The solid (green) line shows the X_{CO} function determined by Nakanishi & Sofue (2006) from CO data and virial masses (adapted to the rotation curve assumed for our analysis). The dashed (gray) points show the previous EGRET measurements in the region of Cepheus and Polaris (Digel et al. 1996).

(A color version of this figure is available in the online journal.)

suggests that unresolved sources and separation of the different gas phases do not significantly influence the result. The results shown in Figure 12 indicate significantly smaller X_{CO} values in the outer Galaxy than those used by Strong et al. (2004b) in GALPROP and systematically smaller values than the $X_{CO}(R)$ relation determined by Arimoto et al. (1996) and Nakanishi & Sofue (2006) using CO data and virial masses.

The X_{CO} values shown in Table 2 have been used to estimate cloud masses using Equation (3),

$$M = 2\ \mu\ m_H\ d^2\ X_{CO} \int W_{CO}(l, b)\, d\Omega, \qquad (3)$$

where d is the distance of the cloud, m_H is the H atom mass, and $\mu = 1.36$ is the mean atomic weight per H atom in the ISM. We did not use the kinematic distances inferred from CO surveys, but we adopted more precise estimates available in the literature. The results are given in Table 3. The errors include only the statistical uncertainties on X_{CO}.

To investigate the discrepancies found between the different determinations of X_{CO}, we calculated the virial masses for well-resolved clouds off the plane. The virial masses have been obtained from the CO velocity dispersion for a spherical mass distribution with density profile $\propto 1/r$, following Equation (4),

$$M = \frac{3}{2}\,\frac{r}{G}\,\sigma_v^2, \qquad (4)$$

where r is the cloud radius, σ_v is the velocity dispersion, and G is Newton's constant. The velocity dispersion has been measured for each line of sight and the average value in the sample has been taken as the characteristic σ_v in the cloud. This method limits the impact of the obvious velocity gradients in these clouds. Because the virial mass heavily depends on the estimate of the characteristic radius and on the cutoff applied in its evaluation, we considered both the effective radius $r_A = \sqrt{A/\pi}$ (where A is the geometrical area of the cloud) and the intensity-weighted radius $\langle r \rangle = \left(\sum_\iota W_{CO\iota}\, r_\iota\right) / \left(\sum_\iota W_{CO\iota}\right)$ (where r_ι is the distance of pixel ι to the peak W_{CO} pixel). We truncated the calculation at 1% of the W_{CO} peak in both cases. We find that the virial masses are systematically larger than the X_{CO} derived masses by a factor 1.5–3. This discrepancy in the nearby clouds is comparable to that shown in Figure 12 between the γ-ray estimates of X_{CO} and the $X_{CO}(R)$ function by Nakanishi & Sofue (2006) which relies on virial masses. The γ-ray estimates are independent from the chemical, dynamical, and thermodynamical state of the clouds, but they can suffer from the limited resolution of γ-ray surveys and the non-uniform penetration of CRs into the dense CO cores. Conversely, the assumption of a spherical cloud in virial equilibrium against turbulent motions is rather crude. Intrinsic velocity gradients and magnetic pressure can easily bias the virial mass results.

4.2.2. Dark Gas

In order to quantify the significance of the correlation between the γ-ray intensities and the $E(B-V)_{res}$ map, we have repeated the last step of Section 3.3.2 without including it in the analysis. The corresponding test statistics, TS $= 2\Delta(\ln \mathscr{L})$, obtained in the five energy bands are given in Table 4. With the addition of two free parameters (q_{EBV} and a spectral index), in the null hypothesis that there is no γ-ray emission associated with the $E(B-V)_{res}$ map TS should follow a χ^2 distribution with two degrees of freedom. Therefore, the correlation between γ rays and $E(B-V)$ residuals is verified at a confidence level $> 99.9\%$ in all energy bands.

The magnitudes of the dust masses and dust IR emission are too low to explain this correlation by CR interactions with dust

Table 3
Masses for Specific Clouds, Complexes or Regions Obtained from CO Intensities and the X_{CO} Values in Table 2

Region	l	b	d (kpc)	M_{CO}	$M_{vir}(r_A)$	$M_{vir}(\langle r \rangle)$	M_{dark}
Cepheus	[100, 117]	[6, 22]	0.3[a]	0.37 ± 0.02	0.687	0.903	0.160 ± 0.011
Polaris	[117, 129]	[18, 30]	0.25[b]	0.052 ± 0.003	0.208	0.159	0.031 ± 0.002
Cassiopeia	[117, 145]	[2, 18]	0.3[a]	0.61 ± 0.03	0.893	1.062	0.34 ± 0.02
Gould Belt	[100, 145]	[−15, 30]	0.3	1.47 ± 0.08			
NGC 7538	[107, 115]	[−5, 5]	2.65[c]	20 ± 2			
NGC 281	[120, 125]	[−9, −5]	3.0[d]	0.79 ± 0.08	1.205	1.047	
Perseus arm	[100, 145]	[−10, 10]	3.0	57 ± 6			

Notes. For selected clouds, we also report virial masses and, in the Gould Belt, the dark-gas mass obtained from the X_{EBV} conversion factor determined in Section 4.2.2. All masses are in units of $10^5\ M_\odot$ and the errors include only the statistical uncertainties on X_{CO} or X_{EBV}.

[a] Grenier et al. (1989).

[b] Heithausen & Thaddeus (1990).

[c] Moscadelli et al. (2009).

[d] Sato et al. (2007).

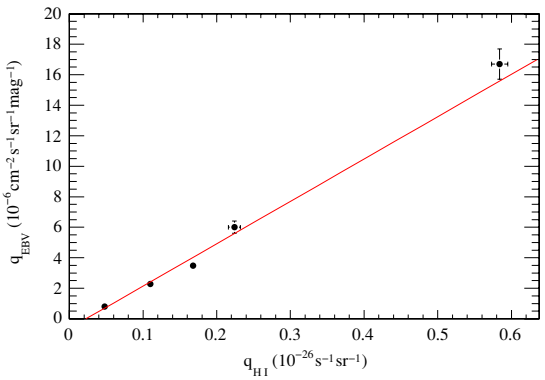

Figure 13. Correlation in the Gould Belt between the H I emissivities and the emissivities per unit of $E(B-V)_{\rm res}$. Error bars show the statistical errors obtained on both emissivities in the five energy bands. The (red) line shows the best linear fit.

(A color version of this figure is available in the online journal.)

Table 4
TS = $2\Delta(\ln \mathscr{L})$ for the Inclusion of the $E(B-V)_{\rm res}$ Map in the Fit in the Different Energy Bands

Energy Range (GeV)	TS
0.2–0.4	53.8
0.4–0.6	124
0.6–1	74.6
1–2	91.8
2–10	38.2

grains or their thermal radiation. However, the correlation can be explained by CR interactions in normal gas that is not accounted for in the N(H I) and $W_{\rm CO}$ maps.

In Section 4.2.1, we have used the γ-ray emissivities per H I atom and $W_{\rm CO}$ unit to calibrate the CO-to-H_2 conversion factor, following a well-established method. We can use a similar procedure to correlate the γ-ray emissivities per H I atom and per $E(B-V)_{\rm res}$ unit in the well-resolved Gould Belt clouds (see Figure 4) where the spatial association between the H I, CO, and $E(B-V)_{\rm res}$ maps allows locating the dark gas in the absence of kinematical information.

The $q_{\rm H\,I,\,1}$ and $q_{\rm EBV}$ emissivities found in the five energy bands exhibit a tight correlation (Figure 13). As we did for CO, we fitted a linear relation, $q_{\rm EBV} = X_{\rm EBV} \cdot q_{\rm H\,I,\,1} + \overline{q}$, using a maximum-likelihood method taking into account the errors and covariances of the emissivities. The results are $X_{\rm EBV} = (28 \pm 2) \times 10^{20}$ cm^{-2} mag^{-1} and $\overline{q} = (-0.6 \pm 0.2) \times 10^{-6}$ cm^{-2} s^{-1} sr^{-1} mag^{-1}. The good linear correlation implies similar spectra for the γ-ray emission from gas seen in the H I emission line and that associated with the excess reddening, thus confirming the need for normal additional gas to explain the correlated excess of both γ rays and dust at the interface between the H I and CO emitting phases of the Gould Belt clouds.

Using the $X_{\rm EBV}$ factor in these clouds, we can calculate the additional gas mass and compare it to the molecular mass seen in CO. We restrict the comparison to the CO mass, because the more diffuse H I clouds are difficult to separate from the background H I disc extending to intermediate latitudes. To estimate the dark mass, we use only the positive residuals in the $E(B-V)_{\rm res}$ map. As discussed in Section 2.3, the small negative residuals associated with the CO cores are likely related with local variations in the dust temperature or dust-to-gas ratio. The results are given in Table 3. The errors include only the statistical uncertainties on $X_{\rm EBV}$. The additional mass in the Gould Belt clouds appears to be 40% to 60% of the CO-bright mass. We note that the sum of the dark and CO mass is closer to the virial one. We also note that FIRAS and SIMBA dust spectra in the Cepheus flare led to an independent estimate of its total mass, $M = (0.43 \pm 0.18) \times 10^5\ M_\odot$ (Bot et al. 2007), which relates well with the total (CO plus dark) mass $M = (0.53 \pm 0.02) \times 10^5\ M_\odot$ we have obtained in γ rays.

5. SUMMARY

We have analyzed the interstellar γ-ray emission observed by the *Fermi* LAT in the region of Cassiopeia and Cepheus, successfully modeling the γ-ray data as a linear combination of contributions arising from different gas complexes toward the outer Galaxy.

The separation has allowed us to verify that the γ-ray emissivity of local atomic gas is consistent with production by interactions with CRs with the same spectra as those measured near the Earth, but confirms the higher pion-decay contribution relative to some of the estimates in the literature, as found in Abdo et al. (2009c). This can be plausibly attributed to uncertainties in the local CR spectra, either in the measurement or from differences between the direct measurements and local interstellar space.

Thanks to the correlation between an excess of dust and of γ-ray emission, with a spectrum equivalent to that found for the atomic and molecular gas, we have verified the presence of an excess of gas not properly traced by the standard N(H I) and $W_{\rm CO}$ maps. In the nearby Gould Belt clouds, the dark gas forms a layer between the H I and CO phases and it represents about 50% of the mass traced in the CO-bright molecular cores.

The CR-density gradient in the outer Galaxy appears to be flatter than expectations based on the assumption that CRs are accelerated by SNRs as traced by pulsars. It is also possible that the CR spectrum in the Perseus arm is harder than in the local arm. This hardening, which needs confirmation at high resolution with more LAT data to limit the potential contamination by hard unresolved point sources, could be linked to CR diffusion not far from their sources.

We have measured $X_{\rm CO}$ in several regions from the Gould Belt to the Perseus arm. The γ-ray estimates are independent of the chemical and thermodynamical state of the gas and also from assumptions on the virial equilibrium of the clouds. They correspond to a significant but moderate increase of $X_{\rm CO}$ with Galactocentric radius outside the solar circle, from $(0.87 \pm 0.05) \times 10^{20}$ cm^{-2} (K km s^{-1})$^{-1}$ in the Gould Belt to $(1.9 \pm 0.2) \times 10^{20}$ cm^{-2} (K km s^{-1})$^{-1}$ in the Perseus arm.

The *Fermi* LAT Collaboration acknowledges generous ongoing support from a number of agencies and institutes that have supported both the development and the operation of the LAT as well as scientific data analysis. These include the National Aeronautics and Space Administration and the Department of Energy in the United States, the Commissariat à l'Energie Atomique and the Centre National de la Recherche Scientifique/Institut National de Physique Nucléaire et de Physique des Particules in France, the Agenzia Spaziale Italiana and the Istituto Nazionale di Fisica Nucleare in Italy, the Ministry of Education, Culture, Sports, Science, and Technology (MEXT), High Energy Accelerator Research Organization (KEK) and Japan Aerospace Exploration Agency (JAXA) in Japan, and the K. A. Wallenberg

Foundation, the Swedish Research Council, and the Swedish National Space Board in Sweden.

Additional support for science analysis during the operations phase is gratefully acknowledged from the Istituto Nazionale di Astrofisica in Italy and the Centre National d'Études Spatiales in France.

We thank T. H. Dame for providing moment-masked CO data including from some observations not yet published.

REFERENCES

Abdo, A. A., et al. 2009a, Phys. Rev. Lett., 102, 181101
Abdo, A. A., et al. 2009b, ApJS, 183, 46
Abdo, A. A., et al. 2009c, ApJ, 703, 1249
Abdo, A. A., et al. 2009d, ApJ, 706, L1
Abdo, A. A., et al. 2009e, Phys. Rev. Lett., 103, 251101
Abdo, A. A., et al. 2010, Phys. Rev. Lett., submitted
Acciari, V. A., et al. 2009, ApJ, 698, L133
Adriani, O., et al. 2009, Phys. Rev. Lett., 102, 051101
Aharonian, F., et al. 2008, A&A, 481, 401
Albert, J., et al. 2007, ApJ, 664, L87
Alcaraz, J., et al. 2000, Phys. Lett. B., 472, 215
Arimoto, N., Sofue, Y., & Tsujimoto, T. 1996, PASJ, 48, 275
Atwood, W. B., et al. 2009, ApJ, 697, 1071
Bloemen, H. 1989, ARA&A, 29, 469
Bot, C., et al. 2007, A&A, 471, 103
Case, G. L., & Bhattacharya, D. 1998, ApJ, 504, 761
Cordes, J. M., & Lazio, T. J. W. 2002, arXiv:astro-ph/0207156
Dame, T. M., Hartmann, D., & Thaddeus, P. 2001, ApJ, 547, 792
Dermer, C. D. 1986a, ApJ, 307, 47
Dermer, C. D. 1986b, A&A, 157, 223
Dickey, J. M., et al. 2009, ApJ, 693, 1250
Digel, S. W., Bally, J., & Thaddeus, P. 1990, ApJ, 357, L29
Digel, S. W., et al. 1996, ApJ, 463, 609
Digel, S. W., et al. 2001, ApJ, 555, 12
Gabici, S., Aharonian, F. A., & Blasi, P. 2007, Ap&SS, 309, 365
Gibson, S. J., et al. 2005, ApJ, 626, 195
Grenier, I. A., Casandjian, J. M., & Terrier, R. 2005, Science, 307, 1292
Grenier, I. A., et al. 1989, ApJ, 347, 231
Heithausen, A., & Thaddeus, P. 1990, ApJ, 353, L49
Honda, M., et al. 2004, Phys. Rev. D, 70, 043008
Israel, F. P. 1997, A&A, 328, 471
Israel, F. P. 2000, in Molecular Hydrogen in Space, ed. F. Combes & G. Pineau des Forêts (Cambridge: Cambridge Univ. Press), 293
Kalberla, P. M. W., et al. 2005, A&A, 440, 775
Kamae, T., et al. 2006, ApJ, 647, 692
Koch, H. W., & Motz, J. W. 1959, Rev. Mod. Phys., 31, 920
Lebrun, F., et al. 1983, ApJ, 274, 231
Lorimer, D. R. 2004, in IAU Symp. 218, Young Neutron Stars and Their Environments, ed. F. Camilo & B. M. Gaensler (Dordrecht: Kluwer), 105
Mohan, R., Dwarakanath, K. S., & Srinivasan, G. 2004a, JA&A, 25, 143
Mohan, R., Dwarakanath, K. S., & Srinivasan, G. 2004b, JA&A, 25, 185
Moscadelli, L., et al. 2009, ApJ, 693, 406
Mori, M. 2009, Astropart. Phys., 31, 341
Nakanishi, H., & Sofue, Y. 2006, PASJ, 58, 847
Perrot, C. A., & Grenier, I. A. 2003, A&A, 404, 519
Porter, T. A., et al. 2008, ApJ, 682, 400
Rando, R., et al. 2009, arXiv:0907.0294
Rolleston, W. R. J., et al. 2000, A&A, 363, 537
Sandell, G., & Sievers, A. 2004, ApJ, 600, 269
Sanuki, T., et al. 2000, ApJ, 545, 1135
Sato, M., et al. 2007, PASJ, 59, 743S
Shikaze, Y., et al. 2007, Astropart. Phys., 28, 154
Schlegel, D. J., Finkbeiner, D. P., & Davis, M. 1998, ApJ, 500, 525
Sodroski, T. J., et al. 1995, ApJ, 452, 262
Sodroski, T. J., et al. 1997, ApJ, 480, 173
Solomon, P. M., & Barret, J. W. 1991, in IAU Symp. 218, Dynamics of Galaxies and Their Molecular Cloud Distribution, ed. F. Combes & F. Casoli (Dordrecht: Kluwer), 235
Strong, A. W., & Moskalenko, I. V. 1998, ApJ, 509, 212
Strong, A. W., Moskalenko, I. V., & Ptuskin, V. S. 2007, Annu. Rev. Nucl. Part. Syst., 57, 285
Strong, A. W., Moskalenko, I. V., & Reimer, O. 2000, ApJ, 537, 763
Strong, A. W., Moskalenko, I. V., & Reimer, O. 2004a, ApJ, 613, 962
Strong, A. W., et al. 1988, A&A, 207, 1
Strong, A. W., et al. 2004b, A&A, 422, L47
Taillet, R., & Maurin, D. 2003, A&A, 402, 971
Ungerechts, H., Umbanhowar, P., & Thaddeus, P. 2000, ApJ, 537, 221

4.2 THE SYSTEMATIC UNCERTAINTIES DUE TO THE H I SPIN TEMPERATURE

H I *and CR densities*

Provided that $N(\mathrm{H\,I})$ densities are accurately measured from observations of the 21-cm line, the H I emissivity, $q_{\mathrm{H\,I}}$, is proportional to the average CR densities. Variations of the H I spin temperature, T_S (§ 2.1.2), which lead to substantial uncertainties on $N(\mathrm{H\,I})$, are an important source of systematic errors in this regard, since γ-ray intensities constrain only the product of H I and CR densities.

The interpretation of γ-ray observations often relied on the assumption of a uniform $T_S = 125$ K (e.g. Bloemen et al., 1984; Strong et al., 1988; Digel et al., 1996, 2001; Hunter et al., 1997; Strong et al., 2004a,b; Grenier et al., 2005) . However, T_S is not uniform and for the outer disk of the Milky Way absorption measurements indicate larger average values in the range $250 - 400$ K (Dickey et al., 2009, 250 K is the average T_S suggested for the second quadrant considered in this chapter).

In the subsequent study of the third quadrant (Chapter 5) these systematics, often overlooked by past studies, were recognized to be currently the dominant source of uncertainties for the interpretation of γ-ray observations in terms of CR densities.

I tried to evaluate their impact on our results repeating the analysis for some discrete values of T_S. The spin temperature T_S must be larger than the observed brightness temperature T_B (Eq. 2.10); since we observe in the regions studied many lines of sight with $T_B > 100$ K, I adopted as lower bound in the uniform approximation $T_S = 100$ K. I then explored, beyond the historical value $T_S = 125$ K, the values $T_S = 250$ K and 400 K suggested by Dickey et al. (2009). The limit of infinitely high spin temperature, equivalent to the limit of small optical depth, provides the lower bound on the $N(\mathrm{H\,I})$ densities (Eq. 2.10). We show in Fig. 4.1 the likelihood profile as a function of T_S. γ-

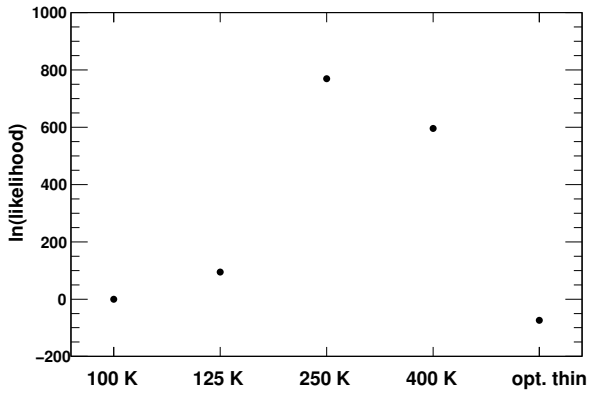

Figure 4.1: Log-likelihood profile as a function of H I spin temperature, T_S, assumed for the optical depth correction in the uniform approximation.

ray data support the results by Dickey et al. (2009) of average spin temperatures in the range of a few hundreds K, corresponding to a blend of $\lesssim 20\%$ H I in the cold phase and the rest warm (§ 2.1.2).

The impact on analysis results

Variations in T_S affect the estimate of the emissivities not only because of the change in overall atomic masses, but also because changes in the structures of the gas impact the component separation procedure.

In Fig. 4.3 I show the integral emissivity as a function of Galactocentric radius. Compared with Fig. 10 of the paper the uncertainties, taking into account the problem of the H I spin temperature, are significantly larger. As explained in the paper, the emissivity of the outermost region is highly uncertain because of possible contamination from point sources not accounted for in the analysis [1]. It is represented by a dashed line in Fig. 4.3.

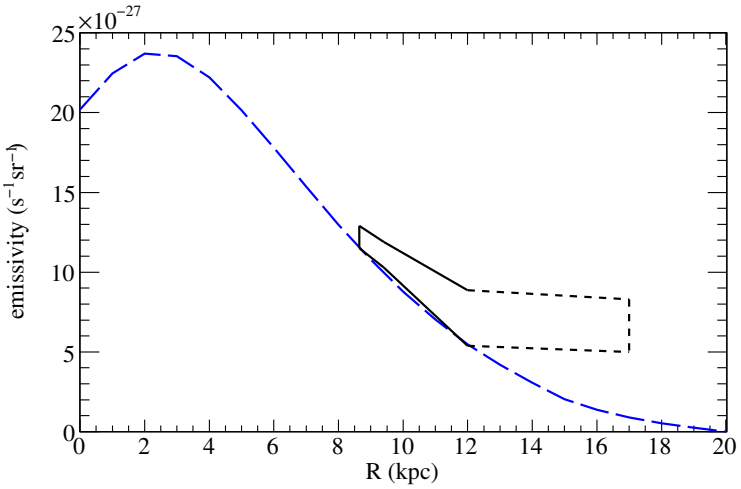

Figure 4.2: $q_{\mathrm{H\,I}}$ integrated above 200 MeV as a function of Galactocentric radius (bow-tie plot), compared with the prediction by a GALPROP model based on the distribution observed for SNRs/pulsars. See Fig. 10 of the paper.

The γ-ray estimate of X_{CO}, $X_\gamma = q_{\mathrm{CO}}/(2\,q_{\mathrm{H\,I}})$, is affected by the choice of the spin temperature, because both $q_{\mathrm{H\,I}}$ and q_{CO} changes, due to the combined effect of different atomic masses and different structures driving the component separation. In Fig. 4.3 I show X_{CO} as a function of Galactocentric radius. The uncertainties due to the H I spin temperature are moderate for the nearby well-resolved clouds in the Gould Belt, and they become larger with increasing distance.

4.3 SUMMARY OF THE RESULTS

In spite of the larger uncertainties due to the H I spin temperatures the main conclusions are confirmed.

- The local H I emissivity is compatible with expectations based on CR spectra measured near the Earth.
- The gradient of H I emissivities toward the outer Galaxy is flatter than expected from the distribution of putative CR sources.

1. However, we note that the value is consistent with the measurement obtained from the analysis of Chapter 5, where the massive gas complexes of the Perseus arm at larger Galactocentric distances make the result perhaps less dubious.

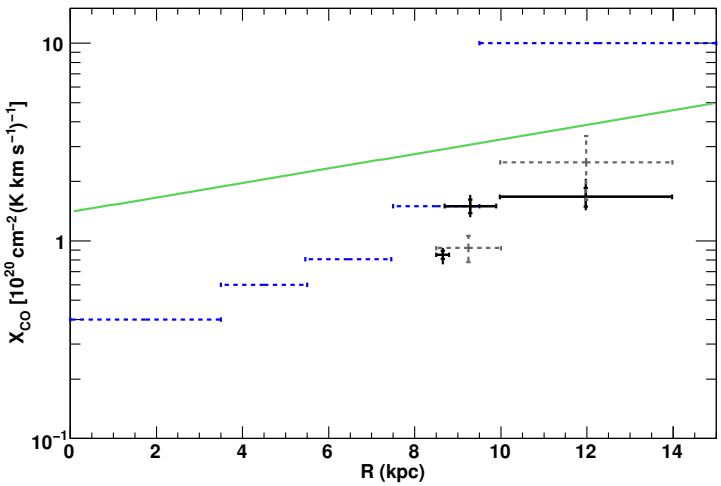

Figure 4.3: X_{CO} as a function of Galactocentric radius. Black points are the estimates in the second quadrant (for $T_S = 250$ K), where horizontal bars mark the ranges of distance considered in the analysis, vertical bars with end-caps indicate the statistical errors and plain vertical bars indicate the total errors including systematic uncertainties due to the H I spin temperature. Grey dashed points are the estimates from the analysis of EGRET data for a similar region in the second quadrant by Digel et al. (1996). The blue step function represents the model by Strong et al. (2004b) and the green line the model by Nakanishi and Sofue (2006). See Fig. 12 of the paper.

- The X_{CO} ratio for the clouds of Cassiopeia and Cepheus is a factor $\lesssim 2$ lower than for clouds in the local/Perseus arms.
- The increase by one order of magnitude of X_{CO} in the outer Galaxy proposed by Strong et al. (2004b) is not supported by LAT measurements.
- γ-ray estimates of X_{CO} are systematically lower than the estimates from virial masses.
- Gas invisible to radio/mm-wave lines for a total mass comparable to that traced by CO is detected in γ-rays for clouds in the Gould Belt.

5

INTERSTELLAR GAMMA-RAY EMISSION FROM THE OUTER GALAXY: THE THIRD GALACTIC QUADRANT

In the third Galactic quadrant there is a longitude window ($210^\circ < l < 250^\circ$) looking toward the outer Galaxy and with a very steep velocity gradient, complementary to the region of Cassiopeia and Cepheus in the second quadrant analysed in the previous Chapter 4. In this portion of the sky we can observe the outer disk of the Milky Way without bright foreground structures and we find remarkable molecular clouds at large Galactocentric distance, notably Maddalena's cloud. The results we obtained strengthen the conclusions of the work on the second quadrant regarding the CR gradient problem and the calibration of X_{CO}.

Additionally, this region is suitable to probe for a possible coupling between densities of CRs and gas in the ISM. Originally motivated by the Galactic structures, e.g. tangent points of the spiral arms, shining in γ-rays, the idea of a dynamical CR-ISM balance was used along the years to model interstellar emission (see § 3.1.2 and 3.3.1). Notably, the model adopted by the EGRET collaboration assumed that CR densities were proportional to the gas surface density, smoothed with a Gaussian kernel whose width is known as "coupling length" (Bertsch et al., 1993; Hunter et al., 1997). In the third quadrant we observe a low-density region situated between the Local Spur and the Perseus spiral arm, therefore, in such models, we expect a contrast in emissivity with should get lower in the interarm space. Analyses of EGRET data were not conclusive in this regard (Digel et al., 2001), but LAT measurements have shown that a contrast, if present, is smaller than expected from the model by Hunter et al. (1997).

5.1 ATTACHMENT: THE THIRD QUADRANT PAPER

I attach here the paper published as Ackermann et al. (2011).

The Astrophysical Journal, 726:81 (15pp), 2011 January 10 doi:10.1088/0004-637X/726/2/81

CONSTRAINTS ON THE COSMIC-RAY DENSITY GRADIENT BEYOND THE SOLAR CIRCLE FROM *FERMI* γ-RAY OBSERVATIONS OF THE THIRD GALACTIC QUADRANT

M. Ackermann[1], M. Ajello[1], L. Baldini[2], J. Ballet[3], G. Barbiellini[4,5], D. Bastieri[6,7], K. Bechtol[1], R. Bellazzini[2], B. Berenji[1], E. D. Bloom[1], E. Bonamente[8,9], A. W. Borgland[1], T. J. Brandt[10,11], J. Bregeon[2], A. Brez[2], M. Brigida[12,13], P. Bruel[14], R. Buehler[1], S. Buson[6,7], G. A. Caliandro[15], R. A. Cameron[1], P. A. Caraveo[16], J. M. Casandjian[3], C. Cecchi[8,9], E. Charles[1], A. Chekhtman[17,18], J. Chiang[1], S. Ciprini[9], R. Claus[1], J. Cohen-Tanugi[19], J. Conrad[20,21,43], C. D. Dermer[17], F. de Palma[12,13], S. W. Digel[1], P. S. Drell[1], R. Dubois[1], C. Favuzzi[12,13], E. C. Ferrara[22], W. B. Focke[1], Y. Fukazawa[23], S. Funk[1], P. Fusco[12,13], F. Gargano[13], S. Germani[8,9], N. Giglietto[12,13], F. Giordano[12,13], M. Giroletti[24], T. Glanzman[1], G. Godfrey[1], I. A. Grenier[3], S. Guiriec[25], D. Hadasch[15], Y. Hanabata[23], A. K. Harding[22], K. Hayashi[23], M. Hayashida[1], R. E. Hughes[11], R. Itoh[23], G. Jóhannesson[1], A. S. Johnson[1], W. N. Johnson[17], T. Kamae[1], H. Katagiri[23], J. Kataoka[26], J. Knödlseder[10], M. Kuss[2], J. Lande[1], L. Latronico[2], S.-H. Lee[1], M. Llena Garde[20,21], F. Longo[4,5], F. Loparco[12,13], M. N. Lovellette[17], P. Lubrano[8,9], A. Makeev[17,18], P. Martin[27], M. N. Mazziotta[13], J. E. McEnery[22,28], J. Mehault[19], P. F. Michelson[1], T. Mizuno[23], C. Monte[12,13], M. E. Monzani[1], A. Morselli[29], I. V. Moskalenko[1], S. Murgia[1], M. Naumann-Godo[3], S. Nishino[23], P. L. Nolan[1], J. P. Norris[30], E. Nuss[19], T. Ohsugi[31], A. Okumura[32], N. Omodei[1], E. Orlando[27], J. F. Ormes[30], M. Ozaki[32], D. Parent[17,18], V. Pelassa[19], M. Pepe[8,9], M. Pesce-Rollins[2], F. Piron[19], T. A. Porter[1], S. Rainò[12,13], R. Rando[6,7], M. Razzano[2], A. Reimer[1,33], O. Reimer[1,33], J. Ripken[20,21], T. Sada[23], H. F.-W. Sadrozinski[34], C. Sgrò[2], E. J. Siskind[35], G. Spandre[2], P. Spinelli[12,13], M. S. Strickman[17], A. W. Strong[27], D. J. Suson[36], H. Takahashi[31], T. Takahashi[32], T. Tanaka[1], J. B. Thayer[1], D. J. Thompson[22], L. Tibaldo[3,6,7,44], D. F. Torres[15,37], A. Tramacere[1,38,39], Y. Uchiyama[1], T. Uehara[23], T. L. Usher[1], J. Vandenbroucke[1], V. Vasileiou[40,41], N. Vilchez[10], V. Vitale[29,42], A. E. Vladimirov[1], A. P. Waite[1], P. Wang[1], K. S. Wood[17], Z. Yang[20,21], and M. Ziegler[34]

[1] W. W. Hansen Experimental Physics Laboratory, Kavli Institute for Particle Astrophysics and Cosmology, Department of Physics and SLAC National Accelerator Laboratory, Stanford University, Stanford, CA 94305, USA
[2] Istituto Nazionale di Fisica Nucleare, Sezione di Pisa, I-56127 Pisa, Italy
[3] Laboratoire AIM, CEA-IRFU/CNRS/Université Paris Diderot, Service d'Astrophysique, CEA Saclay, 91191 Gif sur Yvette, France; isabelle.grenier@cea.fr
[4] Istituto Nazionale di Fisica Nucleare, Sezione di Trieste, I-34127 Trieste, Italy
[5] Dipartimento di Fisica, Università di Trieste, I-34127 Trieste, Italy
[6] Istituto Nazionale di Fisica Nucleare, Sezione di Padova, I-35131 Padova, Italy; luigi.tibaldo@pd.infn.it
[7] Dipartimento di Fisica "G. Galilei," Università di Padova, I-35131 Padova, Italy
[8] Istituto Nazionale di Fisica Nucleare, Sezione di Perugia, I-06123 Perugia, Italy
[9] Dipartimento di Fisica, Università degli Studi di Perugia, I-06123 Perugia, Italy
[10] Centre d'Étude Spatiale des Rayonnements, CNRS/UPS, BP 44346, F-30128 Toulouse Cedex 4, France
[11] Department of Physics, Center for Cosmology and Astro-Particle Physics, The Ohio State University, Columbus, OH 43210, USA
[12] Dipartimento di Fisica "M. Merlin" dell'Università e del Politecnico di Bari, I-70126 Bari, Italy
[13] Istituto Nazionale di Fisica Nucleare, Sezione di Bari, 70126 Bari, Italy
[14] Laboratoire Leprince-Ringuet, École polytechnique, CNRS/IN2P3, Palaiseau, France
[15] Institut de Ciencies de l'Espai (IEEC-CSIC), Campus UAB, 08193 Barcelona, Spain
[16] INAF-Istituto di Astrofisica Spaziale e Fisica Cosmica, I-20133 Milano, Italy
[17] Space Science Division, Naval Research Laboratory, Washington, DC 20375, USA
[18] George Mason University, Fairfax, VA 22030, USA
[19] Laboratoire de Physique Théorique et Astroparticules, Université Montpellier 2, CNRS/IN2P3, Montpellier, France
[20] Department of Physics, Stockholm University, AlbaNova, SE-106 91 Stockholm, Sweden
[21] The Oskar Klein Centre for Cosmoparticle Physics, AlbaNova, SE-106 91 Stockholm, Sweden
[22] NASA Goddard Space Flight Center, Greenbelt, MD 20771, USA
[23] Department of Physical Sciences, Hiroshima University, Higashi-Hiroshima, Hiroshima 739-8526, Japan; mizuno@hep01.hepl.hiroshima-u.ac.jp
[24] INAF Istituto di Radioastronomia, 40129 Bologna, Italy
[25] Center for Space Plasma and Aeronomic Research (CSPAR), University of Alabama in Huntsville, Huntsville, AL 35899, USA
[26] Research Institute for Science and Engineering, Waseda University, 3-4-1, Okubo, Shinjuku, Tokyo 169-8555, Japan
[27] Max-Planck Institut für extraterrestrische Physik, 85748 Garching, Germany
[28] Department of Physics and Department of Astronomy, University of Maryland, College Park, MD 20742, USA
[29] Istituto Nazionale di Fisica Nucleare, Sezione di Roma "Tor Vergata," I-00133 Roma, Italy
[30] Department of Physics and Astronomy, University of Denver, Denver, CO 80208, USA
[31] Hiroshima Astrophysical Science Center, Hiroshima University, Higashi-Hiroshima, Hiroshima 739-8526, Japan
[32] Institute of Space and Astronautical Science, JAXA, 3-1-1 Yoshinodai, Sagamihara, Kanagawa 229-8510, Japan
[33] Institut für Astro- und Teilchenphysik and Institut für Theoretische Physik, Leopold-Franzens-Universität Innsbruck, A-6020 Innsbruck, Austria
[34] Santa Cruz Institute for Particle Physics, Department of Physics and Department of Astronomy and Astrophysics, University of California at Santa Cruz, Santa Cruz, CA 95064, USA
[35] NYCB Real-Time Computing Inc., Lattingtown, NY 11560-1025, USA
[36] Department of Chemistry and Physics, Purdue University Calumet, Hammond, IN 46323-2094, USA
[37] Institució Catalana de Recerca i Estudis Avançats (ICREA), Barcelona, Spain
[38] Consorzio Interuniversitario per la Fisica Spaziale (CIFS), I-10133 Torino, Italy
[39] INTEGRAL Science Data Centre, CH-1290 Versoix, Switzerland
[40] Center for Research and Exploration in Space Science and Technology (CRESST) and NASA Goddard Space Flight Center, Greenbelt, MD 20771, USA
[41] Department of Physics and Center for Space Sciences and Technology, University of Maryland Baltimore County, Baltimore, MD 21250, USA
[42] Dipartimento di Fisica, Università di Roma "Tor Vergata," I-00133 Roma, Italy
Received 2010 July 14; accepted 2010 November 1; published 2010 December 17

ABSTRACT

We report an analysis of the interstellar γ-ray emission in the third Galactic quadrant measured by the *Fermi* Large Area Telescope. The window encompassing the Galactic plane from longitude 210° to 250° has kinematically well-defined segments of the Local and the Perseus arms, suitable to study the cosmic-ray (CR) densities across the outer Galaxy. We measure no large gradient with Galactocentric distance of the γ-ray emissivities per interstellar H atom over the regions sampled in this study. The gradient depends, however, on the optical depth correction applied to derive the H I column densities. No significant variations are found in the interstellar spectra in the outer Galaxy, indicating similar shapes of the CR spectrum up to the Perseus arm for particles with GeV to tens of GeV energies. The emissivity as a function of Galactocentric radius does not show a large enhancement in the spiral arms with respect to the interarm region. The measured emissivity gradient is flatter than expectations based on a CR propagation model using the radial distribution of supernova remnants and uniform diffusion properties. In this context, observations require a larger halo size and/or a flatter CR source distribution than usually assumed. The molecular mass calibrating ratio, $X_{\rm CO} = N({\rm H_2})/W_{\rm CO}$, is found to be $(2.08 \pm 0.11) \times 10^{20}$ cm^{-2}(K km s^{-1})$^{-1}$ in the Local arm clouds and is not significantly sensitive to the choice of H I spin temperature. No significant variations are found for clouds in the interarm region.

Key words: cosmic rays – gamma rays: ISM – ISM: general

Online-only material: color figures

1. INTRODUCTION

Knowledge of the distribution of cosmic-ray (CR) densities within our Galaxy is a key to understanding their origin and propagation. High-energy CRs interact with the gas in the interstellar medium (ISM) or the interstellar radiation field, and produce γ-rays via nucleon–nucleon interactions, electron Bremsstrahlung, and inverse Compton (IC) scattering. Since the ISM is transparent to these γ-rays, we can probe CRs in the local ISM, beyond direct measurements performed in the solar system, as well as in remote locations of the Galaxy. Although much effort has been made since the COS-B era (e.g., Strong et al. 1988; Strong & Mattox 1996; Bloemen et al. 1996), the results have been limited by the angular resolution, effective area, and energy coverage of the instruments. The advent of the *Fermi Gamma-ray Space Telescope* enables studying the spectral and spatial distribution of diffuse γ-rays and CRs with unprecedented sensitivity.

Here, we report an analysis of diffuse γ-ray emission observed in the third Galactic quadrant. The window with Galactic longitude $210° \leqslant l \leqslant 250°$ and latitude $-15° \leqslant b \leqslant +20°$ hosts kinematically well-defined segments of the Local and the Perseus spiral arms and is one of the best regions to study the CR density distribution across the outer Galaxy. The region has already been studied by Digel et al. (2001) using EGRET data. The improved sensitivity and angular resolution of the *Fermi* LAT (Large Area Telescope; Atwood et al. 2009) and recent developments in the study of the ISM allow us to examine the CR spectra and density distribution with better accuracy. We exclude from the analysis the region of the Monoceros R2 giant molecular cloud and the Southern Filament of the Orion–Monoceros complex (e.g., Wilson et al. 2005), in $l \leqslant 222°$ and $b \leqslant -6°$, because (1) star-forming activity and possible high magnetic fields suggested by the filamentary structure (e.g., Morris et al. 1980; Maddalena et al. 1986) could indicate a special CR environment, and (2) an OB association in Monoceros R2 may hamper the determination of ISM densities from dust tracers (see Section 2.1.2 for details).

Study of the $X_{\rm CO}$ conversion factor which transforms the integrated intensity of the 2.6 mm line of carbon monoxide, $W_{\rm CO}$, into the molecular hydrogen column density, $N({\rm H_2})$, is also possible since the region contains well-known molecular complexes. In the Local arm, we find the molecular clouds associated with Canis Major OB 1, NGC 2348, and NGC 2632 (Mel'nik & Efremov 1995; Kaltcheva & Hilditch 2000). At a few kpc from the solar system, in the interarm, lower-density region located between the Local and Perseus arms, we find Maddalena's cloud (Maddalena & Thaddeus 1985), a giant molecular cloud remarkable for its lack of star formation, and the cloud associated with Canis Major OB 2 (Kaltcheva & Hilditch 2000).

This study complements the *Fermi* LAT study of the Cassiopeia and Cepheus region in the second quadrant reported by Abdo et al. (2010a). The paper is organized as follows. We describe the model preparation in Section 2 and the γ-ray observations, data selection, and the analysis procedure in Section 3. The results are presented in Section 4, where we also discuss the emissivity profile measured for the atomic gas and we compare it with predictions by a CR propagation model. A summary of the study is given in Section 5.

2. MODELING THE GAMMA-RAY EMISSION

2.1. Interstellar Gas

2.1.1. H I and CO

In order to derive the γ-ray emissivities associated with the different components of the ISM we need to determine the interstellar gas column densities separately for each region and gas phase. For atomic hydrogen we used the Leiden/Argentine/Bonn Galactic H I survey by Kalberla et al. (2005). In order to turn the H I line intensities into N(H I) column densities, a uniform spin temperature $T_{\rm S} = 125$ K has often been adopted in previous studies. We will consider this option to directly compare our results with the former EGRET analysis of the same region (Digel et al. 2001) and other studies of the Galactic diffuse emission by the LAT (Abdo et al. 2009a, 2010a). Recent H I absorption studies (Dickey et al. 2009), however, point to larger average spin temperatures in the outer Galaxy, so we have tried different choices of $T_{\rm S}$ to evaluate how the optical depth

[43] Royal Swedish Academy of Sciences Research Fellow, funded by a grant from the K. A. Wallenberg Foundation.
[44] Partially supported by the International Doctorate on Astroparticle Physics (IDAPP) program.

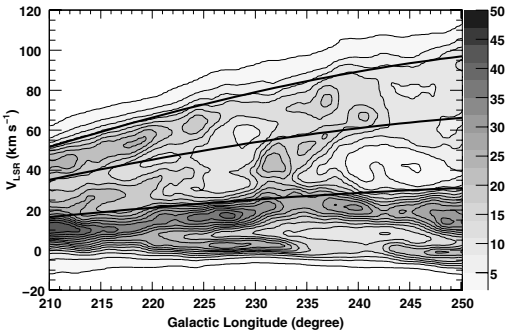

Figure 1. Longitude–velocity diagram of the average intensity of the 21 cm line (in unit of K) for $-15^\circ \leqslant b \leqslant 20^\circ$. Preliminary boundaries between the four Galactocentric annuli are also presented (see Section 2.1.1 for details). The lowest contour corresponds to 2 K and the contour interval is 3 K.

correction affects the results. We will find that the emissivity per H I atom and the inferred CR density is affected by up to ∼50% in the Perseus arm, and will take this uncertainty into account in the discussion.

The integrated intensities of the 2.6 mm line of CO, $W_{\rm CO}$, have been derived from the composite survey by Dame et al. (2001). The data have been filtered with the moment-masking technique in order to reduce the noise while keeping the resolution of the original data.

Figure 1 shows the velocity–longitude profile of H I emission in our region of interest (ROI). The preparation of maps accounting for the different Galactic structures present along the line of sight is similar to that described in detail in Abdo et al. (2010a) and based on a sequence of three steps:

1. preliminary separation within Galactocentric rings;
2. adjustment of the boundaries based on the velocity structures of the interstellar complexes;
3. correction for the spillover due to the velocity dispersion of the broad H I lines between adjacent regions.

Four regions were defined in Galactocentric distance, namely, the Local arm (Galactocentric radius $R \leqslant 10$ kpc), the interarm region ($R = 10$–12.5 kpc), the Perseus arm ($R = 12.5$–16 kpc), and the region beyond the Perseus arm (which hosts a faint segment of the outer arm; $R \geqslant 16$ kpc). The boundaries separating these regions under the assumption of a flat rotation curve (Clemens 1985) for the case of $R_0 = 8.5$ kpc and $\theta_0 = 220\,{\rm km\,s^{-1}}$ (where R_0 and θ_0 are the Galactocentric radius and the orbital velocity of the local group of stars, respectively) are overlaid in Figure 1.

The preparation of the H I and CO gas maps started from these preliminary velocity boundaries, which were then adjusted for each line of sight to the closest minimum in the H I spectrum.[45] Then, the spillover from one velocity interval to the next ones due to the velocity dispersion for the broad H I lines was corrected by fitting each H I spectrum with a combination of Gaussian profiles. We believe that this separation procedure provides more accurate estimates of the ISM column densities of each Galactic region than a simple slicing based on the rotation curve.

In particular, effort was put into separating the outer arm structures from the more massive Perseus arm component, especially at $l \gtrsim 235^\circ$ where the H I lines from the two regions merge into a single broad component. For directions where a minimum in the H I brightness temperature profile was not found near the $R = 16$ kpc velocity boundary, we integrated the profiles on both sides of the $R = 16$ kpc velocity boundary to estimate the Perseus and outer arm contributions. Then, we inserted a line in the Gaussian fitting at the outer-arm velocity extrapolated from the $l - v$ trend observed at $l \gtrsim 235^\circ$ to correct for the spillover due to the velocity dispersion. Given these difficulties we expect large systematic uncertainties in the outer-arm N(H I) column densities and the corresponding γ-ray emissivities will not be considered for the scientific interpretation. We note that the impact on the emissivities associated with the inner regions is small, $\leqslant$10% as described in Section 4.3.

The resulting maps are shown in Figures 2 and 3. They exhibit a low level of spatial degeneracy, and thus allow us to separate the γ-radiation arising from the interaction with CRs in each component.

2.1.2. Interstellar Reddening

It has been long debated whether the combination of H I and CO surveys traces total column densities of neutral interstellar matter. By comparing gas line surveys, the γ-ray observations by EGRET and dust thermal emission, Grenier et al. (2005) reported a considerable amount of neutral gas at the interface between the two H I and CO emitting phases, associated with cold dust but not properly traced by H I and CO observations. Their finding was then confirmed by LAT data for the Gould Belt in the second quadrant (Abdo et al. 2010a).

In order to complement the H I and CO maps, we have prepared a map derived from the $E(B - V)$ reddening map by Schlegel et al. (1998). The residual point sources at low latitudes were masked by setting to zero regions of 0.°2 radius centered on the positions of potential *IRAS* point sources[46] if the $E(B - V)$ magnitude exceeded by $\gtrsim$20% that in surrounding pixels. The masked regions were then restored through an inpainting technique (Elad et al. 2005). In the course of the work, various source masking techniques have been used with negligible impact on the H I and CO emissivity results.

The resulting map was fitted with a linear combination of the set of N(H I) and $W_{\rm CO}$ maps described in Section 2.1.1. The operation was repeated for different choices of H I spin temperature. The fit was performed over the same region as for the γ-ray analysis, excluding a $3^\circ \times 3^\circ$ region centered around Canis Major OB 1 (Mel'nik & Efremov 1995) where the temperature correction applied by Schlegel et al. (1998) to construct the $E(B - V)$ map from the dust thermal emission is highly uncertain. A preliminary fit had led to extremely negative residuals ($\leqslant -1$ mag) around $l = 224^\circ$, $b = -3^\circ$. Therefore, the residual $E(B - V)$ map was calculated masking this region in the fit. We are aware that the temperature corrections used by Schlegel et al. (1998) are less reliable with decreasing latitude, but the improvement we find in the γ-ray fit by adding the dust residual map supports the use of their map at low latitude.

The residual $E(B - V)_{\rm res}$ map, after subtracting the linear combination of N(H I) and $W_{\rm CO}$ maps, is shown in Figure 4 (left panel). The residuals typically range from -0.5 to $+0.5$ mag. Large regions of positive residuals are found along the Galactic plane, in association with molecular/atomic clouds. They are expected to trace gas not correctly traced by H I and CO

[45] The minima are unlikely to be due to self absorption, because the velocity-distance relation is single valued in the outer Galaxy.

[46] http://cdsarc.u-strasbg.fr/viz-bin/Cat?II/274. See Beichman et al. (1988).

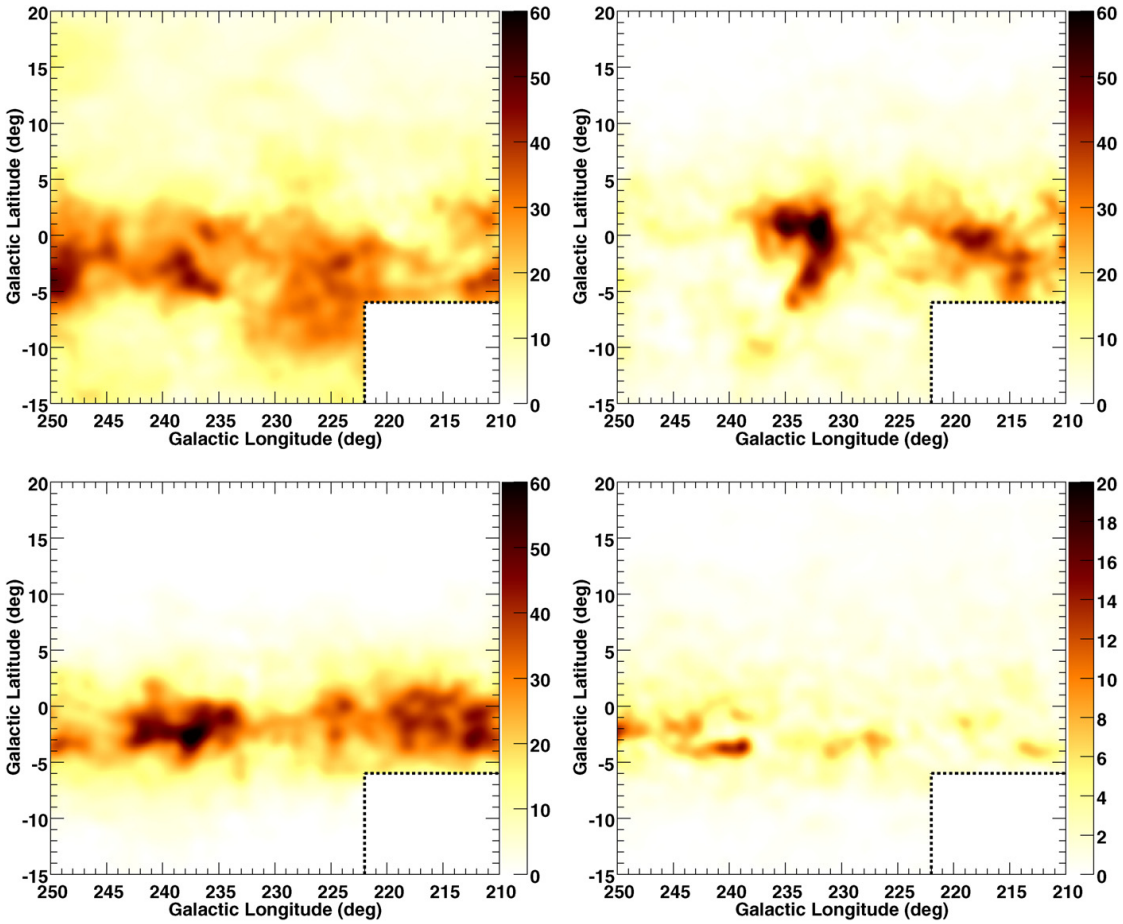

Figure 2. Maps of N(H I) (in unit of 10^{20} atoms cm^{-2}) for the Local arm (top left), interarm (top right), Perseus arm (bottom left), and outer arm (bottom right) regions obtained for a spin temperature $T_S = 125$ K. The outlined area in the bottom right corner is not used in the analysis (see Section 1). The maps have been smoothed with a Gaussian with $\sigma = 1^\circ$ for display.

(A color version of this figure is available in the online journal.)

surveys. A remarkable region of positive residuals is detected at intermediate latitudes around $l = 245^\circ$, $b = +17^\circ$, in a region not covered by CO surveys. It corresponds to positive residuals also in γ-rays (Section 3.2) and may be due to a missing, but possibly CO-bright molecular cloud (already suggested by Dame et al. 2001 discussing the completeness of their survey, see Figure 8 of their paper). The negative residuals are generally small and may result from limitations in the gas column density derivation and/or dust spectral variations. The dust residual map compares well with the γ-ray residual map obtained when using only H I and CO to model the γ-ray emission (Figure 4, right panel). The correlation between the spatial distributions of the dust and γ-ray residuals is statistically confirmed in Section 3.2. Dust and γ-rays are consistent with the presence of missing gas in the positive residual clumps. The faint "glow" of negative residuals on both sides of the Galactic plane is driven by the nearby N(H I) maps and it remains even when using the smallest possible column densities derived in the optically thin case. It may suggest a small change in average spin temperature from the massive, compact clouds sampled in the plane to the more diffuse envelopes sampled off the plane, or it may be due to the presence of more missing gas in the plane than our templates can provide for in the fit. The dust-to-gas ratio as well as the γ-ray emissivity in the H I components would then be driven to higher values by the low latitude data and would slightly overpredict the data off the plane.

The interpretation of the $E(B-V)_{\rm res}$ map in this region of the sky is complicated by the lack of distance information for the dust emission. It is not possible to unambiguously assign the residuals to any of the regions under study. Since we aim at separating different regions along the lines of sight to investigate the CR density gradient in the outer Galaxy, using the H I and CO lines is essential. We have therefore used the $E(B-V)_{\rm res}$ map to correct for the total gas column densities. This approach is supported by the correlation we find between the dust and γ-ray data (Section 3.2). We also note that, since the dust contribution linearly correlated with the H I and CO maps has been removed in the $E(B-V)_{\rm res}$ map, this procedure allows us to extract the

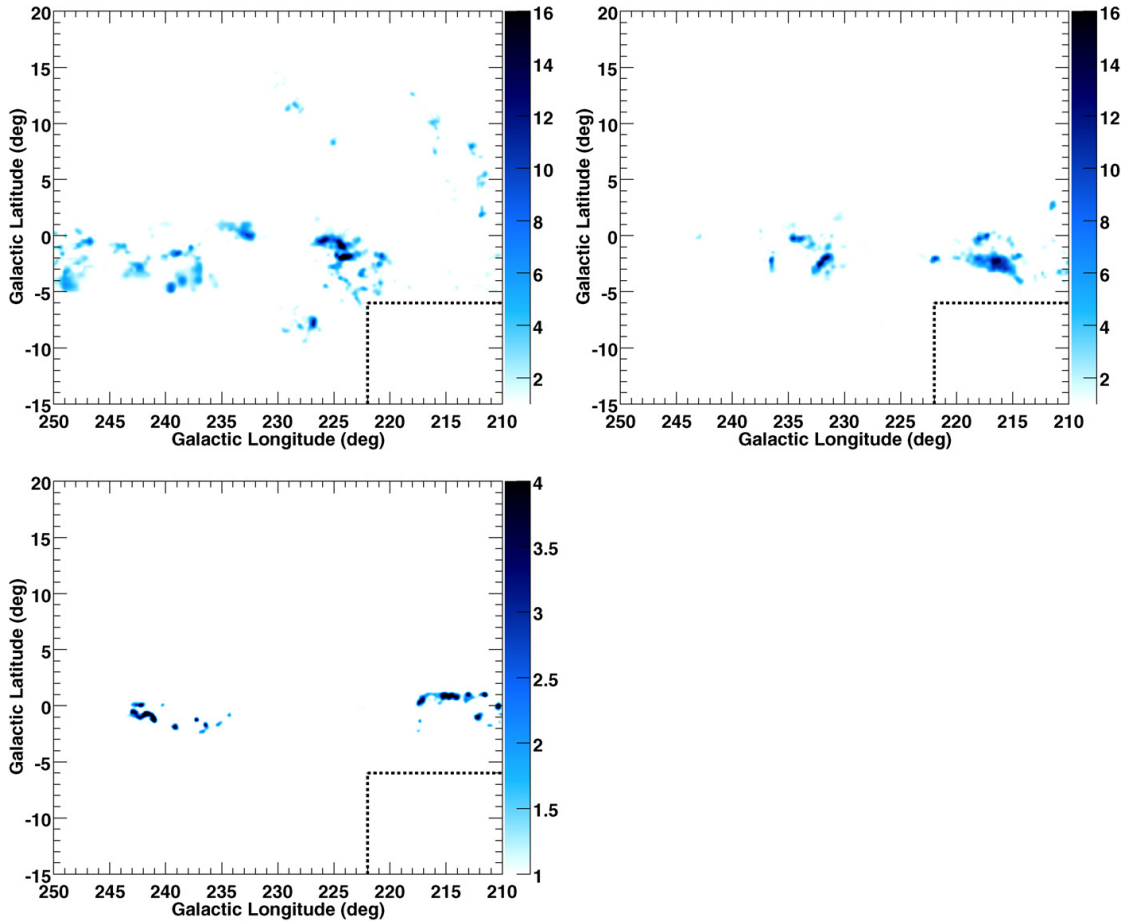

Figure 3. Maps of W_{CO} (in unit of K km s^{-1}) for the Local arm (top left), interarm (top right), and the Perseus arm (bottom left) regions. The small box in the bottom right corner indicates the area not considered in the analysis. The maps have been smoothed with a Gaussian of $\sigma = 0.^{\circ}25$ for display.
(A color version of this figure is available in the online journal.)

γ-ray emissivities that are actually correlated with the H I and CO components.

2.2. IC and Point Sources

To model γ-ray emission not related with interstellar gas, we referred to the GALPROP code (e.g., Strong & Moskalenko 1998; Strong et al. 2007) for γ-rays produced through IC scattering and to the first *Fermi* LAT catalog (1FGL) for point sources (Abdo et al. 2010b).

GALPROP[47] (Strong & Moskalenko 1998; Strong et al. 2007) is a numerical code which solves the CR transport equation within the Galaxy and predicts the γ-ray emission produced via interactions of CRs with interstellar matter (nucleon–nucleon interaction and electron Bremsstrahlung) and low-energy photons (IC scattering). IC emission is calculated from the distribution of (propagated) electrons and the interstellar radiation fields developed by Porter et al. (2008). Here we adopt the IC model map produced in the GALPROP run 54_77Xvarh7S in which the CR electron spectrum is adjusted to agree with that measured by the LAT (Abdo et al. 2009b). This GALPROP model has been used in publications by the LAT collaboration such as Abdo et al. (2010c).

The 1FGL Catalog is based on the first 11 months of the science phase of the mission and contains 1451 sources detected at a significance $\gtrsim 4\sigma$ (the threshold is 25 in term of test statistic, TS[48]). For our analysis we considered 21 point sources in the ROI with TS larger than 50.

[47] http://galprop.stanford.edu

[48] The test statistic is defined as

$$\mathrm{TS} = 2(\ln L - \ln L_0),$$

where L and L_0 is the maximum likelihood with and without including the source in the model, respectively. L is conventionally calculated as $\ln(L) = \Sigma_i n_i \ln(\theta_i) - \Sigma_i \theta_i$, where n_i and θ_i are the data and the model-predicted counts in each pixel denoted by the subscript i, respectively (see, e.g., Mattox et al. 1996). TS is expected to be distributed as a χ^2 with $n - n_0$ degrees of freedom if the numbers of free parameters in the model are respectively n and n_0 (4 for sources in the 1FGL Catalog).

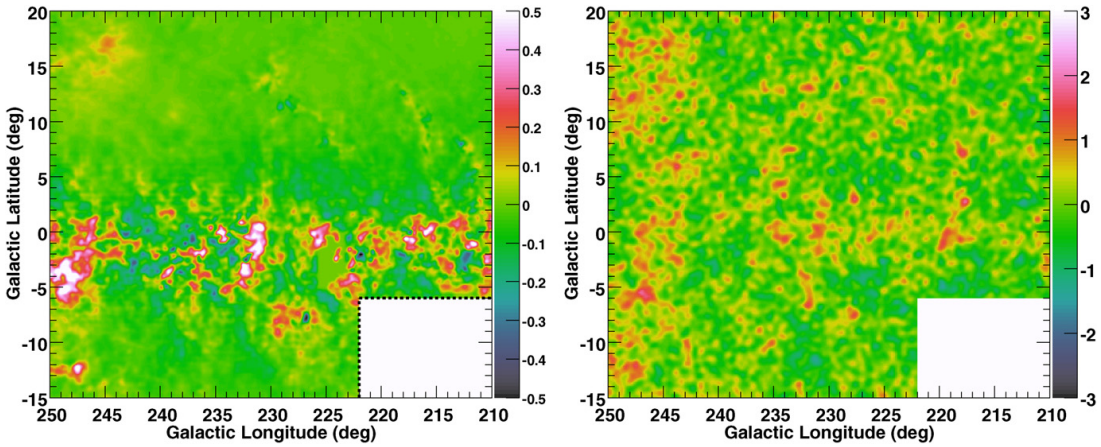

Figure 4. Left: residual $E(B-V)$ map in unit of magnitudes, obtained by subtracting the parts linearly correlated with the combination of $N(\mathrm{H\,I})$ and W_{CO} maps. The small box in the bottom right corner shows the area not considered in the analysis. The map has been smoothed with a Gaussian of $\sigma = 0.^{\circ}25$ for display. Right: γ-ray residual (data minus model) map obtained by the fit without the $E(B-V)_{\mathrm{res}}$ map (only H I and CO maps) in unit of standard deviations (square root of model-predicted counts, saturated between -3σ and $+3\sigma$). The map has been smoothed with a Gaussian of $\sigma = 0.^{\circ}5$.

2.3. Gamma-Ray Analysis Model

Following a well-established approach that dates back to the COS-B era (e.g., Lebrun et al. 1983), we modeled the γ-ray emission as a linear combination of maps tracing the column density of the ISM. This approach is based on a simple, but very plausible assumption: γ-rays are generated through interactions of CRs and the interstellar gas, and the ISM itself is transparent to γ-rays. Then, assuming that CR densities do not significantly vary over the scale of the interstellar complexes under study and that CRs penetrate clouds uniformly to their cores we can model the γ-ray intensities to first order as a linear combination of contributions from CR interactions with the different gas phases in the various regions along each line of sight.

We also added the IC model map by GALPROP and models for point sources taken from the 1FGL Catalog as described in Section 2.2. To represent the extragalactic diffuse emission and the residual instrumental background from misclassified CR interactions in the LAT detector, we also added an isotropic component. CR interactions with ionized gas are not explicitly included in the model. The mass column densities of ionized gas are poorly known, but their contribution is generally lower ($\leqslant 10\%$) than that of the neutral gas and its scale height is much larger ($\sim$1 kpc compared with $\sim$0.2 kpc; Cordes & Lazio 2002). We therefore expect the diffuse γ-ray emission originating from ionized gas to be largely accommodated in the fit by other components with large angular scales, such as the isotropic and IC ones, and to minimally impact the determination of the neutral gas emissivities.

Therefore, the γ-ray intensities $I_\gamma(l,b)$ ($\mathrm{s^{-1}\,cm^{-2}\,sr^{-1}\,MeV^{-1}}$) can be modeled as

$$I_\gamma(l,b) = \sum_{i=1}^{4} q_{\mathrm{H\,I},i} \cdot N(\mathrm{H\,I})(l,b)_i + \sum_{i=1}^{3} q_{\mathrm{CO},i} \cdot W_{\mathrm{CO}}(l,b)_i + q_{\mathrm{EBV}} \cdot E(B\text{-}V)_{\mathrm{res}}(l,b) + I_{\mathrm{IC}}(l,b) + I_{\mathrm{iso}} + \sum_j \mathrm{PS}_j, \quad (1)$$

where sum over i represents the combination of the Galactic regions, $q_{\mathrm{H\,I},i}$ ($\mathrm{s^{-1}\,sr^{-1}\,MeV^{-1}}$) and $q_{\mathrm{CO},i}$ ($\mathrm{s^{-1}\,cm^{-2}\,sr^{-1}\,MeV^{-1}}$ ($\mathrm{K\,km\,s^{-1}}$)$^{-1}$) are the emissivities per H I atom and per W_{CO} unit, respectively. q_{EBV} ($\mathrm{s^{-1}\,cm^{-2}\,sr^{-1}\,MeV^{-1}\,mag^{-1}}$) is the emissivity per unit of the $E(B-V)_{\mathrm{res}}$ map (for which independent normalizations are allowed between the positive and negative residuals; see Section 3.2). I_{IC} and I_{iso} are the IC model and isotropic background intensities ($\mathrm{s^{-1}\,cm^{-2}\,sr^{-1}\,MeV^{-1}}$), respectively, and PS_j represents the point-source contributions. Compared to the EGRET study by Digel et al. (2001), we use two additional maps to better trace the ISM: the CO map in the Perseus arm and the $E(B-V)_{\mathrm{res}}$ map.

3. DATA ANALYSIS

3.1. Observations and Data Selection

The LAT on board the *Fermi Gamma-ray Space Telescope*, launched on 2008 June 11, is a pair-tracking telescope, detecting photons from $\sim$20 MeV to more than 300 GeV. Details on the LAT instrument and pre-launch expectations of the performance can be found in Atwood et al. (2009), and the on-orbit calibration is described in Abdo et al. (2009c).

Routine science operations with the LAT started on 2008 August 4. We have accumulated events from 2008 August 4 to 2010 February 4 to study diffuse γ-rays in our ROI. During this time interval the LAT was operated in sky survey mode nearly all of the time, obtaining complete sky coverage every two orbits and relatively uniform exposures over time. We used the standard LAT analysis software, the *Science Tools*, and selected events satisfying the standard low-background event selection (the so-called *Diffuse* class; Atwood et al. 2009).[49] We also required the reconstructed zenith angles of the arrival direction of photons to be less than 105° and the center of the LAT field of view to be within 52° from the zenith, in order to reduce the contamination of photons from the Earth limb. In addition, we excluded the period of time during which the LAT detected bright GRBs, i.e., GRB080916C (Abdo et al. 2009d),

[49] Data and software are publicly available from the Fermi Science Support Center (http://fermi.gsfc.nasa.gov/ssc/). For this analysis we used the P6 *Diffuse* selection and the *Science Tools* version `v9r16p0`.

Table 1
A Summary of Fit Parameters with 1σ Statistical Errors, Under the Assumption of $T_S = 125$ K

Energy (GeV)	$E^2 \cdot q_{H1,1}$	$E^2 \cdot q_{H1,2}$	$E^2 \cdot q_{H1,3}$	$E^2 \cdot q_{H1,4}$	$E^2 \cdot q_{CO,1}$	$E^2 \cdot q_{CO,2}$	$E^2 \cdot q_{CO,3}$[a]	$E^2 \cdot q_{EBV_{pos}}$	$E^2 \cdot q_{EBV_{neg}}$	$E^2 \cdot q_{iso}$
0.10–0.14	1.19 ± 0.15	1.01 ± 0.18	0.88 ± 0.22	1.1 ± 1.1	0.0 ± 0.1	7 ± 6	6 ± 24	0.00 ± 0.08	1.04 ± 0.45	1.73 ± 0.14
0.14–0.20	1.43 ± 0.11	1.23 ± 0.13	1.14 ± 0.14	0.7 ± 0.8	4.3 ± 1.8	5.0 ± 2.9	0 ± 1	0.77 ± 0.36	0.35 ± 0.34	2.01 ± 0.09
0.20–0.28	1.60 ± 0.08	1.36 ± 0.10	1.25 ± 0.11	1.5 ± 0.6	5.0 ± 1.3	2.7 ± 2.0	0 ± 1	1.13 ± 0.26	0.32 ± 0.24	1.94 ± 0.07
0.28–0.40	1.79 ± 0.07	1.57 ± 0.08	1.25 ± 0.10	1.7 ± 0.5	8.6 ± 1.2	5.2 ± 1.6	11 ± 7	1.28 ± 0.21	0.45 ± 0.20	1.90 ± 0.06
0.40–0.56	1.81 ± 0.07	1.63 ± 0.08	1.61 ± 0.10	1.6 ± 0.5	7.5 ± 1.1	4.9 ± 1.4	8 ± 6	1.30 ± 0.17	0.87 ± 0.18	1.74 ± 0.06
0.56–0.80	1.91 ± 0.07	1.62 ± 0.07	1.50 ± 0.09	2.0 ± 0.5	6.7 ± 1.0	4.7 ± 1.3	3 ± 5	1.43 ± 0.17	0.88 ± 0.17	1.49 ± 0.06
0.80–1.13	1.75 ± 0.07	1.54 ± 0.07	1.48 ± 0.09	2.3 ± 0.5	8.7 ± 1.0	4.6 ± 1.3	16 ± 5	1.07 ± 0.16	0.88 ± 0.16	1.48 ± 0.06
1.13–1.60	1.64 ± 0.07	1.45 ± 0.08	1.42 ± 0.09	1.4 ± 0.5	6.0 ± 1.0	3.7 ± 1.3	11 ± 5	1.13 ± 0.16	0.76 ± 0.16	1.28 ± 0.06
1.60–2.26	1.60 ± 0.08	1.24 ± 0.08	1.07 ± 0.09	1.9 ± 0.5	6.0 ± 1.0	4.1 ± 1.3	7 ± 4	0.97 ± 0.16	0.53 ± 0.16	0.91 ± 0.07
2.26–3.20	1.26 ± 0.08	1.02 ± 0.08	0.94 ± 0.09	1.3 ± 0.5	3.2 ± 1.0	3.1 ± 1.3	3 ± 4	0.82 ± 0.16	0.58 ± 0.16	0.85 ± 0.07
3.20–4.53	0.80 ± 0.09	0.76 ± 0.08	0.75 ± 0.09	0.4 ± 0.5	5.7 ± 1.0	3.5 ± 1.3	11 ± 4	0.74 ± 0.16	0.42 ± 0.16	0.93 ± 0.08
4.53–6.40	0.59 ± 0.09	0.41 ± 0.08	0.57 ± 0.09	0.6 ± 0.5	2.9 ± 1.0	3.6 ± 1.3	0 ± 0	0.74 ± 0.16	0.02 ± 0.17	0.86 ± 0.08
6.40–9.05	0.51 ± 0.09	0.31 ± 0.08	0.28 ± 0.09	0.9 ± 0.5	2.2 ± 1.0	1.0 ± 1.1	2 ± 3	0.52 ± 0.15	0.07 ± 0.16	0.62 ± 0.08
9.05–25.6	0.34 ± 0.05	0.22 ± 0.05	0.09 ± 0.05	0.7 ± 0.3	2.2 ± 0.6	1.4 ± 0.7	3 ± 2	0.07 ± 0.06	0.06 ± 0.08	0.49 ± 0.05

Notes. Units: $E^2 \cdot q_{H1,i}(10^{-24}\,\mathrm{MeV^2\,s^{-1}\,sr^{-1}\,MeV^{-1}})$, $E^2 \cdot q_{CO,i}(10^{-4}\,\mathrm{MeV^2\,s^{-1}\,cm^{-2}\,sr^{-1}\,MeV^{-1}(K\,km\,s^{-1})^{-1}})$, $E^2 \cdot q_{EBV}(10^{-2}\,\mathrm{MeV^2\,s^{-1}\,cm^{-2}\,sr^{-1}\,MeV^{-1}\,mag^{-1}})$, $E^2 \cdot q_{iso}(10^{-3}\,\mathrm{MeV^2\,s^{-1}\,cm^{-2}\,sr^{-1}\,MeV^{-1}})$. The subscripts refer to four regions defined to perform the analysis: (1) Local arm, (2) interarm region, (3) Perseus arm, and (4) beyond the Perseus arm.
[a] Some parameters are not well determined and their best-fit value is consistent with 0. We present them for completeness.

GRB090510 (Abdo et al. 2009e), GRB090902B (Abdo et al. 2009f), and GRB090926A (Abdo et al. 2010e).

3.2. Analysis Procedure

The model described by Equation (1) was fitted to the data using the *Science Tools*, which take into account the energy-dependent instrument point-spread function and effective area. We have analyzed the LAT data from 100 MeV to 25.6 GeV using 13 logarithmically spaced energy bands from 100 MeV to 9.05 GeV, and a single band above 9.05 GeV. We then have compared the model and data in each energy band using a binned maximum-likelihood method with Poisson statistics (in $0.^\circ25 \times 0.^\circ25$ bins); we thus did not assume an a priori spectral shape of each model component except for the IC emission. For the other components the convolution with the instrument response functions was performed assuming an E^{-2} spectrum, and the integrated intensities were allowed to vary in each narrow energy bin. Changing the fixed spectral shape index over the range from -1.5 to -3.0 has a negligible effect on the obtained spectrum. In the highest energy band, we have set both the normalization and the spectral index free to accommodate the wider bin width. We used a post-launch response function, P6_V3_DIFFUSE, developed to account for the γ-ray detection inefficiencies due to pile-up and accidental coincidence in the LAT (Rando et al. 2009). We stopped at 25.6 GeV since the photon statistics do not allow us to reliably separate different gas components above this energy.

We started with point sources detected with high significance ($TS \geqslant 100$) in the 1FGL Catalog; we have 14 sources in our ROI for which the normalizations are set free. We also included eight sources lying just outside ($\leqslant 5^\circ$) of the region boundaries, with all the spectral parameters fixed to those in the 1FGL Catalog. As a starting point we used H I maps prepared for $T_S = 125$ K. We added model components step by step as described below.

We first fitted the LAT data using Equation (1) without the $E(B-V)_{res}$ map and the CO map in the Perseus arm, and then included the CO map and confirmed that the fit improved significantly; the TS summed over 14 bands with separate fits in each band (i.e., 14 more free parameters) is 187.6. The γ-ray emission associated to the gas traced by CO in the Perseus arm is thus significantly detected by the LAT.

Next, we included the $E(B-V)_{res}$ map in the analysis. We allowed the independent normalizations between the positive part and the negative part of the $E(B-V)_{res}$ map, and found that the normalizations differ with each other. We thus will use the independent normalizations hereafter. We chose this model to better represent the LAT data and constrain the CR distributions, and leave a detailed discussion about the use of dust as ISM tracer to a dedicated paper. The improvement of the fit is very significant: $TS = 1119.6$ for 28 more free parameters. The correlation between the $E(B-V)_{res}$ map and the γ-ray residual map obtained by the fit without the $E(B-V)_{res}$ map, shown in Figure 4, further supports the use of $E(B-V)_{res}$ map in our analysis.

We also tried a fit without the IC component to assess the systematics. The effects on the derived emissivities are typically 2%–3% and ~5% for $q_{H\,I}$ and q_{CO}, respectively. They are much smaller than the statistical errors and systematic uncertainties (see below), although the inclusion of the IC map improves the fit to the LAT data. Therefore, the uncertainties on the IC model have no significant impact on our analysis due to its rather flat distribution across the ROI while the gas in the ISM is highly structured. On the other hand, lowering the threshold for point sources down to $TS = 50$ yields an about twice smaller emissivity for the W_{CO} map in the Perseus arm. The emissivities of other components are unchanged within the statistical errors. This is plausibly due to the very clumpy distribution of the clouds in the Perseus arm as seen by a terrestrial observer, see Figure 3, which makes it difficult to separate from that of some discrete sources. We thus use Equation (1) with point sources detected at $TS \geqslant 50$ in the 1FGL Catalog[50] as our baseline model, but we do not consider the highly uncertain CO emissivities in the Perseus arm for the discussion.

We summarize the results in Tables 1 and 2 for $T_S = 125$ K and 250 K, respectively, and the number of counts in each energy bin in Table 3. The differential emissivities are multiplied by E^2

[50] Spectral parameters of point sources of $TS = 50$–100 are fixed to those given in the 1 FGL Catalog in the highest energy bin. (9.05–25.6 GeV).

Table 2
A Summary of Fit Parameters with 1σ Statistical Errors, Under the Assumption of $T_S = 250$ K

Energy (GeV)	$E^2 \cdot q_{H\,I,1}$	$E^2 \cdot q_{H\,I,2}$	$E^2 \cdot q_{H\,I,3}$	$E^2 \cdot q_{H\,I,4}$	$E^2 \cdot q_{CO,1}$	$E^2 \cdot q_{CO,2}$	$E^2 \cdot q_{CO,3}$[a]	$E^2 \cdot q_{EBV_{pos}}$	$E^2 \cdot q_{EBV_{neg}}$	$E^2 \cdot q_{iso}$
0.10–0.14	1.35 ± 0.07	1.09 ± 0.11	1.20 ± 0.11	1.0 ± 0.7	0.1 ± 0.7	9 ± 6	7 ± 66	0.00 ± 0.03	0.96 ± 0.18	1.68 ± 0.07
0.14–0.20	1.56 ± 0.13	1.33 ± 0.15	1.55 ± 0.17	0.5 ± 0.8	5.2 ± 1.8	7.1 ± 3.0	0 ± 1	0.79 ± 0.33	0.44 ± 0.29	1.97 ± 0.10
0.20–0.28	1.82 ± 0.10	1.37 ± 0.11	1.66 ± 0.13	1.2 ± 0.6	6.2 ± 1.3	6.1 ± 2.0	0 ± 1	1.11 ± 0.23	0.24 ± 0.20	1.83 ± 0.07
0.28–0.40	2.00 ± 0.09	1.70 ± 0.09	1.69 ± 0.12	1.7 ± 0.6	9.7 ± 1.2	7.5 ± 1.6	13 ± 8	1.19 ± 0.19	0.55 ± 0.17	1.83 ± 0.06
0.40–0.56	1.95 ± 0.08	1.76 ± 0.09	2.11 ± 0.11	1.5 ± 0.5	8.4 ± 1.1	7.0 ± 1.4	9 ± 6	1.33 ± 0.14	0.83 ± 0.14	1.68 ± 0.06
0.56–0.80	2.10 ± 0.08	1.76 ± 0.08	2.01 ± 0.11	2.1 ± 0.5	7.6 ± 1.0	6.4 ± 1.3	4 ± 5	1.33 ± 0.15	0.92 ± 0.14	1.42 ± 0.06
0.80–1.13	1.90 ± 0.08	1.70 ± 0.08	1.95 ± 0.10	2.4 ± 0.5	9.6 ± 1.0	6.1 ± 1.3	17 ± 5	1.03 ± 0.14	0.88 ± 0.14	1.41 ± 0.06
1.13–1.60	1.79 ± 0.09	1.59 ± 0.09	1.90 ± 0.10	1.4 ± 0.5	6.7 ± 1.0	5.0 ± 1.3	11 ± 5	1.05 ± 0.14	0.79 ± 0.14	1.23 ± 0.07
1.60–2.26	1.74 ± 0.09	1.36 ± 0.09	1.45 ± 0.11	2.0 ± 0.5	6.6 ± 1.0	5.0 ± 1.3	7 ± 4	0.98 ± 0.15	0.57 ± 0.14	0.85 ± 0.07
2.26–3.20	1.37 ± 0.10	1.13 ± 0.09	1.25 ± 0.11	1.5 ± 0.5	3.7 ± 1.0	3.8 ± 1.3	3 ± 4	0.80 ± 0.14	0.57 ± 0.14	0.79 ± 0.08
3.20–4.53	0.84 ± 0.10	0.85 ± 0.09	0.99 ± 0.11	0.4 ± 0.5	6.1 ± 1.0	4.0 ± 1.3	11 ± 4	0.71 ± 0.14	0.43 ± 0.14	0.91 ± 0.08
4.53–6.40	0.65 ± 0.10	0.48 ± 0.09	0.74 ± 0.11	0.7 ± 0.5	3.2 ± 1.0	3.9 ± 1.3	0 ± 0	0.65 ± 0.15	0.13 ± 0.15	0.84 ± 0.09
6.40–9.05	0.54 ± 0.10	0.34 ± 0.09	0.37 ± 0.10	0.9 ± 0.5	2.5 ± 1.0	1.1 ± 1.1	2 ± 3	0.55 ± 0.14	0.06 ± 0.15	0.59 ± 0.09
9.05–25.6	0.38 ± 0.08	0.23 ± 0.13	0.13 ± 0.10	0.7 ± 0.4	2.3 ± 0.6	1.5 ± 0.7	3 ± 2	0.1 ± 0.3	4 ± 1	0.45 ± 0.14

Notes. Units: $E^2 \cdot q_{H\,I,i}(10^{-24}\,\mathrm{MeV^2\,s^{-1}\,sr^{-1}\,MeV^{-1}})$, $E^2 \cdot q_{CO,i}(10^{-4}\,\mathrm{MeV^2\,s^{-1}\,cm^{-2}\,sr^{-1}\,MeV^{-1}(K\,km\,s^{-1})^{-1}})$, $E^2 \cdot q_{EBV}(10^{-2}\,\mathrm{MeV^2\,s^{-1}\,cm^{-2}\,sr^{-1}\,MeV^{-1}\,mag^{-1}})$, $E^2 \cdot q_{iso}(10^{-3}\,\mathrm{MeV^2\,s^{-1}\,cm^{-2}\,sr^{-1}\,MeV^{-1}})$. The subscripts refer to four regions defined to perform the analysis: (1) Local arm, (2) interarm region, (3) Perseus arm, (4) beyond the Perseus arm.
[a] Some parameters are consistent with 0 and thus are not well determined. We present them for reference.

Table 3
Number of Counts in Each Energy Bin

Energy (GeV)	Counts
0.10–0.14	26673
0.14–0.20	71637
0.20–0.28	91336
0.28–0.40	93286
0.40–0.56	78330
0.56–0.80	61337
0.80–1.13	45386
1.13–1.60	30713
1.60–2.26	19351
2.26–3.20	11301
3.20–4.53	6426
4.53–6.40	3761
6.40–9.05	2095
9.05–25.6	2333

where E is the center of each energy bin in logarithmic scale. They are given for each model component. We note that our isotropic term (I_{iso}) includes the contribution of the instrumental background and might partially account also for ionized gas (see Section 2.3), thus it is significantly larger than the extragalactic diffuse emission reported by Abdo et al. (2010d).

To illustrate the fit quality, we give the data and model count maps and the residual map in Figure 5 (for $T_S = 125$ K), in which residuals (data minus model) are expressed in approximate standard deviation units (square root of model-predicted counts). Although some structures (clustering of positive or negative residuals) are observed, the map shows no excesses below -4σ and above 6σ. Over 99% of the pixels are within $\pm 3\sigma$. We thus conclude that our model reasonably reproduces the data.

Figure 6 presents the fitted spectra for each component. The emission from the H I gas dominates the γ-ray flux. Although the emission from the gas in the CO-bright phase and that traced by $E(B-V)_{res}$ is fainter than the IC and isotropic components, their characteristic spatial structures (see Figures 2 and 3) allow their spectra to be reliably constrained.

To examine the effect of the optical depth correction applied to derive the H I maps, as anticipated above we tried several choices of a uniform T_S. We stress that the true T_S is likely to vary within clouds, but we stick to this simple approximation exploring the following values: 100 K (which is a reasonable lower limit in the uniform approximation),[51] 250 K and 400 K (which are the two values indicated by absorption measurements in the outer Galaxy by Dickey et al. 2009),[52] and the optically thin approximation (which yields the lower limit allowed on the atomic column densities). The results on the maximum log-likelihood values are summarized in Table 4 together with the integrated H I emissivities obtained above 100 MeV in each region. The evolution of $\ln(L)$ with T_S is plotted in Figure 7. The H I emissivity varies by $+15\%/-10\%$ for the Local arm, $+10\%/-0\%$ for the interarm region, and $+50\%/-25\%$ for the Perseus arm with respect to the $T_S = 125$ K case. We observe an increase of $\ln(L)$ with increasing spin temperature. Considering the fact that $T_S = 250$ K is a typical value in the second quadrant of the outer Galaxy according to a recent study by Dickey et al. (2009) and because $\ln(L)$ saturates at $T_S \geqslant 250$ K, we regard 250 K as a plausible estimate of the average T_S in our ROI. Unfortunately, the estimates by Dickey et al. (2009) have a rather large uncertainty (about ± 50 K) in each Galactocentric radius bin, and they do not cover the region in the third quadrant we are investigating (see Figure 5 of Dickey et al. 2009). In the following sections, we will concentrate on $T_S = 125$ K for comparison with previous γ-ray measurements and on $T_S = 250$ K which agrees well with H I absorption and the LAT data.

4. RESULTS AND DISCUSSIONS

4.1. Emissivity Spectra of Atomic Gas

In Figures 8 and 9 (left panels), we report the emissivity spectra found per H atom in the Local arm, interarm, Perseus arm

[51] A truncation at 95 K was applied for channels where the brightness temperature was larger.
[52] Note that, however, the data used by Dickey et al. (2009) do not cover the third Galactic quadrant.

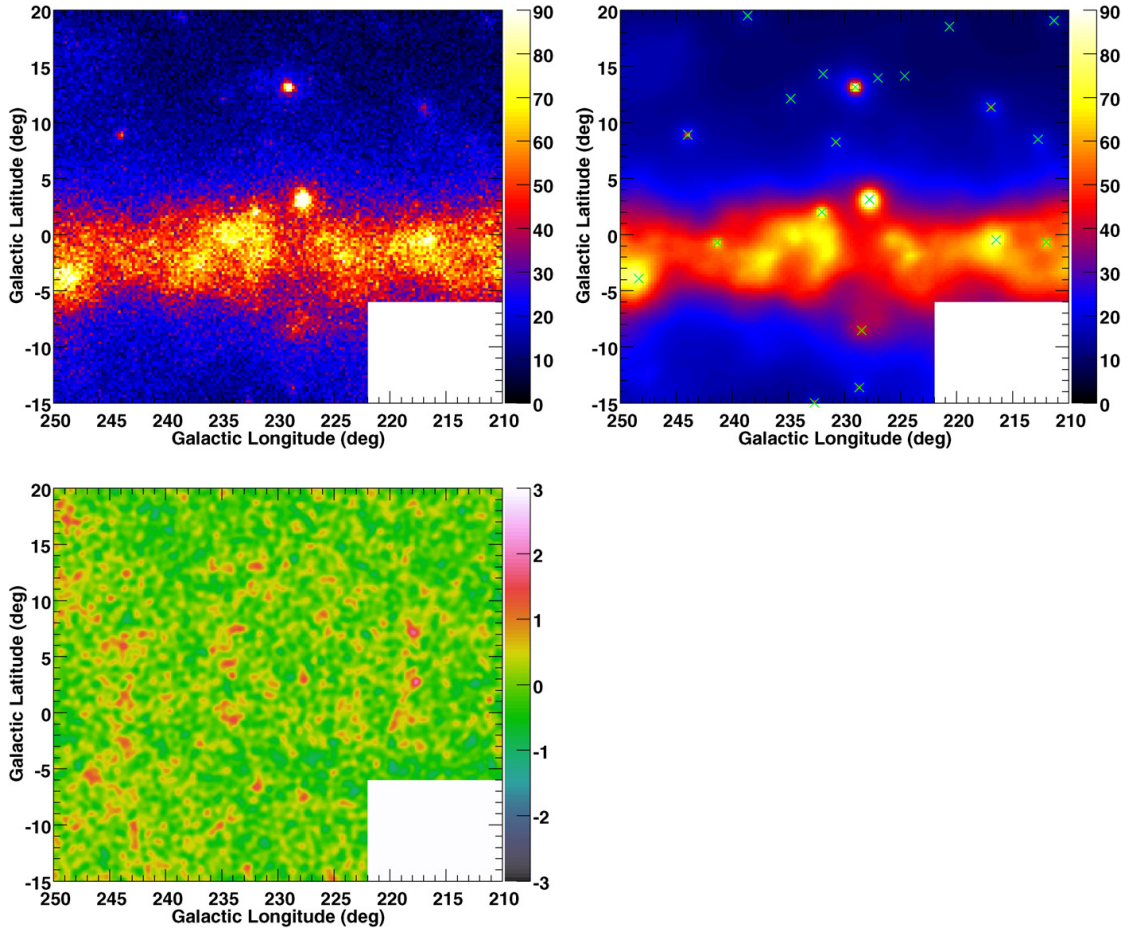

Figure 5. Data count map (top left), model count map (top right), and the residual (data minus model) map in units of standard deviations (bottom left, saturated between -3σ and $+3\sigma$) above 100 MeV obtained by our analysis. Point sources with $TS \geqslant 50$ in the 1FGL included in the fit are shown by crosses in the model map. Data/model count maps are in $0.^{\circ}25 \times 0.^{\circ}25$ pixels, and the residual map has been smoothed with a Gaussian of $\sigma = 0.^{\circ}5$.

Table 4
Log-likelihood and Emissivities for Several Choices of T_S

T_S	ln(L)	$q_{H1,1}(E \geqslant 100\,\mathrm{MeV})$	$q_{H1,2}(E \geqslant 100\,\mathrm{MeV})$	$q_{H1,3}(E \geqslant 100\,\mathrm{MeV})$
100 K	114407.6	1.32 ± 0.04	1.27 ± 0.05	0.86 ± 0.06
125 K	114480.1	1.47 ± 0.05	1.26 ± 0.06	1.14 ± 0.08
250 K	114533.8	1.62 ± 0.04	1.35 ± 0.05	1.53 ± 0.06
400 K	114544.5	1.67 ± 0.07	1.39 ± 0.08	1.64 ± 0.09
Optically thin	114552.8	1.70 ± 0.07	1.39 ± 0.07	1.77 ± 0.09

Notes.
[a] Units: $q_{H1,i}(10^{-26}$ photons s^{-1} sr^{-1} H-atom$^{-1})$.
[b] The subscripts refer to the regions defined to perform the analysis: (1) Local arm, (2) interarm region, (3) Perseus arm.

and outermost regions for $T_S = 125$ and 250 K, respectively. For comparison with the local interstellar spectrum (LIS) we also plot the model spectrum used in Abdo et al. (2009a) which agrees well with LAT data in a mid-to-high-latitude region ($22^{\circ} \leqslant |b| \leqslant 60^{\circ}$) of the third quadrant (assuming $T_S = 125$ K). We see that the spectral shape of the Local arm emissivity agrees well with the model for the LIS and does not depend on the choice of spin temperature. The integral emissivity of the Local arm is 10% lower than that reported by Abdo et al. (2009a) for the same spin temperature. This difference is not significant given the uncertainties in the kinematic separation of the gas components. The present result is also consistent with the measurement in the second quadrant (Abdo et al. 2010a). Together they show that the CR density along the Local arm is rather uniform within 1 kpc around the Sun, both in the second and third quadrants.

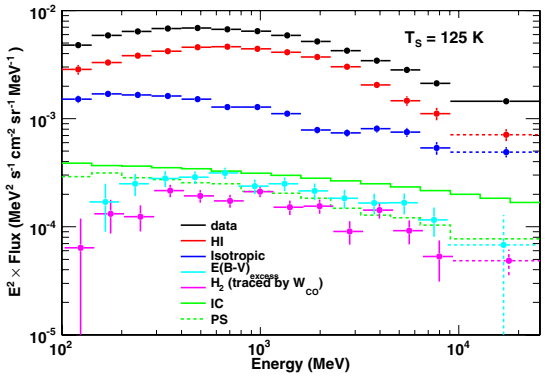

Figure 6. γ-ray spectra over the region of interest obtained from data and from the fitted model (for each gas phase, IC and isotropic components, and for point sources).

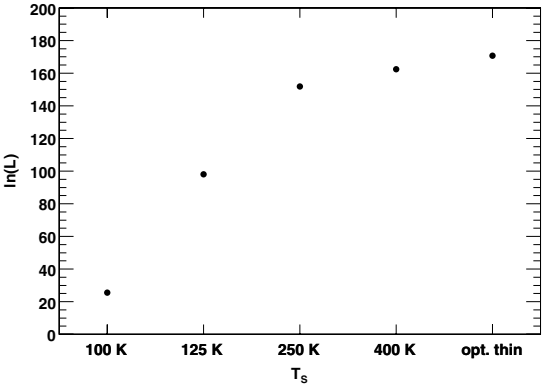

Figure 7. Variations of the log-likelihood value for several choices of T_S (the scale has a fixed offset).

The comparison of the data with the model emissivity expected for the Local arm region based on locally measured CRs (Figures 8 and 9) indicates a better fit for higher T_S; $T_S = 125$ K gives emissivities 15%–20% lower than the model, whereas $T_S = 250$ K shows better agreement by about 10%. Although the theoretical emissivity has uncertainties due to imperfect knowledge of the CR spectrum (see Abdo et al. 2009a), the fact that a high T_S value yields a better match both to the local absolute emissivity and to the spatial distribution of the diffuse emission (Figure 7) leads to larger T_S than a value conventionally used in γ-ray astrophysics (125 K). This is in accord with independent estimates of T_S as discussed in Section 3.2.

We also observe that the emissivity spectra do not vary significantly with Galactocentric distances in the outer Galaxy. To examine the spectral shape more quantitatively, we present the emissivity ratios of the interarm and Perseus regions relative to the Local arm in the right panels of Figures 8 and 9. The spectral shape in the interarm region is found to be consistent with that in the Local arm; a fit to the data for $T_S = 125$ K with a constant ratio gives $\chi^2 = 7.3$ for 13 degrees of freedom. Although the fit is not fully acceptable for the Perseus arm ($\chi^2 = 24.3$), the large χ^2 is driven solely by the last bin. We note a possible interplay between the Perseus arm and the adjacent outer-arm emissivities in the highest energy bins (see left panels of Figures 8 and 9). It can be due to a small but non-negligible spatial difference between the modeled templates and data and/or to the presence of unresolved point sources (generally harder than diffuse emission). Photon fluctuations from the structured gas components can also lead the fit to a slightly different solution in the spatial separation of the components. One would expect these possible systematic uncertainties to become important at high energy given the limited counts in the overall map. It is difficult to quantitatively test these effects without knowledge of the true model distributions, but we can note that the small deviations seen at 400–560 MeV and 1.6–2.2 GeV from a constant ratio are not confirmed by the general trend of the other points. They indicate that there are systematic uncertainties not fully accounted for by the statistical errors in the fit. We thus do not claim nor deny the spectral softening of the Perseus arm at high energy. A test using $T_S = 250$ K for the N(H I) maps gives the same conclusion on the spectral shape. We thus conclude that the spectral shapes are consistent with the LIS in the 0.1–6 GeV energy band, independent of the assumed T_S. Considering that these γ-rays trace CR nuclei of energies from a few GeV to about 100 GeV (see, e.g., Figure 11 of Mori 1997), LAT data indicate that the energy distribution of the main

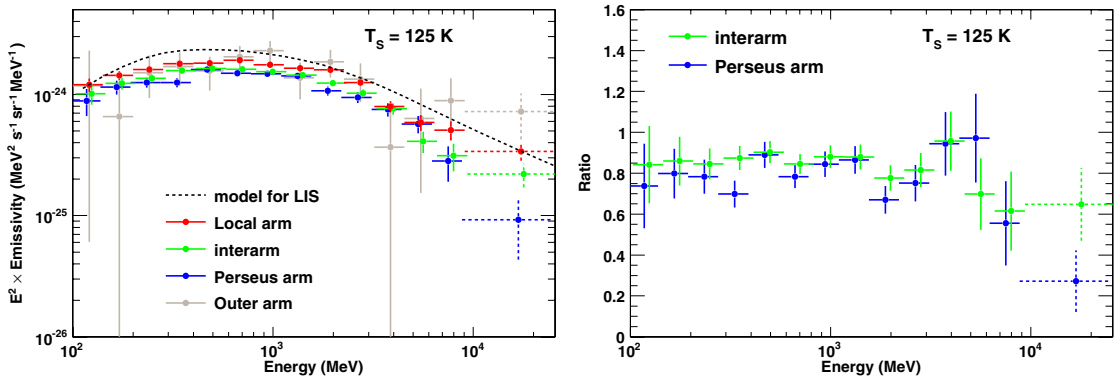

Figure 8. Left: H I emissivity spectra obtained for each region. For reference, the emissivity model spectrum for the LIS adopted by Abdo et al. (2009a) is shown by the black dotted line. Right: The emissivity ratios to that of the Local arm. In both panels, $T_S = 125$ K is assumed and spectra in the interarm region and the Perseus arm are shifted horizontally for clarity.

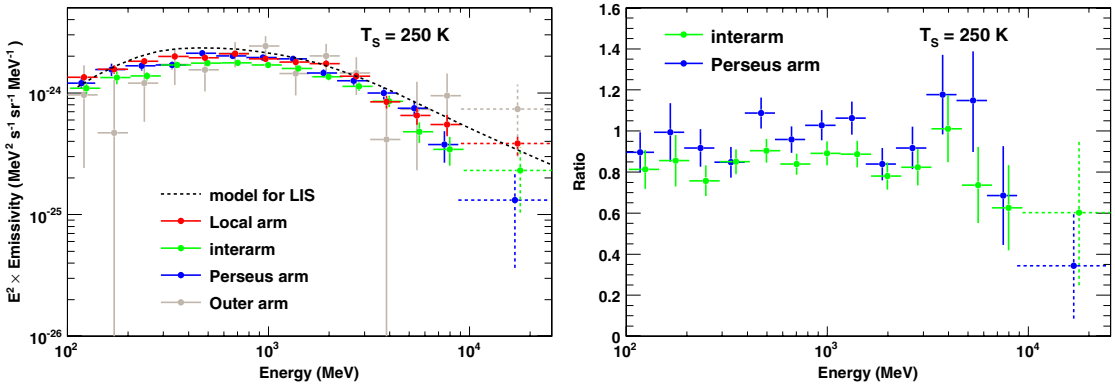

Figure 9. Same as Figure 8 but for $T_S = 250$ K.

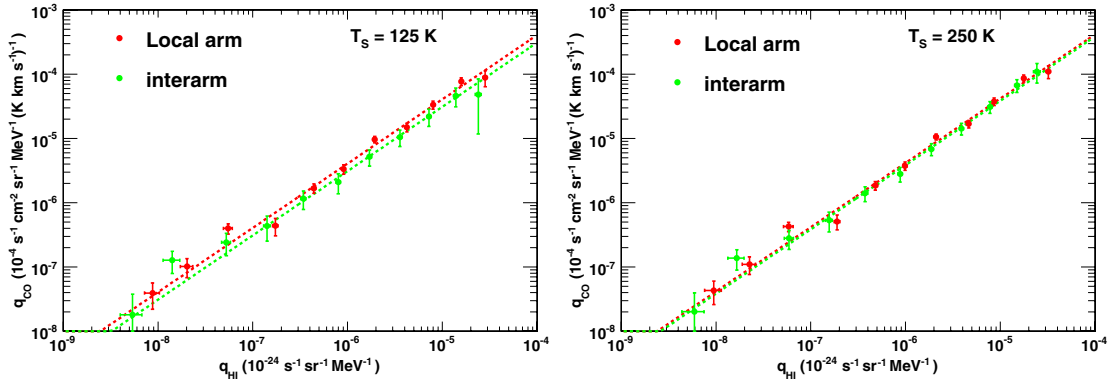

Figure 10. Correlation between the H I and CO emissivities in the 200 MeV–9.05 GeV energy range for the Local arm and the interarm regions. The cases of $T_S = 125$ K and 250 K are shown in the left panel and the right panel, respectively. Dotted lines show the best linear fits. Each data point corresponds to an energy bin used in the γ-ray analysis. (See Tables 1 and 2)

component of Galactic CRs does not vary significantly in the outer Galaxy in the third quadrant. We note that Abdo et al. (2010a) reported a possible spectral hardening in the Perseus arm in the second quadrant. This might be due to the presence of the very active star-forming region of NGC 7538 and of CRs having not diffused far from their sources, or to contamination by hard unresolved point sources. In fact, Abdo et al. (2010a) did not rule out the possibility that their result is due to systematic effects.

4.2. Calibration of Molecular Masses

High-energy γ-rays are a powerful probe to determine the CO-to-H_2 calibration ratio, X_{CO}, if the CR flux is comparable in the different gas phases inside a cloud. Since the γ-ray emission from the molecular gas is primarily due to CR interactions with H_2, and since the molecular binding energy is negligible in processes leading to γ-ray production, the emissivity per H_2 molecule is expected to be twice the emissivity per H I atom. Then, under the hypothesis that the same CR flux penetrates the H I- and CO-bright phases of an interstellar complex, we can calculate X_{CO} as $q_{CO} = 2X_{CO} \cdot q_{H_I}$.

We show q_{CO} as a function of q_{H_I} for the Local arm and the interarm region in Figure 10. We do not consider the correlation in the Perseus arm, because q_{CO} from this region is affected by large systematic uncertainties (see Section 3.2). Since the emissivity associated with the CO-bright gas is not well determined in the lowest energy range (see Tables 1 and 2) because of the poor angular resolution of the LAT, and the fit at very high energy is affected by larger uncertainties (Section 4.1), we have plotted only data in the 200 MeV–9.05 GeV range. The linear correlation supports the assumption that Galactic CRs penetrate molecular clouds uniformly to their cores. It also suggests that contamination from point sources and CR spectral variations within the clouds are small.

We have derived the maximum-likelihood estimates of the slope and intercept of the linear relation between q_{CO} and q_{H_I} taking into account that q_{CO} and q_{H_I} are both measured (not true) values with known uncertainties. The resulting intercepts are compatible with zero. The X_{CO} values we have obtained for $T_S = 250$ K are $(2.08 \pm 0.11) \times 10^{20}$ cm^{-2}(K km s^{-1})$^{-1}$ for the Local arm ($R \leqslant 10$ kpc) and $(1.93 \pm 0.16) \times 10^{20}$cm^{-2}(K km s^{-1})$^{-1}$ for the interarm regions ($R = 10$–12.5 kpc). Decreasing the spin temperature to 125 K does not affect the X_{CO} derivation in the well resolved, not too massive, clouds of the Local arm where we find $X_{CO} = (2.03 \pm 0.11) \times 10^{20}$ cm^{-2}(K km s^{-1})$^{-1}$. On the other hand, the separation in the γ-ray fit between the dense H I peaks and clumpy CO cores becomes more difficult for more distant, less resolved clouds where H I and CO tend to peak in the same directions. A change in the largest N(H I) column

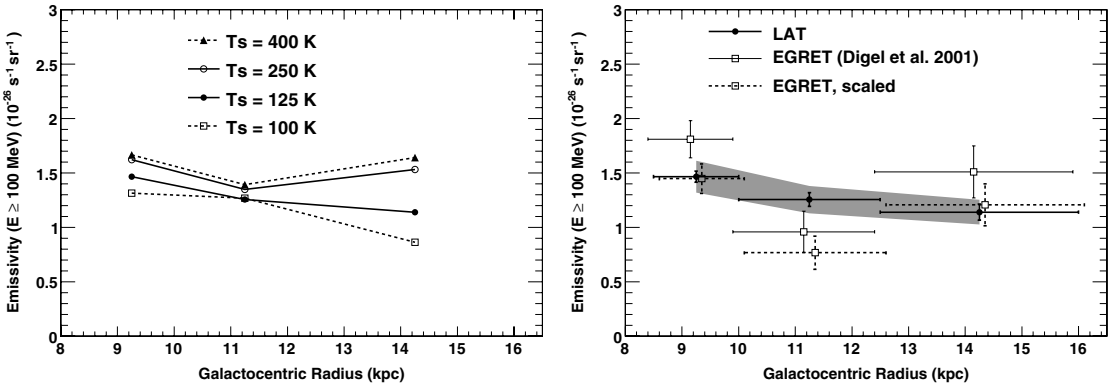

Figure 11. Left: emissivity gradient for several choices of T_S. Right: emissivity gradient obtained by the LAT compared with the EGRET results under the assumption of $T_S = 125$ K. The shaded area indicates the systematic uncertainty in the LAT selection efficiency of ∼10%. The EGRET points have been downscaled by 20% to account for the change in H I survey data between the two studies (see Section 4.3.1).

densities from the optical depth correction can impact the X_{CO} determination in two ways: first by changing the q_{HI} emissivity and second by modifying the N(H I) contrast within the cloud, hence the H I and CO separation. The global impact is mild since we find $X_{CO} = (1.56 \pm 0.17) \times 10^{20}\,\mathrm{cm^{-2}(K\,km\,s^{-1})^{-1}}$ in the interarm region for $T_S = 125$ K.

Abdo et al. (2010a) reported comparable values of X_{CO} in the second quadrant for $T_S = 125$ K: they obtained $(1.59 \pm 0.17) \times 10^{20}\,\mathrm{cm^{-2}(K\,km\,s^{-1})^{-1}}$ and $(1.9 \pm 0.2) \times 10^{20}\,\mathrm{cm^{-2}(K\,km\,s^{-1})^{-1}}$ for the Local arm ($R \leqslant 10$ kpc) and the Perseus arm. Given the systematic uncertainty in X_{CO}, roughly of the order of $0.3 \times 10^{20}\,\mathrm{cm^{-2}(K\,km\,s^{-1})^{-1}}$, due to H I optical depth correction, the results of both studies point to a rather uniform ratio over several kpc in the outer Galaxy. Yet, these values are twice larger than found in the very nearby Gould-Belt clouds of Cassiopeia and Cepheus, $X_{CO} = (0.87 \pm 0.05) \times 10^{20}\,\mathrm{cm^{-2}(K\,km\,s^{-1})^{-1}}$, $T_S = 125$ K. However, we confirm that the increase in X_{CO} beyond the solar circle is significantly lower than the trend adopted in the model of Strong et al. (2004b). What fraction of the Gould-Belt to Local arm differences in the average X_{CO} can be attributed to a difference in the spatial sampling (resolution) of the clouds remains to be investigated.

Nearly the same region has been analyzed by Digel et al. (2001) using EGRET data. The main difference from their analysis is our improved scheme for the kinematical separation of the ISM components along the lines of sight and the inclusion of the reddening residual map. The X_{CO} value measured in the Local arm by EGRET, $(1.64 \pm 0.31) \times 10^{20}\,\mathrm{cm^{-2}(K\,km\,s^{-1})^{-1}}$ (for $T_S = 125$ K), is statistically compatible with ours. The fact that we excluded the region of Monoceros R2 from the analysis can also explain in part this difference.

Because of the pile-up of different clouds along a line of sight, the derivation of individual cloud masses is beyond the scope of this study. Let us just note that Maddalena's cloud, with its very low rate of star formation, seems to share a quite conventional X_{CO} factor. Further investigation, including higher resolution γ-ray maps when more high-energy LAT data become available, is required to fully understand the mass distribution in the clouds.

4.3. The Gradient of CR Densities beyond the Solar Circle

In Figure 11 (left panel) we show the emissivity gradient found beyond the solar circle for different spin temperatures. Here we do not include the results for the optically thin approximation which is equivalent to an infinitely high T_S and gives similar emissivities to $T_S = 400$ K. The typical statistical errors associated with these measurements are illustrated in the right panel for the $T_S = 125$ K case. In the right panel, a shaded area shows the characteristic systematic error due to the LAT event selection efficiency, evaluated to be ∼10% in the energy range under study.

In order to evaluate the impact of the delicate separation of the gas in the outermost region, we have compared two extreme cases. The first one adopts the kinematic $R = 16$ kpc boundary and applies no correction for velocity dispersion and the second assigns all the outer-arm gas to the Perseus arm. The emissivity in the Perseus arm differs by about 5% from the original one, and those in the Local arm and interarm regions hardly change. Therefore, these effects are significantly smaller than the uncertainties due to the optical depth correction of the H I data. We also note that the main effect of the LAT selection efficiency uncertainty is to rigidly shift the profile without any significant impact on the gradient.

We thus conclude that the most important source of uncertainty in the CR density gradient derivation is currently that in the N(H I) determination. This is mainly because the optical depth correction is larger for dense H I clouds in the Local and Perseus arms than for diffuse clouds in the interarm region. The loss in contrast between the dense (low-latitude) and more diffuse (mid-latitude) H I structures resulting from an increase in spin temperature affects the fit, particularly in the Perseus component which is more narrowly concentrated near the plane. When probing the CR densities as the "ratio" between the observed numbers of γ-rays to H atoms, at the precision provided by the LAT the uncertainties in the ISM densities are dominant.

4.3.1. Comparison with EGRET and the Arm/interarm Contrast

An interesting finding of the former EGRET analysis (Digel et al. 2001) was an enhancement of the γ-ray emissivity in the Perseus arm compared with the interarm region. This possibility is relevant for models of diffuse γ-ray emissions based on the assumption that CR and ISM densities are coupled (e.g., Hunter et al. 1997, and references therein).

The Local arm emissivity obtained by the EGRET study for $T_S = 125$ K is $(1.81 \pm 0.17) \times 10^{-26}$ photons s^{-1} sr^{-1} H-atom^{-1}, which is ∼25% larger than our LAT result. However, the two

studies are based on different H I surveys which yield different total N(H I) column densities integrated along the lines of sight. The column density ratios between the surveys varies from 0.6 to 1.0 within the ROI, with an average value of ∼0.8. The difference is likely due to the improved correction for stray-radiation in the more recent survey, as discussed in Kalberla et al. (2005). The EGRET Local arm emissivity scaled by 0.8 is in good agreement with our result for the same spin temperature. If we do not include the $E(B-V)_{\rm res}$ map in the fitting, we obtain an emissivity of $(1.68 \pm 0.05) \times 10^{-26}$ photons s^{-1} sr^{-1} H-atom^{-1} which is still consistent with the down-scaled EGRET result within ∼15%. We thus conclude that our result is consistent with the previous study but is more reliable because of higher γ-ray statistics, finer resolution, and an improved H I gas survey.

We can therefore compare the present emissivity gradient (for consistency in the case $T_{\rm S} = 125$ K) with that reported by the EGRET study, as summarized in Figure 11 (right panel in which the EGRET results multiplied by 0.8 are also shown). Although we observe good agreement between the two studies in the Local and the Perseus arms, this is not true for the arm/interarm contrast. The difference could be due to the simple partitioning in cloud velocity used for the EGRET study. The H I mass obtained for clouds in the interarm region with the simple partitioning is 20%–40% larger (for $T_{\rm S} = 125$ K) than with our separation scheme, exaggerating the amount of gas in the interarm region, and thus lowering the emissivity by the same amount. Our emissivity profile is thus consistent with the previous study, but with improved precision (smaller statistical errors) and accuracy (more reliable region separation method and better estimation of the point source contributions). We thus do not confirm a marked drop in the interarm region.

Low spin temperatures yield a smooth decline in H I emissivity to $R \simeq 16$ kpc in the outer Galaxy, without showing a significant coupling with ISM column densities. The Perseus-to-interarm contrast is at most of the order of 15%–20% for high spin temperatures as shown in the left panel of Figure 11. These profiles are similar at all energies, in particular at high energies where the component separation is more reliable thanks to the better angular resolution. The surface density of H I in the Perseus arm is on average 30%–40% higher than in the interarm region. Therefore, even if we adopt $T_{\rm S} = 400$ K which gives the largest arm–interarm contrast, the coupling scale (or the coupling length) between the CRs and matter (e.g., Hunter et al. 1997) required to agree with the LAT data would be larger than those usually assumed for this type of model (∼2 kpc, see e.g., Digel et al. 2001, Figure 7). Whether the true emissivity profile exhibits a small contrast between the arms or smoothly declines with distance is beyond our measurement capability without further constraints on the H I column density derivation. New H I absorption measurements will allow us to investigate this issue with better accuracy.

4.3.2. Comparison with a Propagation Model: the CR Gradient Problem

To compare with the second quadrant results (Abdo et al. 2010a), we have integrated the emissivities above 200 MeV for $T_{\rm S} = 125$ K. We find values of $(0.817 \pm 0.016) \times 10^{-26}$ photons s^{-1} sr^{-1} H-atom^{-1}, $(0.705 \pm 0.018) \times 10^{-26}$ photons s^{-1} sr^{-1} H-atom^{-1}, and $(0.643 \pm 0.022) \times 10^{-26}$ photons s^{-1} sr^{-1} H-atom^{-1} for the Local arm, interarm, and Perseus arm regions, respectively. The nearer value is about 20% lower than in the second quadrant (which, however, samples very nearby clouds in the Gould Belt) and the outer ones compare very well with the second quadrant measurement over the same Galactocentric distance range. Despite the uncertainties due to the optical-depth correction (that might have a different impact in the two quadrants), both LAT studies consistently point to a slowly decreasing emissivity profile beyond $R = 10$ kpc.

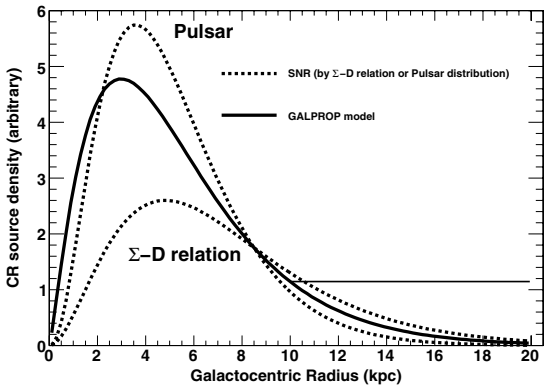

Figure 12. CR source distribution adopted in our baseline GALPROP model (solid line), compared with the SNR distribution obtained by the Σ–D relation (Case & Bhattacharya 1998) and that traced by the pulsar distribution (Lorimer 2004) shown by dotted lines. The thin solid line represents an example of the modified distributions introduced to reproduce the emissivity gradient by the LAT.

Let us consider the predictions by a CR propagation model to see the impact of such a flat profile on the CR source distribution and propagation parameters. We adopted a GALPROP model, starting from the configuration used for the run 54_77Xvarh7S which we used to predict the IC contribution. The CR source distribution in this model is

$$f(R) = \left(\frac{R}{R_\odot}\right)^{1.25} \exp\left(-3.56 \cdot \frac{R - R_\odot}{R_\odot}\right), \qquad (2)$$

where $R_\odot = 8.5$ kpc is the distance of the Sun to the Galactic center. As shown in Figure 12, this function is intermediate between the distribution of supernova remnants (SNRs) obtained from the Σ–D relation (Case & Bhattacharya 1998) and that traced by pulsars (Lorimer 2004). The boundaries of the propagation region are chosen to be $R_{\rm h} = 30$ kpc (maximum Galactocentric radius) and $z_{\rm h} = 4$ kpc (maximum height from the Galactic plane), beyond which free escape is assumed. The spatial diffusion coefficient is assumed to be uniform across the Galaxy and is taken as $D_{xx} = \beta D_0 (\rho/4{\rm GV})^\delta$, where $\beta \equiv v/c$ is the velocity of the particle relative to the speed of light and ρ is the rigidity. We adopted $D_0 = 5.8 \times 10^{28}$ cm^2 s^{-1} and $\delta = 0.33$ (Kolmogorov spectrum). Reacceleration due to the interstellar magnetohydrodynamic turbulence, which is thought to reproduce the observed B/C ratio at low energy, assumes an Alfvén velocity $v_{\rm A} = 30$ km s^{-1}. The CR source distribution and propagation model parameters have been used often in the literature (see e.g., Strong et al. 2004a). We note that the same CR source distribution and similar propagation parameters are adopted in the GALPROP run used by Abdo et al. (2010a).

The left panel of Figure 13 compares the calculated profile (solid line) with LAT constraints (bow-tie plot bracketing the profiles obtained for different $T_{\rm S}$; see the left panel of Figure 11). The model is normalized to the LAT measurement in the innermost region. Despite the large uncertainties, LAT data lead

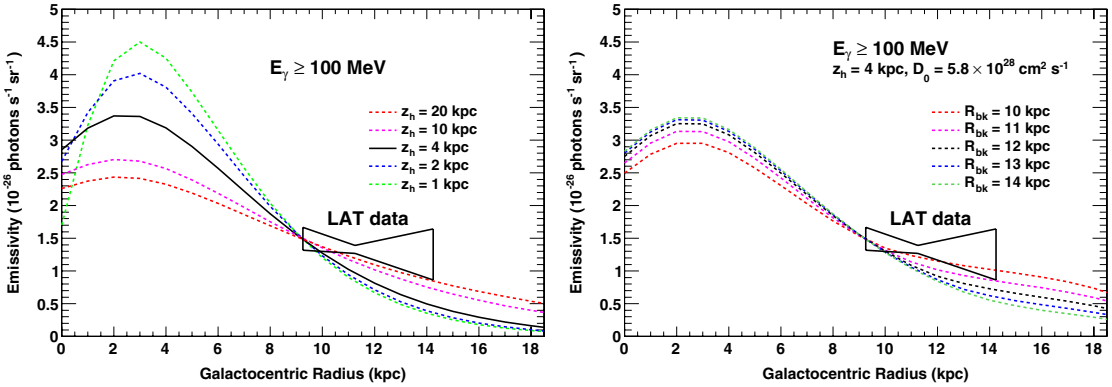

Figure 13. Comparison of the emissivity gradient obtained by the LAT and model expectations using GALPROP. The left panel shows models with different halo sizes and diffusion lengths: (z_h, D_0) = (1 kpc, 1.7×10^{28} cm^2 s^{-1}), (2 kpc, 3.2×10^{28} cm^2 s^{-1}), (4 kpc, 5.8×10^{28} cm^2 s^{-1}), (10 kpc, 12×10^{28} cm^2 s^{-1}), and (20 kpc, 18×10^{28} cm^2 s^{-1}). The solid line is for $z_h = 4$ kpc. The right panel shows different choices of the break distance beyond which a flat CR source distribution is assumed: $R_{bk} = 10$–14 kpc with 1 kpc steps.

to a significantly flatter profile than predicted by our model; the LAT results indicate to a factor of two larger emissivity (CR energy density) in the Perseus arm even if we assume $T_S = 100$ K. The higher T_S makes the discrepancy larger, hence the conclusion is robust. Not using the $E(B-V)_{res}$ map in the analysis does not change the conclusion, since the emissivities in the interarm region and the Perseus arm are almost unaffected by its presence.

The discrepancy between the γ-ray emissivity gradient in the Galaxy and the distribution of putative CR sources has been known as the "gradient problem" since the COS-B era (e.g., Bloemen 1989). It has led to a number of possible interpretations, including, for the specific case of the outer Galaxy, the possibility of a very steep gradient in X_{CO} beyond the solar circle (Strong et al. 2004b). The emissivities in the outer Galaxy were more difficult to determine in the COS-B/EGRET era due to lower statistics and higher backgrounds. Now, thanks to the high quality of the LAT data and the improved component separation technique applied to gas line data, we measure a flat H I emissivity gradient in the outer Galaxy together with a flat evolution of X_{CO} over several kpc, so the gradient problem requires another explanation.

The most straightforward possibility is a larger halo size (z_h), as discussed by, e.g., Stecker & Jones (1977), Bloemen (1989), and Strong & Moskalenko (1998). We therefore tried several choices of z_h and D_0 as summarized in the dotted lines in the same figure. The values of D_0 are chosen to reasonably reproduce the LIS of protons and electrons, B/C ratio and ^{10}Be/^{9}Be ratio at the solar system, and are similar to those given in Strong & Moskalenko (1998). All models are normalized to the LAT data in the Local arm. Models with $z_h = 4$ kpc or smaller are found to give too steep emissivity gradients. A CR source distribution as in Equation (2) with a very large halo ($z_h \geqslant 10$ kpc) provides a gradient compatible with the γ-ray data, if we fully take into account the systematic uncertainties. We note that $z_h = 10$ kpc is still compatible with ^{10}Be/^{9}Be measurements (e.g., Strong & Moskalenko 1998).

Considering the large statistical and systematic uncertainties in the SNR distribution, a flatter CR source distribution in the outer Galaxy also could be possible. We thus tried a modified CR source distribution, in which the distribution is the same as Equation (2) below R_{bk} and constant beyond it (see a thin solid line of Figure 12 as an example). Figure 13 right shows the models with several choices of R_{bk} for $z_h = 4$ kpc and $D_0 = 5.8 \times 10^{28}$ cm^2 s^{-1}. We obtained a reasonable fit to the data using a flat CR source distribution beyond $R = 10$ kpc. Such a constant CR source density in the outer Galaxy is in contrast not only with the (highly uncertain) distribution of SNRs, but also with other tracers of massive star formation and SNRs, like, (1) CO lines which trace the interstellar phase where massive stars form (e.g., Ferrière 2001), (2) OB star counts (e.g., Bronfman et al. 2000), and (3) the ^{26}Al line which is related to the injection of stellar nucleosynthesis products in the ISM by SNRs (Diehl et al. 2006). However, a very large halo size and/or a flat CR source distribution just beyond the solar circle seem to be favored by the LAT data.

The above discussion depends on the propagation parameters and the solution is not unique. The exploration could be extended to other regions of the parameter space or to a non-uniform diffusion coefficient (e.g., Evoli et al. 2008), but examining propagation models in detail is beyond the scope of our study. Our bottom line is that the analysis of LAT data presented here and by Abdo et al. (2010a) consistently show that the CR density gradient in the outer Galaxy is flatter than expectations by commonly used propagation models. In the future, the extension to the inner part and the accurate determination of the gradient over the whole Galaxy will be key to constraining the CR origin and transport.

We also note that a spin temperature $T_S \geqslant 250$ K, which is favored by recent studies in the outer Galaxy (e.g., Dickey et al. 2009), gives a small arm/interarm contrast at the 10%–20% level that is not fully compatible with the propagation models (including the one we adopted here) which predict a monotonic CR gradient.

Even though the present analysis includes a dust template to account for the abundant missing gas present locally at the interface between the H I and CO-bright phases, an alternative way to reconcile the flat emissivity profile and a marked decline in CR density in the outer Galaxy is to invoke an increase in missing gas mass with Galactocentric distance in the low metallicity environments of the outer Galaxy (see, e.g., Papadopoulos et al. 2002; Wolfire et al. 2010) beyond the local correction applied here. We note that the large masses of dark gas in the outer Galaxy suggested by Papadopoulos et al. (2002)

(outweighing that of H I by a factor of 5–15) might explain our results, whereas the remarkably constant dark gas fraction of 30% with mild dependence on metallicity suggested by Wolfire et al. (2010) is not sufficient to explain the large H I emissivities measured by the LAT beyond the solar circle.

5. SUMMARY AND CONCLUSION

We have studied the diffuse γ-ray emission in the third Galactic quadrant using the first 18 months of *Fermi* LAT science data. Thanks to the excellent performance of the LAT, we have obtained high-quality emissivity spectra of the atomic and molecular gas (traced by $W_{\rm CO}$) in the 100 MeV–25.6 GeV energy range.

At the level of accuracy allowed by the LAT, the study of CR densities from γ-ray observations is now mostly limited by the understanding of the ISM mass tracers, notably by the uncertainties in the derivation of atomic gas column densities from H I surveys and by the distribution of gas not accounted for by radio and microwave line surveys. In spite of those uncertainties, robust conclusions can be drawn concerning the ISMs and CRs.

The molecular mass calibration ratio of the Local arm is found to be $\sim 2 \times 10^{20}\,{\rm cm}^{-2}({\rm K\,km\,s}^{-1})^{-1}$, significantly larger than that for the very local Gould-Belt clouds in the second Galactic quadrant reported by Abdo et al. (2010a). No significant differences of the ratio are found between the Local arm and the interarm regions.

No significant variations in the CR spectra are found across the outer Galaxy in the region studied, and no large contrast in emissivity is seen in the interarm region between the Local and Perseus arms (a contrast $< 10\%$–20% is allowed by data). The measured gradient is much flatter than predictions by a widely used propagation model assuming that the CR source distribution largely peaks in the inner Galaxy. A larger halo size and/or a flatter CR source distribution beyond the solar circle than those usually assumed are required to reproduce the LAT data, while other scenarios such as a non-uniform diffusion coefficient or vast amounts of missing gas in the outer Galaxy are also possible. Reliable determinations of the amount of atomic hydrogen in the plane are key to better constraining the property of CRs in our Galaxy.

The *Fermi* LAT Collaboration acknowledges generous ongoing support from a number of agencies and institutes that have supported both the development and the operation of the LAT as well as scientific data analysis. These include the National Aeronautics and Space Administration and the Department of Energy in the United States, the Commissariat à l'Energie Atomique and the Centre National de la Recherche Scientifique/Institut National de Physique Nucléaire et de Physique des Particules in France, the Agenzia Spaziale Italiana and the Istituto Nazionale di Fisica Nucleare in Italy, the Ministry of Education, Culture, Sports, Science and Technology (MEXT), High Energy Accelerator Research Organization (KEK), and Japan Aerospace Exploration Agency (JAXA) in Japan, and the K. A. Wallenberg Foundation, the Swedish Research Council, and the Swedish National Space Board in Sweden.

Additional support for science analysis during the operations phase is gratefully acknowledged from the Istituto Nazionale di Astrofisica in Italy and the Centre National d'Études Spatiales in France.

This paper makes use of a development version of GALPROP provided by the GALPROP team to the LAT collaboration solely for interpretation of the LAT data. GALPROP development is supported by NASA Grant NNX09AC15G.

We thank T. M. Dame for providing the moment-masked CO data.

REFERENCES

Abdo, A. A., et al. 2009a, ApJ, 703, 1249
Abdo, A. A., et al. 2009b, Phys. Rev. Lett., 102, 181101
Abdo, A. A., et al. 2009c, Astropart. Phys., 32, 193
Abdo, A. A., et al. 2009d, Science, 323, 1688
Abdo, A. A., et al. 2009e, Nature, 462, 331
Abdo, A. A., et al. 2009f, ApJ, 706, L138
Abdo, A. A., et al. 2010a, ApJ, 710, 133
Abdo, A. A., et al. 2010b, ApJS, 188, 405
Abdo, A. A., et al. 2010c, ApJS, 187, 460
Abdo, A. A., et al. 2010d, Phys. Rev. Lett., 104, 101101
Abdo, A. A., et al. 2010e, submitted
Atwood, W. B., et al. 2009, ApJ, 697, 1071
Beichman, C., Neugebauer, G., Habing, H. J., Clegg, P. E., & Chester, T. J. (ed.) 1988, in IRAS Catalogs and Atlases Explanatory Supplement (Washington, DC: GPO), 1
Bloemen, H. 1989, ARA&A, 27, 469
Bloemen, J. B. G., et al. 1986, A&A, 154, 25
Bronfman, L., Casassus, S., May, J., & Nyman, L.-Å. 2000, A&A, 358, 521
Case, G. L., & Bhattacharya, D. 1998, ApJ, 504, 761
Cordes, J. M., & Lazio, T. J. W. 2002, arXiv:astro-ph/0207156
Clemens, D. P. 1985, ApJ, 295, 422
Dame, T. M., Hartmann, D., & Thaddeus, P. 2001, ApJ, 547, 792
Dickey, J. M., Strasser, S., Gaensler, B. M., Haverkorn, M., Kavars, D., McClure-Griffiths, N. M., Stil, J., & Taylor, A. R. 2009, ApJ, 693, 1250
Diehl, R., et al. 2006, Nature, 439, 45
Digel, S. W., Grenier, I. A., Hunter, S. D., Dame, T. M., & Thaddeus, P. 2001, ApJ, 555, 12
Elad, M., Starck, J.-L., Querre, P., & Donoho, D. L. 2005, Appl. Comput. Harmon. Anal., 19, 340
Evoli, C., Gaggero, D., Grasso, D., & Maccione, L. 2008, J. Cosmology Astropart. Phys., 10, 18
Ferrière, K. M. 2001, Rev. Mod. Phys., 73, 1031
Grenier, I. A., Casandjian, J.-M., & Terrier, R. 2005, Science, 307, 1292
Hunter, S. D., et al. 1997, ApJ, 481, 205
Kalberla, P. M. W., Burton, W. B., Hartmann, D., Arnal, E. M., Bajaja, E., Morras, R., & Pöppel, W. G. L. 2005, A&A, 440, 775
Kaltcheva, N. T., & Hilditch, R. W. 2000, MNRAS, 312, 753
Lebrun, F., et al. 1983, ApJ, 274, 231
Lorimer, D. R. 2004, in IAU Symp. 218, Young Neutron Stars and Their Environments, ed. F. Camilo & B. M. Gaensler (San Francisco, CA: ASP), 105
Maddalena, R. J., & Thaddeus, P. 1985, ApJ, 294, 231
Maddalena, R. J., Morris, M., Moscowitz, J., & Thaddeus, P. 1986, ApJ, 303, 375
Mattox, J. R., et al. 1996, ApJ, 461, 396
Mel'nik, A. M., & Efremov, Yu. N. 1995, Astron. Lett., 21, 10
Mori, M. 1997, ApJ, 478, 225
Morris, M., Montani, J., & Thaddeus, P. 1980, in IAU Symp. 87, Interstellar Molecules, ed. B. H. Andrew (Dordrecht: Reidel), 197
Papadopoulos, P. P., Thi, W. -F., & Viti, S. 2002, ApJ, 579, 270
Porter, T. A., Moskalenko, I. V., Strong, A. W., Orlando, E., & Bouchet, L. 2008, ApJ, 682, 400
Rando, R., et al. 2009, arXiv:0907.0626
Schlegel, D. J., Finkbeiner, D. P., & Daris, M. 1998, ApJ, 500, 525
Stecker, F. W., & Jones, F. C. 1977, ApJ, 217, 843
Strong, A. W., & Mattox, J. R. 1996, A&A, 308, L21
Strong, A. W., & Moskalenko, I. V. 1998, ApJ, 509, 212
Strong, A. W., Moskalenko, I. V., & Ptuskin, V. S. 2007, Annu. Rev. Nucl. Part. Syst., 57, 285
Strong, A. W., Moskalenko, I. V., & Reimer, O. 2004a, ApJ, 613, 962
Strong, A. W., Moskalenko, I. V., Reimer, O., Digel, S., & Diehl, R. 2004b, A&A, 422, L47
Strong, A. W., et al. 1988, A&A, 207, 1
Wilson, B. A., Dame, T. M., Masheder, M. R. W., & Thaddeus, P. 2005, ApJ, 430, 523
Wolfire, M. G., Hollenbach, D., & McKee, C. F. 2010, ApJ, 716, 1191

5.2 SUMMARY OF THE RESULTS

- The H I opacity correction is recognized for the first time as the dominant source of uncertainty in the interpretation of γ-ray measurements regarding interstellar emission.
- The X_{CO} ratio in the Local Spur is consistent with that found in the second quadrant; no significant variations are observed in the outer disc of the Milky Way.
- Models of CR propagation based on the observed distributions of CR sources predict a gradient of H I emissivity steeper than inferred from LAT observations.
- Standard propagation models would require a large halo, with height $\gtrsim 10$ kpc or unexpectedly large densities of CR sources in the outer Galaxy to match LAT measurements.
- Less conventional propagation scenarios or a systematic bias due to dark gas in the outer Galaxy are alternative possibilities.

6

INTERSTELLAR GAMMA-RAY EMISSION FROM MASSIVE-STAR FORMING REGIONS: CYGNUS

Galactic CRs are supposed to be accelerated by remnants of the explosions of massive stars at the end of their life (§ 2.2.2), either individual supernova remnants (SNRs) or superbubbles (SBs). LAT observations unveiled a correlation between γ-ray emission and tracers of massive-star formation in the LMC and a correlation between global γ-ray luminosity and star-formation rate for a few external galaxies (§ 3.4).

In this chapter I present an analysis of LAT measurements in the region of the Cygnus SB, also known as Cygnus X region due to its extreme brightness at X-ray wavelengths. This region hosts a super massive interstellar complex, which is also one of the most active star-forming sites of the Galaxy, with numerous OB associations and stellar clusters.

The Cygnus SB is located at $\sim$ 1.4 kpc from the solar system, in the tangent direction of the Local Spur. There are no remarkable structures acting as foregrounds in this direction, and we observe two modest segments of the Perseus and outer spiral arms located beyond the Cygnus complex in the distant outer Galaxy. The main challenge in the analysis consisted in the separation of interstellar emission and the numerous bright individual sources.

6.1 OVERVIEW

The Cygnus SB, located around $l = 80^\circ$ in the tangent direction of the Local Spur, was identified by its strong X-ray emission (Cash et al., 1980), and it contains numerous H II regions and OB associations (Uyanıker et al., 2001). It has been long debated whether it represents a coherent complex or the alignment of different structures along the line of sight. Recent high-resolution observations by Schneider et al. (2006) pointed out that all the interstellar clouds in the Cygnus region are connected and partly show evidence for interactions with the massive stellar cluster Cygnus OB2 and other OB associations in the region (Cyg OB1 and OB9). At a distance of $\sim$ 1.4 kpc from the Sun (e.g. Hanson, 2003), the cloud complex would appear as one of the most massive in the Galaxy. There are thusly both large densities of gas and intense radiation fields acting as targets for CR interactions. The MILAGRO experiment measured TeV emission from the Cygnus region, possibly of interstellar origin and pointing to CR densities higher than in the local ISM (Abdo et al., 2007). With stars of masses $> 85 M_\odot$ still in the main sequence, the Cyg OB2 cluster may be too young (2 Myr, Hanson, 2003) to supply many active CR sources. The interactions of clouds with other OB associations in the region and the presence of the γ Cygni SNR, which is at a distance of 1.5 kpc (Ladouceur and Pineault, 2008) from the Earth and therefore co-located with the Cygnus complex, suggest that freshly accelerated CRs may pervade the clouds in addition to the older CR sea.

I present here a global analysis of the γ-ray emission from the Cygnus region measured by the LAT in the energy range between 100 MeV and 100 GeV, focusing on the interstellar emission to search for signatures of CR acceleration and to complement gas and dust observations at other wavelengths to constrain the census of the ISM. This analysis also provides an improved interstellar background framework for future studies of individual objects.

6.2 DATA ANALYSIS

6.2.1 *Gamma-ray data*

Observations and data selection

I accumulated data for our region of interest from August 5 2008 (MET [1] 239587201) to August 5 2010 (MET 302659202). I selected data with the tightest available background rejection criteria, corresponding to the *Dataclean* event class (Abdo et al., 2010j). In order to limit the contamination from the Earth atmospheric γ-ray emission, I selected events with measured arrival directions within 100° from the local zenith and within 65° from the instrument boresight, taken during periods when the LAT rocking angle was less than 52°.

The angular resolution of the LAT strongly depends on the photon energy, improving as the energy increases (§ 1.2). Confusion at low energies is an issue since I aim at separating the different components in the crowded Cygnus region. I therefore accepted below 1 GeV only photons which produced electron-positron pairs in the thin converter planes of the *front* section of the tracker, which provides a superior angular resolution.

I analysed data at $72° \leq l \leq 88°$ and $-15° \leq b \leq +15°$. The longitude window contains the interstellar complexes associated with the Cygnus SB; the latitude window is large enough to allow a reliable separation of the large-scale emission from atomic gas and IC emission and isotropic background. I analysed data in the 100 MeV–100 GeV energy band. Below 100 MeV the instrumental systematics are large (Rando et al., 2009) and the angular resolution is poor, whereas above 100 GeV photon statistics are low.

Analysis method

I fit the various models described in the following sections to the LAT data using a binned maximum-likelihood with Poisson statistics [2]. I used a $0.125° \times 0.125°$ binning in Cartesian projection, comparable with the LAT angular resolution at the highest energies. I considered three energy bands: low (100 MeV–1 GeV), mid (1 GeV–10 GeV) and high energies (10 GeV–100 GeV). The low and mid-energy bands were further divided in four logarithmic-spaced energy bins. The higher-energy band in two because of the limited statistics. A total count-map is provided for illustration in Fig. 6.1.

The analysis was based on the post-launch Instrument Response Functions (IRFs) of the `P6_V3` series, which take into account efficiency losses due to pile-up and accidental coincidence effects in the detector (§ 1.2.2).

1. *Fermi* Mission Elapsed Time.
2. As implemented in the standard LAT analysis tools `09-18-05`.

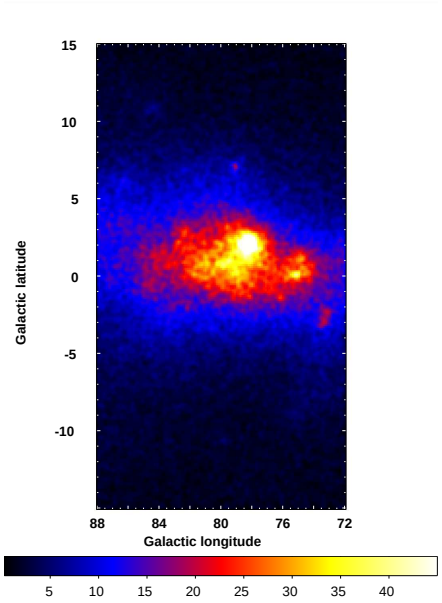

Figure 6.1: Total count map in the energy range 100 MeV–100 GeV corresponding to the selection criteria reported in the text (§ 6.2.1) and the low-emission phase intervals of the three bright pulsars (§ 6.2.1). Counts saturated between 0 and 45, smoothed for display with a Gaussian kernel of $\sigma = 0.25°$.

The γ-ray emission in the region of interest results from the combination of individual sources, both point-like and extended, and interstellar signals. The modeling of the interstellar γ-ray emission is described in § 6.2.2. Three bright pulsars are the dominant contributors below a few GeV: the radio pulsar PSR J2021+3651 (Abdo et al., 2009n) and the two LAT-discovered pulsars PSR J2021+4026 and PSR J2032+4127 (Abdo et al., 2009b). Their signal was largely removed by excluding photons detected in time intervals corresponding to their emission peaks (see § 6.2.1). Other sources were modeled and included in the analysis as described in § 6.2.3.

Bright pulsars

To increase the sensitivity to faint sources and to the spatial structure of the diffuse emission, I reduced the contribution from the three bright pulsars by excluding the periodic time intervals when their pulsed emission peaks. For each pulsar, the photon arrival times were phase-folded according to their previously published ephemerides (Abdo et al., 2010l; Ray et al., 2010) [3]. Fig. 6.2 shows the three light curves and the vertical lines indicate the phase intervals with bright pulsed emission. The phase boundaries are reported in Table 6.1 to-

3. Evenly-spaced time of arrival (TOA) measurements, with typical spacing of a few weeks per TOA, were fitted using TEMPO2 (Hobbs et al., 2006) to generate a model with the minimum phase residuals over the data span for use in the following analysis. For the three pulsars, the RMS of the timing residuals is below 1.1% of their rotational period.

PSR	on-pulse phase interval	off-pulse %
J2021+3651	$0.12 - 0.22, 0.59 - 0.7$	79
J2021+4026	$0.94 - 0.18, 0.5 - 0.62$	64
J2032+4127	$0.94 - 0.14, 0.49 - 0.55$	74

Table 6.1: Phase boundaries of the on-pulse intervals and off-pulse time fraction for the three bright pulsars.

gether with the fraction of time in the off-pulse interval (suitable for our study). From Fig. 6.2 it is obvious that there is a considerable level of unpulsed emission toward PSR J2021+4026 that cannot be removed; however, given the brightness of the source, the removal of the on-peak interval is useful for our aims.

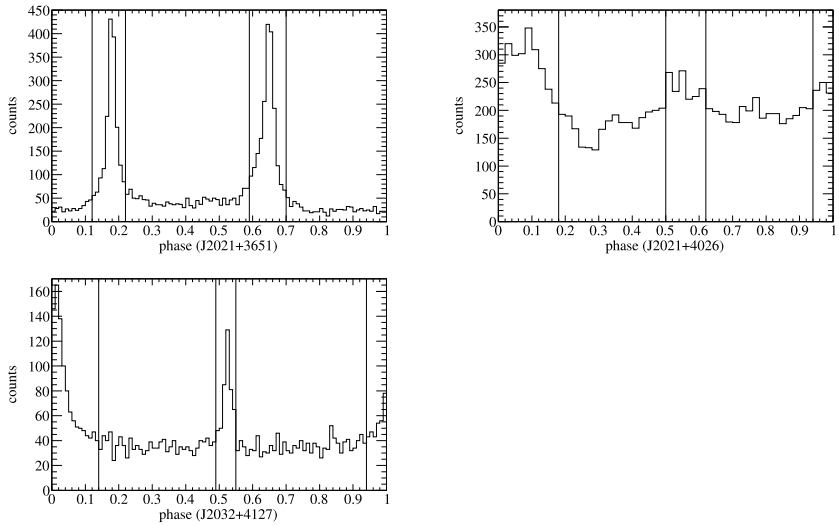

Figure 6.2: Light curves and on-pulse phase intervals for the three bright pulsars. The light curve is constructed for illustration purposes with photons recorded in a circular region of radius 0.5° around the pulsar position and energies > 200 MeV.

To remove the pulsar signal without excessively sacrificing the photon statistics in other directions, I restricted the timing selection to a circular region around the pulsar position with an energy-dependent radius $r_{\rm cut}(E) = \max\left[0.25^\circ, r_{95}(E)\right]$ where E is the lower bound of each energy bin. The minimum radius of 0.25° corresponds to 2 bins in the angular grid. r_{95} is an approximate representation of the LAT 95% containment angle as a function of energy

$$r_{95}(E) = 2 \cdot \left[0.8^\circ \left(\frac{E}{1\,\mathrm{GeV}}\right)^{-0.8} \oplus 0.07^\circ\right] \tag{6.1}$$

where the symbol $\oplus$ indicates addition in quadrature. Let us note that the accurate parametrization of the LAT Point Spread Function (PSF) depends on energy, conversion point in the tracker and, to a lower extent, on the incidence angle. The IRFs are the best representation of the LAT PSF and must be used for science data analysis (exposure

calculation, convolution with the PSF). The above acceptance-averaged approximation for the containment angle is only useful to calculate the radius $r_{\rm cut}$, and I verified that the results are insensitive to reasonable variations of this parameter.

To take into account the cut on pulsar phases, for each pulsar I multiplied the model maps of the other components (already convolved with the LAT PSF and multiplied by the exposures) by the fraction of the corresponding off-pulse time within the radius $r_{\rm cut}$ around the pulsar position.

The remainder of the pulsar emission was included in the model using:

- a point source to represent emission in the off-pulse interval;
- a second point source, for which the number of expected counts is set to null at $r < r_{cut}(E)$ from the pulsar position, to represent on-pulse γ-rays spilling over at $r > r_{cut}(E)$.

Since the three pulsars have exponential spectral cutoffs near $2-3$ GeV (Abdo et al., 2010l) this procedure was not applied above 10 GeV where the level of pulsed emission is low and the good angular resolution leads to a reliable component separation. On the other hand, given the sufficient statistics but poor angular resolution at low energies, to stabilize the fitting procedure I simply analysed events in the low-emission windows at energies[4] < 300 MeV. I verified that the results do not critically depend on the latter value.

6.2.2 *Modeling of interstellar γ-ray emission*

Interstellar gas

Since CRs in the relevant energy ranges are expected to have diffusion lengths exceeding the typical dimensions of interstellar clouds and to penetrate uniformly all the phases of the ISM, the γ-ray emission produced by CR-gas interactions can be modeled to first order as a linear combination of the gas column densities summed for the different phases and different regions along the line of sight.

Neutral atomic hydrogen, H I, is traced by its 21-cm line. Where available[5] I used data from the Canadian Galactic Plane Survey (CGPS; Taylor et al., 2003) rebinned onto the $0.125^\circ \times 0.125^\circ$ grid used for the γ-ray and CO maps (see below). Elsewhere, I used data from the Leiden/Argentine/Bonn (LAB; Kalberla et al., 2005) survey, with a coarser binning of 0.5°. I checked the consistency of the two survey calibrations in the overlap region.

Molecular hydrogen cannot be observed directly in its most abundant cold phase. The velocity-integrated brightness temperature of the ^{12}CO 2.6-mm line, $W_{\rm CO}$, is often assumed to linearly scale with the $N({\rm H_2})$ column density (§ 2.1.3). I used CO data from the composite survey by Dame et al. (2001), filtered with the moment-masking technique in order to reduce the noise while preserving the faint cloud edges and keeping the resolution of the original data.

The Doppler shift of radio/mm-wave lines can be used to kinematically separate the Cygnus complex at 1.4 kpc (e.g. Hanson, 2003) from two faint segments of the Perseus and outer spiral arms seen beyond

4. Given the broad PSF at low energies, more than half of the region of interest would have been subject to on-pulse event removal

5. The CGPS coverage is almost complete at $-3.5^\circ \leq b \leq +5.5^\circ$ for this longitude range.

Cygnus in the same direction. I applied the kinematic separation procedure illustrated in Appendix B, starting from a preliminary boundary located at a Galactocentric radius $R = 9.4$ kpc and then adapting the separation to the cloud structures and correcting for the spill-over due to the broad velocity dispersion of H I lines. The separation into two regions is sufficient to model the interstellar γ-ray emission since in Chapter 4 and 5 no significant gradients of CR densities were found in the outer region of the Milky Way. I applied such kinematic separation procedure to prepare maps of the column densities of atomic gas, $N(\mathrm{H\,I})$, and of W_{CO}.

Substantial uncertainties in the determination of $N(\mathrm{H\,I})$ arise from the choice of spin temperature for the optical depth correction (§ 2.1.2). I adopted as baseline case a uniform $T_S = 250$ K, which is the average spin temperature that best reproduces the blending of cold and warm atomic gas according to observations of emission-absorption pairs in the region covered by the CGPS (Dickey et al., 2009). Other values $100\ \mathrm{K} \leq T_S < \infty$ will be considered later to evaluate the related systematic uncertainties affecting the results of our analysis. The maps are shown in Fig. 6.3 for H I and Fig. 6.4 for CO.

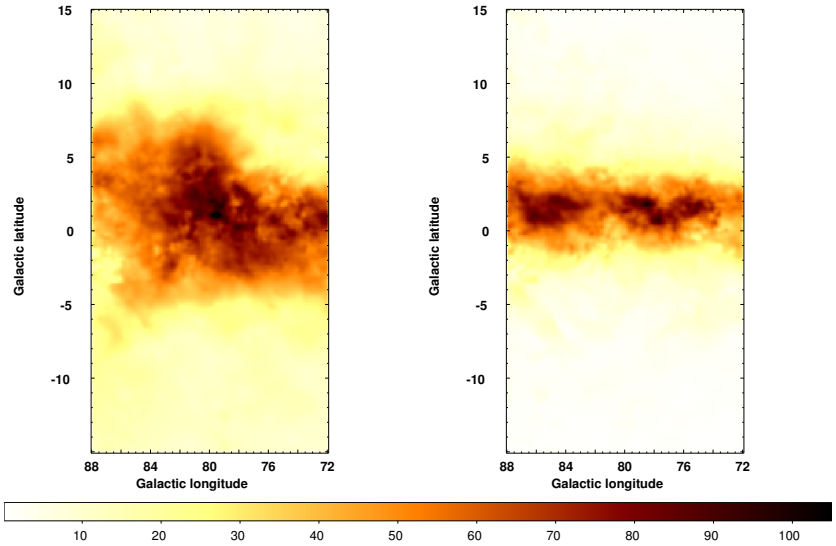

Figure 6.3: Maps of $N(\mathrm{H\,I})$ column densities in the Cygnus complex in the Local Spur (left) and in the outer Galaxy (right), under the assumption of a uniform spin temperature of 250 K. The color scales with $N(\mathrm{H\,I})$ in units of 10^{20} atoms cm^{-2}. The maps were smoothed with a Gaussian kernel of $\sigma = 0.25^\circ$ for display.

Observational evidences at various wavelengths indicate that the combination of H I and CO lines does not properly trace the total column densities of the neutral ISM (§ 3.3.3). Since the work by Grenier et al. (2005), dust tracers have been used in γ-ray analyses to complement H I and CO lines. In Grenier et al. (2005) and Chapter 4 the $\mathrm{E(B-V)}$ color excess map by Schlegel et al. (1998) was adopted as a tracer of the total column densities, and $\mathrm{E(B-V)}$ residuals –i.e. $\mathrm{E(B-V)}$ minus the best-fit linear combination of $N(\mathrm{H\,I})$ and W_{CO} maps– were used as a tracer of the dark-gas column densities in nearby clouds of the Gould Belt.

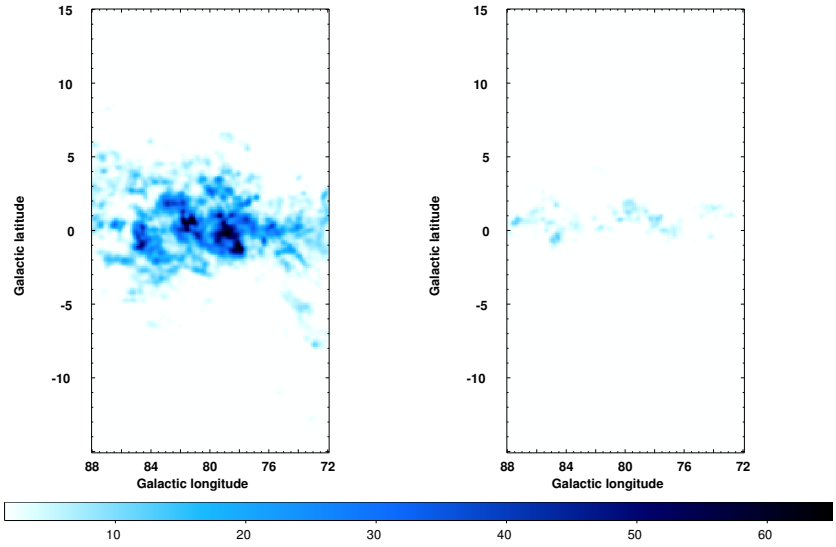

Figure 6.4: Maps of W_{CO} intensities in the Cygnus complex in the Local Spur (left) and in the outer Galaxy (right). The color scales with W_{CO} in units of K km s^{-1} above 1.5 K km s^{-1}. The maps were smoothed with a Gaussian kernel of $\sigma = 0.25^\circ$ for display.

The use of the $E(B-V)$ map is problematic in the Cygnus region for different reasons.

- numerous infrared point sources contaminate the map;
- the temperature correction used by Schlegel et al. (1998) to derive the dust column-density map from *IRAS*/ISSA measurements is highly uncertain in regions of massive-star formation because of the enhanced radiation fields;
- it is impossible to separate different structures seen along a line of sight on the Galactic plane (where most of the Cygnus complex is located).

I therefore resorted to the visual extinction A_V as derived from the reddening of near-infrared sources in the 2MASS catalog (Skrutskie et al., 2006). The A_V maps produced by Rowles and Froebrich (2009); Froebrich and Rowles (2010) were used for $A_V < 5$ mag. They exhibit saturation effects at higher extinction values, so I complemented them with a A_V map obtained from 2MASS data using the method developed by Schneider et al. (2010). The latter includes an improved photometric calibration and uses the Besançon stellar population model (Robin and Creze, 1986; Robin et al., 2003) to filter out the contribution from the bluest foreground stars. The second A_V map was built in a 12° region centered on $(l, b) = (80^\circ, 0^\circ)$; compared with the first set of maps, it presented an offset of 0.46 mag at low extinction. The final A_V map was constructed from the direct Rowles and Froebrich (2009); Froebrich and Rowles (2010) maps below 5 mag and from the second map, offset by 0.46 mag, at higher extinction.

All the dust maps were binned onto the same $0.125^\circ \times 0.125^\circ$ grid in Cartesian projection as for the γ-ray and CO maps. Dust excess maps were obtained for both the $E(B-V)$ and A_V maps by subtracting the best-fit linear combination of $N(\mathrm{H\,I})$ and W_{CO} maps previously described. Only residuals corresponding to input $A_V > 0.3$ mag were

kept to limit the noise off the plane. The final A_V excess map is shown in Fig. 6.5.

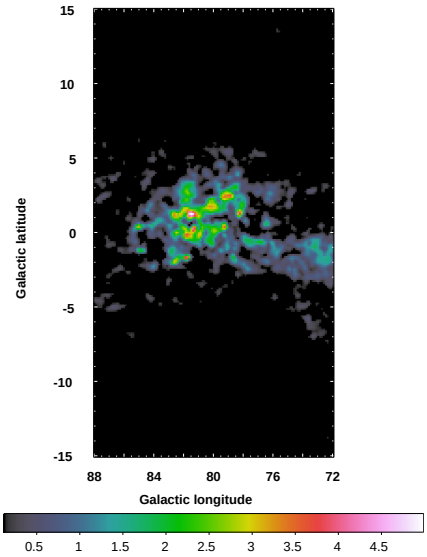

Figure 6.5: Dust excess map as traced by the optical extinction A_V (in magnitude) estimated from 2MASS data. Black pixels correspond to null or negative dust residuals. The map was smoothed using a Gaussian kernel of $\sigma = 0.25^\circ$ for display.

Away from H II regions around massive stars and stellar clusters, the ionized gas constitutes a layer of characteristic height $\gtrsim 1$ kpc over the Galactic plane with little mass compared to the neutral phases (Cordes and Lazio, 2002), therefore it has often been neglected in previous γ-ray studies. However, we find in the Cygnus region many conspicuous H II regions excited by the intense radiation fields of the numerous massive stars (Uyanıker et al., 2001; Paladini et al., 2003). To probe for γ-ray emission from ionized gas, following Sodroski et al. (1989, 1997) the ionized gas column densities $N(\mathrm{H\,II})$ were assumed to be proportional to the free-free emission intensities

$$N(\mathrm{H\,II}) = 1.2 \times 10^{15}\ \mathrm{cm}^{-2} \left(\frac{T_e}{1\,\mathrm{K}}\right)^{0.35} \left(\frac{n_{\mathrm{eff}}}{1\,\mathrm{cm}^{-3}}\right)^{-1} \left(\frac{\nu}{1\,\mathrm{GHz}}\right)^{0.1} \frac{I_{\mathrm{ff}}}{1\,\mathrm{Jy\,sr}^{-1}} \tag{6.2}$$

where I_{ff} is the free-free emission intensity at the frequency ν, T_e is the electron temperature and n_{eff} the effective electron number density. The free-free emission map used here was derived from the 7-year *WMAP* data in the Q band (40 GHz) by Gold et al. (2010) using the maximum entropy method from the prior template given by the extinction-corrected Hα map by Finkbeiner (2003). It was rebinned onto the $0.125^\circ \times 0.125^\circ$ grid used for the other maps, as shown in Fig. 6.6.

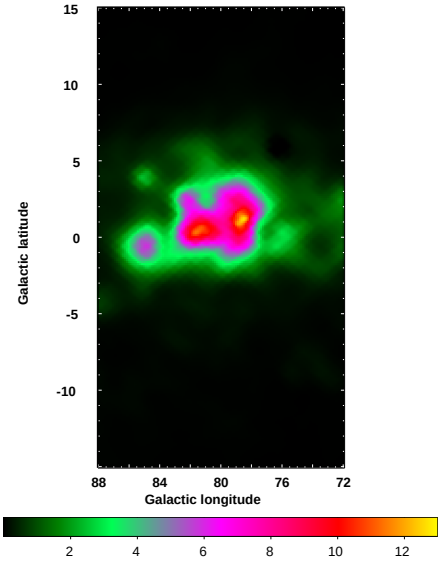

Figure 6.6: Free-free emission intensities from *WMAP* data. The color scales with brightness temperature in mK. The map was smoothed using a Gaussian kernel of $\sigma = 0.25^\circ$ for display.

To summarize, the γ-ray intensities produced by interactions of CRs with interstellar gas, $I_{\rm gas}$ (cm^{-2} s^{-1} sr^{-1}), integrated in each energy bin are modeled by Equation 6.3:

$$\begin{aligned} I_{\rm gas}(l,b) &= \sum_{i=1}^{2} q_{{\rm HI},i} \cdot N({\rm HI})(l,b)_i + \sum_{i=1}^{2} q_{{\rm CO},i} \cdot W_{\rm CO}(l,b)_i + \\ &+ q_{\rm dust} \cdot I_{\rm dust,res}(l,b) + q_{\rm ff} \cdot I_{\rm ff}(l,b) \end{aligned} \tag{6.3}$$

The sum over i represents the combination of the two regions: 1) Cygnus complex and 2) outer Galaxy. The free parameters are the emissivities of H I gas, $q_{{\rm HI},i}$ (s^{-1} sr^{-1}), the emissivities per unit of $W_{\rm CO}$ intensity, $q_{{\rm CO},i}$ (cm^{-2} s^{-1} sr^{-1} (K km s^{-1})$^{-1}$), the emissivity per dust excess unit, $q_{\rm dust}$ (cm^{-2} s^{-1} sr^{-1} mag^{-1}) and the emissivity per free-free emission intensity unit, $q_{\rm ff}$ (cm^{-2} s^{-1} Jy^{-1}).

Inverse Compton emission and isotropic background

Hereinafter in the chapter we will refer to the local CR spectrum, both for electrons and nuclei, as the volume and energy density of particles which, corrected for solar modulation, is consistent with direct measurements performed either at the Earth or in the interplanetary space in the solar system. The γ-ray emissivity of the H I gas in the local interstellar space within 1 kpc from the solar system is consistent with the local CR spectrum (§ 3.2.2). For explicit calculations the local CR electron spectrum was derived from measurements by the LAT (Abdo et al., 2009l; Ackermann et al., 2010) and by AMS-01 (Alcaraz et al., 2000) at energies < 7 GeV, as parametrized in Abdo et al. (2011).

The interstellar inverse Compton (IC) emission is produced by interactions of CR electrons and positrons with the low energy ISRF. To account for large-scale IC emission I adopted a template calculated using the GALPROP CR propagation code (§ 2.2.3), run `54_87Xexph7S`. The IC emission was calculated on the basis of a propagated CR electron population consistent at the solar circle with the local spectrum and the new calculation of the Galactic ISRF by Porter et al. (2008).

Due to the presence of numerous OB associations in the Cygnus region (Uyanıker et al., 2001), there are strong local radiation fields that are not accounted for in the Galactic axisymmetric model by Porter et al. (2008). Pre-launch studies suggested the detectability by *Fermi* of the IC emission arising from interactions of CR electrons with the stellar light in the Cyg OB2 cluster (Orlando and Strong, 2007, 2008), therefore we tested their model. The model was computed for this analysis using the local CR electron spectrum and considering radiation from 85 type O and 2489 type B stars. The stars were uniformly distributed in a region of 2° diameter (corresponding to the extension of the cluster according to Knödlseder, 2000) at a distance of 1.4 kpc (Hanson, 2003); the model was produced for a square region of 20° width centered on Cygnus OB2. Uncertainties in the IC emission with a given electron spectrum comes mainly from the unknown luminosity of the stars. In order to evaluate the maximal contribution from an electron population consistent with the local one, the stars were supposed to be of luminosity class I, with the parameters described in Martins et al. (2005): O stars were assumed to have an effective temperature $T_{\rm eff} = 42551$ K and radius $R = 18.47\ R_\odot$, and B stars $T_{\rm eff} = 15200$ K and $R = 4\ R_\odot$. The IC contribution comes almost exclusively from the O stars; the contribution of the 6000 F stars in the cluster was estimated to be fully negligible.

Both the GALPROP template and the model by (Orlando and Strong, 2007) are based on a distribution of CR electrons which smoothly varies as a function of Galactocentric radius and height above the Galactic plane. Local electron sources, very plausible in such an active region, and the small propagation length of high-energy electrons could leave unmodeled structures in IC emission. This issue will be discussed in § 6.3.3.

In each energy bin I added also as a free parameter the intensity of the isotropic background, $I_{\rm iso}$, which combines the residual backgrounds from misclassified CR interactions in the LAT and the isotropic, presumably extragalactic, γ-ray emission (§ A.1).

6.2.3 *Analysis procedure*

1. Input model

The input model included interstellar emission, using as gas tracers H I and CO only [6], the three bright pulsars, and other sources that were added as needed in subsequent steps. I first introduced the identified sources in the region of interest: Cygnus X-3 (Abdo et al., 2009m), PSR J1957+5033 (Saz Parkinson et al., 2010) and PSR J2030+3641 (Camilo et al., in preparation). The pulsars included in the LAT pulsar cata-

6. H I and CO correspond to the two major, well-established components of interstellar emission from gas. The contribution from dark neutral gas (dust excesses) and ionized gas (free-free emission) will be investigated later.

log (Abdo et al., 2010l) were modeled with the spectral function described therein, letting the flux as a free parameter in each energy bin. All other sources were modeled using power-law spectra with a free flux in each energy bin and the spectral index reported in the internal 24 month source list (which is the base for the two-year LAT source catalog in preparation). A power-law spectrum with index -2.1 was assumed to convolve the gas templates (and other sources modeled by geometrical templates hereinafter) with the PSF. The results do not significantly depend on this value.

I then included 1FGL point sources (Abdo et al., 2010c) coincident with γ-ray excesses in the residuals, either associated with Active Galactic Nuclei (AGN) or characterized by variability; these were modeled as point sources with the position and spectral index given in the 24 month source list and with free flux in each energy bin; the sources were added with decreasing brightness: J2116.1+3338, J2021.1+4351, J2027.6+3335, J2015.5+2937, J2015.7+3708, J2029.2+4924, J2012.2+4629 and J2128.0+3623. The iterative procedure is useful to stabilize the likelihood fitting procedure and to assess the significance of sources added at each step. The residuals after inclusion of all the aforementioned point sources are shown in Fig. 6.7.

2. The Cygnus Loop region

Several excesses are still evident. A remarkable extended excess is present below 10 GeV around $(l, b) = (74°, -8.5°)$. It coincides with four point sources of the 1FGL Catalog (Abdo et al., 2010c): J2046.4+3041, J2049.1+3142, J2055.2+3144, J2057.4+3057, reported to be spatially associated with the rim of Cygnus Loop. In Fig. 6.8 I compare the γ-ray residuals of the input model (§ 6.2.3) in the $1 - 10$ GeV band with X-ray emission measured by ROSAT (see Aschenbach and Leahy, 1999).

I explored three different models for the Cygnus Loop region:

2.a four point sources at the positions given in the 1FGL Catalog (Abdo et al., 2010c);

2.b a uniform ellipsoid centered at $(l, b) = (74.0, -8.5)$ with semi-axes of 1.9° and 1.3° (Green, 2009);

2.c a ring centered at $(l, b) = (74.21, -8.57)$ and with inner and outer radii of 0.6° and 1.7°, respectively (see below).

The correlation seen between the γ and X-ray emissions (Fig. 6.8) and the likelihood increase (Table 6.2) obtained for an extended source over the set of point sources, in spite of the smaller number of free parameters, strengthens the association between the γ-ray excess and the Cygnus Loop. A dedicated analysis will be reported in a subsequent paper (*Fermi* LAT collaboration, in preparation). The highest likelihood model (2.c) derived from that study is used hereinafter so that the presence of the extended source does not bias the estimates of quantities related to interstellar emission.

3. Dark gas

To probe for potential neutral gas not properly traced by the H I and CO maps, I tested two different dust residual maps calculated from:

3.a the $E(B - V)$ map by Schlegel et al. (1998);

3.b the A_V map derived from 2MASS observations;

the maps were previously described in § 6.2.2.

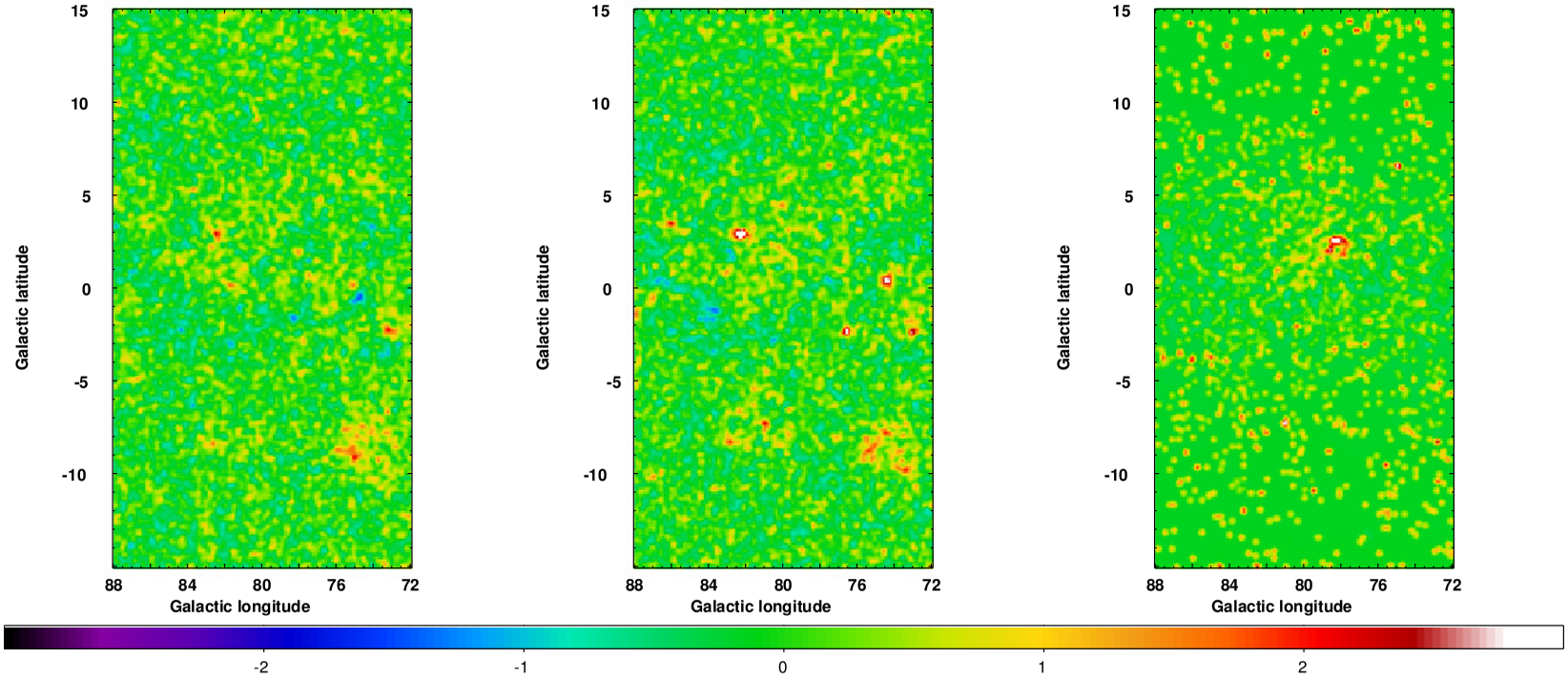

Figure 6.7: Residuals (data–model) of the input model including all the point sources (§ 6.2.3). Left: low energies (100 MeV–1 GeV); center: mid-energies (1 GeV–10 GeV); right: high energies (10 GeV–100 GeV). Units are approximate standard deviations (square root of model counts) saturated between $\pm 3\sigma$ and smoothed for display with a Gaussian kernel of $\sigma = 0.25°$.

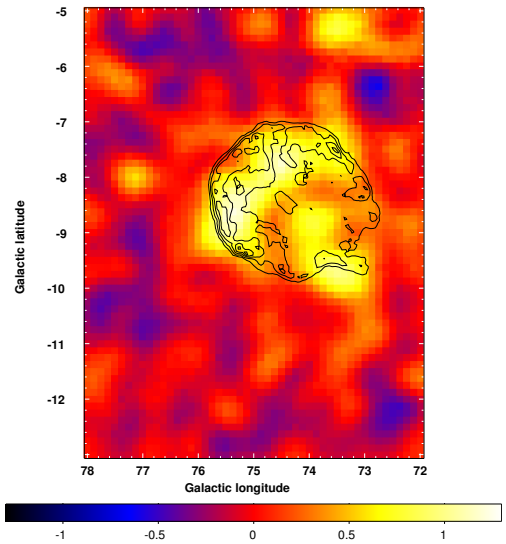

Figure 6.8: Photon residuals corresponding to the input model around the Cygnus Loop in the $1 - 10$ GeV energy band; the color scale saturates at ± 1.3 counts. The map is smoothed for display with a Gaussian kernel of $\sigma = 0.5^\circ$. Overlaid X-ray contours from the ROSAT all sky survey, equally spaced in square-root from 0 to 182 counts.

Likelihood values are reported in Table 6.2. The log-likelihood increase of 250.6 for 10 additional free parameters obtained when adding the A_V residuals is very significative, so I kept the A_V residual map in the model hereinafter. The likelihood response to the $E(B-V)$ residual map was less pronounced because of the limitations described above.

4. The region of γ Cygni

In the higher energy band a remarkable excess (Fig. 6.9) is observed along the rim of the SNR in γ Cygni (alias G78.2+2.1, e.g. Ladouceur and Pineault, 2008). On the North-East side it coincides also with the source 1FGL J2020+4049 (Abdo et al., 2010c) and with the moderately extended TeV source VER 2019+407 (Weinstein et al., 2009).

I tested different models for the excess:

4.a a point source at the position of 1FGL J2020+4049;

4.b an asymmetric Gaussian as reported for VER 2019+407 (Weinstein et al., 2009);

4.c a disc centered at $(l, b) = (78.2, +2.1)$ and a radius of 0.5° (G78.2+2.1; Green, 2009);

4.d both Gaussian and disc.

Likelihood values are reported in Table 6.2. Whereas the detection of a point source at the position of 1FGL J2020+4049 is only marginal, significant emission is detected in association with both the TeV source and the remnant. I therefore adopt the Gaussian plus disc template in the model hereinafter. A detailed study of this region should be pursued in the future.

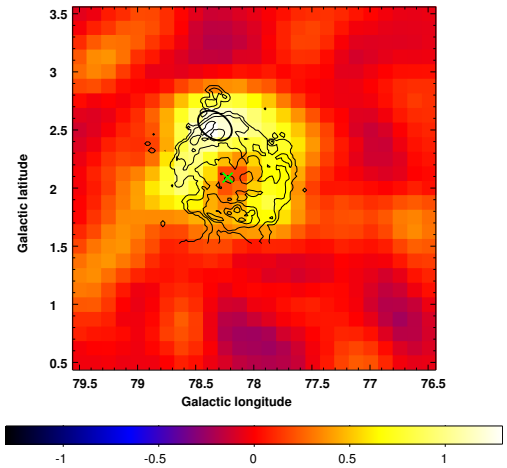

Figure 6.9: Photon residuals in the $10 - 100$ GeV band around γ Cygni, from model 3.b. The colour scale saturates at ± 1.3 counts and the map is smoothed for display with a Gaussian kernel of $\sigma = 0.375°$. Overlaid contours of continuum radio emission at 1420 MHz from the CGPS (equally spaced in square-root from 0.1 K to 70 K). The cross marks the position of PSR J2021+4026, at the center of the remnant, and the ellipsoid corresponds to the TeV source VER 2019+407 (Weinstein et al., 2009), also coincident with 1FGL J2020+4049.

5. The inner Cygnus complex

Model 4.d leaves a cluster of positive residuals coincident with the innermost part of the Cygnus complex, displayed above 10 GeV in Fig. 6.10 Given the LAT angular resolution > 10 GeV (68% containment radius $< 0.2°$), the excess is clearly extended. The positive residuals are associated with a region of enhanced free-free emission intensity (compare with Fig. 6.6) and therefore of ionized gas density. On the other hand they partially overlap with the massive stellar cluster Cyg OB2.

I explored different models for the inner Cygnus region, namely:

a the free-free emission map as a tracer of ionized gas (§ 6.2.2);
b the model for IC radiation from Cyg OB2, with a free normalization coefficient in each energy bin;
c an alternative geometrical model for Cyg OB2, given by a 2D Gaussian centered on $(l, b) = (80.16°, 0.76°)$ with a $\sigma = 1°$ width comparable to the cluster size (Knödlseder, 2000).

Likelihood values are reported in Table 6.2. I obtain a significant likelihood increase for both the free-free map and Cyg OB2 (the two models for Cyg OB2 are almost equivalent in terms of likelihood). I consider the combination of the free-free map and the physical model of Cyg OB2 as model 5.d.

To further probe the nature of the excess in the inner Cyg region, I added to model 4.d a 2D Gaussian source with free centroid and width. The best-fit Gaussian is centered on $(l, b) = (79.5° \pm 0.5°, 1.4° \pm 0.8°)$ and has a width $\sigma = 2.1° \pm 0.2°$, as shown in Fig 6.10. I will refer to this model as model 5.e. The likelihood increase for this model corresponds to a detection at a 9.5σ confidence level[7]. It provides a likeli-

7. Assuming that $\mathrm{TS} = 2\Delta$ is distributed as a χ^2 with n degrees of freedom.

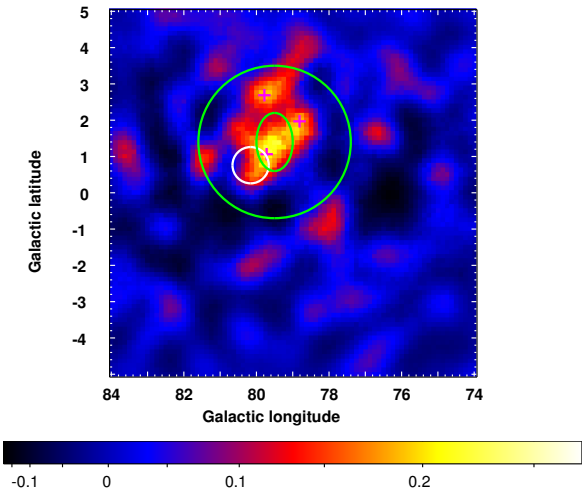

Figure 6.10: Photon residuals in the energy band $10 - 100$ GeV from model 4.d. The map was smoothed for display with a Gaussian kernel of $\sigma = 0.75^\circ$ and saturated between -0.2 and $+0.25$. The green ellipsoid represents the 1σ error region for the centroid of the Gaussian model, and the green circle its 1σ width. The white circle corresponds to the core of the Cyg OB2 stellar cluster (Hanson, 2003). The magenta crosses correspond to the position of the three point sources of model 4.f.

hood increase larger than the combination of the free-free map and the model of Cyg OB2 in spite of the smaller number of free parameters.

The radial profile of the excess emission is displayed in Fig. 6.11. The profile strongly suggests a truly diffuse excess over a combination of point sources. To test the latter possibility, I iteratively added to model 4.d a few point sources with free positions. I stopped when the cumulative likelihood increase exceeded that of model 5.b. The resulting model includes three point sources whose positions are shown in Fig 6.10. It is called model 5.f hereinafter. Given the much larger number of free parameters involved, the increase in likelihood is quite modest. All three sources exhibit consistent and hard spectra, so there is no evidence for spectral variations across the excess. The radial profile, spectral uniformity, and modest likelihood increase obtained for a set of discrete point sources all point to the presence of a diffuse and hard excess in the core of the Cygnus region.

While we expect some excess emission because of CR interactions with ionized gas and IC radiation from Cyg OB2 and possibly other stellar clusters, I will show later in § 6.3.3 that the excess has a harder spectrum than expected from the local CR spectrum. Since the nature of the excess is not clear I will adopt the best-fit Gaussian model 5.e as baseline model hereinafter, and a detailed discussion about the excess is deferred to § 6.3.3.

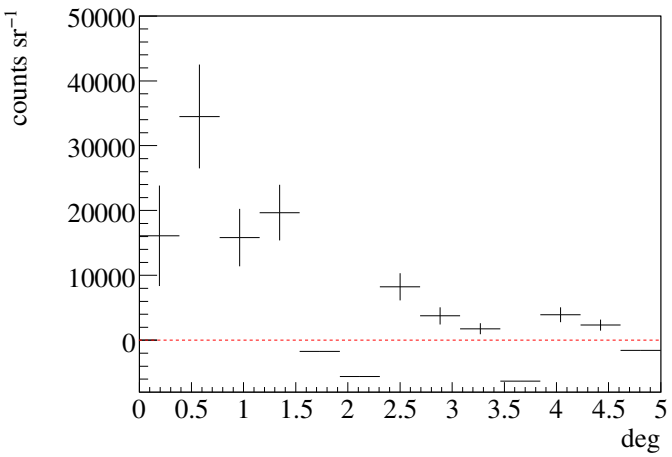

Figure 6.11: Profile of the residual photons shown in Fig. 6.10 as function of the radial distance from $(l, b) = (79.5°, 1.4°)$.

6.3 RESULTS AND DISCUSSION

6.3.1 *Summary of results and uncertainties*

I will now summarize the fitting results referring to model 5.e, which provides the best likelihood as deduced from Table 6.2. The residuals corresponding to this model are shown in Fig. 6.12 They indicate that the model satisfactorily reproduces the morphology of the γ-ray emission in all the energy bands. Unmodeled localized positive residuals are still present. Some of them coincide with unassociated 1FGL sources, notably J2030.9+4411 and J2034.7+3639, which are therefore confirmed by this analysis.

Fig. 6.13 shows the γ-ray spectral energy distribution measured by the LAT over the whole region of interest for the same selection criteria and energy grid used in the analysis. LAT measurements are compared with the best-fit model, and the different components are outlined. The data sample is dominated by emission from interstellar gas in the Cygnus complex. The largest contributor is H I. Emission associated with CO and A_V residuals exceeds the signals from individual sources for the whole energy range considered. The γ-ray excess detected toward the inner part of the complex has a very hard spectrum and becomes comparable to emission from CO-bright gas at energies > 10 GeV.

I summarize in Table 6.3 the fit parameters related to interstellar emission from gas, which will be the basis of the discussion in paragraph 6.3.2.

All the results presented so far are based on the assumption of a uniform H I spin temperature of 250 K. To gauge the impact of the optical depth correction of H I data on the results, I repeated the analysis with other assumptions. $T_S = 400$ K is considered since it is the value best reproducing pairs of emission/absorption H I spectra over most of the regions analysed by Dickey et al. (2009), although they found that $T_S = 250$ K is preferred in the region covered by CGPS data. We also considered two extreme assumptions: a low [8] $T_S = 100$ K, and the

8. The spin temperature is higher than the brightness temperature (Eq. 2.10), measured > 100 K along many directions in the region.

		100 MeV–1 GeV	1 GeV–10 GeV	10 GeV–100 GeV	100 MeV–100 GeV	Δ	n
Input Model	1	−48901.3	−44952.2	−9054.6	−102908.1		
Cygnus Loop	*2.a*	*−48775.7*	*−44882.5*	*−9053.8*	*−102712.0*	*196.1*	*40*
	2.b	*−48787.8*	*−44865.3*	*−9053.3*	*−102706.4*	*201.7*	*10*
	2.c	−48777.3	−44860.7	−9053.3	−102691.3	216.8	10
Dark Gas	*3.a*	*−48765.4*	*−44832.3*	*−9053.1*	*−102650.8*	*40.5*	*10*
	3.b	−48689.4	−44726.1	−9025.2	−102440.7	250.6	10
γ Cygni	*4.a*	*−48687.5*	*−44725.7*	*−9010.0*	*−102423.2*	*17.5*	*10*
	4.b	*−48689.1*	*−44724.9*	*−8989.6*	*−102403.6*	*37.1*	*10*
	4.c	*−48686.0*	*−44725.7*	*−8981.3*	*−102393.0*	*47.7*	*10*
	4.d	−48685.3	−44724.8	−8963.6	−102373.7	67.0	20
inner Cyg	*5.a*	*−48682.4*	*−44702.2*	*−8944.9*	*−102329.5*	*44.2*	*10*
	5.b	*−48681.1*	*−44712.7*	*−8955.7*	*−102349.5*	*24.2*	*10*
	5.c	*−48679.9*	*−44715.5*	*−8954.7*	*−102350.1*	*23.6*	*10*
	5.d	*−48679.2*	*−44699.6*	*−8943.1*	*−102321.9*	*51.8*	*20*
	5.e	−48678.0	−44690.8	−8939.3	−102308.1	65.6	13
	5.f	*−48676.8*	*−44715.0*	*−8954.8*	*−102346.6*	*27.1*	*36*

Table 6.2: Log-likelihood values for the different models presented in § 6.2.3. Each step in the model building is separated by a line. Models discarded at each step are marked in italic. Δ gives the log-likelihood increment over the previous step for the whole $0.1 - 100$ GeV band and n gives the corresponding number of additional free parameters.

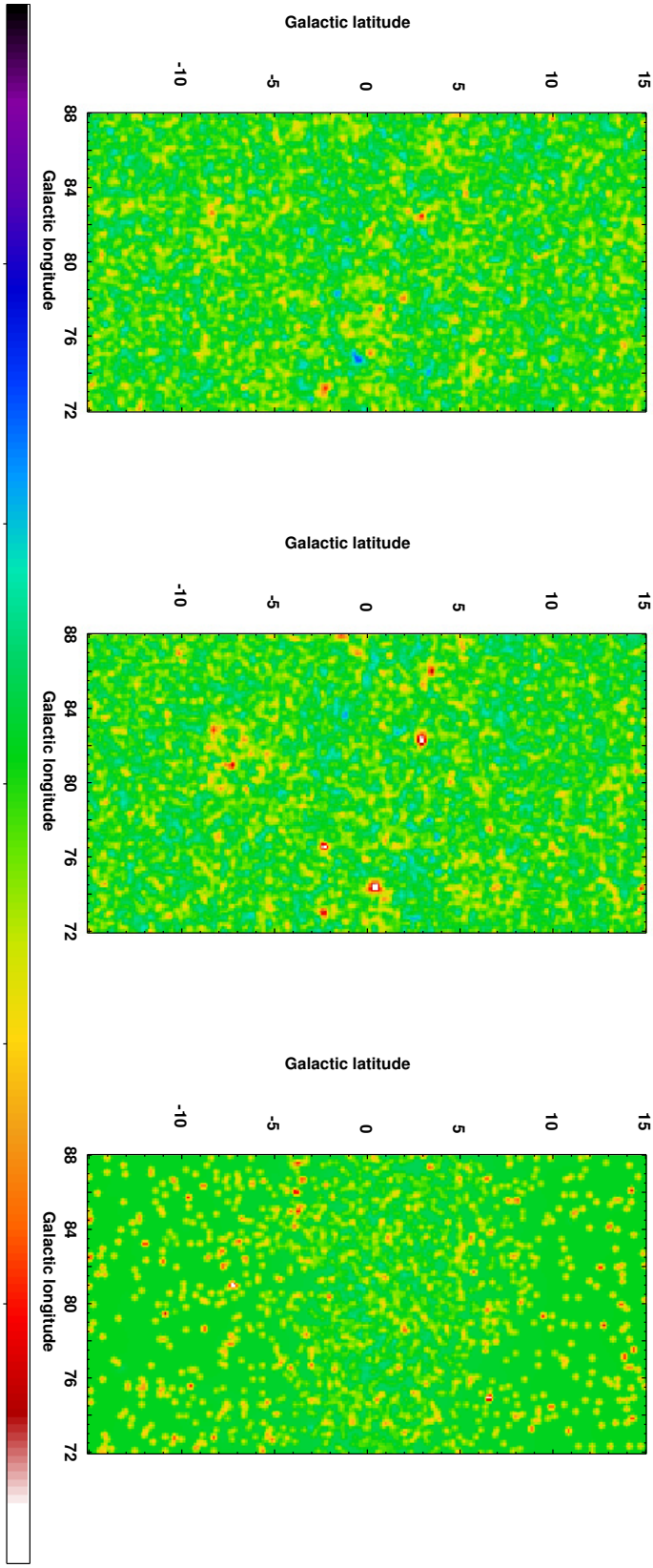

Figure 6.12: Photon residuals (data–model) as in Fig. 6.7 for the best-fit model 5.e.

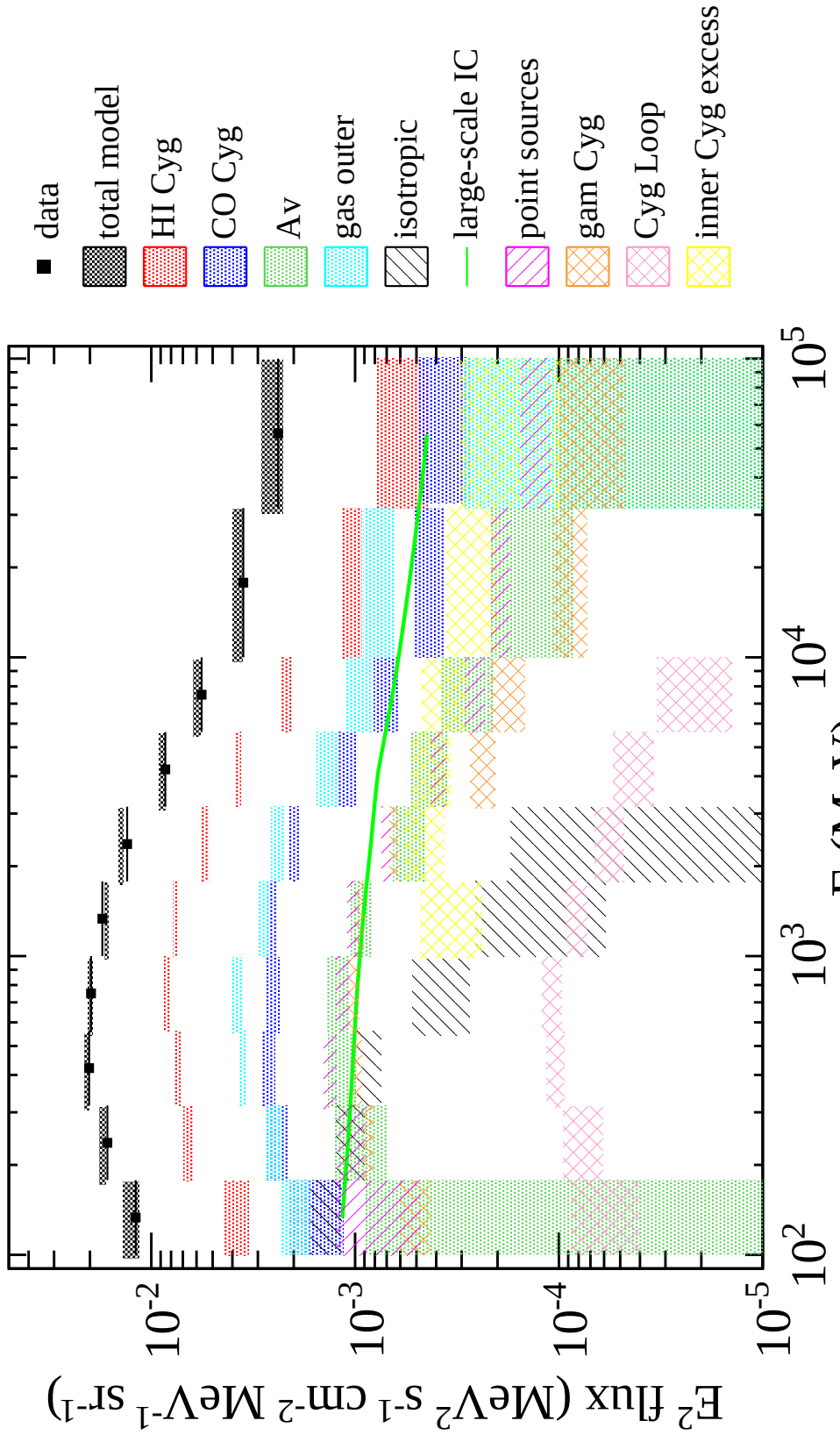

Figure 6.13: Spectral energy distribution of γ-ray emission measured by the LAT compared with our best-fit model. Statistical errors only.

energy bin	$q_{\mathrm{H\,I},1}$	$q_{\mathrm{H\,I},2}$	$q_{\mathrm{CO},1}$	$q_{\mathrm{CO},2}$	q_{dust}
[GeV]	$[10^{-27}\ \mathrm{s^{-1}\ sr^{-1}}]$		$[10^{-6}\ \mathrm{cm^{-2}\ s^{-1}\ sr^{-1}\ (K\ km\ s^{-1})^{-1}}]$		$[10^{-6}\ \mathrm{cm^{-2}\ s^{-1}\ sr^{-1}\ mag^{-1}}]$
$0.1 - 0.178$	7.9 ± 1.1	8.5 ± 1.4	3.3 ± 1.0	0.00 ± 0.06	14 ± 26
$0.178 - 0.316$	5.9 ± 0.3	4.7 ± 0.4	2.2 ± 0.3	0.000 ± 0.002	19 ± 5
$0.316 - 0.562$	3.27 ± 0.11	3.23 ± 0.14	1.16 ± 0.08	0.00 ± 0.06	11.0 ± 1.8
$0.562 - 1$	1.95 ± 0.06	1.72 ± 0.10	0.59 ± 0.04	0.5 ± 0.3	6.2 ± 0.7
$1 - 1.78$	0.98 ± 0.03	0.74 ± 0.04	0.328 ± 0.016	0.12 ± 0.13	2.6 ± 0.3
$1.78 - 3.16$	0.389 ± 0.016	0.36 ± 0.02	0.141 ± 0.008	0.02 ± 0.06	0.86 ± 0.15
$3.16 - 5.62$	0.151 ± 0.005	0.113 ± 0.013	0.044 ± 0.004	0.02 ± 0.03	0.39 ± 0.08
$5.62 - 10$	0.050 ± 0.003	0.046 ± 0.006	0.016 ± 0.002	0.000 ± 0.005	0.15 ± 0.04
$10 - 31.6$	0.0085 ± 0.0015	0.021 ± 0.003	0.0059 ± 0.0010	0.002 ± 0.008	0.043 ± 0.019
$31.6 - 100$	0.0024 ± 0.0007	0.0007 ± 0.0014	0.0016 ± 0.0004	0.002 ± 0.003	0.002 ± 0.007

Table 6.3: Best-fit parameters from model 5.e describing emission from interstellar gas (Eq. 6.3) under the assumption of a uniform H I spin temperature $T_S = 250$ K.Subscripts refer to the two regions separated in analysis: 1) the Cygnus complex in the Local Spur, 2) the outer Galaxy. Some parameters are poorly determined but they are reported for completeness.

optically thin approximation (equivalent to infinitely high spin temperature). In Fig. 6.14 I show the maximum likelihood profile obtained for model 5.e as a function of T_S. The results support the average

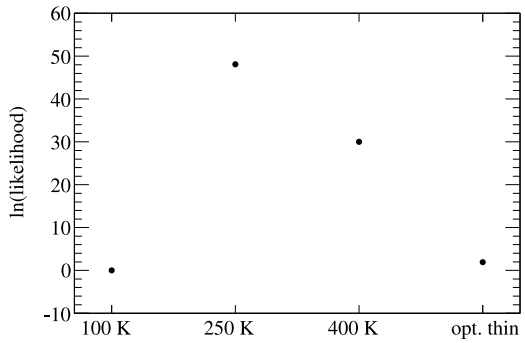

Figure 6.14: Maximum likelihood obtained for model 5.e as a function of the uniform spin temperature adopted for the optical depth correction of H I data. Values are offset so that log-likelihood is null for a spin temperature of 100 K.

spin temperatures of a few hundred K deduced from radio absorption/emission measurements by Dickey et al. (2009), implying a mix of $< 25\%$ cold and $> 75\%$ warm H I.

Other systematic uncertainties are due to the γ-ray selection efficiency. They are estimated to be 10% at 100 MeV, 5% at 560 MeV, and 20% above 10 GeV for the IRFs we used here (Abdo et al., 2010j). All the sources of uncertainties presented will be taken into account for the forthcoming discussion.

6.3.2 *Interstellar gas*

Atomic gas

The H I emissivity per hydrogen atom relates to the average CR density in the region under study. In § 3.2.2, Chapter 4 and 5 I have discussed that the H I emissivity spectrum in the Local Spur is consistent with production via electron Bremsstrahlung and nucleon-nucleon interactions due to CRs with the local spectrum.

In Fig. 6.15 I show the H I emissivity spectrum obtained for the Cygnus complex and I compare it with the local spectrum estimated by Abdo et al. 2009g (Fig. 3.4). The latter includes a nuclear enhancement factor of 1.84 and is compatible (within 10%) with LAT observations at mid latitudes in the third Galactic quadrant in the energy range 100 MeV–10 GeV. The spectrum is presented for a uniform spin temperature $T_S = 250$ K; systematic uncertainties due to the H I opacity correction and to the γ-ray selection efficiency are added in quadrature for display. The latter give a non-negligible contribution only at energies larger than a few GeV.

The emissivity of atomic gas in the Cygnus region, averaged over ~ 400 pc around the complex, is consistent with the local emissivity with good confidence in the 100 MeV–10 GeV energy range, and possibly up to 100 GeV. The emissivity in the energy range $10 - 30$ GeV slightly deviates from the local spectrum, but there might be a separation problem between H I and CO due to the low statistics and the

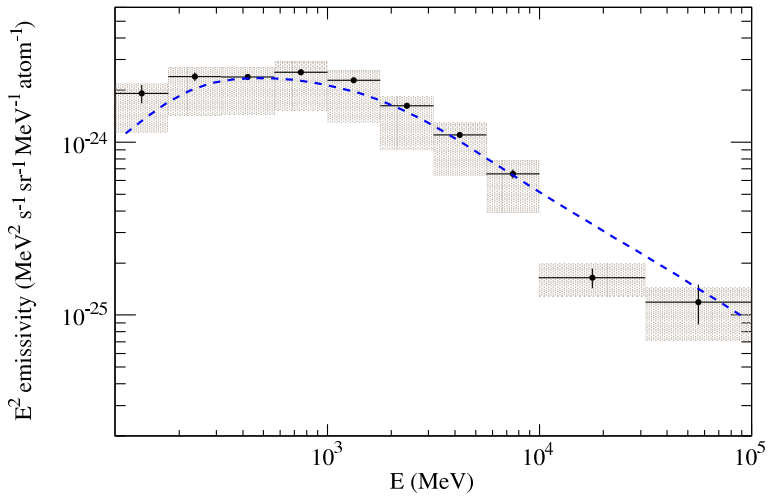

Figure 6.15: H I emissivity spectrum in the Cygnus complex. Points: the best-fit estimate for the spin temperature $T_S = 250$ K. Hatched rectangles: systematic uncertainties taking into account H I opacity and γ-ray selection efficiency. Line: model of the local interstellar spectrum by Abdo et al. 2009g (with a nuclear enhancement factor of 1.84).

increasing brightness of the excess in the inner region of the Cygnus complex (Fig. 6.13). The emissivity spectrum implies that the CR spectra in the relevant energy ranges ($\sim 1-10$ GeV for electrons, $\sim 1-100$ GeV/n for nucleons) are similar to those measured in the vicinity of the Earth and inferred from γ-ray observations in the nearby interstellar space within 1 kpc.

The $< 20\%$ variations in average CR densities recorded along the Local Spur between the dense Cygnus complex, the two segments in the second and third quadrants that exhibit ~ 2 lower surface densities of gas (Chapter 4 and 5), and the mid-latitude diffuse medium with a factor ~ 5 lower surface density (§ 3.2.2) are difficult to reconcile with the idea of a dynamical coupling between gas and CR densities (e.g. Bertsch et al., 1993; Hunter et al., 1997). They are consistent on the other hand with the small arm-interarm emissivity contrast we estimated in the third Galactic quadrant in Chapter 5.

In spite of the large column densities of gas, exceeding 10^{22} atoms cm^{-2} over many directions in the core of the Cygnus complex, we find no hints of exclusion of CRs from the densest parts of the atomic clouds due to the increased magnetic fields. See § 6.3.2 for further discussion on results for the denser molecular cores.

Due to the bright foreground given by the Cygnus complex and individual sources, studying in detail the gas emissivity in the outer disc of the Milky Way is beyond the scope of this study. However, the ratio of the integral H I emissivity of the outer region over that in the Local Spur is $(90 \pm 7)\%$, in very good agreement with the results presented in Chapter 4 and 5. It confirms in another direction the presence of large CR densities beyond the solar circle.

CO-bright molecular gas

If molecular and atomic gas are illuminated by the same CR fluxes, we expect the emissivity per hydrogen molecule to be twice as the emissivity per hydrogen atom; we can therefore calibrate the $X_{CO} = N(H_2)/W_{CO}$ ratio as $q_{CO}/(2q_{HI})$ (§ 3.3.2). I performed a linear fit taking into account the uncertainties on both emissivities to derive the best linear relation shown in Fig. 6.16; I also show the residuals in units of standard deviations.

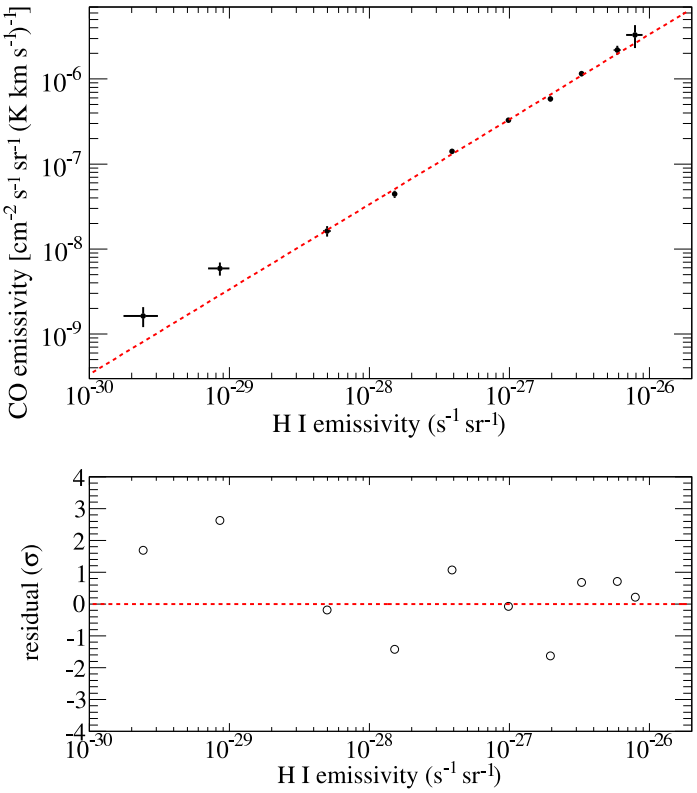

Figure 6.16: Top: emissivity per W_{CO} intensity unit versus emissivity per $N(HI)$ unit in the Cygnus complex (for $T_S = 250$ K). The points correspond to the different energy bins; the emissivities decrease with increasing energy. The red line gives the best linear fit taking into account uncertainties on both axes. Bottom: residuals in units of standard deviations as a function of HI emissivity.

A good linearity is found over two decades in energy. The highest-energy (lowest-emissivity) points show a small ($< 3\sigma$) excess of emission associated with CO with respect to the best-fit linear relation. The high CO emissivity recorded at $10 - 30$ GeV (second point) corresponds to a low emissivity in HI (Fig. 6.15) and may result from a fluctuation in the difficult spatial separation between the atomic and molecular components when photons are sparse. Up to 10 GeV the linearity is good and therefore there is no sign of CR exclusion from the dense cores of this giant molecular complex. Residual maps obtained above 10 GeV using the X_{CO} ratio extrapolated from lower energies show that the CO emissivity is driven up in regions of potentially high

(and hard) IC emission near conspicuous H II regions, south-east of DR 17 and south of DR 13 (see later § 6.3.3, Fig. 6.20).

The slope of the best-fit linear relation provides a value of $X_{\rm CO} = (1.68 \pm 0.05) \times 10^{20}$ cm^{-2} (K km s^{-1})$^{-1}$ in the case of $T_S = 250$ K. I obtain $X_{\rm CO} = (1.58 \pm 0.04) \times 10^{20}$ cm^{-2} (K km s^{-1})$^{-1}$ in the case of small H I optical depth and $X_{\rm CO} = (2.55 \pm 0.08) \times 10^{20}$ cm^{-2} (K km s^{-1})$^{-1}$ in the case of $T_S = 100$ K. The uncertainties in $q_{\rm HI}$ associated with the H I spin temperature are particularly severe for the high-density clouds of the Cygnus complex. High optical depths (low spin temperatures) imply a large increase in $N({\rm H\,I})$, therefore substantially lower CR densities. Given the γ-ray luminosity of the molecular clouds they subsequently imply a significant increase in their mass [9]. The systematic errors on the γ-ray selection efficiency cancel out to first order in the estimate of the linear relation slope, therefore they are completely negligible with respect to the uncertainties associated with the H I opacity.

The conversion factor $X_{\rm CO} = [1.68 \pm 0.05\,({\rm stat.})\ ^{+0.87}_{-0.10}\,({\rm H\,I\ opacity})] \times 10^{20}$ cm^{-2} (K km s^{-1})$^{-1}$ is consistent with other LAT measurements in the Local Spur which range from $(1.5 - 2) \times 10^{20}$ cm^{-2} (K km s^{-1})$^{-1}$ (Chapter 4 and 5). Located at ~ 1.4 kpc from the Sun and $l = 80^\circ$, the Cygnus complex lies at $R \simeq 8.4$ kpc from the Galactic center. From these different measurements in the Galactic plane the $X_{\rm CO}$ ratio at the solar circle appears well defined. It is, however, significantly larger than in nearby well-resolved clouds off the plane in Cassiopeia and Cepheus (Chapter 4); the origin of the difference is not understood yet (§ 7.2.2).

Using the $X_{\rm CO}$ ratio I estimated the CO-bright molecular mass in the complex. For this purpose I considered the region at $74^\circ < l < 86^\circ$, $-5^\circ < b < 8^\circ$, where most of the gas associated with the Cygnus complex is located. Assuming a distance of 1.4 kpc (e.g. Hanson, 2003) and a mean atomic weight per hydrogen atom in the ISM of 1.36, I obtained a mass $2.3\ ^{+1.2}_{-0.1} \times 10^6 M_\odot$ (where the uncertainties are dominated by the H I opacity correction). This value (taking into account the different assumption on the distance) is consistent with the results by Schneider et al. (2006) based on higher-resolution, multi-isotopologue CO observations and it depicts Cygnus as a super-massive molecular complex.

Due to the small amount of CO-bright molecular gas in the outer region of the Milky Way in this longitude window (Fig. 6.4), the determination of its emissivities is extremely sensitive to the details of the model (including point sources) and I do not consider it for scientific interpretation.

Dark gas

In Fig. 6.17 I show the emissivity per A_V unit, $q_{\rm dust}$, versus the emissivity per hydrogen atom column density, $q_{\rm HI}$, in the Cygnus complex. A good linear correlation is found between the two emissivities over three decades in energy, proving that γ-ray emission associated with dust residuals is originated in the same physical processes as that associated with H I. A_V residuals therefore trace interstellar gas.

9. The same level of uncertainty would affect the $X_{\rm CO}$ derivation from another total gas tracer such as the dust column-density.

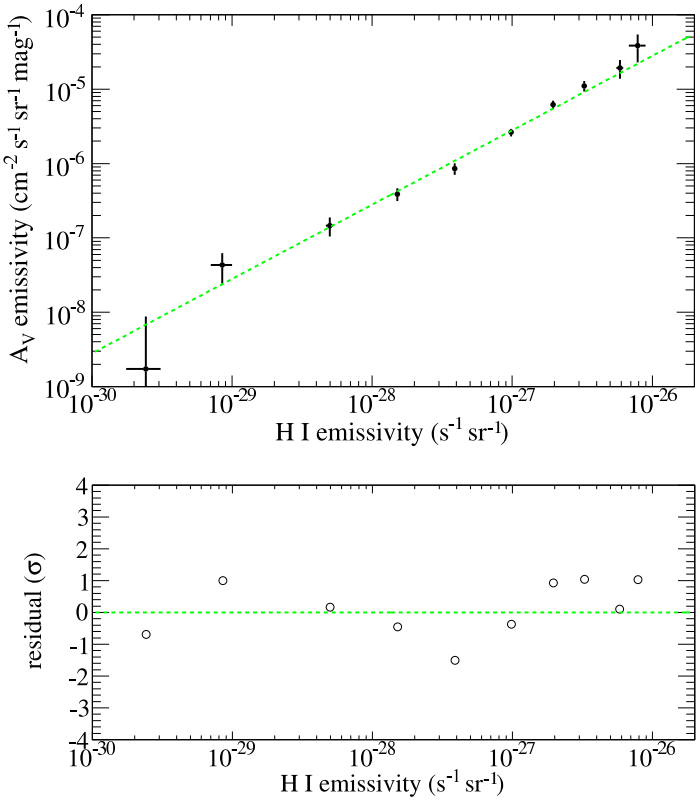

Figure 6.17: Top: emissivity per A_V residual unit versus emissivity per hydrogen atom in the Cygnus complex (for $T_S = 250$ K). The points correspond to the different energy bins; the emissivities decrease with increasing energy. The green line gives the best linear fit taking into account uncertainties on both axes. Bottom: residuals in units of standard deviations as a function of H I emissivity.

With a procedure analogous to that adopted to estimate X_{CO}, we can use the emissivity per hydrogen atom to calibrate the dust-to-gas ratio in the dark phase $X_{A_V} \equiv N(H)/A_{V,res}$. I obtained $X_{A_V} = (28 \pm 2) \times 10^{20}$ cm^{-2} mag^{-1} in the case of $T_S = 250$ K, $X_{A_V} = (48 \pm 3) \times 10^{20}$ cm^{-2} mag^{-1} in the case of $T_S = 100$ K and $X_{A_V} = (27 \pm 2) \times 10^{20}$ cm^{-2} mag^{-1} in the case of optically thin medium. X_{A_V} is therefore $[28 \pm 2\,(\text{stat.})\ ^{+20}_{-1}\,(\text{H I opacity})] \times 10^{20}$ cm^{-2} mag^{-1}.

Assuming a standard total-to-selective extinction ratio $R_V = A_V/E(B-V) = 3.10$ (Wegner, 2003), the dust-to-gas ratio just estimated is $\sim$ 50% higher than the average value in the diffuse ISM (Bohlin et al., 1978) and a factor of 3 higher than what is inferred for the dark phase in local clouds from γ-ray measurements (Grenier et al. 2005, Chapter 4). On the other hand in the fitting procedure to obtain the A_V residual map (§ 6.2.2) I got a consistent estimate for the atomic phase of $N(H\,I)/A_V = 29.6 \pm 0.1 \times 10^{20}$ cm^{-2} mag^{-1} (statistical error only for $T_S = 250$ K). A possible explanation is provided by variations in the interstellar extinction curve, determined by the distribution of dust grain sizes (Cardelli et al., 1989). Straižys et al. (1999) reported an anomalous extinction law in the Cygnus region, showing stronger extinction in the violet and near UV region, that is supportive to the above hypothesis.

The nature of the dark gas cannot be deduced from γ-ray observations. Whereas there are compelling theoretical and observational reasons to believe that CO-quiet H_2 is ubiquitous in the ISM (see § 3.3.3), we cannot exclude that part of the dark gas traced by A_V residuals is missing cold atomic gas, especially since the dark phase appears at the interface between the atomic and CO-bright phases in the nearby clouds (Grenier et al., 2005). Temperatures as low as $40-70$ K were measured in cold H I clouds (Heiles and Troland, 2003) and self absorption can be large when cold clouds are seen against more diffuse warm H I. The A_V residuals in Fig. 6.5 are partially correlated with an H I self-absorption feature associated with the Cygnus complex (Gibson et al., 2005, Fig. 1d). Yet, the H I to H_2 transition is very dynamical, both in space and time, and it is difficult at this stage to conclude on the exact mix of cold dense H I and relatively diffuse CO-quiet H_2 that forms the dark phase on the outskirts of CO-bright molecular clouds.

Regardless of its nature, the mass of the dark gas in the Cygnus complex amounts (at 1.4 kpc) to $0.9^{+0.4}_{-0.1} \times 10^6 M_\odot$. Given an atomic mass of $5^{+4}_{-1} \times 10^6 M_\odot$ and including the CO-bright mass estimated above the total interstellar mass of the Cygnus complex amounts to $8^{+5}_{-1} \times 10^6 M_\odot$.

Assuming that all the dark gas is molecular, we can calculate the molecular dark-gas fraction $f_{DG} = (M_{mol} - M_{CO})/M_{mol}$, which amounts to [10] 0.27 ± 0.02, in excellent agreement with the model by Wolfire et al. (2010). The dark-gas fraction is also consistent with our estimate given in Chapter 4 for the nearby Cepheus and Cassiopeia clouds, which have a factor of 2 lower column densities and a total masses $< 2\%$ of that contained in the Cygnus complex. This also agrees with the prediction by Wolfire et al. (2010) that the dark-gas fraction is almost independent from the mean cloud column density and total mass.

6.3.3 *The γ-ray excess in the inner Cygnus complex*

Properties of the excess

In § 6.2.3 I got the detection of an extended excess of γ-ray emission associated with the innermost ~ 100 pc of the Cygnus complex, partially associated with the stellar cluster Cyg OB2 and a conspicuous concentration of ionized gas. Fig. 6.18 shows the residual map obtained above 10 GeV using model 5.e. The excess is also partially associated with the Cyg OB9 association and the giant H II region S108 (Uyanıker et al., 2001), as well as with an expanding CO shell enclosing a clump of atomic hydrogen (plausibly dissociated H_2 produced by the shell overtaking the surrounding molecular cloud, Butt et al., 2003). The shell rim is populated by numerous H II regions (Paladini et al., 2003).

In Fig. 6.19 I show the spectral energy distribution of the excess, obtained by using model 5.e. I give upper limits at the 95% confidence level below 1 GeV where the detection is not significant. The spectra obtained by using other templates, like the free-free emission map (supposed to trace ionized gas) in model 5.a, are well consistent with that shown in Fig. 6.19. The excess flux in the energy band $1-100$ GeV

10. The dark gas fraction is very stable against the choice of H I spin temperature, therefore the error on the dark-gas fraction is statistical only.

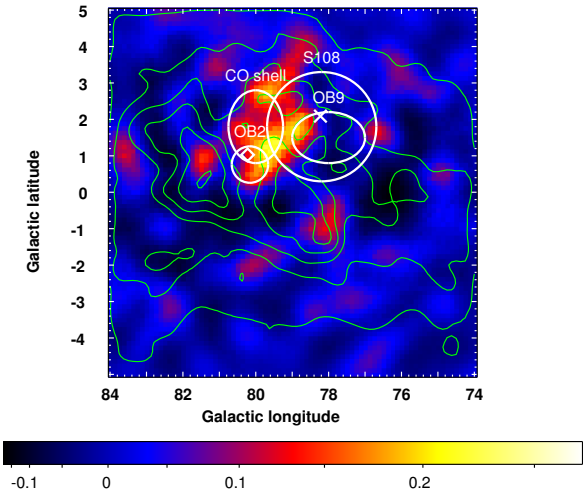

Figure 6.18: Photon residuals ans in Fig. 6.10. We show different astrophysical objects associated with the excess: the star clusters Cyg OB2 and OB9, the giant H II region S108 (Uyanıker et al., 2001) and the expanding CO shell described in Butt et al. (2003); the cross marks the position of PSR J2021+4026/γ Cygni and the diamond that of PSR J2032+4127/TeV J2032+4130. Overlaid also contours of total gas column density from 5×10^{21} cm^{-2} to 3×10^{22} cm^{-2}, equally spaced by 5×10^{21} cm^{-2}.

amounts to $(4.9 \pm 0.8) \times 10^{-8}$ cm^{-2} s^{-1}; at the distance of 1.4 kpc the corresponding luminosity is $(7.3 \pm 1.8) \times 10^{27}$ W.

Interstellar emission or sources?

At energies of $1 - 10$ TeV HEGRA detected within the boundary of Cyg OB2 a source called J2032+4130 (Aharonian et al., 2005) with an angular size of $\sim 0.2°$, significantly smaller than our excess. The source, recently confirmed by VERITAS (Weinstein et al., 2009), coincides with PSR J2032+4127. Camilo et al. (2009) detected radio emission from the pulsar and the dispersion measure gives a distance of 3.6 kpc, placing it farther beyond the Cygnus complex and therefore making its hypothetical pulsar wind nebula an unlikely counterpart to our 2°-wide excess. While the extension of TeV J2032+4130 (of the order of 10 pc at a distance of 3.6 kpc) is compatible with being powered by the pulsar wind of J2032+4127, these sources do not seem to be related with our broader excess.

Synchrotron radiation shows that particle acceleration takes place in the colliding winds of massive stars within binary systems, and the predicted flux up to tens of GeV is close to the LAT sensitivity threshold (Reimer et al., 2006). However, the peak of the excess is offset from stellar clusters in the region, and only partially overlaps with the most massive stars of Cyg OB2 (see later Fig. 6.20), so it appears unlikely that the γ-ray emission is mainly powered by this process.

In model 5.f, where the excess is modeled by three discrete sources, they all exhibit hard spectra, consistent with that of the extended templates, thus indicating that no obvious spectral variations can be detected across the excess. The diffuse character of the excess therefore

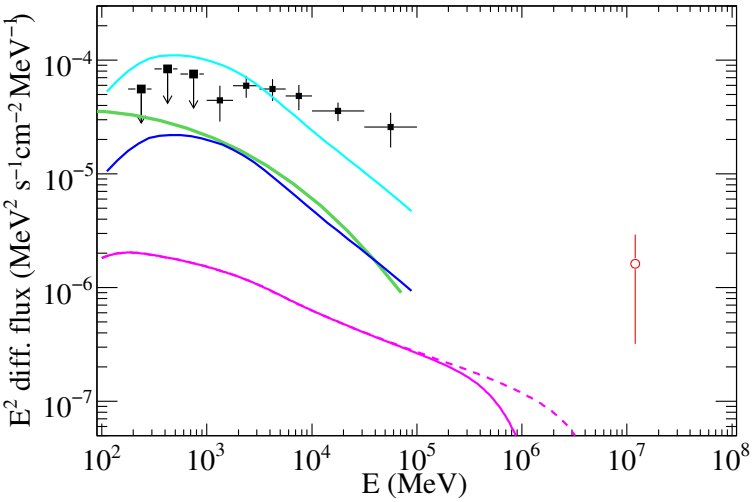

Figure 6.19: Spectral energy distribution of the excess γ-ray emission in the inner Cygnus region (statistical errors only); 95% confidence-level upper limits are given below 1 GeV. The open circle represents the flux measured by the Milagro experiment (see Abdo et al., 2007) in a region of $3^\circ \times 3^\circ$ centered on the HEGRA source J2032+413 (Aharonian et al., 2005) minus the flux of the HEGRA source extrapolated to the Milagro energy band (see Abdo et al., 2007). The solid curves represent the spectral energy distribution expected from the local CR spectrum pervading the ionized gas (blue for $n_{\rm eff} = 10$ cm^{-3}, cyan for $n_{\rm eff} = 2$ cm^{-3}, see text), up-scattering the stellar light from Cyg OB2 (green), and up-scattering the dust and stellar radiation present in the shell and along its ionization front (magenta). For the latter, extending the local electron spectrum to 10 TeV yields the magenta dashed curve.

appears genuine although we cannot firmly rule out a superposition of many hard sources in this crowded direction along the tangent of the Local Spur.

Interstellar emission

The excess is located in a region of high gas density (Fig. 6.18), therefore the uncertainties on the interstellar masses and the modeling of diffuse emission may cast doubts on the significance of the detection. However, a left-over of emission arising from gas illuminated by CRs with the local spectrum (as in Fig. 6.15) cannot explain the observed hardness of the excess.

The excess is partially associated with a dense clump of ionized gas traced by free-free emission. As noted above, the spectral shape of the excess cannot be explained by interactions of gas with CRs with the local spectrum. I used Eq. 6.2 to turn the free-free emission intensities into column densities of H II, adopting $T_e = 8000$ K and $n_{\rm eff} = 2 - 10$ cm^{-3} (Sodroski et al., 1997). I thus obtained in a region encompassing the bubble at $77.5^\circ < l < 82^\circ$, $-1.5^\circ < b < +3.5^\circ$ a H II mass of $2 - 10 \times 10^5 M_\odot$ at a distance of 1.4 kpc ($\lesssim 10\%$ of the neutral gas). The conversion is highly uncertain, but Fig. 6.18 shows that the γ-ray fluxes expected from ionized gas irradiated by the lo-

cal CR spectrum is indicatively lower or comparable to the flux of the excess and the spectrum is significantly softer.

Inverse Compton emission from the Cyg OB2 cluster was predicted to approach the LAT detection threshold (Orlando and Strong, 2007), but the present excess flux > 1 GeV of $(4.9 \pm 0.8) \times 10^{-8}$ cm^{-2} s^{-1} is larger by a factor ~ 2.5 than the flux expected from the upscattered optical stellar light by CR electrons with the local spectrum. The spectral energy distribution predicted from the cluster using such electron spectrum and the stellar properties described in § 6.2.2 is displayed in Fig. 6.19. It is softer than the LAT excess, which is very hard up to 100 GeV.

The Milagro experiment measured extended γ-ray emission at energies > 10 TeV from the Cygnus region (Abdo et al., 2007), with a remarkable enhancement (sometimes called MGRO J2031+41) in the direction of our excess. With an average angular resolution of 0.5°, Milagro could not determine the extension of the excess. Abdo et al. (2007) estimated that its flux exceeds by a factor of ~ 3 the extrapolation of the flux from TeV J2032+4130 to Milagro energies and they possibly attributed the difference to diffuse emission. We added the excess Milagro flux in Fig. 6.19. Note that both HEGRA and VERITAS could miss the $> 2°$ wide excess seen by the LAT: HEGRA observed only a $1° \times 1°$ region centered on J2032+4130 and the analysis of the VERITAS Cygnus survey was optimized to detect either point-like or moderately extended ($r \simeq 0.2°$) sources (Weinstein et al., 2009).

In Fig. 6.20, a zoom around the excess has been overlaid on top of the 8 μm map of the region as observed by the MSX experiment (band A, see Mill et al., 1994). The γ-ray excess only partially overlaps the cluster of 85 O stars belonging to the Cyg OB2 association (Hanson, 2003). It follows the 130 pc long cavity which apparently extends from Cyg OB2 to the γ Cyg remnant (Butt et al., 2003). Since there is no evidence in H I or CO that the supernova shock wave blows up into a hollow shell along this part of the rim (Ladouceur and Pineault, 2008), it is not clear whether the shell actually connects Cyg OB2 and γ Cygni or if we are facing a chance alignment. The γ-ray excess also correlates with the photon-dominated regions (PDRs) which are excited along the edges of the molecular clouds by the intense ionizing radiation from the Cyg OB2 cluster, the Cyg OB9 association, and possibly a still unidentified population of OB stars lying inside IC 1318 b/c (Schneider et al., 2006). Along the ionization fronts, recombination lines, excited polycyclic aromatic hydrocarbons (PAH) lines, and heated dust in the PDR layers produce an intense optical and infrared radiation field that can provide pockets of inverse-Compton γ-ray emission in addition to the large-scale contribution that we took into account in the model and in addition to the emission from the OB2 cluster described above. While the spectrum of IC emission from stellar radiation cuts off in the $10 - 100$ GeV energy range due to the energy dependence of the Klein-Nishina cross section, IC scattering on the infrared radiation might extend the spectrum to higher energies.

Figure 6.21 shows an estimate of the average spectral energy density of the soft radiation estimated within the contours of the γ-ray excess of Fig. 6.20 for $l > 78°$. It includes the cosmological background radiation, two components for the stellar light scaled to an energy density of 10 eV cm^{-3} for a temperature of 2900 K and 50 eV cm^{-3} for the field expected at a distance of 10 pc from a 35000 K B-type star (Orlando

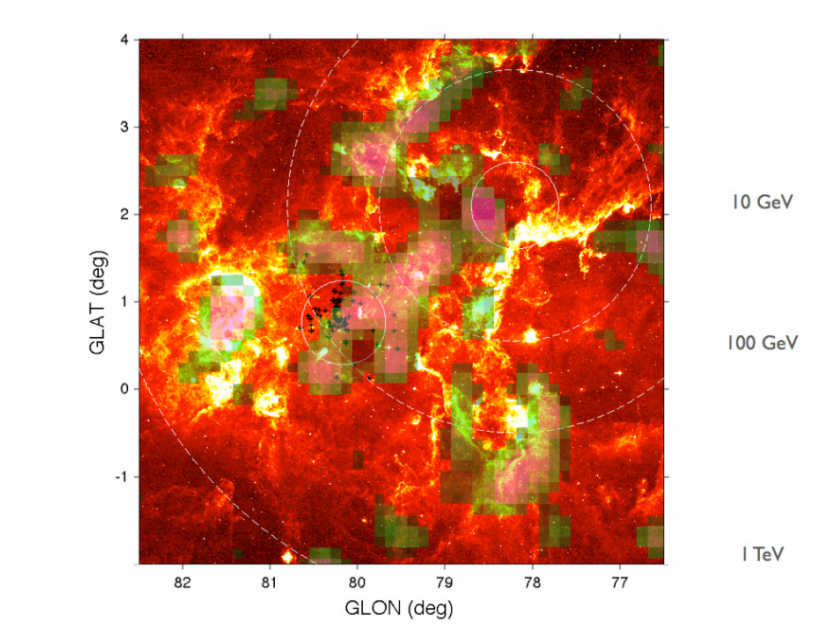

Figure 6.20: 8 μm map of the inner Cygnus complex as obtained from MSX data (band A). Overlaid γ-ray residuals from model 5.e (modified forcing X_{CO} to the best-fit value derived in the 100 MeV-10 GeV energy band) smoothed with a Gaussian kernel of $\sigma = 0.2°$. Solid circles mark the core of the Cyg OB2 association (Hanson, 2003, bottom left) and the γ Cyg SNR (top right). Crosses mark the positions of the 85 O members of Cyg OB2 reported in Hanson (2003). Dashed circles represent the distances around γ Cygni to which particles of 10 GeV, 100 GeV and 1 TeV can diffuse (see text).

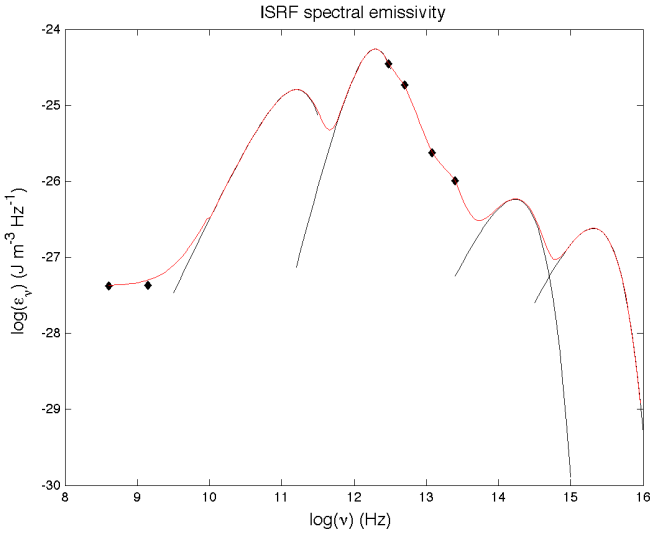

Figure 6.21: Spectral energy distribution of the average interstellar radiation field in the region coincident with γ-ray excess. See text for a description of the model.

and Strong, 2007). The data points were derived from measurements

at 408 MHz (Haslam et al., 1981), 1.42 GHz (CGPS), and the 12, 25, 60, and 100 μm channels of *IRAS*. They were obtained by subtracting the average intensity measured in three $1^\circ \times 2^\circ$ regions away from the excess (in the corners of Fig. 6.20) from the average intensity found within the excess contours. This procedure aims at estimating magnitude of the local IC contribution due to the PDRs and massive stars in addition to the large-scale Galactic component calculated with GALPROP. IR points were fit using a standard dust emission law with a temperature of 20 K, an opacity index of 1.8 and the intensity scaled to the data point at 100 μm. The IC flux was estimated for the local electron spectrum within the 50 pc radius region encompassed by the best-fit Gaussian source and it is shown in Fig. 6.19. The enhanced radiation field can explain the hardness of the LAT diffuse excess, but not its flux, nor the Milagro measurement. A much larger electron flux is required to match the data. Electron densities higher than those in the solar neighborhood are also suggested by radio synchrotron emission from the Cygnus region (Orlando et al., 2009).

CR acceleration in the inner Cygnus complex?

OB associations have been proposed as possible CR sources. In the superbubble (SB) scenario, illustrated in § 2.2.2, CRs are accelerated by the collective action of massive-star winds and multiple SN explosions. Cyg OB2, which is the most conspicuous stellar cluster in the region, has an estimated age of 2 Myr (Hanson, 2003), which makes the explosion of a series of supernovae unlikely. Alternatively, mechanical energy of powerful stellar winds alone in massive-star clusters might sustain CR acceleration (e.g. Cesarsky and Montmerle, 1983; Domingo-Santamaría and Torres, 2006). However, the peak of the excess is offset from stellar clusters in the region, notably from Cygnus OB2.

Another possibility is that freshly accelerated CRs diffuse out from the SNR in γ Cygni, whose rim shows a hard spectrum up to 100 GeV (Fig. 6.13), possible signature of the presence of high-energy particles. The maximum energy of particles accelerated by γ Cygni was approximately evaluated following the procedure illustrated in Baring et al. (1999). From optical observations Mavromatakis (2003) inferred that the remnant is in the Sedov expansion phase, and estimated an age of $\sim$ 7 kyr for an ambient medium of density $\sim$ 0.3 cm^{-3} (Lozinskaya et al., 2000). From X-ray observations Uchiyama et al. (2002) estimated a shock velocity of 800^{+50}_{-60} km s^{-1} and a subsequent age of $\sim$ 6.6 kyr at a distance of 1.5 kpc given the diameter of 1°. This sets the transition between the free and the Sedov expansion phases approximately 5 kyr ago. CR streaming can amplify magnetic fields in SNRs and lead to compression ratios $r > 6$ (e.g. Ellison et al., 2004); this in turns can amplify the efficiency of diffusive shock acceleration so that CR acceleration efficiently takes place in the free expansion phase (e.g. Parizot et al., 2006). The maximum energy of protons and electrons accelerated by γ Cygni was therefore evaluated at the onset of the Sedov phase, assuming a massive star progenitor (explosion energy of 10^{44} J and ejecta mass of $9\,M_\odot$), the ambient density of 0.3 cm^{-3} quoted above, an upstream magnetic field of 6 μG (since the ambient density is almost the same as the local one) and a ratio of downstream to upstream magnetic field strength of $B_\mathrm{d}/B_\mathrm{u} = 0.83\,r$ (e.g. Parizot et al., 2006) with a compression ratio $r = 7$. By equating the diffusion length to the size of the remnant 5 kyr ago the maximum energy for accelerated pro-

tons resulted $\sim$ 30 TeV. The maximum energy of accelerated electrons is limited by radiative losses: at the same epoch an upper energy of $\sim$ 20 TeV was obtained in the Bohm limit due to synchrotron radiation in the amplified magnetic field and IC scattering on the CMB. While the energies available are large enough to explain the LAT excess either as the result of proton or electron interactions, an IC origin of the Milagro excess seems problematic (Fig. 6.19) for particles accelerated by γ Cygni.

For illustration purposes we also calculated the distances to which particles of 10, 100, and 1000 GeV can diffuse from γ Cygni. According to Gabici et al. (2009), after a travel time τ particles diffuse over a characteristic length $L(E,\tau) = \sqrt{4\,D(E)\,\tau}$ with $D(E) = 10^{24} \times (E/10\ \mathrm{GeV})^{0.5}\ \mathrm{m^2\ s^{-1}}$. The results are shown in Fig. 6.20 for $\tau = 5$ kyr. This illustrates that most of the excess region is compatible with an enhanced CR flux originated from γ Cygni.

The correlation between the LAT excess and the bright regions near Cyg OB2 and along the PDRs may favor a significant IC contribution to the LAT flux. A puzzling fact is the concentration of γ-rays within the rarefied shell rather than in the massive clouds where the SNR is located. This would call for a scenario like the "champagne bubble" described in Völk (1983); Grenier (2008). When the SNR shock wave breaks away into a champagne flow (Tenorio-Tagle, 1979) toward a low-density region, magnetic field lines are swept away in a mushroom-like configuration (Völk, 1983, Fig. 2). Particles advected with the shock can stream along the field lines and flow back to the shell rim to produce γ-rays through IC scattering in the PDRs at the edges of the clouds or π^0 decay in their dense photo-dissociated layers. In this scenario, the Cygnus region would offer the first resolved example of a γ-ray champagne flow to be studied.

Interestingly, the HESS collaboration reported the detection of very high-energy extended γ-ray emission toward other massive-star forming regions. Aharonian et al. (2007) reported an extended source coincident with the massive stellar cluster Westerlund 2 in the Carina region: the extension and variability studies indicate that the source is associated to the massive H II region and its ionizing cluster, perhaps because of CRs accelerated inside bubbles or at their termination shock and interacting with the surrounding environment. HESS also detected emission from the Galactic center ridge with a hard spectral index of about -2.3 (Aharonian et al., 2006). Such emission coincides with the conspicuous star-forming regions of the Arches, Quintuplet and Sgr B2 clusters. In this case, the authors seemed to favor a hadronic origin because of the correlation between γ-ray emission and dense molecular material traced by CS (carbon monosulfide), while the association with PDRs favor an IC origin of our excess toward the inner Cygnus complex. However, attributing the Galactic ridge emission to a passing wave of ions produced by a central source like Sgr A East leaves open issues (e.g. Grenier, 2008) and, given the Milagro measurement in Cygnus, a suggestive analogy between our excess and the very high-energy emission measured by HESS toward massive star forming regions is possibly foreseen.

6.4 SUMMARY OF THE RESULTS

- Interstellar γ-ray emission averaged over $\sim$ 400 pc around the Cygnus complex highlights a CR population similar to that in the local interstellar space.
- The X_{CO} ratio inferred from γ-ray data is consistent with other LAT estimates for the Local Spur.
- Dark gas not traced by the combination of H I and CO lines is detected for a mass equivalent to $\sim$ 40% of that traced by CO. Its γ-ray emissivity shows a good proportionality to that of atomic gas from 100 MeV to 100 GeV.
- Extended excesses of γ-ray emission are detected in association with the Cygnus Loop and γ Cygni SNRs.
- An extended hard-spectrum excess of γ-ray emission is detected toward the innermost 100 pc of the Cygnus complex, partially associated with the massive star clusters Cyg OB2 and OB9, TeV emission detected by Milagro and an expanding gas shell possibly connecting Cyg OB2 to the γ Cygni SNR and bordered by bright PDRs and H II regions. The excess may indicate the presence of larger densities of high-energy particles with respect to the surrounding clouds.

Acknowledgements

The use of multiwavelength data was invaluable to this study. Data products directly provided by the authors were referenced along the text. We also made use of data from:

- the Canadian Galactic Plane Survey (CGPS), a project based at the Dominion Radio Astrophysical Observatory (operated as a national facility by the National Research Council of Canada) and supported by a grant from the Natural Sciences and Engineering Research Council of Canada;
- the ROSAT Data Archive of the Max-Planck-Institut für extraterrestrische Physik (MPE) at Garching, Germany;
- the Legacy Archive for Microwave Background Data Analysis (LAMBDA), supported by the NASA Office of Space Science;
- the NASA/IPAC Infrared Science Archive;
- the databases operated at the Centre de Données Astronomiques de Strasbourg (CDS), Strasbourg, France.

7 SUMMARY AND CONCLUSIONS

High-energy γ-ray emission carries information about energetic processes occurring in the interstellar space, notably the interactions between CRs and interstellar matter and radiation fields. In the previous chapters I presented in-depth analyses of LAT observations for three regions of the sky, the outer Galaxy seen in the second and third quadrants and the Cygnus complex.

The results provide insights on the relation between CR densities and the distribution of putative CR sources. The results also constrain the census of the interstellar medium over a few kpc from the solar system.

In this chapter I summarize those results and I discuss their implications for the origin of Galactic CRs, the use of the $J = 1 \rightarrow 0$ line of ^{12}CO as a tracer of molecular masses and the ubiquitous dark gas missed by the most conventional radio/mm-wave lines.

7.1 THE DISTRIBUTION OF COSMIC RAYS IN THE GALAXY

7.1.1 *Summary of the results*

Fig. 7.1 summarizes the measurements of H I emissivities presented along the thesis, spanning a few kpc from the solar circle to the outer Galaxy. The uncertainties are due to the opacity correction applied

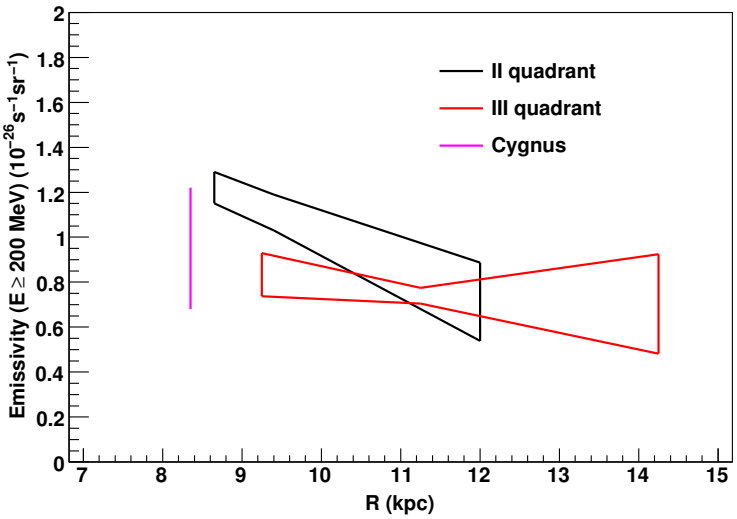

Figure 7.1: H I emissivity integrated above 200 MeV as a function of Galactocentric radius for the different regions studied in the thesis.

to H I data, based on the assumption of a uniform spin temperature (§ 2.1.2).

γ-ray data support average spin temperatures > 200 K for the outer Galaxy, corresponding to a blend of $\lesssim 20\%$ cold gas and the rest warm,

as deduced from absorption/emission pairs (Dickey et al., 2009). The thermodynamic temperature, however, varies from $\sim$ 40 K for cold atomic clouds to several thousands K in the warm diffuse medium. We evaluated the uncertainties due to the opacity correction procedure varying the uniform spin temperature in the range 100 K $< T_S <$ ∞. The value of 100 K was chosen as lower bound in the uniform approximation since Eq 2.10 yields that $T_S > T_B$, and a $T_B > 100$ K is observed over many lines of sight in the regions studied.

The spin temperature impacts the determination of the emissivity in two different ways, by modifying the total mass of gas and by shaping the structures of $N(\mathrm{H\,I})$ maps which are driving the component separation procedure. The impact is more severe in regions with higher gas densities, like the Cygnus complex and the Perseus arm. This is currently the dominant source of uncertainty in the estimate of H I emissivities and, subsequently, of CR densities from γ-ray observations.

The H I emissivities in Fig. 7.1 are remarkably uniform: variations are $\lesssim$ 20% over 1 kpc around the Sun and less than a factor 2 over 6 kpc in Galactocentric radius toward the outer Galaxy. The small differences $\lesssim$ 20% between the regions studied in the second and third quadrants are interesting in relation to the possible accuracy of axisymmetric models of CR propagation in reproducing γ-ray data.

7.1.2 *The coupling of cosmic-ray and interstellar medium densities*

The association between γ-ray emission and remarkable structures of the ISM, like the tangent points of the spiral arm, led to the idea of a dynamical coupling between CR and ISM densities (§ 3.3.1). LAT accurate measurements of H I emissivity provide a new ground for confronting this idea with observational evidence.

We obtained a few estimates of H I emissivity along the Local Spur. The Cygnus complex exhibits a factor of $\sim$ 2 higher gas surface densities than the segments of the Local Spur studied in the second and third quadrants, and a factor of $\sim$ 5 higher than the diffuse medium observed in the mid-latitude region of the third quadrant used to estimate the local H I emissivity (§ 3.2.2). In spite of such sizable variations, no significant differences are seen in Fig. 7.1 between the emissivities inferred from LAT data.

In Chapter 5 we also studied the gradient of H I emissivity along a line of sight where there is an interarm region with lower gas surface densities between the Local Spur and the Perseus spiral arm. Although a small contrast in emissivity $< 10\% - 20\%$ is compatible with data (Fig. 7.1), this was found to be much smaller than what expected from a coupling length of $\sim 1 - 2$ kpc (Bertsch et al., 1993; Hunter et al., 1997), given the difference of $30\% - 40\%$ in average gas surface densities. Studies of individual regions considered so far did not provide any evidences of coupling between CR and ISM densities, although small-scale effects cannot be excluded at the present stage.

7.1.3 *The cosmic-ray gradient problem in the outer Galaxy*

In spite of a steep decrease of putative CR sources beyond the solar circle (Fig. 2.5), no significant variations of gas emissivity are evident from Fig. 7.1. Widely used propagation models predict a sizable de-

crease of CR densities in the outer Galaxy (e.g. Fig. 4.3), therefore LAT measurements strengthen the CR *gradient problem* (§ 3.3.1).

An unknown parameter with large impact on the radial gradient of CR densities is the size of the propagation halo (e.g. Stecker and Jones, 1977; Strong and Moskalenko, 1998). The distribution of putative CR sources in the Galaxy is also highly uncertain (§ 2.2.2), so a flatter distribution in the outer Galaxy is, a priori, a viable possibility. We explored these tentative solutions of the *gradient problem* in § 5.1. In Fig. 7.2 I compare the summary of H I emissivities collected along the thesis (Fig. 7.1) with the CR propagation models presented there.

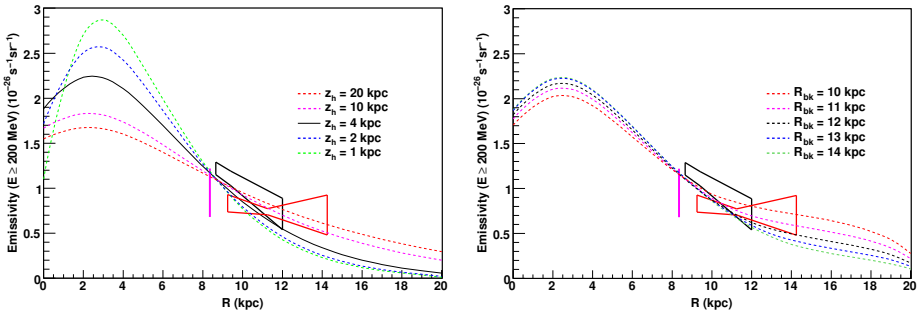

Figure 7.2: H I emissivity integrated above 200 MeV as a function of Galactocentric radius, compared with different CR propagation models. With respect to § 5.1 (Fig. 13) the model-predicted emissivities were integrated above 200 MeV and renormalized to match the average of the measurements at the solar circle.

Based on the observed distribution of pulsars and SNRs, LAT data favor large propagation halos, with heights $z_h \gtrsim 10$ kpc. Let us note that $z_h = 10$ kpc is approximately the maximum halo height allowed by ^{10}Be/^{9}Be measurements (§ 2.2.3). On the other hand, assuming $z_h = 4$ kpc as in Fig. 7.2 (right panel) and in many pre-*Fermi* studies (e.g. Strong et al., 2004a,b), the LAT profile would imply a flat CR source distribution at the solar circle and beyond. This would be in contrast with all the available tracers of CR sources and their progenitors, massive OB stars (Fig. 2.5) as well as with the observations of the ^{26}Al line, which is a tracer of explosive nucleosynthesis products (Diehl et al., 2006).

Different propagation scenarios need to be considered before firm conclusions can be drawn. Let us mention, e.g., that Evoli et al. (2008) proposed a propagation model with non-uniform diffusion satisfactorily reproducing EGRET data.

Missing gas might bias the estimate of H I γ-ray emissivities and origin of the *gradient problem*. Strong et al. (2004b) proposed for this reason an increase of one order of magnitude in $X_{\rm CO}$ beyond the solar circle. The analyses reported in the thesis do not confirm such a large increase as I will summarize in § 7.2.2, yet, a strong $X_{\rm CO}$ gradient would not explain the small H I-emissivity variations. Abundant quantities of warm, diffuse, dark molecular gas were suggested to be present in the low-metallicity environments of the outer Galaxy (Papadopoulos et al., 2002); other models (e.g. Wolfire et al., 2010) of the dark phase, however, do not provide enough dark gas to explain our emissivities.

7.2 CO AS MOLECULAR MASS TRACER

7.2.1 *Summary of the results*

The results presented along the thesis support the use of W_{CO} as a tracer of molecular masses for the cold CO-bright clouds. In particular, the good correlation between CO and H I γ-ray emissivities over more than two decades in energy and more than a factor of 2 column densities of gas (Fig. 11 of § 4.1, Fig. 10 of § 5.1 and Fig. 6.16) indicates that systematic biases due to effects like incomplete penetration of CRs into the dense molecular cores or interactions with freshly accelerated CRs from sources embedded in the clouds, if present, are generally small.

In Fig. 7.3 I summarize the X_γ values derived from the studies dedicated to the second quadrant, the third quadrant and the Cygnus region. The X_{CO} ratio as deduced from γ-ray observations is remarkable constant for clouds in the plane, from the solar circle to the outer disk of the Milky Way up to $R \simeq 14$ kpc, in good agreement with global estimates derived from γ-ray observations (e.g. Strong and Mattox, 1996) and other total gas tracers such as dust (e.g. Dame et al., 2001). The mid-latitude clouds of Cassiopeia, Cepheus and Polaris show a factor of 2 lower X_γ, consistently with previous estimates based on EGRET data (Digel et al., 1996).

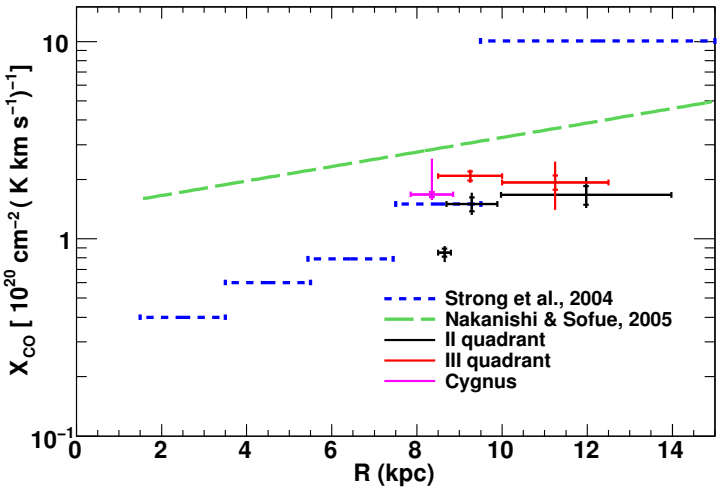

Figure 7.3: X_{CO} as a function of Galactocentric radius R. Points give the values reported along the thesis for the different regions analysed in the second and third quadrants and the Cygnus complex. Mean values are provided for the case of a uniform value of $T_S = 250$ K adopted for the H I opacity correction. End-cap bars mark statistical errors, whereas plain bars mark the systematic uncertainties due to the H I opacity correction. For reference we report the two models by Strong et al. (2004b); Nakanishi and Sofue (2006). EGRET results were summarized in Fig. 3.5.

The calibration of X_{CO} based on γ-ray observations provides values systematically lower than estimates based on virial masses, as one can deduce comparing our results in Fig. 7.3 with the conversion function by Nakanishi and Sofue (2006) and I verified studying the masses of individual clouds in Chapter 4.

7.2.2 *Variations in X_{CO}?*

Many evidences suggest that X_{CO} might vary over the Galactic scale (§ 3.3.2). The low metallicity of the outer disk of the Milky Way would be expected to lead to an increase in X_{CO}, also because of the diminished self-shielding effect and subsequent CO photodissociation by UV radiation. Virial masses (Digel et al., 1990) and observations of metal-poor external galaxies support this idea (Israel, 1997). No significant variations, however, are suggested in the Galactic disc by our results from the solar circle to the Perseus spiral arm over distances of a few kpc. Notably, our results are not consistent with the model developed by Strong et al. (2004b) predicting a steep increase in X_{CO} just beyond the solar circle, and therefore strengthen the CR gradient problem in the outer Galaxy (§ 7.1.3).

The nearby, well-resolved clouds of the Gould Belt of the Cas/Cep complex have a factor of $\sim$ 2 lower X_γ with respect to the clouds studied in the plane. The origin of this difference is not understood yet. Our results, however, are consistent with previous estimates based on EGRET data for the Cepheus and Polaris flares (Digel et al., 1996) and other mid-latitude nearby clouds like Ophiuchus (Hunter et al., 1994). In addition to metallicity, other physical parameters should influence X_{CO}, notably density and temperature in the cloud [1]. Let us also note that, because of the different linear resolution, for distant clouds in the plane we predominantly sample the cores, whereas for nearby clouds we are more sensitive to the outer layers, and translucent high-latitude clouds are known to have low X_{CO} ratios (e.g. de Vries et al., 1987).

Contamination from unresolved point sources which mimic the spatial distribution of the clouds is expected in massive-star forming regions. This effect can be ruled out for the Cas/Cep clouds which produce few high-mass stars and, at a distance of $\sim$ 300 pc, are observed in γ-rays with a linear resolution of $\sim$ 3 pc. It might bias, on the other hand, the X_{CO} estimate for more distant, less resolved clouds associated with regions of massive star formation like Cygnus and NGC 7538/Cas A. Resolution problems are also becoming more severe with increasing distance and may influence the determination of X_γ because of the increasingly less reliable separation between the CO-bright cores of interstellar clouds and their CO-quiet/atomic envelopes.

7.2.3 *X_{CO}: γ-rays and other calibrators*

The calibration of X_{CO} with γ-ray data (§ 3.3.2) is based on the assumptions the CR densities are almost uniform over the characteristic scales of interstellar complexes and that they penetrate uni-

1. We can illustrate the dependence of X_{CO} on density and temperature with a toy calculation.

$$W_{CO} \simeq T_{CO}\,\sigma_v$$
$$N(H_2) \simeq \frac{M}{r^2}$$

For a cloud in virial equilibrium

$$\sigma_v^2 \simeq \frac{GM}{r}$$

so that

$$X_{CO} \equiv \frac{N(H_2)}{W_{CO}} \simeq \frac{M}{r^2\,T_{CO}\,\sigma_v} \propto \frac{\sqrt{n(H_2)}}{T_{CO}}$$

formly clouds to their cores in spite of the possibly enhanced magnetic fields. In addition to failures of these hypotheses other important limitations are given by possible contamination by unresolved γ-ray sources, unmodeled structures in IC emission and resolution problems. The methodology used to calibrate X_{CO} based on γ-ray measurements makes X_γ an estimate of $X_{CO} \equiv N(H_2)_{CO}/W_{CO}$, with $N(H_2)_{CO}$ column density of molecular gas directly proportional to W_{CO}, rather than of total molecular masses.

We have shown that virial masses of clouds are systematically higher than masses inferred by CO luminosity calibrated through γ-ray observations. We first note that virial masses are total dynamical masses and therefore intrinsically different from the CO-bright masses obtained from γ-rays. On the other hand the differences can be attributed to the limitations of both approaches. For virial estimates the main issues are linked to the assumption of clouds held in equilibrium against gravitational collapse by turbulent motion only, whereas magnetic support probably plays an important role, to the estimate of turbulent velocity from the width of the CO lines and to the working hypotheses of simple geometrical shapes and mass distributions in the clouds (e.g. spherical clouds with mass density varying as $1/r$).

It is interesting to note that new results are being released by the *Planck* and *Herschel* satellites concerning the gas distribution in the Galaxy. Dust can be used as a total mass tracer in the very same way as γ-ray emission (§ 2.1.3). Past whole-sky analyses (e.g. Dame et al., 2001) provided a calibration consistent with that obtained from γ-ray observations (e.g. Strong and Mattox, 1996). Early results from *Planck*, based on the assumption of an analogous emissivity for the dust in the atomic and molecular phases, indicate higher average values in the solar neighborhood (Ade et al., 2011). Further comparisons for individual clouds or complexes will bring interesting insights on the census of the ISM and on possible variations of the dust emissivity in different environments (e.g. Paradis et al., 2009).

7.3 DARK GAS

Total mass tracers such as dust and interstellar γ-ray emission are a useful probe of the completeness of our census of the ISM mainly based on the 21-cm HI line and the 2.6-mm CO line. Grenier et al. (2005) reported the presence of correlated excesses of dust and γ-ray emission in EGRET data over the HI and CO maps, forming structured envelopes at the interface between the CO-bright cores and the HI outskirts of nearby clouds in the Gould Belt. Because of the location at the interface between the CO-bright and atomic phases of the clouds, and the lack of plausible alternative emission mechanisms, Grenier et al. (2005) attributed the excess to neutral dark gas (§ 3.3.3).

We confirmed the presence of such excess in nearby clouds of the Gould Belt in the Cas/Cep complex (Chapter 4). Detecting dark gas in the disc of the Milky Way is more challenging, due to confusion along the line of sight and dust-emissivity gradients in regions of massive-star formation. Resorting to visual extinction of near-infrared sources as dust tracer, for first time we detected an analogous excess in the massive star-forming region of Cygnus (Chapter 6).

In both cases we were also able to study the emissivity spectrum of the excess, and we found a good linear correlation with the HI

emissivity spectrum over more than two decades in energy (Fig. 13 of § 4.1 and Fig. 6.17). This is a very strong evidence which supports the interpretation of the dust/γ-ray excess as additional gas not properly traced by the radio/mm-wave lines rather than pockets of IC emission or problems of source contamination.

The dust-to-gas ratio inferred for the dark phase from γ-ray measurements for the clouds of the Cas/Cep complex using as dust tracer the $E(B-V)$ color excess is consistent with the estimate derived for local clouds by Grenier et al. (2005) based on EGRET data. This is a factor of 2 lower than the reference value in the diffuse ISM (Bohlin et al., 1978), but consistent, as shown by Grenier et al. (2005) with the average for the CO-bright phase in local clouds. On the other hand, the dust-to-gas ratio obtained for the Cygnus complex using as dust tracer the visual extinction A_V is 50% higher than the reference value for a standard total-to-selective extinction ratio $R_V = A_V/E(B-V) = 3.10$ (Wegner, 2003), but consistent with the estimate of the dust-to-gas ratio in the atomic phase derived in the analysis. The high dust-to-gas ratio in the atomic and dark phase might be due to variations in the interstellar extinction curve (Cardelli et al., 1989; Straižys et al., 1999).

γ-ray emission from dark gas provides a calibrator of its masses. The mass in the dark phase results $40\% - 60\%$ of that traced by CO (Table 3 of § 4.1 and § 6.3.2). If we assume that all the dark gas is molecular, the dark molecular fraction results to be $\sim 30\%$ almost independently from mean column density and total mass in the clouds, in remarkably good agreement with the model by Wolfire et al. (2010). However, the nature of the dark gas, either molecular or atomic, is not clear yet. Large uncertainties are due to the limited knowledge of the masses of atomic gas related to the opacity correction (§ 2.1.2).

7.4 INTERSTELLAR EMISSION IN MASSIVE-STAR FORMING REGIONS

Over last years observational results strengthened the link between massive-star formation activity and CR acceleration. On one hand, ground-based instruments detected TeV emission from massive-star forming regions in the Galaxy, including the Carina (Aharonian et al., 2007) and Cygnus complexes (Abdo et al., 2007) and perhaps the Arches, Quintuplet and Sgr B2 clusters in the inner Galactic ridge (Aharonian et al., 2006); on the other hand, they revealed starbust galaxies as very high-energy γ-ray sources (The VERITAS Collaboration, 2009; Acero et al., 2009). The LAT detected so far intense γ-ray emission from the starbust region 30 Dor in the Large Magellanic Cloud (§ 3.4.2) and correlation between γ-ray luminosity and star-formation rate in a few external galaxies (§ 3.4.3).

A direct evidence for a relation between star-formation activity and interstellar emission intensities was missing so far in our Galaxy. In Chapter 6 we detected hard extended emission associated with the innermost 100 pc of the Cygnus region and the TeV emission measured by Milagro (Abdo et al., 2007). The excess partially overlaps the Cyg OB2 and OB9 stellar clusters, the giant H II region S108 and an expanding cavity in the interstellar clouds possibly connecting Cyg OB2 to the γ Cygni SNR, whose edges are populated by bright photon-dominated regions (PDRs) and numerous H II regions.

While the association between γ-ray emission and PDRs suggests a significant IC contribution, electron fluxes larger by about one or-

der of magnitude than those measured near the Earth are required to reproduce the observed γ-ray fluxes at energies > 10 GeV. Particle acceleration in the nearby γ Cygni SNR can provide the needed CR densities, but the morphology of γ-ray emission would call for an efficient advection of freshly accelerated particles in the gas cavity, like in the "champagne bubble" scenario depicted by Völk (1983); Grenier (2008). This would offer the first resolved example of a γ-ray champagne flow to be studied in γ-rays. In this scenario, however, it is difficult to explain the Milagro excess in terms of IC emission if the CR source is identified in the γ Cygni SNR because of the cutoff in the electron spectrum due to their severe radiative energy losses in amplified magnetic fields.

This finding seems to support the link between star formation activity and CR acceleration and offers a possible GeV counterpart to TeV emission unveiled by ground-based instruments in massive-star forming regions.

7.5 FUTURE PROSPECTS

The main limitation in the interpretation of high-energy interstellar γ-ray emission in terms of CR and ISM densities is currently the H I opacity problem (§ 7.1). Reliable determinations of the atomic gas masses are required to improve the accuracy of the results; larger surveys of emission/absorption pairs and the modeling of the ISM thermo-hydrodynamics are complementary to achieve this objective.

In spite of current uncertainties, the gradient problem in the outer Milky Way challenges our picture of CR origin and propagation in the Galaxy. LAT studies of interstellar emission from other local clouds and from the inner disc of the Milky Way will add further pieces to the puzzle. The large scale modeling of interstellar γ-ray emission, ongoing in the *Fermi* LAT collaboration (e.g. Strong, 2011), will help to consider LAT measurements in the context of multiwavelength/-multimessenger constraints on CR propagation. This will complement observations of putative CR sources in γ-rays and at other wavelengths to constrain CR acceleration and transport.

The systematic study of emission from local clouds with LAT data, also at higher resolution when more high-energy photons will be available, is fundamental to better understand the properties of ISM tracers and constrain the census of the interstellar gas in the Galaxy, to probe for variations of X_{CO} from cloud to cloud, to investigate the difference found between clouds in the plane and the clouds in the Cas/Cep complex and to evaluate the dust-to-gas ratio in the dark phase and gauge the dark masses.

On both the CR and ISM side, complementary results are being provided by the *Planck* satellite, which observes in the microwave domain the synchrotron emission from high-energy electrons and ISM tracers such as free-free emission and dust thermal emission.

The γ-ray excess in the inner Cygnus complex provides the first evidence at GeV energies in our Galaxy of the apparent link between massive-star formation activity and interstellar γ-ray emission. Further observational results are needed to consolidate this finding, primarily from the analysis of LAT observations in other massive-star forming regions where VHE γ-ray emission was detected, namely the Carina complex and the inner Galactic ridge, where, however, the inter-

pretation of data is complicated by the confusion along the line of sight and the loss of linear resolution with increasing distance. Other important insights are expected from a systematical search for emission from external galaxies in LAT data, and the implications in terms of the γ-ray luminosity/star formation rate relation. The study of massive-star forming regions should be pursued also with deeper observations at very high energies by current (VERITAS, HESS, MAGIC) and future experiments (CTA/AGIS). Studies in the energy band around 100 GeV, bridging spaceborne to ground-based γ-ray observations, will be key to constrain the underlying emission mechanisms and investigate CR acceleration and transport in superbubbles and regions hosting massive stellar clusters.

Part III

TECHNICAL MATERIAL

When a distinguished but elderly scientist
states that something is possible,
he is almost certainly right;
when he states that something is impossible,
he is probably wrong.

— Arthur C. Clarke, Profiles of the Future

A

RESIDUAL BACKGROUNDS IN LAT DATA

Keeping under control residual backgrounds is a fundamental part of LAT data analysis. Residual backgrounds are made of misclassified CR interactions in the LAT, which can be further distinguished in reducible and irreducible backgrounds. A second component is given by γ-rays produced by interactions between CRs and the Earth atmosphere.

In this appendix I will report on some activities where I gave a personal contribution concerning the monitoring of reducible backgrounds, performed by comparing contaminated and purer classes, the modeling of residual CR backgrounds for high-level analysis and the contamination from the Earth's atmospheric emission.

A.1 RESIDUAL BACKGROUNDS FROM MISCLASSIFIED CR INTERACTIONS

The event classification described in § 1.1.2 leads to the definition of event classes; they differ in the tuning of the instrument performance and the residual background contamination. Even in the purest classes, which partially sacrifice the efficiency to get lower backgrounds, the presence of some residual background contamination from misclassified CR interactions is unavoidable.

The residual CR backgrounds can be distinguished in two classes (Atwood et al., 2009):

REDUCIBLE BACKGROUNDS: background events hitting the LAT and erroneously classified as γ-rays, which in principle could be recognized as background events and discarded;

IRREDUCIBLE BACKGROUNDS: background events originated by CR interactions with the passive materials (e.g. the thermal blanket) surrounding the detector and producing γ-rays which then are detected by the LAT.

The latter class cannot be eliminated and it constitutes the majority of residual background in the purest classes.

The CR fluxes hitting the LAT depend on the position along the orbit (more specifically, on the geomagnetic coordinates), but for observations lasting many orbits the residual background contamination is expected to be almost isotropic with respect to celestial coordinates. The scientific objectives of the *Fermi* mission require to keep the background contamination under control, especially to study broadly distributed diffuse components, but also for the detailed spectral modeling of individual sources.

Monitoring reducible backgrounds

The monitoring of reducible backgrounds is possible from the comparison between contaminated and purer data samples. This purpose can be achieved using vertex only events as purer class (§ 1.1.2; see Atwood et al., 2009), since background events can hardly mimic a vertex.

An alternative option is to define event classes with tighter selection criteria.

I will describe in this paragraph a method I developed to evaluate the spectrum of reducible backgrounds without resorting to Monte-carlo simulations. Let us suppose to have a data sample 1 containing t_1 events

$$t_1 = b_1 + s_1 \tag{A.1}$$

where s_1 is the number of signal events (true photons) and b_1 is the number of residual background events.

I will assume three working hypotheses:

1. we can extract a subsample, data sample 2, with a higher purity (using vertex events or tighter rejection criteria); let us say that the data sample 2 is composed by

   $$t_2 = b_2 + s_2 \tag{A.2}$$

   events ($s_2 < s_1$, $b_2 \ll b_1$);
2. we can estimate the ratio between signal in the data sample 2 and 1

   $$r = \frac{s_2}{s_1} \tag{A.3}$$

   (which can be done, e.g., considering on-pulse events from bright pulsars or events associated with AGNs at high energies);
3. we can select a time-scale for our analysis which allows to approximate the background as isotropic.

We obtain the system

$$\begin{cases} t_1 = b_1 + s_1 \\ t_2 = b_2 + s_2 \\ r = \frac{s_2}{s_1} \end{cases} \tag{A.4}$$

The system has not a single solution. Let us introduce the auxiliary variable

$$x = t_1 - t_2 \tag{A.5}$$

The difference between first and the second equation of the system A.4 yields

$$\begin{aligned} x &= b_1 + s_1 - b_2 - s_2 = \\ &= b_1 \left(1 - \frac{b_2}{b_1}\right) + s_1 \left(1 - \frac{s_2}{s_1}\right) = \\ &= b_1 \left(1 - \frac{b_2}{b_1}\right) + s_1 (1 - r) \end{aligned} \tag{A.6}$$

Eq. A.6 yields

$$s_1 = \frac{x - b_1 \left(1 - \frac{b_2}{b_1}\right)}{1 - r} \tag{A.7}$$

Let us introduce a second auxiliary variable

$$y = t_1 + t_2$$

Eq. A.7 yields

$$\begin{aligned} y &= b_1\left(1+\frac{b_2}{b_1}\right)+s_1\,(1+r)= \\ &= b_1\left(1+\frac{b_2}{b_1}\right)+\frac{1+r}{1-r}\left[x-b_1\left(1-\frac{b_2}{b_1}\right)\right]= \\ &= \frac{1+r}{1-r}x+b_1\left[-\frac{2r}{1-r}+\frac{2}{1-r}\frac{b_2}{b_1}\right] \end{aligned} \tag{A.8}$$

If we introduce the *cleaning parameter*

$$w = r-\frac{b_2}{b_1} \tag{A.9}$$

Eq. A.8 yields

$$2wb_1 = (1+r)x-(1-r)y \tag{A.10}$$

$$wb_1 = r\,\frac{x+y}{2}-\frac{y-x}{2} \tag{A.11}$$

and subsequently

$$b_1 = \frac{rt_1-t_2}{w} \tag{A.12}$$

If data sample 2 were background free ($b_2 = 0$), then $w = r$ (and $b_1 = t_1 - t_2/r$). In fact r and b_2/b_1 have the same order of magnitude. But we know the quantity

$$z = \frac{t_2}{t_1}$$

We will show later that we can approximate $w \simeq z$ and so

$$b_1 \simeq \frac{rt_1-t_2}{z} \tag{A.13}$$

The procedure illustrated is performed over a grid in energy to derive the spectrum of reducible backgrounds in the contaminated class, and it is useful especially to understand if any spectral features are real or due to background leakage.

Let us show now the limits of applicability of Eq. A.13. Eq. A.12 can be written as

$$b_1 = \frac{rt_1-t_2}{z\left(1+\frac{w-z}{z}\right)} \tag{A.14}$$

and so Eq. A.13 provides a good approximation of b_1 when

$$\frac{w-z}{z} \ll 1 \tag{A.15}$$

If we introduce the *contaminations* of class 1 and 2

$$c_1 = \frac{b_1}{t_1} \qquad c_2 = \frac{b_2}{t_2} \tag{A.16}$$

we can write

$$\begin{aligned} w &= \frac{t_2-b_2}{t_1-b_1}-\frac{b_2}{b_1}= \\ &= z\left(\frac{1-c_2}{1-c_1}-\frac{c_2}{c_1}\right)= \\ &= z\,\frac{1-\frac{c_2}{c_1}}{1-c_1} \end{aligned}$$

and so

$$\frac{w-z}{z} = \frac{1-\frac{c_2}{c_1}}{1-c_1} - 1 = \\ = \frac{c_1}{1-c_1} \cdot \left(1 - \frac{c_2}{c_1^2}\right) \tag{A.17}$$

Let us define two functions

$$f(c_1) = \frac{c_1}{1-c_1} \tag{A.18}$$

and

$$g(c_1, c_2) = \left(1 - \frac{c_2}{c_1^2}\right) \tag{A.19}$$

Eq. A.17 can be written as

$$\frac{w-z}{z} = f(c_1) \cdot g(c_1, c_2)$$

and Eq. A.14 yields

$$b_1 = \frac{rt_1 - t_2}{z\,(1 + f(c_1) \cdot g(c_1, c_2))} \tag{A.20}$$

Fig. A.1 shows f as a function of c_1. f is small when c_1 is small, i.e. for

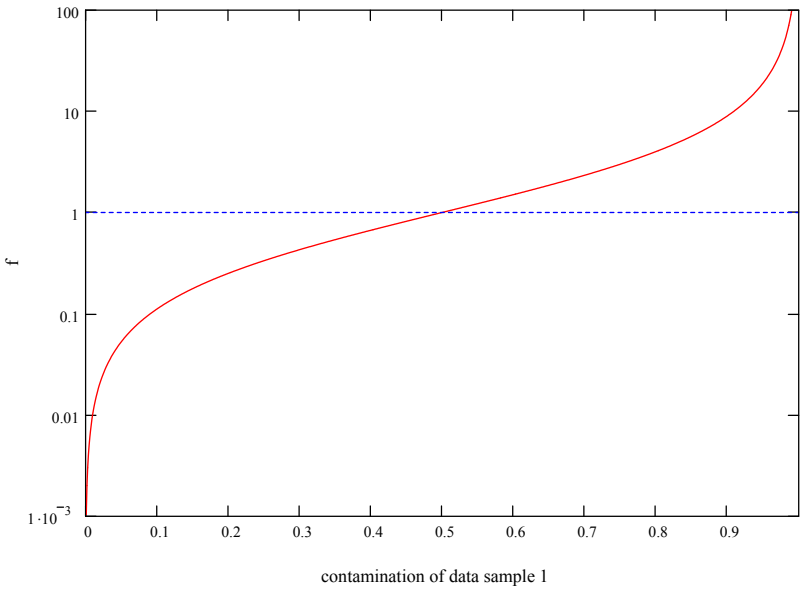

Figure A.1: f as a function of c_1.

data samples with a reasonably low contamination. On the other hand Fig. A.2 shows g as a function of c_1 (fixed c_2/c_1): the modulus of g is big for very small contaminations of data sample 1, which, however, are quite unrealistic. Fig. A.3 finally shows $f \cdot g = (w-z)/z$ as a function of c_1 (fixed c_2/c_1): there is a wide range of contaminations where

$$\frac{w-z}{z} \lesssim 20\%$$

and so the approximation of Eq. A.13 can be practically used; this can be verified using Montecarlo simulations.

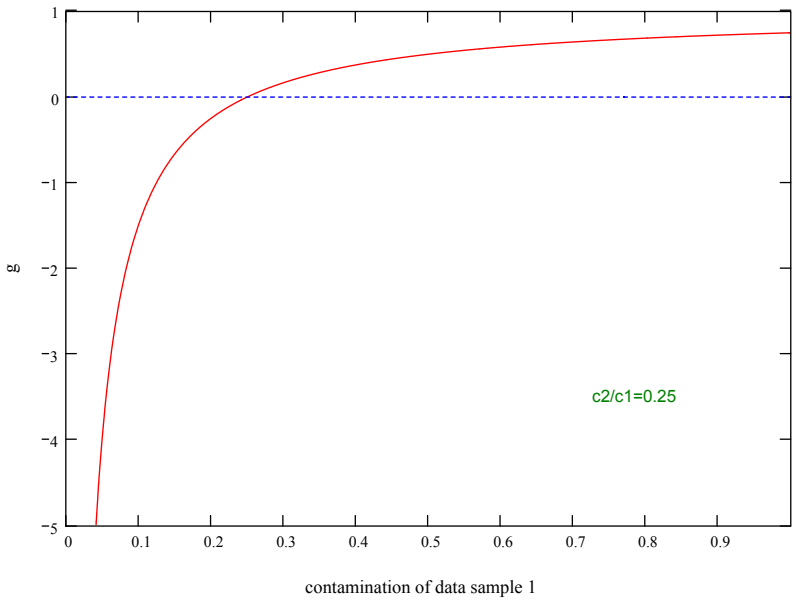

Figure A.2: g as a function of c_1 for $c_2/c_1 = 0.25$.

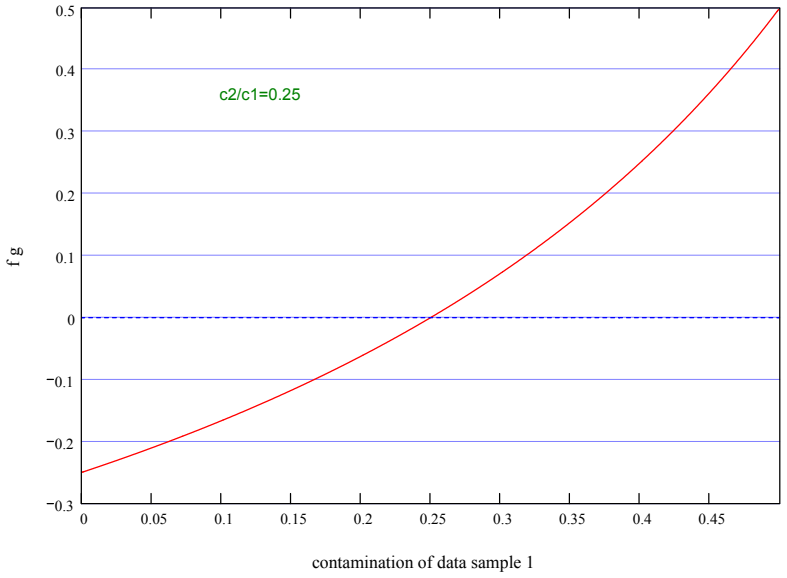

Figure A.3: $f \cdot g$ as a function of c_1 for $c_2/c_1 = 0.25$.

Modeling the CR residual background: the isotropic background template

Even in the purest event classes there is some level of residual CR background contamination, mostly from irreducible events. Over short time-scales the residual backgrounds have a strongly anisotropic distribution depending on the position of the LAT along its orbit; therefore in short-time observations, e.g. of transient phenomena, the modeling of residual background as a function of the satellite position is required (for details see Abdo et al., 2009i).

Over time scales of some days/weeks the distribution of accumulated residual CR backgrounds are expected to be isotropic with respect to the sky, as CRs show highly isotropic arrival directions in the relevant energy range. Thus, there is no need to separate the residual CR contamination from the isotropic γ-ray emission (EGB, see § 3.1.1), except for the study of the EGB itself. The residual CR contamination and the EGB form together the *isotropic background*.

The spectrum of the isotropic background has to be careful modeled to avoid systematic effects. It is not modeled assuming an *a priori* model, but instead directly from LAT data allowing for an isotropic component with free flux in several independent energy bins, over a grid fine enough to meet the needs of the analysis. The isotropic background can be estimated along with the analysis, or can be pre-computed for standard studies, especially those of individual sources.

The LAT collaboration releases with the data a model of the Galactic interstellar emission and the isotropic background template for the recommended analysis classes [1]. The isotropic spectrum is pre-computed through a fit to LAT data avoiding the Galactic plane (namely $b > 30^\circ$) to minimize the effect of Galactic emission; the underlying sky model assumes an isotropic component as well as the Galactic emission model and individual sources from a LAT catalog. Since in the fitting procedure the isotropic background potentially overtakes any smooth large-scale foreground component not included in the sky model, it is important to use it in association with the very same Galactic diffuse model that was used for its derivation. It is worth to note that the distributed isotropic spectrum is only a template of pseudo γ-ray fluxes, i.e. a fictitious γ-ray source which convolved with the IRFs produce an isotropic signal equivalent to that observed. For this reason it depends on the event selection applied to data and the IRFs used for analysis. Fig. A.4 shows the publicly available pre-computed spectrum of the isotropic background for the `P6` *Diffuse* event selection (`P6_V3_DIFFUSE` IRFS), compared with the results of other studies based on the same event selection/criteria/IRFs.

A.2 CONTAMINATION FROM THE EARTH'S ATMOSPHERIC γ-RAY EMISSION

CR interactions with Earth's atmosphere originate γ-rays which trigger the LAT. The Earth's atmosphere is bright compared to celestial γ-ray sources for the LAT because of its proximity. It therefore constitutes not only an interesting physical phenomenon, but also an excellent observational target for calibration purposes (Abdo et al., 2009d). However, it is also an insidious background for studies of celestial emission. Being made from real γ-rays, the only criterion to limit the atmospheric contamination is provided by the directional information. Residual Earth's atmospheric contamination is a potential issue for data analysis since it is strongly anisotropic and not straightforward to model.

At an height of $\sim$ 565 km, the LAT sees the Earth's limb at $\sim 112^\circ$ from the zenith. In the standard survey mode the LAT rocks by 50° toward either orbital pole on alternate orbits [2]. The Earth's limb is

1. http://fermi.gsfc.nasa.gov/ssc/data/access/lat/BackgroundModels.html
2. The rocking angle changed over the mission in the range $35^\circ - 50^\circ$; the chosen value is a trade-off between the needs of getting almost uniform exposures toward the

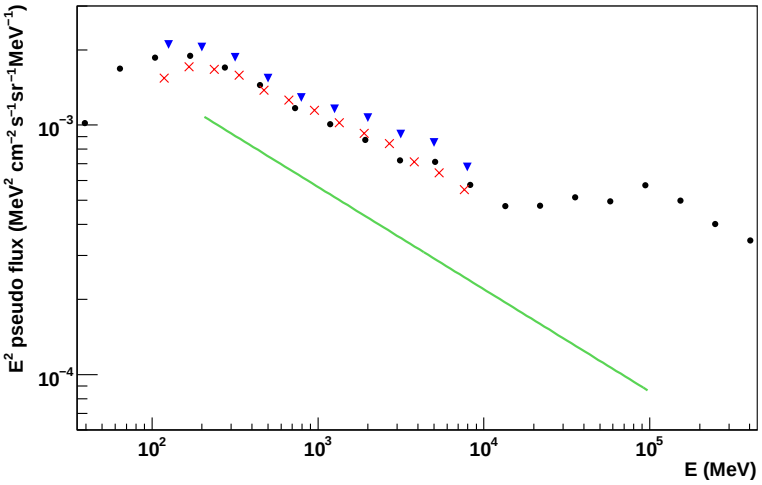

Figure A.4: Pseudo spectrum of the isotropic background for the `P6` *Diffuse* event selection (`P6_V3_DIFFUSE` IRFS). Black circles: the pre-computed spectrum distributed by the FSSC as `isotropic_iem_v02.fits`. Blue triangles and red crosses: the spectra derived by Abdo et al. (2009c,g), respectively, for mid-to-high latitude regions of the sky. For reference the green line gives the estimate by Abdo et al. (2010j) of the EGB, i.e. the γ-ray component of the isotropic background; the rest is due to misclassified CR interactions.

always at $112^\circ - 90^\circ = 22^\circ$ from the orbital pole. The orbital poles are offset from the celestial poles by 25.6° (the inclination of the orbit), and they precess around the celestial poles with a period of ~ 53.5 days. Therefore, Earth's atmospheric emission over day scales forms rings centered at 25.6° from the celestial poles peaking at a radius of 22° (see Fig. A.5). The width of the rings depends on the rocking angle (how deep the Earth's limb enters the FoV) and the energy (notably due to the PSF). The rings rotate around the celestial poles with the precession period of ~ 53.5 days.

The Earth's atmospheric emission can be limited only using directional information. Selecting events seen at zenith angles smaller than a threshold value (usually in the $100^\circ - 105^\circ$ range) largely limits the atmospheric γ-ray contamination in data (see Fig. A.6). Selecting events within a threshold angle from the LAT boresight (θ angle) pursue the same objective by restricting the instrument FoV. Both selections on zenith angles and θ angles need to be accounted for in the calculation of the exposures (in fact of cumulative livetimes, see § 1.3.2).

To calculate the exposures, the selection on zenith angles can be treated in two different ways: 1) for small regions of interest one can discard the observation time intervals when any part of the region of interest is seen below the threshold zenith angle; 2) discarding time intervals when the rocking angle is larger than the maximum value in standard observation mode (to exclude periods when the Earth limb deeply enters the FoV) and excluding in the accumulation of livetimes

celestial poles, allowing for an efficient cooling of the spacecraft batteries and keeping under control the Earth's atmospheric contamination.

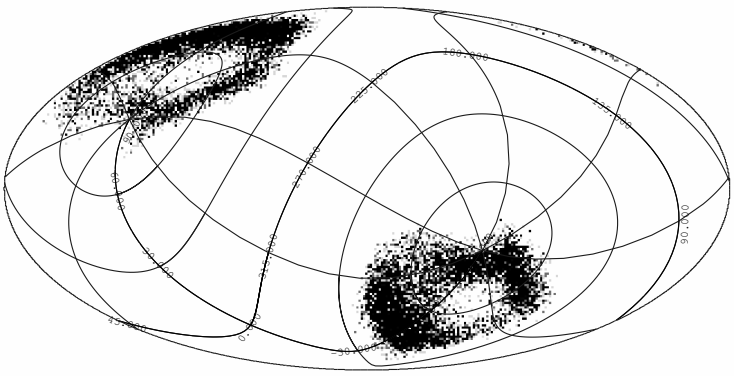

Figure A.5: Skymap of events detected by the LAT (P6 *Diffuse* class) at zenith angles $> 105^\circ$ and energies > 200 MeV during one week of operations ($\sim 1/6$ of the precession period). In that week the LAT was operated in normal sky survey mode with a rocking angle of 35°. Aitoff projection in Galactic coordinates; overlaid a grid in celestial coordinates.

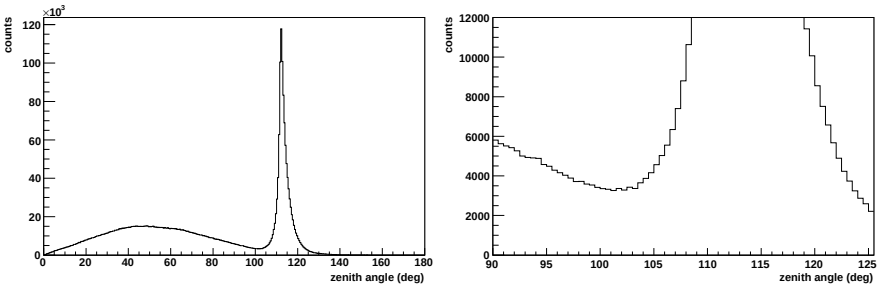

Figure A.6: Counts in the *Diffuse* event class as a function of zenith angle during LAT operations in normal sky survey mode. Left: full histogram; note the population of celestial γ-rays peaking at 50° (the rocking angle) and the population of Earth's atmospheric γ-rays peaking at 112° (Earth's limb). Right: zoom in the $90^\circ - 120^\circ$ range: note the dip around $100^\circ - 105^\circ$.

the time intervals when a region was observed at zenith angles larger than the threshold. The combination of the two procedures is the most conservative option, often adopted for analysis of limited regions of the sky. The second strategy is usually adopted for large scale analysis.

The selection on θ angles in principle should be accounted for in the generation of the IRFs. It is practically treated blanking the effective area for Montecarlo θ larger than the thresholds or, alternatively, the cumulative livetimes at such angles.

The thresholds to be adopted depend on the aims of the analysis. As we have seen that Earth's atmospheric γ-rays are seen around the celestial poles, to study regions at high declinations ($|\mathrm{Dec}| > 30^\circ$) more severe selection criteria are required. Also analyses at low energies ($\lesssim$ 300 MeV) need to be careful in this respect, because Earth's at-

mospheric emission has a soft spectrum and the PSF is wider. Since tight selection criteria will also lower the exposures around the celestial poles a trade-off is needed (Fig. A.6).

Any selection will leave some level of residual Earth's atmospheric γ-ray emission, notably made from misreconstructed events which have estimated zenith angles smaller than the real ones. The level of residual contamination depends on the rocking angle of the telescope, the celestial declination of the region studied and the energy band considered. Dealing with such residual contamination is not straightforward since it is strongly anisotropic. The modeling of residual atmospheric emission would require in turn the modeling of the underlying phenomenon and dedicated calculations to determine the morphology and spectrum based on the the selection criteria applied and on the pointing history of the telescope during the observing period.

B

KINEMATIC SEPARATION OF INTERSTELLAR MEDIUM STRUCTURES

The Doppler shift of interstellar gas lines due to the Galactic rotation allows us to separate structures seen along a line of sight. In this appendix I will provide some technical details about this procedure, skipped for brevity in Chapter 2, including the discussion of the rotation curve for the outer Galaxy relevant for the analyses presented in Part II.

The kinematic separation was often used in γ-ray studies, usually splitting the content of the ISM in some Galactocentric rings (see e.g. § 3.3.1). I will present here a novel methodology to separate the structures seen along a line of sight, not based on distances but on the physical structures of the ISM itself, that I developed and successfully applied for all the analyses presented in Part II.

B.1 GALACTIC ROTATION AND KINEMATIC DISTANCES

The motion of the Galaxy seen from the solar system

Let us assume that the Galaxy rotates with purely circular motion around its center and that the velocity in each point depends only on the Galactocentric radius R. We will determine under these hypotheses the velocity of each point P with respect to the local standard of rest (LSR), $V_{\rm LSR}$, as seen by an observer in the solar system. Let us assume for simplicity that the point P is located in the Galactic plane. The relevant quantities are defined in Fig. B.1.

The point P rotates around the Galactic center with a velocity $V(R)$. Its projection on the direction Sun–P is

$$\begin{aligned} V_r(R) &= V(R)\sin\alpha = \\ &= V(R)\frac{\sin\alpha}{R_\odot}R_\odot = \\ &= V(R)\frac{\sin l}{R}R_\odot \end{aligned} \tag{B.1}$$

On the other hand the Sun rotates around the GC with a velocity $V(R_\odot) = V_\odot$, whose projection on the direction Sun–P is

$$\begin{aligned} V_r(R_\odot) &= V_\odot\cos\left(l-\frac{\pi}{2}\right) = \\ &= V_\odot\sin l \end{aligned} \tag{B.2}$$

The velocity of P with respect to the LSR, $V_{\rm LSR}$, is

$$\begin{aligned} V_{\rm LSR} &= V_r(R) - V_r(R_\odot) = \\ &= R_\odot\sin l\left[\frac{V(R)}{R}-\frac{V_\odot}{R_\odot}\right] \end{aligned} \tag{B.3}$$

The generalization to a point P out of the Galactic plane at a latitude b is straightforward.

$$V_{\rm LSR} = R_\odot\sin l\cos b\left[\frac{V(R)}{R}-\frac{V_\odot}{R_\odot}\right] \tag{B.4}$$

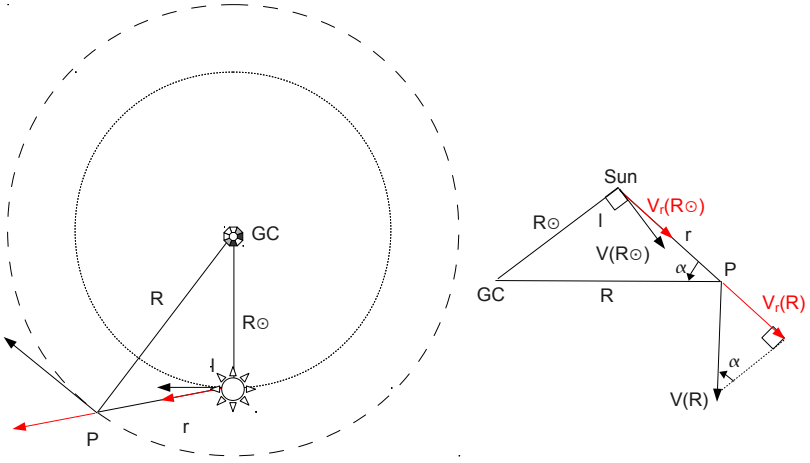

Figure B.1: Visual illustration of the procedure to determine the velocity with respect to the LSR, $V_{\rm LSR}$, of a point P under the hypothesis of a cylindrical symmetric velocity field. Left: the Sun is located at a Galactocentric radius $R_\odot$ from the Galactic center (GC). The unknown distance of the point P from the GC is R, whereas the distance from the Sun is r. The Galactic longitude l of the point P is the angle between the directions GC–Sun and Sun–P. Right: the triage Sun–GC–P. The projection of $V(R_\odot)$ on the direction of Sun–P is $V_r(R_\odot)$, the projection of $V(R)$ is $V_r(R)$. α is the angle between the directions Sun–P and P–GC.

Given the rotation curve of the Galaxy, $V(R)$, we can determine R from $V_{\rm LSR}$, which is observed thanks to the Doppler shift of ISM lines. The relation is single-valued outside the solar circle, whereas the possible solutions are two in the inner Galaxy (there are two points at the same R along each line of sight). We can determine as well the distance from the Sun, r, which is known in this case as kinematic distance. It is evident from Eq. B.4 that the kinematic separation does not work toward the Galactic center ($l = 0°$) and anticenter ($l = 180°$).

The Galactic rotation curve

Eq. B.4 requires the knowledge of the rotation curve $V(R)$ in order to connect position and $V_{\rm LSR}$. The determination of the rotation curve is based on several different observables, like H I and CO lines, the distribution of H II regions, globular clusters, stars. Parametric rotation curves are given, e.g., in Clemens (1985); Sofue et al. (2009); Francis and Anderson (2009).

The works reported in this thesis investigated regions outside the solar circle. For a specific discussion of the velocity field in the outer Galaxy I refer to Brand and Blitz (1993). Using a sample of H II regions and reflection nebulae, they found that the curve is approximately flat $V(R) \approx V_\odot$ for $R > R_\odot$, with a slight rise in rotational velocity for the outermost region. This gives credence to the long-standing

assumption of flat velocities beyond the solar circle in the literature mainly based on observations of external galaxies (Rubin et al., 1978, 1982). Brand and Blitz (1993) found for the outer Galaxy velocity residuals plausibly indicating streaming (i.e. non-circular) motion of the order of 12 km s^{-1} (hereafter all numeric values are based on the values recommended by the International Astronomical Union, IAU, $R_\odot = 8.5$ kpc and $V_\odot = 220$ km s^{-1}; Kerr and Lynden-Bell 1986). The observed pattern is consistent with spiral wave streaming. They also found only slightly North-South differences, implying to first order a cylindric symmetry in the velocity field. From a sample of local molecular clouds within 2 kpc from the Sun they derived the height of the Sun above the Galactic plane to be 13 ± 7 pc.

B.2 A NOVEL METHOD FOR KINEMATIC SEPARATION

The Doppler velocity $V_{\rm LSR}$ is used in studies of interstellar γ-ray emission to separate the contributions from different structures seen along a line of sight and therefore extract information about the distribution of CR densities and the census of the ISM throughout the Galaxy. Past studies often separated the gas into several ranges of Galactocentric radius R (rings, § 3.3.1).

However, the physical structures observed in the $l - b - V_{\rm LSR}$ space provides more natural separation criteria. Starting from this idea I developed a new method suitable for the analysis of selected regions of the sky, taking care also of the cross-contamination between adjacent regions due to the large velocity dispersion characteristic of H I emission lines.

From rings to physical structures

In selected regions of the sky rings are known to well approximate the spiral-arm structures of the Milky Way (e.g. Digel et al., 1996, 2001). My method therefore starts for each region from the definition of some preliminary rings, which are then *stretched* to accommodate the structures of the ISM.

For each line of sight the boundaries between the different structures are moved to the closest minimum in the H I spectrum, or to the closest saddle if a minimum is not found. The H I spectrum is used, rather than the CO spectrum, since H I emission is observed along almost all the lines of sight, contrarily to CO emission, while, if both are present, CO and H I lines peak at about the same $V_{\rm LSR}$; moreover the H I lines are broader due to the larger velocity dispersion, being therefore the most difficult to separate. The procedure is reliable in the regions we studied in the outer Galaxy, since minima of H I spectra are unlikely to be due to self absorption.

The procedure is illustrated in Fig. B.2–B.5 for some example lines of sight taken from the regions studied in Chapter 4, 5 and 6. One more example can be found in Fig. 2 of the paper attached to Chapter 4. Along lines of sight where there is no significant emission associated with one of the preliminary rings, the corresponding boundaries collapse and the $N(\mathrm{H\,I})$ density ($W_{\rm CO}$ intensity) is set to null for the corresponding structure (Fig. B.4). This procedure can underestimate the gas densities for faint structures not clearly visible in H I emission;

ad-hoc solutions need to be found in such cases, see later, e.g., the separation of outer and Perseus arms in the third quadrant.

The velocity-dispersion broadening of H I *lines*

H I lines are broader than CO lines because of their characteristic velocity dispersion. This makes the separation of $N(\mathrm{H\,I})$ densities belonging to different structures more difficult, because the corresponding lines often overlap.

To correct for the spill-over between adjacent regions, I performed a fit of each H I spectrum with a combination of Gaussian lines (plus a constant). The centroids of the Gaussians were fixed to the maxima of the H I spectrum; if no maxima were found in the velocity range corresponding to a certain structure a saddle was looked for. The widths and normalizations of the Gaussians were determined through the fit to the H I spectrum, with the first parameter constrained between the width of the velocity channel and the width of the velocity range under consideration.

The best-fit functions for the example H I spectra are shown in Fig. B.2–B.5. It is evident that this procedure can only approximately reproduce the H I spectra, e.g. in Fig. B.3 the two lines at -80 km s^{-1} $< V_{\mathrm{LSR}} < -40$ km s^{-1} are fit with a single broad peak (superposition of two broad Gaussians). However, the use of this best-fit function only to correct for the spill-over between adjacent lines provides a more accurate estimate of the $N(\mathrm{H\,I})$ densities associated with each structure than completely neglecting such issue.

A challenging case: the separation of the outer arm in the third Galactic quadrant

The method I presented cannot be applied blindly, since we often face delicate cases which need an ad-hoc treatment. As an example, I will illustrate the separation of the faint segment of the outer arm seen in the third quadrant from the Perseus arm; this task was accomplished for the work presented in Chapter 5.

To illustrate the issue I will make use of three H I, CO spectra, namely those observed in the directions $(l, b) = (243^\circ, 0^\circ)$, $(236.5^\circ, -1.5^\circ)$ and $(215^\circ, 0.5^\circ)$, see Fig. B.6. They were selected among the few directions with a CO emission line in the velocity range corresponding to the Perseus arm.

The H I spectrum in Fig. B.6 (left) shows a faint line at $V_{\mathrm{LSR}} \simeq 115$ km s^{-1}, corresponding to the outer arm. There is a CO line at $V_{\mathrm{LSR}} \simeq 75$ km s^{-1}, associated with the Perseus arm, mirrored by a H I line separated from the outer-arm line by ~ 40 km s^{-1}.

Fig. B.6 (middle) shows a fainter H I line at $V_{\mathrm{LSR}} \simeq 110$ km s^{-1}, again associated with the outer arm. There is then a couple made from a CO and a bright H I lines peaking at $V_{\mathrm{LSR}} \simeq 80$ km s^{-1} (Perseus arm). The separation between the outer-arm and the Perseus-arm components is reduced to ~ 30 km s^{-1}. Let us note that the ratio of the width of the CO line over the width of the H I line is $\sim 1:3$.

In Fig. B.6 (right) no H I lines are visible beyond the bright Perseus-arm line at $V_{\mathrm{LSR}} \simeq 50$ km s^{-1}, but the ratio of the width of the CO line over the width of the H I line is $\sim 1:5$, and the Perseus-arm line has a large tail toward larger velocities, i.e. toward the outer arm.

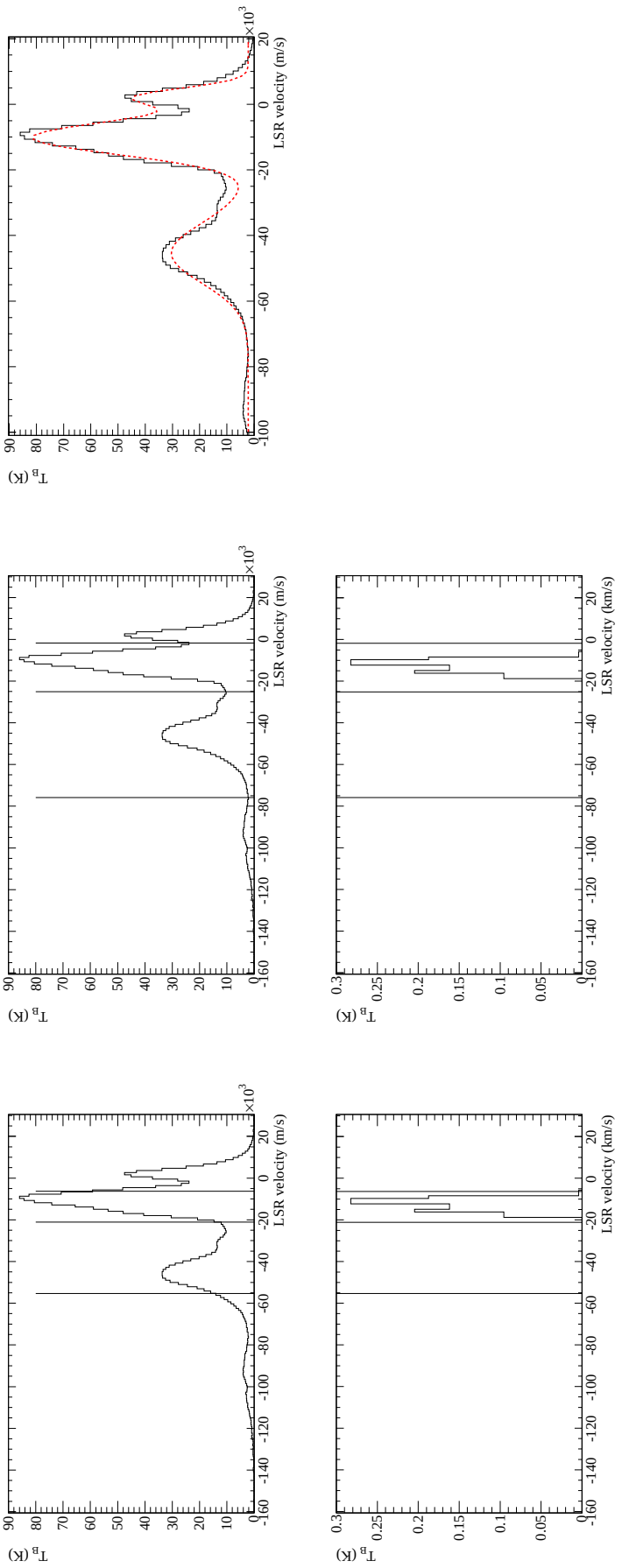

Figure B.2: HI (top) and CO (bottom) spectra in the direction $(l, b) = (140°, +5.5°)$. The vertical lines represent the boundaries between the different structures seen along the line of sight, from right to left Gould Belt, Local Arm, Perseus arm and outer arm. The three columns illustrate the steps of the kinematic separation procedure: left, preliminary boundaries (Galactocentric rings); middle, physical boundaries adjusted to accomodate the ISM structures; right, Gaussian fit of the HI spectrum to correct for the overlapping of lines corresponding to different structures.

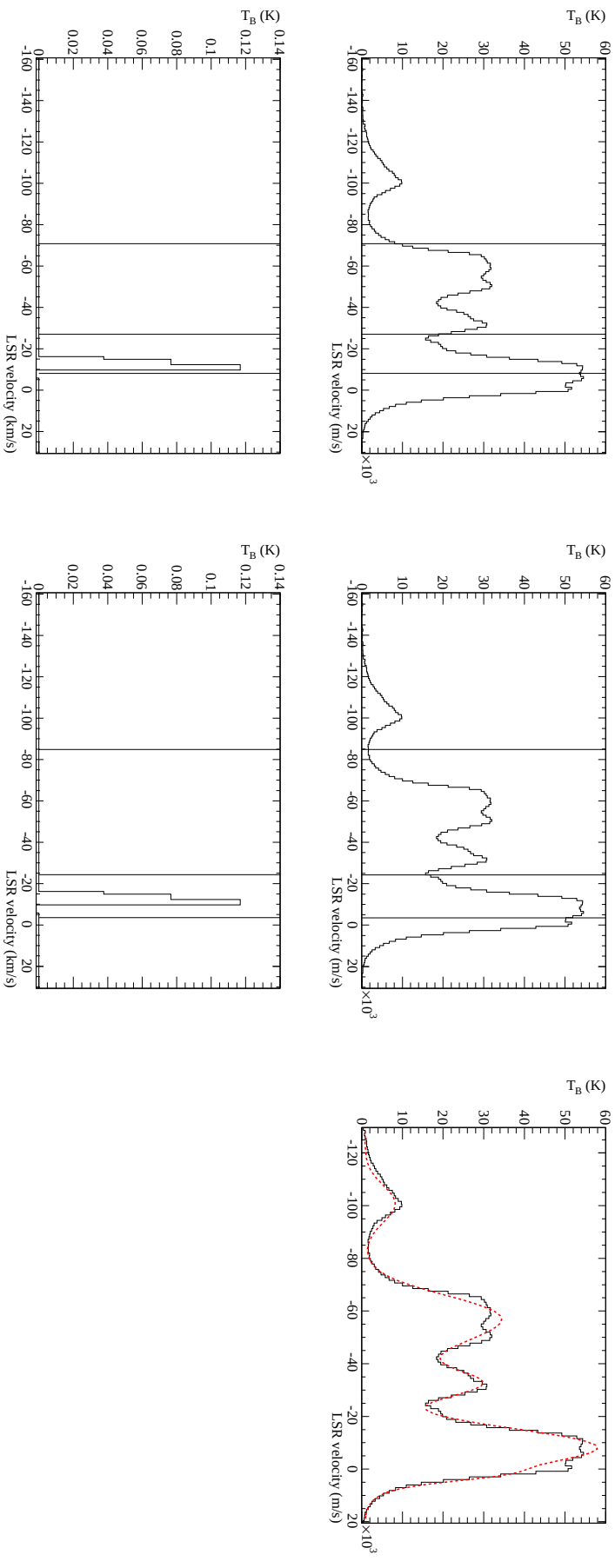

Figure B.3: H I and CO spectra in the direction $(l, b) = (125°, -2°)$, as in Fig. B.2.

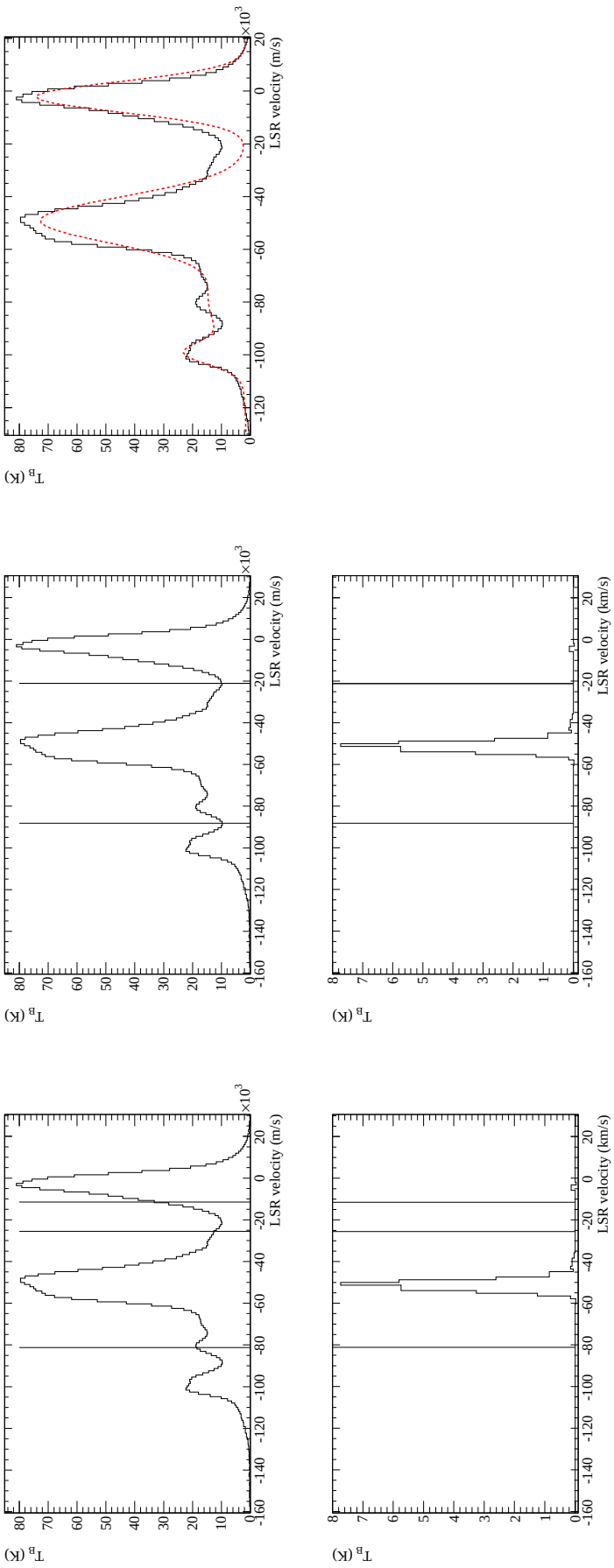

Figure B.4: HI and CO spectra in the direction $(l, b) = (110°, 0°)$, as in Fig. B.2. No lines are found for the Local Arm in this direction, therefore the boundaries Gould Belt–Local Arm and Local Arm-Perseus arm merge in the second row.

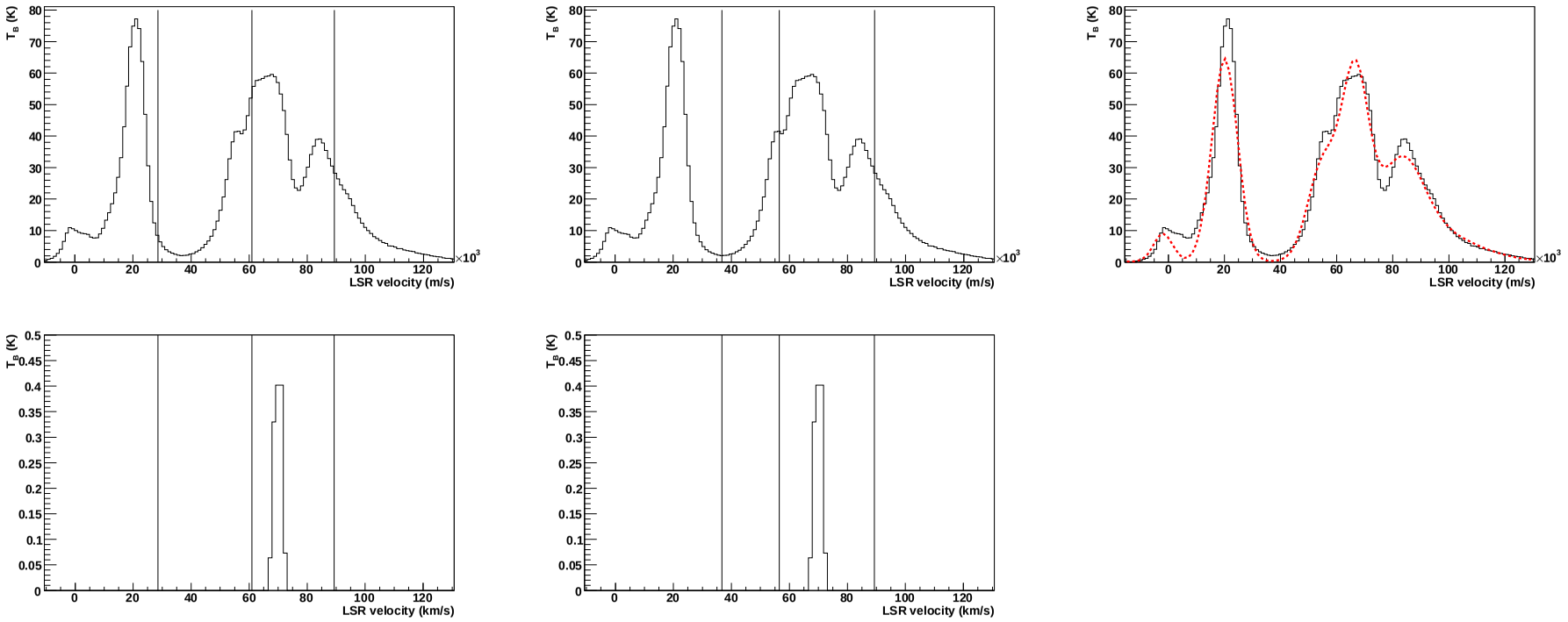

Figure B.5: H I and CO spectra in the direction $(l, b) = (240°, 0.5°)$, as in Fig. B.2. The structures along the line of sight in this case are, from left to right, Local Arm, interarm region, Perseus arm and outer arm.

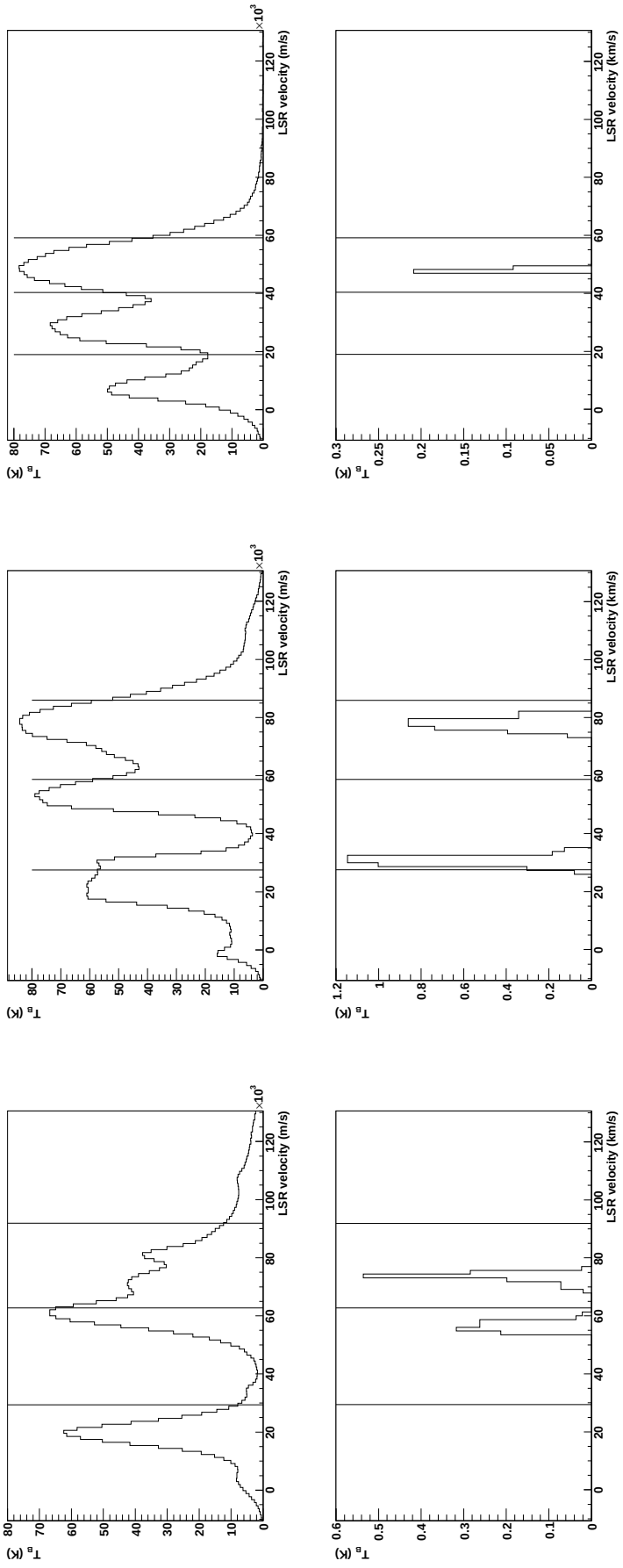

Figure B.6: HI (top) and CO (bottom) spectra in the directions $(l, b) = (243^\circ, 0^\circ)$, left, $(l, b) = (236.5^\circ, -1.5^\circ)$, middle, and $(l, b) = (215^\circ, 0.5^\circ)$, right. The vertical lines represent the preliminary circle-boundaries which separate (from left to right) Local Arm, interarm region, Perseus arm and outer arm.

We argued that going toward smaller longitudes the faint H I lines corresponding to the outer arm were hidden by the bright lines associated with the Perseus arm, which were therefore becoming broader. Our solution for this challenging case is illustrated in Fig. B.7.

The circle boundary between Perseus and outer arm is adjustedwe only if a peak corresponding to the outer arm is found, otherwise it is kept (Fig. B.7, top right). In the latter case in the fitting of the H I spectrum I added a Gaussian line centered at the velocity corresponding to the approximate position expected for the outer arm ($R = 16.5$ kpc). The resulting fitting function for $(l, b) = (215°, 0.5°)$ is shown in Fig. B.7 (bottom). Obviously the $N(\mathrm{H\,I})$ densities associated to the outer arm are not reliably determined in this case, so the emissivities of the outermost region were not considered for scientific interpretation in Chapter 5, but the impact on the inner regions is small.

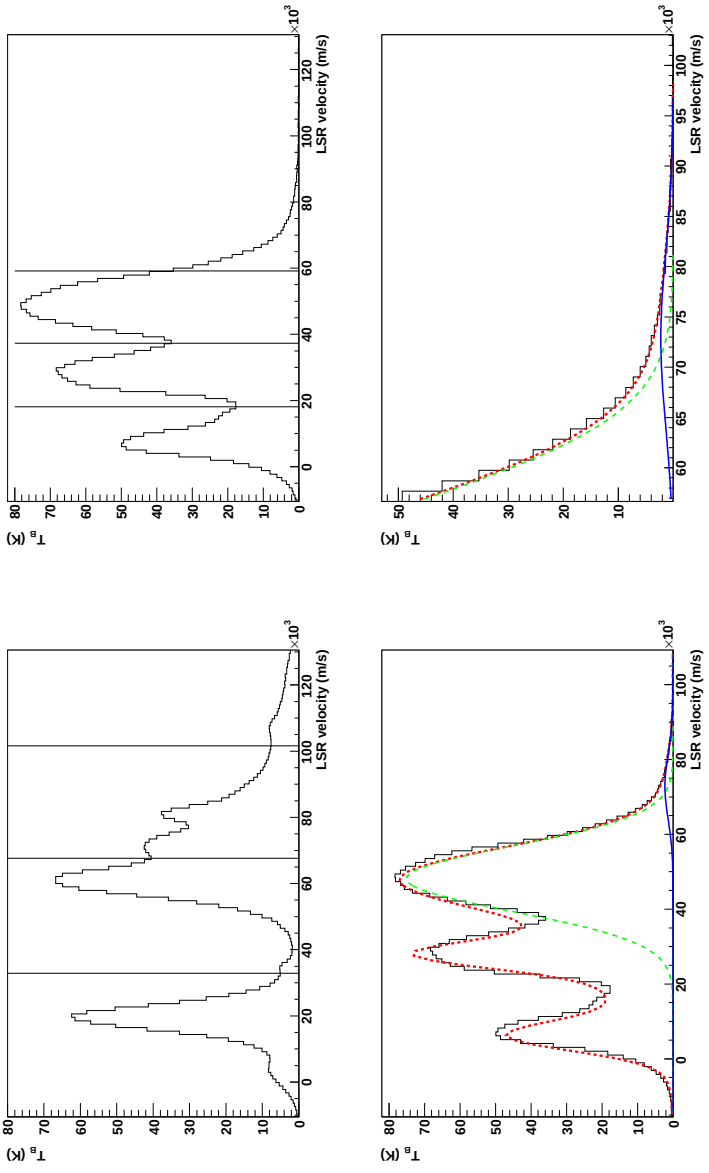

Figure B.7: Top: H I spectra in the directions $(l, b) = (243°, 0°)$ (left panel) and $(l, b) = (215°, 0.5°)$ (right panel). Vertical lines correspond to the physical boundaries which separate (from left to right) Local Arm, interarm region, Perseus arm and outer arm. Note that in the top right panel the boundary at highest velocity is unchanged from Fig. B.6, preserving the N(H I) densities associated with the faint line corresponding to the outer arm, not visible as a peak in the H I spectrum toward this direction.

C

FULL-COVARIANT LINEAR FIT

Linear fits are ubiquitous in Physics, but often based on the assumption that the two variables tentatively linked by a linear relation are statistically independent and that only one of them is affected by significant uncertainties.

This appendix describes the procedure to derive the best-fit parameters of a linear function between two statistical variables with Gaussian distribution, that we will call a and b, both affected by non-negligible uncertainties and not statistically independent.

I applied this method in the work presented in Chapter 4 to estimate the $X_{\rm CO}$ ratio from $q_{\rm HI}$ and $q_{\rm CO}$ emissivities previously obtained fitting a model to γ-ray data, thus both affected by uncertainties and correlated with each other.

C.1 THE COVARIANCE ROTATION

In this section I will describe the linear transformation (rotation) which turns a couple of statistically correlated variables into a couple of statistically independent variables. I will proceed backwards, defining a couple of statistically independent variables and showing that a rotation transforms it into a couple of statistically correlated variables. I will thus derive the formulas to obtain from a couple of statistically correlated variables and their covariance matrix a couple of statistically independent variables and their variances.

Let us define a couple of statistically independent variables $(x, y) \in \mathbb{R}^2$, with variances (σ_x^2, σ_y^2). The covariance matrix of the variables (x, y) is thus defined as

$$\Sigma_{xy} = \begin{pmatrix} \sigma_x^2 & 0 \\ 0 & \sigma_y^2 \end{pmatrix} \tag{C.1}$$

Consider the couple of variables $(a, b) \in \mathbb{R}^2$, which are the image of (x, y) through a rotation of angle α

$$R(\alpha) = \begin{pmatrix} \cos\alpha & \sin\alpha \\ -\sin\alpha & \cos\alpha \end{pmatrix} \tag{C.2}$$

$$\begin{pmatrix} a \\ b \end{pmatrix} = R(\alpha) \begin{pmatrix} x \\ y \end{pmatrix} = \begin{pmatrix} \cos\alpha\ x + \sin\alpha\ y \\ -\sin\alpha\ x + \cos\alpha\ y \end{pmatrix} \tag{C.3}$$

Being $R(\alpha)$ a linear transformation, the covariance matrix of the variables (a, b) is

$$\begin{aligned} \Sigma_{ab} &= R(\alpha)\ \Sigma_{xy}\ R^T(\alpha) = \\ &= \begin{pmatrix} \cos^2\alpha\ \sigma_x^2 + \sin^2\alpha\ \sigma_y^2 & -\cos\alpha\sin\alpha\ (\sigma_x^2 - \sigma_y^2) \\ -\cos\alpha\sin\alpha\ (\sigma_x^2 - \sigma_y^2) & \sin^2\alpha\ \sigma_x^2 + \cos^2\alpha\ \sigma_y^2 \end{pmatrix} \end{aligned} \tag{C.4}$$

Therefore, given a couple of statistical variables $(a, b) \in \mathbb{R}^2$ with a covariance matrix

$$\Sigma_{ab} = \begin{pmatrix} \sigma_a^2 & \sigma_{ab}^2 \\ \sigma_{ab}^2 & \sigma_b^2 \end{pmatrix} \tag{C.5}$$

we can define a couple of statistically independent variables

$$\begin{pmatrix} x \\ y \end{pmatrix} = R^{-1}(\alpha) \begin{pmatrix} a \\ b \end{pmatrix} = \begin{pmatrix} \cos\alpha\ a - \sin\alpha\ b \\ \sin\alpha\ a + \cos\alpha\ b \end{pmatrix} \tag{C.6}$$

Indeed, following Eq. C.5

$$\begin{cases} \sigma_a^2 + \sigma_b^2 &= \sigma_x^2 + \sigma_y^2 \\ \sigma_a^2 - \sigma_b^2 &= \cos 2\alpha\ (\sigma_x^2 - \sigma_y^2) \\ \sigma_{ab}^2 &= -\cos\alpha \sin\alpha\ (\sigma_x^2 - \sigma_y^2) \end{cases} \tag{C.7}$$

which is equivalent to

$$\begin{cases} \sigma_x^2 + \sigma_y^2 &= \sigma_a^2 + \sigma_b^2 \\ \sigma_x^2 - \sigma_y^2 &= \dfrac{\sigma_a^2 - \sigma_b^2}{\cos 2\alpha} \\ \sigma_{ab}^2 &= -\dfrac{1}{2}\dfrac{\sin 2\alpha}{\cos 2\alpha}(\sigma_a^2 - \sigma_b^2) \end{cases} \tag{C.8}$$

and thus [1]

$$\begin{cases} \tan 2\alpha &= -2\ \dfrac{\sigma_{ab}^2}{\sigma_a^2 - \sigma_b^2} \\ \sigma_x^2 &= \dfrac{1}{2}\left[\sigma_a^2 + \sigma_b^2 + \dfrac{\sigma_a^2 - \sigma_b^2}{\cos 2\alpha}\right] \\ \sigma_y^2 &= \dfrac{1}{2}\left[\sigma_a^2 + \sigma_b^2 - \dfrac{\sigma_a^2 - \sigma_b^2}{\cos 2\alpha}\right] \end{cases} \tag{C.9}$$

C.2 THE PROBABILITY DENSITY

In this section I will derive the probability density of getting a couple of values (a, b) for two statistical correlated variables with Gaussian distribution.

Let us consider a couple of stastistically independent variables (x, y) with Gaussian distribution with mean [2] values $(\bar{x}, \bar{y})$ and variances

1. The solution is not defined if $\sigma_a^2 = \sigma_b^2$. In this case we can obtain a couple of statistically independent variables by taking

$$\begin{cases} \alpha &= \dfrac{\pi}{4} \\ \sigma_x^2 &= \dfrac{1}{2}\left(\sigma_a^2 + \sigma_b^2 - 2\sigma_{ab}^2\right) \\ \sigma_y^2 &= \dfrac{1}{2}\left(\sigma_a^2 + \sigma_b^2 + 2\sigma_{ab}^2\right) \end{cases}$$

In the following sections we will give the formulas for the more general case, but the application to $\sigma_a^2 = \sigma_b^2$ is straightforward.

2. In consideration of the use in physical applications I will afterwards refer to the mean values of the distribution as the *true* values.

(σ_x^2, σ_y^2). The probability density of getting a couple of values (x, y) is (neglecting a normalization value)

$$f(x,y) = e^{-\frac{1}{2}F(x,y)} \tag{C.10}$$

with

$$F(x,y) = \frac{(x-\bar{x})^2}{\sigma_x^2} + \frac{(y-\bar{y})^2}{\sigma_y^2} \tag{C.11}$$

Applying the rotation given by Eq. C.3 I transform (x, y) into the couple of variables (a, b), which are not statistically independent. According to Eq. C.10, C.11, C.6, C.9 the probability density of getting the couple of values (a, b) is

$$f(a,b) = e^{-\frac{1}{2}F(a,b)} \tag{C.12}$$

with

$$\begin{aligned} & F(a,b) = \\ = \; & 2\left[\frac{(\cos\alpha\, a - \sin\alpha\, b - \cos\alpha\, \bar{a} + \sin\alpha\, \bar{b})^2}{\sigma_a^2+\sigma_b^2+\frac{\sigma_a^2-\sigma_b^2}{\cos 2\alpha}} + \frac{(\sin\alpha\, a + \cos\alpha\, b - \sin\alpha\, \bar{a} - \cos\alpha\, \bar{b})^2}{\sigma_a^2+\sigma_b^2-\frac{\sigma_a^2-\sigma_b^2}{\cos 2\alpha}}\right] = \\ = \; & 2\left[\frac{\cos^2\alpha\,(a-\bar{a})^2 + \sin^2\alpha\,(b-\bar{b})^2 - \sin 2\alpha\,(a-\bar{a})(b-\bar{b})}{\sigma_a^2+\sigma_b^2+\frac{\sigma_a^2-\sigma_b^2}{\cos 2\alpha}} + \right. \\ & \left. + \frac{\sin^2\alpha\,(a-\bar{a})^2 + \cos^2\alpha\,(b-\bar{b})^2 + \sin 2\alpha\,(a-\bar{a})(b-\bar{b})}{\sigma_a^2+\sigma_b^2-\frac{\sigma_a^2-\sigma_b^2}{\cos 2\alpha}}\right] \end{aligned} \tag{C.13}$$

C.3 THE LIKELIHOOD FUNCTION

Let us suppose to have two sets of statistical variables $\{a_i\}$ and $\{b_i\}$, with variances $\{\sigma_{a\,i}^2\}$ and $\{\sigma_{b\,i}^2\}$ and covariances $\{\sigma_{ab\,i}^2\}$. Let us suppose that a linear relation exists between the *true* values of the two variables, so that

$$\bar{b}_i = q + m \cdot \bar{a}_i \tag{C.14}$$

In this section I will derive the likelihood function associated to a couple of parameters (m, q), which will be maximized in order to obtain the best-fit parameters.

The likelihood function, i.e. the probability density of getting the set $\{(a_i, b_i)\}$, is, according to Eq. C.13

$$\mathscr{L} = \prod_i f(a_i, b_i | \sigma_{a\,i}^2, \sigma_{b\,i}^2, \sigma_{ab\,i}^2; \bar{a}_i, \bar{b}_i) \tag{C.15}$$

where the variables on the left of the semicolon ";" are those we obtain from the measurements, whereas those on the right are the unknown *true* values. I assumed that different measurements (i.e. quantities with different indexes i) are statistically independent.

Since the logarithm is a monotonic function we can consider, following Eq. C.13, the function

$$\mathrm{FCN} = -2 \cdot \ln \mathscr{L} = \sum_i F(a_i, b_i | \sigma_{a\,i}^2, \sigma_{b\,i}^2, \sigma_{ab\,i}^2; \bar{a}_i, \bar{b}_i) \tag{C.16}$$

If we consider the linear relation given by Eq. C.14 we obtain

$$\mathrm{FCN} = \sum_i 2 \left[\frac{\cos^2\alpha_i\,(a_i-\bar{a}_i)^2+\sin^2\alpha_i\,(b_i-q-m\bar{a}_i)^2-\sin 2\alpha_i\,(a_i-\bar{a}_i)(b_i-q-m\bar{a}_i)}{\sigma_{a\,i}^2+\sigma_{b\,i}^2+\frac{\sigma_{a\,i}^2-\sigma_{b\,i}^2}{\cos 2\alpha_i}} + \right.$$
$$\left. + \frac{\sin^2\alpha_i\,(a_i-\bar{a}_i)^2+\cos^2\alpha_i\,(b_i-q-m\bar{a}_i)^2+\sin 2\alpha_i\,(a_i-\bar{a}_i)(b_i-q-m\bar{a}_i)}{\sigma_{a\,i}^2+\sigma_{b\,i}^2-\frac{\sigma_{a\,i}^2-\sigma_{b\,i}^2}{\cos 2\alpha_i}} \right] \qquad \text{(C.17)}$$

I want to stress that the only unknown arguments of the function FCN are the *true* values of the variables $\{\bar{a}_i\}$ and the two parameters of the linear function q and m (the angles $\{\alpha_i\}$ are a function of $\{\sigma_{a\,i}^2\}$, $\{\sigma_{b\,i}^2\}$ and $\{\sigma_{ab\,i}^2\}$ through Eq. C.9).

The maximum of the likelihood function $\mathscr{L}$ (Eq. C.15) corresponds to the minimum of the function FCN (Eq. C.17), that provides the most likely values for the parameters q and m.

ACRONYMS

ACD	Anticoincidence Detector (of the LAT)
AGN	Active Galactic Nucleus
CGPS	Canadian Galactic Plane Survey
CGRO	*Compton Gamma-Ray Observatory*
CMB	Cosmic Microwave Background
COBE	*Cosmic Background Explorer*
COMPTEL	Imaging Compton Telescope
CR	Cosmic Ray
CT	Classification Tree
CU	Calibration Unit (of the LAT)
DAQ	Data Acquisition System (of the LAT)
DSA	Diffusive Shock Acceleration
EGB	Extragalactic γ-ray Background
EGRET	Energetic Gamma-Ray Experiment Telescope
EPU	Event Processor Unit (of the LAT)
FIR	Far Infrared
FoV	Field of View
FSSC	*Fermi* Science Support Center
GBM	γ-ray Burst Monitor
GC	Galactic Center
GLAST	*γ-ray Large Area Space Telescope* (now, *Fermi γ-ray Space Telescope*)
GLEAM	*GLAST* LAT Event Analysis Machine
GRB	γ-ray Burst
GZK	Greisen/Zatsepin/Kuzmin (cutoff of CR spectrum)
HE	High Energy
HESS	High-Energy Stereoscopic System
IAU	International Astronomical Union
IC	Inverse Compton
INTEGRAL	*International Gamma-Ray Astrophysics Laboratory*
IR	Infrared
IRAS	*Infrared Astronomy Satellite*
ISM	Interstellar Medium
ISRF	Interstellar Radiation Field
LAB	Leiden/Argentine/Bonn (H I survey)
LAMBDA	Legacy Archive for Microwave Background Data Analysis
LAT	Large Area Telescope
LMC	Large Magellanic Cloud
LRT	Likelihood Ratio Test
LSR	Local Standard of Rest

MET	Mission Elapsed Time (of *Fermi*)
MHD	Magnetohydrodynamic
PAH	Polycyclic Aromatic Hydrocarbon
PDR	Photon-Dominated Region
PMT	Photomultiplier Tube
PSF	Point Spread Function
SAA	South Atlantic Anomaly
SB	Superbubble
SFR	Star Formation Rate
SMC	Small Magellanic Cloud
SN	Supernova
SNR	Supernova Remnant
TEM	Tower Electronics Module (of the LAT)
TOA	Time of Arrival
UV	Ultraviolet
VHE	Very High Energy
WMAP	*Wilkinson Microwave Anisotropy Probe*
WIMP	Weakly Interacting Massive Particle

Abdo, A. A., et al. (2007) Discovery of TeV Gamma-Ray Emission from the Cygnus Region of the Galaxy. *Astrophys. J. Lett.*, **658**, L33. arXiv:astro-ph/0611691. (Cited on pages 55, 115, 142, 143, and 155.)

— (2009a) A limit on the variation of the speed of light arising from quantum gravity effects. *Nature*, **462**, 331. 0908.1832.

— (2009b) Detection of 16 Gamma-Ray Pulsars Through Blind Frequency Searches Using the Fermi LAT. *Science*, **325**, 840. (Cited on page 117.)

— (2009c) Fermi Large Area Telescope Measurements of the Diffuse Gamma-Ray Emission at Intermediate Galactic Latitudes. *Phys. Rev. Lett.*, **103, 25**, 251101. 0912.0973. (Cited on pages 47, 57, 58, and 169.)

— (2009d) Fermi Large Area Telescope observations of the cosmic-ray induced γ-ray emission of the Earth's atmosphere. *Phys. Rev. D*, **80, 12**, 122004. 0912.1868. (Cited on page 168.)

— (2009e) Fermi Large Area Telescope Observations of the Vela Pulsar. *Astrophys. J.*, **696**, 1084. 0812.2960. (Cited on page 59.)

— (2009f) Fermi LAT Discovery of Extended Gamma-Ray Emission in the Direction of Supernova Remnant W51C. *Astrophys. J. Lett.*, **706**, L1. (Cited on page 42.)

— (2009g) Fermi LAT Observation of Diffuse Gamma Rays Produced Through Interactions Between Local Interstellar Matter and High-energy Cosmic Rays. *Astrophys. J.*, **703**, 1249. 0908.1171. (Cited on pages 59, 60, 135, 136, and 169.)

— (2009h) Fermi Observations of GRB 090902B: A Distinct Spectral Component in the Prompt and Delayed Emission. *Astrophys. J. Lett.*, **706**, L138. 0909.2470.

— (2009i) Fermi Observations of High-energy Gamma-ray Emission from GRB 080825C. *Astrophys. J.*, **707**, 580. 0910.4192. (Cited on page 167.)

— (2009j) Fermi Observations of High-Energy Gamma-Ray Emission from GRB 080916C. *Science*, **323**, 1688.

— (2009k) Fermi/Large Area Telescope Bright Gamma-Ray Source List. *Astrophys. J. Suppl. S.*, **183**, 46. 0902.1340. (Cited on page 25.)

— (2009l) Measurement of the Cosmic Ray $e^+ + e^-$ Spectrum from 20 GeV to 1 TeV with the Fermi Large Area Telescope. *Phys. Rev. Lett.*, **102, 18**, 181101. 0905.0025. (Cited on page 123.)

— (2009m) Modulated High-Energy Gamma-Ray Emission from the Microquasar Cygnus X-3. *Science*, **326**, 1512. (Cited on page 124.)

— (2009n) Pulsed Gamma-rays from PSR J2021+3651 with the Fermi Large Area Telescope. *Astrophys. J.*, **700**, 1059. 0905.4400. (Cited on page 117.)

— (2009o) The on-orbit calibration of the Fermi Large Area Telescope. *Astropart. Phys.*, **32**, 193. (Cited on pages 12, 13, and 17.)

— (2010a) Detection of Gamma-Ray Emission from the Starburst Galaxies M82 and NGC 253 with the Large Area Telescope on Fermi. *Astrophys. J. Lett.*, **709**, L152. 0911.5327. (Cited on page 68.)

— (2010b) Detection of the Small Magellanic Cloud in gamma-rays with Fermi/LAT. *Astron. Astrophys.*, **523**, A46. (Cited on page 67.)

— (2010c) Fermi Large Area Telescope First Source Catalog. *Astrophys. J. Suppl. S.*, **188**, 405. 1002.2280. (Cited on pages 18, 21, 125, and 127.)

— (2010d) Fermi Large Area Telescope observations of Local Group galaxies: detection of M 31 and search for M 33. *Astron. Astrophys.*, **523**, L2. 1012.1952. (Cited on pages 67 and 68.)

— (2010e) Fermi Observations of Cassiopeia and Cepheus: Diffuse Gamma-ray Emission in the Outer Galaxy. *Astrophys. J.*, **710**, 133. 0912.3618. (Cited on page 75.)

— (2010f) Gamma-Ray Emission from the Shell of Supernova Remnant W44 Revealed by the Fermi LAT. *Science*, **327**, 1103. (Cited on page 42.)

— (2010g) Observation of Supernova Remnant IC 443 with the Fermi Large Area Telescope. *Astrophys. J.*, **712**, 459. 1002.2198. (Cited on page 42.)

— (2010h) Observations of Milky Way Dwarf Spheroidal Galaxies with the Fermi-Large Area Telescope Detector and Constraints on Dark Matter Models. *Astrophys. J.*, **712**, 147. 1001.4531. (Cited on page 66.)

— (2010i) Observations of the Large Magellanic Cloud with Fermi. *Astron. Astrophys.*, **512**, A7. (Cited on pages 66 and 67.)

— (2010j) Spectrum of the Isotropic Diffuse Gamma-Ray Emission Derived from First-Year Fermi Large Area Telescope Data. *Phys. Rev. Lett.*, **104, 10**, 101101. 1002.3603. (Cited on pages 15, 54, 59, 116, 135, and 169.)

— (2010k) The Fermi-LAT High-Latitude Survey: Source Count Distributions and the Origin of the Extragalactic Diffuse Background. *Astrophys. J.*, **720**, 435. 1003.0895. (Cited on page 54.)

— (2010l) The First Fermi Large Area Telescope Catalog of Gamma-ray Pulsars. *Astrophys. J. Suppl. S.*, **187**, 460. 0910.1608. (Cited on pages 55, 117, 119, and 125.)

Abdo, A. A. et al. (2011) *Fermi*-LAT Observations of Two Gamma-Ray Emission Components from the Quiescent Sun. Submitted. (Cited on page 123.)

Abraham, J. et al. (2007) Correlation of the highest energy cosmic rays with nearby extragalactic objects. *Science*, **318**, 938. 0711.2256. (Cited on page 40.)

Abraham, J., et al. (2008) Observation of the Suppression of the Flux of Cosmic Rays above 4×10^{19} eV. *Phys. Rev. Lett.*, **101, 6**, 061101. (Cited on page 40.)

Acciari, V. A., et al. (2009) Observation of Extended Very High Energy Emission from the Supernova Remnant IC 443 with VERITAS. *Astrophys. J. Lett.*, **698**, L133. 0905.3291.

Acero, F., et al. (2009) Detection of Gamma Rays from a Starburst Galaxy. *Science*, **326**, 1080. 0909.4651. (Cited on pages 68 and 155.)

Ackermann, M., et al. (2010) Fermi LAT observations of cosmic-ray electrons from 7 GeV to 1 TeV. *Phys. Rev. D*, **82, 9**, 092004. (Cited on pages 13 and 123.)

— (2011) Constraints on the Cosmic-ray Density Gradient Beyond the Solar Circle from Fermi γ-ray Observations of the Third Galactic Quadrant. *Astrophys. J.*, **726**, 81. (Cited on page 97.)

Ade, P. A. R., et al. (2011) Planck Early Results: All sky temperature and dust optical depth from Planck and IRAS: Constraints on the "dark gas" in our galaxy. *ArXiv e-prints*. 1101.2029. (Cited on page 154.)

Adriani, O., et al. (2009a) An anomalous positron abundance in cosmic rays with energies 1.5 – 100 GeV. *Nature*, **458**, 607. 0810.4995. (Cited on page 47.)

— (2009b) New Measurement of the Antiproton-to-Proton Flux Ratio up to 100 GeV in the Cosmic Radiation. *Phys. Rev. Lett.*, **102, 5**, 051101. 0810.4994.

— (2010) PAMELA Results on the Cosmic-Ray Antiproton Flux from 60 MeV to 180 GeV in Kinetic Energy. *Phys. Rev. Lett.*, **105, 12**, 121101. 1007.0821. (Cited on page 46.)

Aharonian, F., et al. (2005) The unidentified TeV source (TeV J2032+4130) and surrounding field: Final HEGRA IACT-System results. *Astron. Astrophys.*, **431**, 197. (Cited on pages 141 and 142.)

— (2006) Discovery of very-high-energy γ-rays from the Galactic Centre ridge. *Nature*, **439**, 695. arXiv:astro-ph/0603021. (Cited on pages 55, 146, and 155.)

— (2007) Detection of extended very-high-energy γ-ray emission towards the young stellar cluster Westerlund 2. *Astron. Astrophys.*, **467**, 1075. arXiv:astro-ph/0703427. (Cited on pages 146 and 155.)

— (2008) Discovery of very high energy gamma-ray emission coincident with molecular clouds in the W 28 (G6.4-0.1) field. *Astron. Astrophys.*, **481**, 401. 0801.3555. (Cited on page 42.)

Aharonian, F. A. and Atoyan, A. M. (2000) Broad-band diffuse gamma ray emission of the galactic disk. *Astron. Astrophys.*, **362**, 937. arXiv:astro-ph/0009009. (Cited on page 56.)

Albert, J., et al. (2007) Discovery of Very High Energy Gamma Radiation from IC 443 with the MAGIC Telescope. *Astrophys. J. Lett.*, **664**, L87. 0705.3119.

Alcaraz, J., et al. (2000) Leptons in near earth orbit. *Phys. Lett. B*, **484**, 10. (Cited on page 123.)

Allen, G. E., et al. (1997) Evidence of X-Ray Synchrotron Emission from Electrons Accelerated to 40 TeV in the Supernova Remnant Cassiopeia A. *Astrophys. J. Lett.*, **487**, L97. arXiv:astro-ph/9707110. (Cited on page 41.)

Allen, R. J., Sancisi, R., and Baldwin, J. E. (1978) Radio continuum observations of the edge-on disc galaxy NGC 891. *Astron. Astrophys.*, **62**, 397. (Cited on page 50.)

Allison, J., et al. (2006) Geant4 developments and applications. *IEEE T. Nucl. Sci.*, **53**, 270. (Cited on page 13.)

Ambrosio, M., et al. (2003) Search for cosmic ray sources using muons detected by the MACRO experiment. *Astropart. Phys.*, **18**, 615. arXiv:hep-ph/0204188. (Cited on page 40.)

Amenomori, M., et al. (2005) Large-Scale Sidereal Anisotropy of Galactic Cosmic-Ray Intensity Observed by the Tibet Air Shower Array. *Astrophys. J. Lett.*, **626**, L29. (Cited on page 40.)

Arimoto, N., Sofue, Y., and Tsujimoto, T. (1996) CO-to-H_2 Conversion Factor in Galaxies. *Publ. Astron. Soc. Jpn.*, **48**, 275.

Aschenbach, B. and Leahy, D. A. (1999) ROSAT all-sky survey map of the Cygnus Loop: Overall structure and comparison with radio map. *Astron. Astrophys.*, **341**, 602. (Cited on page 125.)

Asplund, M., Grevesse, N., and Jacques Sauval, A. (2006) The solar chemical composition. *Nucl. Phys. A*, **777**, 1. arXiv:astro-ph/0410214. (Cited on page 28.)

Atwood, W. B., et al. (2007) Design and initial tests of the Tracker-converter of the Gamma-ray Large Area Space Telescope. *Astropart. Phys.*, **28**, 422. (Cited on page 10.)

— (2009) The Large Area Telescope on the Fermi Gamma-Ray Space Telescope Mission. *Astrophys. J.*, **697**, 1071. 0902.1089. (Cited on pages 10, 17, and 163.)

Audit, E. and Hennebelle, P. (2010) On the structure of the turbulent interstellar clouds . Influence of the equation of state on the dynamics of 3D compressible flows. *Astron. Astrophys.*, **511**, A76. (Cited on page 31.)

Axford, W. I., Leer, E., and Skadron, G. (1977) The Acceleration of Cosmic Rays by Shock Waves. In volume 11 of *International Cosmic Ray Conference*, p. 132. (Cited on page 41.)

Badhwar, G. D., et al. (1977) The cosmic-ray antiproton flux - an upper limit near that predicted for secondary production. *Astrophys. J. Lett.*, **217**, L135. (Cited on page 46.)

Baldini, L., et al. (2006) The Silicon Tracker Readout Electronics of the Gamma-Ray Large Area Space Telescope. *IEEE T. Nucl. Sci.*, **53**, 466. (Cited on page 11.)

— (2007) Preliminary results of the LAT Calibration Unit beam tests. In S. Ritz, P. Michelson, & C. A. Meegan (Editor), *The First GLAST Symposium*, volume 921 of *American Institute of Physics Conference Series*, pp. 190–204. (Cited on page 13.)

Bania, T. M., et al. (2010) The Green Bank Telescope Galactic H II Region Discovery Survey. *Astrophys. J. Lett.*, **718**, L106. 1006.5929. (Cited on page 43.)

Baring, M. G., et al. (1999) Radio to Gamma-Ray Emission from Shell-Type Supernova Remnants: Predictions from Nonlinear Shock Acceleration Models. *Astrophys. J.*, **513**, 311. arXiv:astro-ph/9810158. (Cited on page 145.)

Beck, R. (2009a) Galactic and extragalactic magnetic fields - a concise review. *Astrophys. Space Sci. T.*, **5**, 43. (Cited on page 49.)

— (2009b) Galactic dynamos and galactic winds. *Astrophys. Space Sci.*, **320**, 77. 0711.4700. (Cited on page 50.)

Beichman, C. A., et al. (Editors) (1988) *Infrared astronomical satellite (IRAS) catalogs and atlases. Volume 1: Explanatory supplement*, volume 1.

Bell, A. R. (1978a) The acceleration of cosmic rays in shock fronts. I. *Mon. Not. R. Astron. Soc.*, **182**, 147. (Cited on page 41.)

— (1978b) The acceleration of cosmic rays in shock fronts. II. *Mon. Not. R. Astron. Soc.*, **182**, 443. (Cited on page 41.)

Berezinsky, V. S. (1990) Cosmic Ray Propagation in the Galaxy. In volume 11 of *International Cosmic Ray Conference*, p. 115. (Cited on page 45.)

Bergström, L., Edsjö, J., and Ullio, P. (1998) Possible indications of a clumpy dark matter halo. *Phys. Rev. D*, **58, 8**, 083507. arXiv:astro-ph/9804050. (Cited on page 57.)

Berkhuijsen, E. M., Haslam, C. G. T., and Salter, C. J. (1971) Are the galactic loops supernova remnants? *Astron. Astrophys.*, **14**, 252. (Cited on page 50.)

Bertone, G., Sigl, G., and Silk, J. (2002) Annihilation radiation from a dark matter spike at the Galactic Centre. *Mon. Not. R. Astron. Soc.*, **337**, 98. arXiv:astro-ph/0203488. (Cited on page 57.)

Bertsch, D. L., et al. (1993) Diffuse Gamma-Ray Emission in the Galactic Plane from Cosmic-Ray, Matter, and Photon Interactions. *Astrophys. J.*, **416**, 587. (Cited on pages 97, 136, and 150.)

Bignami, G. F. and Fichtel, C. E. (1974) Galactic Arm Structure and Gamma-Ray Astronomy. *Astrophys. J. Lett.*, **189**, L65. (Cited on pages 55, 60, and 62.)

Binns, W. R., et al. (2007) OB Associations, Wolf Rayet Stars, and the Origin of Galactic Cosmic Rays. *Space Sci. Rev.*, **130**, 439. 0707.4645. (Cited on pages 43 and 44.)

Bland-Hawthorn, J. and Cohen, M. (2003) The Large-Scale Bipolar Wind in the Galactic Center. *Astrophys. J.*, **582**, 246. arXiv:astro-ph/0208553. (Cited on page 45.)

Blandford, R. D. and Ostriker, J. P. (1978) Particle acceleration by astrophysical shocks. *Astrophys. J. Lett.*, **221**, L29. (Cited on page 41.)

Blasi, P., Amato, E., and Caprioli, D. (2007) The maximum momentum of particles accelerated at cosmic ray modified shocks. *Mon. Not. R. Astron. Soc.*, **375**, 1471. arXiv:astro-ph/0612424. (Cited on page 41.)

Bloemen, H. (1989) Diffuse Galactic gamma-ray emission. *Annu. Rev. Astron. Astr.*, **27**, 469. (Cited on pages 55 and 61.)

Bloemen, J. B. G. M., et al. (1984) The radial distribution of galactic gamma rays. II - The distribution of cosmic-ray electrons and nuclei in the outer galaxy. *Astron. Astrophys.*, **135**, 12. (Cited on pages 61, 65, and 93.)

— (1986) The radial distribution of galactic gamma rays. III - The distribution of cosmic rays in the Galaxy and the CO-H_2 calibration. *Astron. Astrophys.*, **154**, 25. (Cited on page 61.)

Bohlin, R. C., Savage, B. D., and Drake, J. F. (1978) A survey of interstellar H I from L_α absorption measurements. II. *Astrophys. J.*, **224**, 132. (Cited on pages 139 and 155.)

Boinee, P., et al. (2003) Gleam: the GLAST Large Area Telescope Simulation Framework. In S. Ciprini, A. de Angelis, P. Lubrano, & O. Mansutti (Editor), *Science with the New Generation of High Energy Gamma-Ray Experiments : Between Astrophysics and Astroparticle Physics*, p. 141. arXiv:astro-ph/0308120. (Cited on page 13.)

Bot, C., et al. (2007) Millimeter dust continuum emission revealing the true mass of giant molecular clouds in the Small Magellanic Cloud. *Astron. Astrophys.*, **471**, 103.

Bowers, R. L. and Deeming, T. (1984) *Astrophysics. Volume 2 - Interstellar matter and galaxies*. (Cited on pages 31 and 32.)

Brand, J. and Blitz, L. (1993) The Velocity Field of the Outer Galaxy. *Astron. Astrophys.*, **275**, 67. (Cited on pages 174 and 175.)

Breiman, L., et al. (1984) *Classification and Regression Trees*. Monterey, CA: Wadsworth and Brooks. (Cited on page 14.)

Breitschwerdt, D. and Komossa, S. (2000) Galactic Fountains and Galactic Winds. *Astrophys. Space Sci.*, **272**, 3. arXiv:astro-ph/9908003. (Cited on page 45.)

Bronfman, L., et al. (1988) A CO survey of the southern Milky Way - The mean radial distribution of molecular clouds within the solar circle. *Astrophys. J.*, **324**, 248. (Cited on page 63.)

— (2000) The radial distribution of OB star formation in the Galaxy. *Astron. Astrophys.*, **358**, 521. arXiv:astro-ph/0006104. (Cited on page 43.)

Burton, W. B., et al. (1975) The overall distribution of carbon monoxide in the plane of the Galaxy. *Astrophys. J.*, **202**, 30. (Cited on page 34.)

Butt, Y. M., et al. (2003) Chandra/Very Large Array Follow-Up of TeV J2032+4131, the Only Unidentified TeV Gamma-Ray Source. *Astrophys. J.*, **597**, 494. arXiv:astro-ph/0302342. (Cited on pages 140, 141, and 143.)

Bykov, A. M. (1999) Nonthermal Particles in Star Forming Regions. In R. Ramaty, E. Vangioni-Flam, M. Cassé, & K. Olive (Editor), *LiBeB Cosmic Rays, and Related X- and Gamma-Rays*, volume 171 of *Astronomical Society of the Pacific Conference Series*, p. 146. (Cited on page 43.)

Bykov, A. M. and Fleishman, G. D. (1992) On non-thermal particle generation in superbubbles. *Mon. Not. R. Astron. Soc.*, **255**, 269. (Cited on page 43.)

Bykov, A. M. and Toptygin, I. N. (2001) A Model of Particle Acceleration to High Energies by Multiple Supernova Explosions in OB Associations. *Astron. Lett.*, **27**, 625. (Cited on pages 43 and 44.)

Camilo, F., et al. (2009) Radio Detection of LAT PSRs J1741-2054 and J2032+4127: No Longer Just Gamma-ray Pulsars. *Astrophys. J.*, **705**, 1. 0908.2626. (Cited on page 141.)

Cappellaro, E., et al. (1997) The rate of supernovae from the combined sample of five searches. *Astron. Astrophys.*, **322**, 431. arXiv:astro-ph/9611191. (Cited on page 42.)

Cardelli, J. A., Clayton, G. C., and Mathis, J. S. (1989) The relationship between infrared, optical, and ultraviolet extinction. *Astrophys. J.*, **345**, 245. (Cited on pages 139 and 155.)

Carruthers, G. R. (1970) Rocket Observation of Interstellar Molecular Hydrogen. *Astrophys. J. Lett.*, **161**, L81. (Cited on page 34.)

Casanova, S. and Dingus, B. L. (2006) Contribution Of Unresolved Point Sources To The Galactic Diffuse Emission. In volume 9 of *AAS/High Energy Astrophysics Division*, p. 21.06. (Cited on page 55.)

Case, G. L. and Bhattacharya, D. (1998) A New Sigma-D Relation and Its Application to the Galactic Supernova Remnant Distribution. *Astrophys. J.*, **504**, 761. arXiv:astro-ph/9807162. (Cited on pages 42 and 43.)

Cash, W. (1979) Parameter estimation in astronomy through application of the likelihood ratio. *Astrophys. J.*, **228**, 939. (Cited on page 22.)

Cash, W., et al. (1980) The X-ray superbubble in Cygnus. *Astrophys. J. Lett.*, **238**, L71. (Cited on page 115.)

Cassam-Chenaï, G., et al. (2004) XMM-Newton observations of the supernova remnant RX J1713.7-3946 and its central source. *Astron. Astrophys.*, **427**, 199. arXiv:astro-ph/0407333. (Cited on page 41.)

Cassé, M., Vangioni-Flam, E., and Paul, J. (1999) Nuclear gamma ray line astronomy in the perspective of the *INTEGRAL* satellite. *Nucl. Phys. A*, **654**, 895. arXiv:astro-ph/9902090. (Cited on page 49.)

Cesarsky, C. J. and Montmerle, T. (1983) Gamma rays from active regions in the galaxy - The possible contribution of stellar winds. *Space Sci. Rev.*, **36**, 173. (Cited on page 145.)

Chevalier, R. A., Kirshner, R. P., and Raymond, J. C. (1980) The optical emission from a fast shock wave with application to supernova remnants. *Astrophys. J.*, **235**, 186. (Cited on page 41.)

Churchwell, E. and the Glimpse team (2005) Selected First Results from the GLIMPSE Survey. In S. Torres-Peimbert & G. MacAlpine (Editor), volume 23 of *Revista Mexicana de Astronomia y Astrofisica Conference Series*, pp. 53–59. (Cited on page 28.)

Clark, G. W., Garmire, G. P., and Kraushaar, W. L. (1968) Observation of High-Energy Cosmic Gamma Rays. *Astrophys. J. Lett.*, **153**, L203. (Cited on page 55.)

Clemens, D. P. (1985) Massachusetts-Stony Brook Galactic plane CO survey - The Galactic disk rotation curve. *Astrophys. J.*, **295**, 422. (Cited on page 174.)

Compton, A. H. (1933) The Significance of Recent Measurements of Cosmic Rays. *Science*, **77**, 480. (Cited on page 39.)

Cordes, J. M. and Lazio, T. J. W. (2002) NE2001.I. A New Model for the Galactic Distribution of Free Electrons and its Fluctuations. *ArXiv Astrophysics e-prints*. arXiv:astro-ph/0207156. (Cited on pages 37 and 122.)

Cramer, H. (1946) *Mathematical Methods of Statistics*. (Cited on page 22.)

Cronin, J. W. (1999) Cosmic rays: the most energetic particles in the universe. *Rev. Mod. Phys. Suppl.*, **71**, 165. (Cited on page 40.)

Crutcher, R. M., Troland, T. H., and Kazes, I. (1987) Magnetic field strengths in molecular clouds. *Astron. Astrophys.*, **181**, 119. (Cited on page 48.)

Dame, T. M., Hartmann, D., and Thaddeus, P. (2001) The Milky Way in Molecular Clouds: A New Complete CO Survey. *Astrophys. J.*, **547**, 792. arXiv:astro-ph/0009217. (Cited on pages 34, 35, 36, 119, 152, and 154.)

Dame, T. M., et al. (1987) A composite CO survey of the entire Milky Way. *Astrophys. J.*, **322**, 706. (Cited on pages 34 and 63.)

Davis, J. E. (2001) The Formal Underpinnings of the Response Functions Used in X-Ray Spectral Analysis. *Astrophys. J.*, **548**, 1010. arXiv:astro-ph/0011068. (Cited on page 16.)

Davis, J. L. and Greenstein, J. L. (1951) The Polarization of Starlight by Aligned Dust Grains. *Astrophys. J.*, **114**, 206. (Cited on page 48.)

de Avillez, M. A. and Breitschwerdt, D. (2004) Volume filling factors of the ISM phases in star forming galaxies. I. The role of the disk-halo interaction. *Astron. Astrophys.*, **425**, 899. arXiv:astro-ph/0407034. (Cited on page 28.)

de Boer, W., et al. (2005) EGRET excess of diffuse galactic gamma rays as tracer of dark matter. *Astron. Astrophys.*, **444**, 51. arXiv:astro-ph/0508617. (Cited on page 57.)

de Vries, H. W., Thaddeus, P., and Heithausen, A. (1987) Molecular and atomic clouds associated with infrared cirrus in Ursa Major. *Astrophys. J.*, **319**, 723. (Cited on page 153.)

Dermer, C. D. (1986a) Binary collision rates of relativistic thermal plasmas. II - Spectra. *Astrophys. J.*, **307**, 47. (Cited on pages 46 and 60.)

— (1986b) Secondary production of neutral pi-mesons and the diffuse galactic gamma radiation. *Astron. Astrophys.*, **157**, 223. (Cited on pages 46 and 60.)

— (2007) The Extragalactic γ Ray Background. In S. Ritz, P. Michelson, & C. A. Meegan (Editor), *The First GLAST Symposium*, volume 921 of *American Institute of Physics Conference Series*, pp. 122–126. 0704.2888. (Cited on page 54.)

Dickey, J. M., et al. (2009) The Outer Disk of the Milky Way Seen in λ 21 cm Absorption. *Astrophys. J.*, **693**, 1250. 0901.0968. (Cited on pages 30, 33, 93, 120, 130, 135, and 150.)

Dickman, R. L. (1975) A survey of carbon monoxide emission in dark clouds. *Astrophys. J.*, **202**, 50. (Cited on page 36.)

Diehl, R., et al. (2006) Radioactive ^{26}Al from massive stars in the Galaxy. *Nature*, **439**, 45. arXiv:astro-ph/0601015. (Cited on pages 42 and 151.)

Digel, S., Thaddeus, P., and Bally, J. (1990) Giant molecular clouds in the outer arm of the galaxy. *Astrophys. J. Lett.*, **357**, L29. (Cited on pages 63 and 153.)

Digel, S. W., et al. (1996) Diffuse High-Energy Gamma-Ray Emission beyond the Solar Circle: The Cepheus and Polaris Flares and the Perseus Arm. *Astrophys. J.*, **463**, 609. (Cited on pages 61, 63, 64, 93, 95, 152, 153, and 175.)

— (2001) EGRET Observations of Monoceros: Diffuse Gamma-Ray Emission in the Outer Galaxy. *Astrophys. J.*, **555**, 12. (Cited on pages 56, 59, 61, 62, 63, 64, 93, 97, and 175.)

Domingo-Santamaría, E. and Torres, D. F. (2006) Hadronic processes within collective stellar winds. *Astron. Astrophys.*, **448**, 613. arXiv:astro-ph/0510769. (Cited on page 145.)

Donato, F., Maurin, D., and Taillet, R. (2002) β-radioactive cosmic rays in a diffusion model: Test for a local bubble? *Astron. Astrophys.*, **381**, 539. arXiv:astro-ph/0108079. (Cited on page 46.)

Draine, B. T. (2003) Interstellar Dust Grains. *Annu. Rev. Astron. Astr.*, **41**, 241. arXiv:astro-ph/0304489. (Cited on page 38.)

Drury, L. O., et al. (2001) Test of galactic cosmic-ray source models - Working Group Report. *Space Sci. Rev.*, **99**, 329. (Cited on page 41.)

Elad, M., et al. (2005) Simultaneous cartoon and texture image inpainting using morphological component analysis. *Appl. Comput. Harmon. A.*, **19**, 340.

Ellison, D. C., Decourchelle, A., and Ballet, J. (2004) Hydrodynamic simulation of supernova remnants including efficient particle acceleration. *Astron. Astrophys.*, **413**, 189. arXiv:astro-ph/0308308. (Cited on page 145.)

Elmegreen, B. G. and Scalo, J. (2004) Interstellar Turbulence I: Observations and Processes. *Annu. Rev. Astron. Astr.*, **42**, 211. arXiv:astro-ph/0404451. (Cited on page 44.)

Esposito, J. A., et al. (1999) In-Flight Calibration of EGRET on the Compton Gamma-Ray Observatory. *Astrophys. J. Suppl. S.*, **123**, 203. (Cited on page 57.)

Evoli, C., et al. (2008) Cosmic ray nuclei, antiprotons and gamma rays in the galaxy: a new diffusion model. *J. Cosmol. Astropart. P.*, **10**, 18. 0807.4730. (Cited on pages 47, 61, and 151.)

Ewen, H. I. and Purcell, E. M. (1951) Observation of a Line in the Galactic Radio Spectrum: Radiation from Galactic Hydrogen at 1,420 Mc./sec. *Nature*, **168**, 356. (Cited on page 30.)

Fermi, E. (1949) On the Origin of the Cosmic Radiation. *Phys. Rev.*, **75**, 1169. (Cited on page 41.)

Ferrand, G. and Marcowith, A. (2010) On the shape of the spectrum of cosmic rays accelerated inside superbubbles. *Astron. Astrophys.*, **510**, A101. 0911.4457. (Cited on page 44.)

Ferrière, K. M. (2001) The interstellar environment of our galaxy. *Rev. Mod. Phys.*, **73**, 1031. arXiv:astro-ph/0106359. (Cited on pages 27, 28, and 42.)

Fichtel, C. E., Simpson, G. A., and Thompson, D. J. (1978) Diffuse gamma radiation. *Astrophys. J.*, **222**, 833. (Cited on page 55.)

Fiebig, D. and Guesten, R. (1989) Strong magnetic fields in interstellar H_2O maser clumps. *Astron. Astrophys.*, **214**, 333. (Cited on page 48.)

Field, G. B., Goldsmith, D. W., and Habing, H. J. (1969) Cosmic-Ray Heating of the Interstellar Gas. *Astrophys. J. Lett.*, **155**, L149. (Cited on page 30.)

Finkbeiner, D. P. (2003) A Full-Sky Hα Template for Microwave Foreground Prediction. *Astrophys. J. Suppl. S.*, **146**, 407. arXiv:astro-ph/0301558. (Cited on page 122.)

Forbush, S. E. (1954) World-Wide Cosmic-Ray Variations, 1937-1952. *J. Geophys. Res.*, **59**, 525. (Cited on page 39.)

Francis, C. and Anderson, E. (2009) Calculation of the local standard of rest from 20574 local stars in the New Hipparcos Reduction with known radial velocities. *New Astron.*, **14**, 615. 0812.4032. (Cited on page 174.)

Froebrich, D. and Rowles, J. (2010) The structure of molecular clouds - II. Column density and mass distributions. *Mon. Not. R. Astron. Soc.*, **406**, 1350. 1004.0117. (Cited on page 121.)

Frühwirth, R., et al. (2000) *Data Analysis Techniques for High-Energy Physics*. (Cited on page 13.)

Funk, S. (2008) VHE Gamma-ray supernova remnants. *Adv. Space Res.*, **41**, 464. arXiv:astro-ph/0701471. (Cited on page 42.)

Gabici, S., Aharonian, F. A., and Blasi, P. (2007) Gamma rays from molecular clouds. *Astrophys. Space Sci.*, **309**, 365. arXiv:astro-ph/0610032. (Cited on page 62.)

Gabici, S., Aharonian, F. A., and Casanova, S. (2009) Broad-band non-thermal emission from molecular clouds illuminated by cosmic rays from nearby supernova remnants. *Mon. Not. R. Astron. Soc.*, **396**, 1629. 0901.4549. (Cited on pages 62 and 146.)

Gaisser, T. K. and Schaefer, R. K. (1992) Cosmic-ray secondary antiprotons - A closer look. *Astrophys. J.*, **394**, 174. (Cited on page 46.)

Gibson, S. J., et al. (2005) A Self-Absorption Census of Cold H I Clouds in the Canadian Galactic Plane Survey. *Astrophys. J.*, **626**, 195. arXiv:astro-ph/0503117. (Cited on page 140.)

Ginzburg, V. L. and Syrovatskii, S. I. (1964) *The Origin of Cosmic Rays*. (Cited on page 40.)

Gold, B., et al. (2010) Seven-Year Wilkinson Microwave Anisotropy Probe (WMAP) Observations: Galactic Foreground Emission. *ArXiv e-prints*. 1001.4555. (Cited on page 122.)

Golden, R. L., et al. (1979) Evidence for the existence of cosmic-ray antiprotons. *Phys. Rev. Lett.*, **43**, 1196. (Cited on page 46.)

Górski, K. M., et al. (2005) HEALPix: A Framework for High-Resolution Discretization and Fast Analysis of Data Distributed on the Sphere. *Astrophys. J.*, **622**, 759. arXiv:astro-ph/0409513. (Cited on page 59.)

Gralewicz, P., et al. (1997) The energy spectrum of cosmic ray protons in the local interstellar medium. *Astron. Astrophys.*, **318**, 925. (Cited on page 56.)

Grasso, D., et al. (2009) On possible interpretations of the high energy electron-positron spectrum measured by the Fermi Large Area Telescope. *Astropart. Phys.*, **32**, 140. 0905.0636. (Cited on page 47.)

Green, D. A. (2009) A revised Galactic supernova remnant catalogue. *B. Astron. Soc. India*, **37**, 45. 0905.3699. (Cited on pages 125 and 127.)

Greisen, K. (1966) End to the Cosmic-Ray Spectrum? *Phys. Rev. Lett.*, **16**, 748. (Cited on page 40.)

Grenier, I. A. (2008) The Galactic gamma-ray club. *ArXiv e-prints*. 0804.0410. (Cited on pages 146 and 156.)

Grenier, I. A., Casandjian, J.-M., and Terrier, R. (2005) Unveiling Extensive Clouds of Dark Gas in the Solar Neighborhood. *Science*, **307**, 1292. (Cited on pages 63, 93, 120, 139, 140, 154, and 155.)

Grenier, I. A., et al. (1989) CO observations of the Cepheus flare. I - Molecular clouds associated with a nearby bubble. *Astrophys. J.*, **347**, 231.

Hall, J. S. (1949) Observations of the Polarized Light from Stars. *Science*, **109**, 166. (Cited on page 48.)

Hanson, M. M. (2003) A Study of Cygnus OB2: Pointing the Way toward Finding Our Galaxy's Super-Star Clusters. *Astrophys. J.*, **597**, 957. arXiv:astro-ph/0307540. (Cited on pages 115, 119, 124, 129, 138, 143, 144, and 145.)

Hartmann, J. (1904) Investigations on the spectrum and orbit of delta Orionis. *Astrophys. J.*, **19**, 268. (Cited on page 27.)

Haslam, C. G. T., Salter, C. J., and Stoffel, H. (1981) *A 408 MHz all-sky continuum survey. 2. The atlas of contour maps*. (Cited on pages 50 and 145.)

Heald, G. H., et al. (2006) Integral Field Unit Observations of NGC 891: Kinematics of the Diffuse Ionized Gas Halo. *Astrophys. J.*, **647**, 1018. arXiv:astro-ph/0604588. (Cited on page 50.)

Heiles, C. and Troland, T. H. (2003) The Millennium Arecibo 21 Centimeter Absorption-Line Survey. II. Properties of the Warm and Cold Neutral Media. *Astrophys. J.*, **586**, 1067. arXiv:astro-ph/0207105. (Cited on pages 28, 30, 31, 34, 65, and 140.)

Heithausen, A. and Thaddeus, P. (1990) The Polaris Flare - Extensive molecular gas near the north celestial pole. *Astrophys. J. Lett.*, **353**, L49.

Helder, E. A., et al. (2009) Measuring the Cosmic-Ray Acceleration Efficiency of a Supernova Remnant. *Science*, **325**, 719. 0906.4553. (Cited on page 41.)

Hess, F. V. (1912) Über Beobachtungen der durchdringenden Strahlung bei sieben Freiballonfahrt. *Physikalische Zeitschrift*, **13**, 1084. (Cited on page 39.)

Higdon, J. C., Lingenfelter, R. E., and Ramaty, R. (1998) Cosmic-Ray Acceleration from Supernova Ejecta in Superbubbles. *Astrophys. J. Lett.*, **509**, L33. (Cited on page 43.)

Hobbs, G. B., Edwards, R. T., and Manchester, R. N. (2006) TEMPO2, a new pulsar-timing package - I. An overview. *Mon. Not. R. Astron. Soc.*, **369**, 655. arXiv:astro-ph/0603381. (Cited on page 117.)

Hollenbach, D. and Salpeter, E. E. (1971) Surface Recombination of Hydrogen Molecules. *Astrophys. J.*, **163**, 155. (Cited on pages 34 and 38.)

Honda, M., et al. (2004) New calculation of the atmospheric neutrino flux in a three-dimensional scheme. *Phys. Rev. D*, **70, 4**, 043008. arXiv:astro-ph/0404457.

Hooper, D. and Dingus, B. (2002) Improving the Angular Resolution of EGRET and New Limits on Supersymmetric Dark Matter Near the Galactic Center. *ArXiv Astrophysics e-prints*. arXiv:astro-ph/0212509. (Cited on page 57.)

Hunter, S. D., et al. (1994) Gamma-ray observations of Ophiuchus with EGRET: The diffuse emission and point sources. *Astrophys. J.*, **436**, 216. (Cited on page 153.)

— (1997) EGRET Observations of the Diffuse Gamma-Ray Emission from the Galactic Plane. *Astrophys. J.*, **481**, 205. (Cited on pages 56, 63, 93, 97, 136, and 150.)

Israel, F. (2000) Extragalactic H_2 and its Variable Relation to CO. In F. Combes & G. Pineau Des Forets (Editor), *Molecular Hydrogen in Space*, p. 293. arXiv:astro-ph/0001250.

Israel, F. P. (1997) H_2 and its relation to CO in the LMC and other magellanic irregular galaxies. *Astron. Astrophys.*, **328**, 471. arXiv:astro-ph/9709194. (Cited on pages 63 and 153.)

Jenkins, E. B. and Meloy, D. A. (1974) A survey with Copernicus of interstellar O VI absorption. *Astrophys. J. Lett.*, **193**, L121. (Cited on page 37.)

Jenkins, E. B. and Savage, B. D. (1974) Ultraviolet photometry from the Orbiting Astronomical Observatory. XIV. An extension of the survey of Lyman-alpha absorption from interstellar hydrogen. *Astrophys. J.*, **187**, 243. (Cited on page 38.)

Jones, F. C. and Ellison, D. C. (1991) The plasma physics of shock acceleration. *Space Sci. Rev.*, **58**, 259. (Cited on page 41.)

Kalberla, P. M. W. and Dedes, L. (2008) Global properties of the H I distribution in the outer Milky Way. Planar and extra-planar gas. *Astron. Astrophys.*, **487**, 951. (Cited on pages 28 and 30.)

Kalberla, P. M. W., et al. (2005) The Leiden/Argentine/Bonn (LAB) Survey of Galactic H I. Final data release of the combined LDS and IAR surveys with improved stray-radiation corrections. *Astron. Astrophys.*, **440**, 775. arXiv:astro-ph/0504140. (Cited on pages 33, 59, and 119.)

Kaltcheva, N. T. and Hilditch, R. W. (2000) The distribution of bright OB stars in the Canis Major-Puppis-Vela region of the Milky Way. *Mon. Not. R. Astron. Soc.*, **312**, 753.

Kamae, T. et al. (2006) Parameterization of γ, $e^{+/-}$, and Neutrino Spectra Produced by *p-p* Interaction in Astronomical Environments. *Astrophys. J.*, **647**, 692. arXiv:astro-ph/0605581. (Cited on pages 46, 56, and 60.)

Kerr, F. J. and Lynden-Bell, D. (1986) Review of galactic constants. *Mon. Not. R. Astron. Soc.*, **221**, 1023. (Cited on pages 28 and 175.)

Knödlseder, J. (2000) Cygnus OB2 - a young globular cluster in the Milky Way. *Astron. Astrophys.*, **360**, 539. arXiv:astro-ph/0007442. (Cited on pages 124 and 128.)

Koch, H. W. and Motz, J. W. (1959) Bremsstrahlung Cross-Section Formulas and Related Data. *Rev. Mod. Phys.*, **31**, 920.

Koyama, K., et al. (1995) Evidence for shock acceleration of high-energy electrons in the supernova remnant SN1006. *Nature*, **378**, 255. (Cited on page 41.)

— (1997) Discovery of Non-Thermal X-Rays from the Northwest Shell of the New SNR RX J1713.7−3946: The Second SN 1006? *Publ. Astron. Soc. Jpn.*, **49**, L7. arXiv:astro-ph/9704140. (Cited on page 41.)

Krymskii, G. F. (1977) A regular mechanism for the acceleration of charged particles on the front of a shock wave. *Akademiia Nauk SSSR Doklady*, **234**, 1306. (Cited on page 41.)

Ladouceur, Y. and Pineault, S. (2008) New perspectives on the supernova remnant G78.2+2.1. *Astron. Astrophys.*, **490**, 197. (Cited on pages 115, 127, and 143.)

Lallement, R. (2009) Some Observations Related to the Origin and Evolution of the Local Bubble/Local ISM. *Space Sci. Rev.*, **143**, 427. (Cited on page 30.)

Langer, W. D., et al. (2010) C^+ detection of warm dark gas in diffuse clouds. *Astron. Astrophys.*, **521**, L17. 1007.3048. (Cited on page 65.)

Larson, R. B. (1981) Turbulence and star formation in molecular clouds. *Mon. Not. R. Astron. Soc.*, **194**, 809. (Cited on page 34.)

Lebrun, F., et al. (1983) Gamma-rays from atomic and molecular gas in the first galactic quadrant. *Astrophys. J.*, **274**, 231. (Cited on pages 36, 55, and 62.)

— (2004) Compact sources as the origin of the soft γ-ray emission of the Milky Way. *Nature*, **428**, 293. (Cited on page 55.)

Leung, C. M., Kutner, M. L., and Mead, K. N. (1982) On the origin and structure of isolated dark globules. *Astrophys. J.*, **262**, 583. (Cited on page 35.)

Lin, Y. C., et al. (1996) EGRET Observations of the Region to the South of $b = -30$ degrees in Phase 1 and Phase 2 of the Compton Gamma Ray Observatory Viewing Program. *Astrophys. J. Suppl. S.*, **105**, 331. (Cited on page 66.)

Lorimer, D. R. (2004) The Galactic Population and Birth Rate of Radio Pulsars. In F. Camilo & B. M. Gaensler (Editor), *Young Neutron Stars and Their Environments*, volume 218 of *IAU Symposium*, p. 105. arXiv:astro-ph/0308501. (Cited on pages 42, 43, and 61.)

Lozinskaya, T. A., Pravdikova, V. V., and Finoguenov, A. V. (2000) The Supernova Remnant G78.2+2.1: New Optical and X-ray Observations. *Astron. Lett.*, **26**, 77. (Cited on page 145.)

Mac Low, M. and McCray, R. (1988) Superbubbles in disk galaxies. *Astrophys. J.*, **324**, 776. (Cited on page 43.)

Maddalena, R. J. and Thaddeus, P. (1985) A large, cold, and unusual molecular cloud in Monoceros. *Astrophys. J.*, **294**, 231.

Maddalena, R. J., et al. (1986) The large system of molecular clouds in Orion and Monoceros. *Astrophys. J.*, **303**, 375.

Magnani, L., et al. (2003) CH, CO, and E(B-V) as Molecular Gas Tracers in a Translucent Cloud. *Astrophys. J.*, **586**, 1111. (Cited on page 64.)

Martins, F., Schaerer, D., and Hillier, D. J. (2005) A new calibration of stellar parameters of Galactic O stars. *Astron. Astrophys.*, **436**, 1049. arXiv:astro-ph/0503346. (Cited on page 124.)

Mashnik, S. G., et al. (2004) CEM2K and LAQGSM codes as event generators for space-radiation-shielding and cosmic-ray-propagation applications. *Adv. Space Res.*, **34**, 1288. arXiv:nucl-th/0210065. (Cited on page 47.)

Mattox, J. R., et al. (1996) The Likelihood Analysis of EGRET Data. *Astrophys. J.*, **461**, 396. (Cited on pages 22 and 24.)

Maurin, D., Putze, A., and Derome, L. (2010) Systematic uncertainties on the cosmic-ray transport parameters. Is it possible to reconcile B/C data with $\delta = 1/3$ or $\delta = 1/2$? *Astron. Astrophys.*, **516**, A67. 1001.0553. (Cited on page 44.)

Maurin, D., Taillet, R., and Donato, F. (2002) New results on source and diffusion spectral features of Galactic cosmic rays: I B/C ratio. *Astron. Astrophys.*, **394**, 1039. arXiv:astro-ph/0206286. (Cited on pages 45, 46, and 47.)

Mavromatakis, F. (2003) Deep optical observations of the supernova remnant G 78.2+2.1. *Astron. Astrophys.*, **408**, 237. (Cited on page 145.)

McCammon, D. and Sanders, W. T. (1990) The soft X-ray background and its origins. *Annu. Rev. Astron. Astr.*, **28**, 657. (Cited on page 37.)

McClure-Griffiths, N. M. and Dickey, J. M. (2007) Milky Way Kinematics. I. Measurements at the Subcentral Point of the Fourth Quadrant. *Astrophys. J.*, **671**, 427. 0708.0870. (Cited on page 28.)

McKee, C. F. and Ostriker, J. P. (1977) A theory of the interstellar medium - Three components regulated by supernova explosions in an inhomogeneous substrate. *Astrophys. J.*, **218**, 148. (Cited on page 37.)

Mel'Nik, A. M. and Efremov, Y. N. (1995) A new list of OB associations in our galaxy. *Astronomy Letters*, **21**, 10.

Mihalas, D. and Binney, J. (1981) Book-Review - Galactic Astronomy - Structure and Kinematics. *Science*, **214**, 829. (Cited on page 29.)

Mill, J. D., et al. (1994) Midcourse space experiment: Introduction to the spacecraft, instruments, and scientific objectives. *J. Spacecraft Rockets*, **31**, 900. (Cited on page 143.)

Mitchell, J. W., et al. (1996) Measurement of 0.25-3.2 GeV Antiprotons in the Cosmic Radiation. *Phys. Rev. Lett.*, **76**, 3057. (Cited on page 46.)

Mohan, R., Dwarakanath, K. S., and Srinivasan, G. (2004a) A High Galactic Latitude H I 21 cm-line Absorption Survey using the GMRT: II. Results and Interpretation. *J. Astrophys. Astron.*, **25**, 185. arXiv:astro-ph/0410627.

— (2004b) A High Galactic Latitude H I 21 cm-line Absorption Survey using the GMRT: I. Observations and Spectra. *J. Astrophys. Astron.*, **25**, 143. arXiv:astro-ph/0410626.

Moiseev, A. A., et al. (2007) The anti-coincidence detector for the GLAST large area telescope. *Astropart. Phys.*, **27**, 339. arXiv:astro-ph/0702581. (Cited on page 11.)

Montmerle, T. (1979) On gamma-ray sources, supernova remnants, OB associations, and the origin of cosmic rays. *Astrophys. J.*, **231**, 95. (Cited on page 43.)

Mori, M. (1997) The Galactic Diffuse Gamma-Ray Spectrum from Cosmic-Ray Proton Interactions. *Astrophys. J.*, **478**, 225. arXiv:astro-ph/9611233. (Cited on page 56.)

— (2009) Nuclear enhancement factor in calculation of Galactic diffuse gamma-rays: A new estimate with DPMJET-3. *Astropart. Phys.*, **31**, 341. 0903.3260. (Cited on pages 46, 56, and 60.)

Morlino, G., et al. (2010) Spatial structure of X-ray filaments in SN 1006. *Mon. Not. R. Astron. Soc.*, **405**, L21. 0912.2972. (Cited on page 42.)

Morris, M., Montani, J., and Thaddeus, P. (1980) Molecular clouds in Orion and Monoceros. In B. H. Andrew (Editor), *Interstellar Molecules*, volume 87 of *IAU Symposium*, pp. 197–202.

Morris, M. and Rickard, L. J. (1982) Molecular clouds in galaxies. *Annu. Rev. Astron. Astr.*, **20**, 517. (Cited on page 36.)

Moscadelli, L., et al. (2009) Trigonometric Parallaxes of Massive Star-Forming Regions. II. Cep A and NGC 7538. *Astrophys. J.*, **693**, 406. 0811.0679.

Moskalenko, I. V. and Porter, T. A. (2009) Isotropic Gamma-Ray Background: Cosmic-Ray-Induced Albedo from Debris in the Solar System? *Astrophys. J. Lett.*, **692**, L54. 0901.0304. (Cited on page 54.)

Moskalenko, I. V., Strong, A. W., and Reimer, O. (1998) Diffuse galactic gamma rays, cosmic-ray nucleons and antiprotons. *Astron. Astrophys.*, **338**, L75. arXiv:astro-ph/9808084. (Cited on page 56.)

Murphy, E. J., et al. (2006) The Effect of Star Formation on the Far-Infrared-Radio Correlation within Galaxies. *Astrophys. J. Lett.*, **651**, L111. arXiv:astro-ph/0609724. (Cited on page 68.)

Nakanishi, H. and Sofue, Y. (2006) Three-Dimensional Distribution of the ISM in the Milky Way Galaxy: II. The Molecular Gas Disk. *Publ. Astron. Soc. Jpn.*, **58**, 847. arXiv:astro-ph/0610769. (Cited on pages 64, 95, and 152.)

Orito, S., et al. (2000) Precision Measurement of Cosmic-Ray Antiproton Spectrum. *Phys. Rev. Lett.*, **84**, 1078. arXiv:astro-ph/9906426. (Cited on page 47.)

Orlando, E. and Strong, A. W. (2007) Gamma rays from halos around stars and the Sun. *Astrophys. Space Sci.*, **309**, 359. arXiv:astro-ph/0607563. (Cited on pages 48, 124, and 143.)

— (2008) Inverse-Compton emission from halos around stars. In volume 2 of *International Cosmic Ray Conference*, pp. 505–508. 0709.3841. (Cited on page 124.)

Orlando, E., et al. (2009) Cosmic-ray electrons, synchrotron and magnetic fields in the Galaxy. *ArXiv e-prints*. 0907.0553. (Cited on page 145.)

Ormes, J. F., et al. (2007) The GLAST Background Model. In S. Ritz, P. Michelson, & C. A. Meegan (Editor), *The First GLAST Symposium*, volume 921 of *American Institute of Physics Conference Series*, pp. 560–561. (Cited on page 13.)

Osterbrock, D. E. (1989) Book-Review - Astrophysics of Gaseous Nebulae and Active Galactic Nuclei. *Sky and Telescope*, **78**, 491. (Cited on page 36.)

Paladini, R., et al. (2003) A radio catalog of Galactic H II regions for applications from decimeter to millimeter wavelengths. *Astron. Astrophys.*, **397**, 213. arXiv:astro-ph/0210226. (Cited on pages 122 and 140.)

Papadopoulos, P. P., Thi, W., and Viti, S. (2002) Molecular Gas in Spiral Galaxies: A New Warm Phase at Large Galactocentric Distances? *Astrophys. J.*, **579**, 270. arXiv:astro-ph/0208535. (Cited on pages 64 and 151.)

Paradis, D., Bernard, J., and Mény, C. (2009) Dust emissivity variations in the Milky Way. *Astron. Astrophys.*, **506**, 745. 0909.3236. (Cited on page 154.)

Parizot, E. (2001) Galactic Cosmic Rays and the Light Elements. *Space Sci. Rev.*, **99**, 61. (Cited on page 43.)

Parizot, E. and Drury, L. (1999) Superbubbles as the source of (6) Li, Be and B in the early Galaxy. *Astron. Astrophys.*, **349**, 673. arXiv:astro-ph/9906298. (Cited on page 43.)

Parizot, E., et al. (2006) Observational constraints on energetic particle diffusion in young supernovae remnants: amplified magnetic field and maximum energy. *Astron. Astrophys.*, **453**, 387. arXiv:astro-ph/0603723. (Cited on page 145.)

Parker, E. N. (1965) The passage of energetic charged particles through interplanetary space. *Planet. Space Sci.*, **13**, 9. (Cited on page 39.)

— (1992) Fast dynamos, cosmic rays, and the Galactic magnetic field. *Astrophys. J.*, **401**, 137. (Cited on page 49.)

Perrot, C. A. and Grenier, I. A. (2003) 3D dynamical evolution of the interstellar gas in the Gould Belt. *Astron. Astrophys.*, **404**, 519. arXiv:astro-ph/0303516. (Cited on page 29.)

Pohl, M. and Esposito, J. A. (1998) Electron Acceleration in Supernova Remnants and Diffuse Gamma Rays above 1 GeV. *Astrophys. J.*, **507**, 327. arXiv:astro-ph/9806160. (Cited on page 56.)

Pollock, A. M. T., et al. (1981) Search for gamma-radiation from extragalactic objects using a likelihood method. *Astron. Astrophys.*, **94**, 116. (Cited on page 22.)

Poppel, W. (1997) The Gould Belt System and the Local Interstellar Medium. *Fundamentals of Cosmic Physics*, **18**, 1. (Cited on page 29.)

Porter, T. A. and Protheroe, R. J. (1997) Cosmic-ray electrons and the diffuse gamma-ray spectrum. *J. Phys. G Nucl. Part.*, **23**, 1765. arXiv:astro-ph/9608182. (Cited on page 56.)

Porter, T. A., et al. (2008) Inverse Compton Origin of the Hard X-Ray and Soft Gamma-Ray Emission from the Galactic Ridge. *Astrophys. J.*, **682**, 400. 0804.1774. (Cited on pages 47, 55, and 124.)

Protassov, R., et al. (2002) Statistics, Handle with Care: Detecting Multiple Model Components with the Likelihood Ratio Test. *Astrophys. J.*, **571**, 545. arXiv:astro-ph/0201547. (Cited on page 23.)

Rando, R. et al. (2009) Post-launch performance of the Fermi Large Area Telescope. *ArXiv e-prints*. 0907.0626. (Cited on pages 18, 20, and 116.)

Rao, R. C. (1945) Information and the accuracy attainable in the estimation of statistical parameters. *Bull. Calcutta Math. Soc.*, **37**, 81. (Cited on page 22.)

Ray, P. S., et al. (2010) Precise Gamma-Ray Timing and Radio Observations of 17 Fermi Gamma-Ray Pulsars. *ArXiv e-prints*. 1011.2468. (Cited on page 117.)

Reimer, A., Pohl, M., and Reimer, O. (2006) Nonthermal High-Energy Emission from Colliding Winds of Massive Stars. *Astrophys. J.*, **644**, 1118. arXiv:astro-ph/0510701. (Cited on page 141.)

Robin, A. and Creze, M. (1986) Stellar populations in the Milky Way - Comparisons of a synthetic model with star counts in nine fields. *Astron. Astrophys. Sup.*, **64**, 53. (Cited on page 121.)

Robin, A. C., et al. (2003) A synthetic view on structure and evolution of the Milky Way. *Astron. Astrophys.*, **409**, 523. (Cited on pages 28 and 121.)

Rolleston, W. R. J., et al. (2000) The Galactic metallicity gradient. *Astron. Astrophys.*, **363**, 537.

Roman-Duval, J., et al. (2010) Dust/gas correlations from Herschel observations. *Astron. Astrophys.*, **518**, L74. 1005.2537. (Cited on page 65.)

Rowles, J. and Froebrich, D. (2009) The structure of molecular clouds - I. All-sky near-infrared extinction maps. *Mon. Not. R. Astron. Soc.*, **395**, 1640. 0902.3403. (Cited on page 121.)

Rubin, V. C., Thonnard, N., and Ford, W. K., Jr. (1978) Extended rotation curves of high-luminosity spiral galaxies. IV - Systematic dynamical properties, SA through SC. *Astrophys. J. Lett.*, **225**, L107. (Cited on page 175.)

Rubin, V. C., et al. (1982) Rotational properties of 23 SB galaxies. *Astrophys. J.*, **261**, 439. (Cited on page 175.)

Rybicki, G. B. and Lightman, A. P. (1986) *Radiative Processes in Astrophysics*. (Cited on page 50.)

Sandell, G. and Sievers, A. (2004) Submillimeter Continuum Observations of NGC 7538. *Astrophys. J.*, **600**, 269.

Sanuki, T., et al. (2000) Precise Measurement of Cosmic-Ray Proton and Helium Spectra with the BESS Spectrometer. *Astrophys. J.*, **545**, 1135. arXiv:astro-ph/0002481.

Sasaki, M., Breitschwerdt, D., and Supper, R. (2004) SNR Surface Density Distribution in Nearby Galaxies. *Astrophys. Space Sci.*, **289**, 283. (Cited on page 42.)

Sato, M., et al. (2007) Absolute Proper Motions of H_2O Masers Away from the Galactic Plane Measured with VERA in the "Superbubble" Region NGC 281. *Publ. Astron. Soc. Jpn.*, **59**, 743. 0704.3315.

Saz Parkinson, P. M., et al. (2010) Eight γ-ray Pulsars Discovered in Blind Frequency Searches of Fermi LAT Data. *Astrophys. J.*, **725**, 571. 1006.2134. (Cited on page 124.)

Schlegel, D. J., Finkbeiner, D. P., and Davis, M. (1998) Maps of Dust Infrared Emission for Use in Estimation of Reddening and Cosmic Microwave Background Radiation Foregrounds. *Astrophys. J.*, **500**, 525. arXiv:astro-ph/9710327. (Cited on pages 38, 39, 63, 120, 121, and 125.)

Schlickeiser, R. (2002) *Cosmic Ray Astrophysics*. (Cited on pages 28, 40, and 45.)

Schneider, N., et al. (2006) A new view of the Cygnus X region. KOSMA ^{13}CO 2 to 1, 3 to 2, and ^{12}CO 3 to 2 imaging. *Astron. Astrophys.*, **458**, 855. (Cited on pages 115, 138, and 143.)

— (2010) The link between molecular cloud structure and turbulence. *ArXiv e-prints*. 1001.2453. (Cited on page 121.)

Scott, P., et al. (2010) Direct constraints on minimal supersymmetry from Fermi-LAT observations of the dwarf galaxy Segue 1. *J. Cosmol. Astropart. P.*, **1**, 31. 0909.3300. (Cited on page 66.)

Scoville, N. Z. and Solomon, P. M. (1975) The galactic distribution of molecules (a CO survey). In T. L. Wilson & D. Downes (Editor), H II *regions and related topics*, volume 42 of *Lecture Notes in Physics, Berlin Springer Verlag*, p. 272. (Cited on page 34.)

Shikaze, Y., et al. (2007) Measurements of $0.2 - 20$ GeV/n cosmic-ray proton and helium spectra from 1997 through 2002 with the BESS spectrometer. *Astroparticle Physics*, **28**, 154. arXiv:astro-ph/0611388.

Shull, J. M. and Beckwith, S. (1982) Interstellar molecular hydrogen. *Annu. Rev. Astron. Astr.*, **20**, 163. (Cited on page 38.)

Skrutskie, M. F., et al. (2006) The Two Micron All Sky Survey (2MASS). *Astronom. J.*, **131**, 1163. (Cited on page 121.)

Smith, A. M. and Stecher, T. P. (1971) Interstellar CO in the Spectrum of ζ Oph. In volume 3 of *Bulletin of the American Astronomical Society*, p. 250. (Cited on page 34.)

Snowden, S. L., et al. (1998) Progress on Establishing the Spatial Distribution of Material Responsible for the 1/4 keV Soft X-Ray Diffuse Background Local and Halo Components. *Astrophys. J.*, **493**, 715. (Cited on page 37.)

Sodroski, T. J., et al. (1989) Dust energetics in the gas phases of the interstellar medium - The origin of the Galactic large-scale far-infrared emission observed by IRAS. *Astrophys. J.*, **336**, 762. (Cited on page 122.)

— (1995) The Ratio of H_2 Column Density to ^{12}CO Intensity in the Vicinity of the Galactic Center. *Astrophys. J.*, **452**, 262. (Cited on page 63.)

— (1997) A Three-dimensional Decomposition of the Infrared Emission from Dust in the Milky Way. *Astrophys. J.*, **480**, 173. (Cited on pages 122 and 142.)

Sofue, Y., Honma, M., and Omodaka, T. (2009) Unified Rotation Curve of the Galaxy – Decomposition into de Vaucouleurs Bulge, Disk, Dark Halo, and the 9-kpc Rotation Dip –. *Publ. Astron. Soc. Jpn.*, **61**, 227. 0811.0859. (Cited on page 174.)

Solomon, P. M. and Barrett, J. W. (1991) The CO-H_2 Mass Conversion Factor. In F. Combes & F. Casoli (Editor), *Dynamics of Galaxies and Their Molecular Cloud Distributions*, volume 146 of *IAU Symposium*, p. 235.

Spitzer, L. (1958) Mass Exchange with the Interstellar Medium and the Formation of Type I Stars. *Ricerche Astronomiche*, **5**, 445. (Cited on page 49.)

Sreekumar, P., et al. (1992) Observations of the Large Magellanic Cloud in high-energy gamma rays. *Astrophys. J. Lett.*, **400**, L67. (Cited on page 65.)

Stecker, F. W. (1970) The Cosmic γ-Ray Spectrum from Secondary Particle Production in Cosmic-Ray Interactions. *Astrophys. Space Sci.*, **6**, 377. (Cited on page 46.)

Stecker, F. W., Hunter, S. D., and Kniffen, D. A. (2008) The likely cause of the EGRET GeV anomaly and its implications. *Astroparticle Physics*, **29**, 25. 0705.4311. (Cited on page 56.)

Stecker, F. W. and Jones, F. C. (1977) The galactic halo question - New size constraints from galactic gamma-ray data. *Astrophys. J.*, **217**, 843. (Cited on pages 61 and 151.)

Straižys, V., Corbally, C. J., and Laugalys, V. (1999) Interstellar Extinction Law in the Vicinity of the North America and Pelican Nebulae. *Baltic Astronomy*, **8**, 355. (Cited on pages 139 and 155.)

Strong, A. W. (2007) Source population synthesis and the Galactic diffuse gamma-ray emission. *Astrophys. Space Sci.*, **309**, 35. arXiv:astro-ph/0609359. (Cited on page 55.)

— (2011) Interstellar gamma rays and cosmic rays: new insights from Fermi-LAT AND INTEGRAL. *ArXiv e-prints*. 1101.1381. (Cited on page 156.)

Strong, A. W. and Mattox, J. R. (1996) Gradient model analysis of EGRET diffuse Galactic γ-ray emission. *Astron. Astrophys.*, **308**, L21. (Cited on pages 61, 63, 64, 152, and 154.)

Strong, A. W. and Moskalenko, I. V. (1998) Propagation of Cosmic-Ray Nucleons in the Galaxy. *Astrophys. J.*, **509**, 212. arXiv:astro-ph/9807150. (Cited on pages 45, 46, and 151.)

Strong, A. W., Moskalenko, I. V., and Ptuskin, V. S. (2007) Cosmic-Ray Propagation and Interactions in the Galaxy. *Annu. Rev. Nucl. Part. S.*, **57**, 285. arXiv:astro-ph/0701517. (Cited on pages 44, 46, and 47.)

Strong, A. W., Moskalenko, I. V., and Reimer, O. (2000) Diffuse Continuum Gamma Rays from the Galaxy. *Astrophys. J.*, **537**, 763. arXiv:astro-ph/9811296. (Cited on page 56.)

— (2004a) Diffuse Galactic Continuum Gamma Rays: A Model Compatible with EGRET Data and Cosmic-Ray Measurements. *Astrophys. J.*, **613**, 962. arXiv:astro-ph/0406254. (Cited on pages 56, 57, 93, and 151.)

Strong, A. W., et al. (1988) The radial distribution of galactic gamma rays. IV - The whole galaxy. *Astron. Astrophys.*, **207**, 1. (Cited on pages 55, 61, 63, and 93.)

— (2004b) The distribution of cosmic-ray sources in the Galaxy, γ-rays and the gradient in the CO-to-H_2 relation. *Astron. Astrophys.*, **422**, L47. arXiv:astro-ph/0405275. (Cited on pages 61, 63, 64, 93, 95, 151, 152, and 153.)

— (2010) Global Cosmic-ray-related Luminosity and Energy Budget of the Milky Way. *Astrophys. J. Lett.*, **722**, L58. 1008.4330. (Cited on pages 67 and 69.)

Struve, O. and Elvey, C. T. (1938) Emission Nebulosities in Cygnus and Cepheus. *Astrophys. J.*, **88**, 364. (Cited on page 37.)

Su, M., Slatyer, T. R., and Finkbeiner, D. P. (2010) Giant Gamma-ray Bubbles from Fermi-LAT: Active Galactic Nucleus Activity or Bipolar Galactic Wind? *Astrophys. J.*, **724**, 1044. 1005.5480. (Cited on page 45.)

Taillet, R. and Maurin, D. (2003) Spatial origin of Galactic cosmic rays in diffusion models. I. Standard sources in the Galactic disk. *Astron. Astrophys.*, **402**, 971. arXiv:astro-ph/0212112.

Tammann, G. A., Loeffler, W., and Schroeder, A. (1994) The Galactic supernova rate. *Astrophys. J. Suppl. S.*, **92**, 487. (Cited on page 42.)

Taylor, A. R., et al. (2003) The Canadian Galactic Plane Survey. *Astronom. J.*, **125**, 3145. (Cited on page 119.)

Tenorio-Tagle, G. (1979) The gas dynamics of H II regions. I - The champagne model. *Astron. Astrophys.*, **71**, 59. (Cited on page 146.)

The VERITAS Collaboration (2009) A connection between star formation activity and cosmic rays in the starburst galaxy M82. *Nature*, **462**, 770. 0911.0873. (Cited on pages 68 and 155.)

Thompson, D. J., et al. (1993) Calibration of the Energetic Gamma-Ray Experiment Telescope (EGRET) for the Compton Gamma-Ray Observatory. *Astrophys. J. Suppl. S.*, **86**, 629. (Cited on page 56.)

Uchiyama, Y., et al. (2002) ASCA View of the Supernova Remnant γ Cygni (G78.2+2.1): Bremsstrahlung X-Ray Spectrum from Loss-flattened Electron Distribution. *Astrophys. J.*, **571**, 866. arXiv:astro-ph/0202414. (Cited on page 145.)

— (2007) Extremely fast acceleration of cosmic rays in a supernova remnant. *Nature*, **449**, 576. (Cited on page 41.)

Ungerechts, H., Umbanhowar, P., and Thaddeus, P. (2000) A CO Survey of Giant Molecular Clouds near Cassiopeia A and NGC 7538. *Astrophys. J.*, **537**, 221.

Uyanıker, B., et al. (2001) The Cygnus superbubble revisited. *Astron. Astrophys.*, **371**, 675. (Cited on pages 115, 122, 124, 140, and 141.)

Völk, H. J. (1983) Cosmic-ray acceleration and transport, and diffuse galactic gamma-ray emission. *Space Sci. Rev.*, **36**, 3. (Cited on pages 146 and 156.)

Wegner, W. (2003) The total-to-selective extinction ratio determined from near IR photometry of OB stars. *Astronomische Nachrichten*, **324**, 219. (Cited on pages 38, 139, and 155.)

Weinstein, A. et al. (2009) The VERITAS Survey of the Cygnus Region of the Galactic Plane. In D. J. Thompson (Editor), *Proceedings of 2009 Fermi Symposium*, eConf C0911022. 0912.4492. (Cited on pages 127, 128, 141, and 143.)

Wiedenbeck, M. E., et al. (2000) Constraints on cosmic-ray acceleration and transport from isotope observations. In R. A. Mewaldt, J. R. Jokipii, M. A. Lee, E. Möbius, & T. H. Zurbuchen (Editor), *Acceleration and Transport of Energetic Particles Observed in the Heliosphere*, volume 528 of *American Institute of Physics Conference Series*, pp. 363–370. (Cited on page 46.)

Wilk, S. S. (1938) The large-sample distribution of the likelihood ratio for testing composite hypotheses. *Ann. Math. Stat.*, **9**, 60. (Cited on page 23.)

Wilson, B. A., et al. (2005) A uniform CO survey of the molecular clouds in Orion and Monoceros. *Astron. Astrophys.*, **430**, 523. arXiv:astro-ph/0411089.

Wolfire, M. G., Hollenbach, D., and McKee, C. F. (2010) The Dark Molecular Gas. *Astrophys. J.*, **716**, 1191. 1004.5401. (Cited on pages 64, 65, 140, 151, and 155.)

Wolfire, M. G., et al. (2003) Neutral Atomic Phases of the Interstellar Medium in the Galaxy. *Astrophys. J.*, **587**, 278. arXiv:astro-ph/0207098. (Cited on pages 28 and 31.)

Yan, H. and Lazarian, A. (2004) Cosmic-Ray Scattering and Streaming in Compressible Magnetohydrodynamic Turbulence. *Astrophys. J.*, **614**, 757. arXiv:astro-ph/0408172. (Cited on page 44.)

Yusifov, I. and Küçük, I. (2004) Revisiting the radial distribution of pulsars in the Galaxy. *Astron. Astrophys.*, **422**, 545. arXiv:astro-ph/0405559. (Cited on pages 42 and 43.)

Zatsepin, G. T. and Kuz'min, V. A. (1966) Upper Limit of the Spectrum of Cosmic Rays. *Soviet Journal of Experimental and Theoretical Physics Letters*, **4**, 78. (Cited on page 40.)

CONTENTS